# Self-organized Nanoscale Patterning under Ion Beam Irradiation

by

Qiangmin Wei

A dissertation submitted in partial fulfillment
of the requirements for the degree of
Doctor of Philosophy
(Materials Science and Engineering)
in The University of Michigan
2009

Doctoral Committee:

Professor Lumin Wang, Chair
Professor Wei Lu
Professor Xiaoqing Pan
Professor Anton Van der Ven

To my family

## ACKNOWLEDGEMENTS

First and foremost I would like to thank my advisor Prof. Lumin Wang for providing this great research opportunity, consistent encouragement and financial support through the entire Ph.D. work that made this work possible. His insightful discussion, patience in explaining science, critical thinking, and direction of the project have been invaluable.

I would like to thank other members in the defense committee, Prof. Wei Lu, Prof. Xiaoqing Pan, and Prof. Anton Van der Ven for their guidance and suggestions that helped shape this thesis.

I am also grateful to Prof. Jie Lian at Rensselaer Polytechnic Institute for his valuable comments and encouragement. I would like to thank Dr. Kai Sun in the Electron Microbeam Analysis Laboratory (EMAL) for his tremendous support on microscopy experiments and his hospitality of passing on to me his expertise in materials nanostructure and composition characterization. I would like to thank Dr. Sha Zhu for teaching me sample preparation. My special thanks go to Dr. Kun-Dar Li for his generous help on simulation; Dr. Ovidiu Toader and Dr. Fabian Naab at the Michigan Ion Beam Laboratory for the assistance in ion irradiation experiments; Dr. Fuxiang Zhang in the department of Geological Sciences and Prof. Qihuo Wei at Kent State University for helping with optical measurements; Dr. Yanwen Zhang in Pacific Northwest National Laboratory for providing samples; Dr. Haiping Sun and Ying Qi in the EMAL for their assistant on experiments.

I would like to thank my colleagues and friends Dr. Yanbin Chen, Dr, Zhijie Jiao, Dr. Tianhua Ding, Dr. Jiaming Zhang, Weixing Li, Alex Perez-Bergquist, Michaela Eddy, Pantip Ampornrat and Por Pavenayotin. I appreciate their friendship and support during this period. Various other individuals (Jiashi Miao, Wei Guo, Yiying Zhao, and Xiang Li) as well as the technical and administrative staff in Department of Nuclear Engineering and Radiological and Department of Sciences Materials Science and Engineering at the University of Michigan deserve mention.

I would like to express my deepest gratitude to my parents, my wife, Xuemei and my daughter, Maleah. Without their understanding and support, I would not make it through.

# TABLE OF CONTENTS

# LIST OF FIGURES

**Figure**

# LIST OF TABLES

**Table**

# LIST OF APPENDICES

**Appendix**

# ABSTRACT

Self-organized Nanoscale Patterning under Ion Beam Irradiation

by
Qiangmin Wei

Chair: Lumin Wang

Energetic ion bombardment can lead to the development of complex and diverse nanostructures on or near the material surface. One of interests in these structures is the formation of highly ordered patterns whose optical, electronic and magnetic properties are different from bulk materials and might have important technological applications. In this work, the ordered pattern formation in a broad range of materials was fabricated and investigated, including one-dimension periodic arrays of nanoparticles and ripples, two-dimensional patterns of highly ordered Ga droplet on the surface of GaAs, ordered nanocrystals on argon ion sputtered polymer film, hexagonally ordered nanoholes on the surface of Ge, and three-dimensional void/bubble formation inside materials. In addition, angular and curvature dependence of sputtering yield was also discussed. Special emphasis was placed on the fundamental understanding of ordered pattern formation under irradiation. Sputtering, redeposition, viscous flow, and surface diffusion which are responsible for ordered pattern formation are investigated through a combination of modeling and in situ and ex-situ observations. It was proposed that a common feature of mechanism responsible for pattern formation during ion irradiation is the anisotropic

movement of species. This anisotropy movement can take place either on the surface of materials driven by the off-normal angle ion bombardment, for example ripple and ordered droplet formation, or inside materials driven by crystalline structure, such as void/bubble lattice formation. Other mechanisms, such as redeposition, viscous flow and surface diffusion can enhance or weaken the tendency of the pattern formation and give rise to the change of initial patterns with a long time limit, such as ordered hole formation on Ge surface. It was suggested that dynamic balance between anisotropic mass loss and gain can lead to the formation of highly ordered Ga droplet on the ion irradiated GaAs surface. With computer modeling, it was found that nonlinear effects for long time limit determine the hexagonally ordered, honeycomb-like structure of nano-scale holes induced by the ion beam bombardment on the Ge surface.

# CHAPTER I

# Introduction

Ion beam irradiation provides a highly controlled means of manipulating materials microstructure at the nano-scale and represents an effective way to modify materials physical properties (e.g., structural, optical, electric and magnetic properties). One of particular interests in this ion-induced structures is the self-assembly of ordered patterns on the surface or in the interior of materials. This chapter provides technological context and background fundamentals relevant to this research. A short summary of experimental observations on one dimensional to three dimensional ordered patterns and widely accepted models for ion-induced pattern formation are presented to provide a basis of fabrication and analysis of ordered patterns in this work.

## 1.1 Self-assembly of Ordered Patterns under Ion Beam Bombardment

Evolution of structure under ion bombardment has been intensively investigated during last three decades. For low ion energy, the structure modification mainly occurs on the surface, thus leading to clean, modify or remove material from the surfaces for different purposes. One to two dimensionally ordered patterns such as ripples and dots are formed in this regime. Under high ion energy bombardment, ion-solid interaction mainly occurs below the surface, and thus three dimensionally

ordered patterns such as void or bubble lattice are created inside materials. It was found that existence of fully or partially ordered ano- and microstructure in materials under energetic particle irradiation is universal, and not confined to one type of material.

### 1.1.1 Ripple formation

Different morphologies of quadratic, hexagonal or wave like patterns under oblique or normal incidence were demonstrated using low energy ion-bombardment of solid surfaces. The first experimental observation of ordered pattern induced by ion beam is ripple. In 1962, Navez *et al.* observed for the first time ripple formation by bombarding a glass surface with an ion beam of air at 4 keV [1]. The experiment was performed on a clean glass surface for 6 h at incident angles ranging from 30° to 80°. Depending on the angle of incidence, two oriented ripples was found. For incident angles less than a critical value, the ripples are perpendicular to the ion beam direction (Fig. 1.1b), while they rotate by 90° when the beam reaches the surface at incidence larger than this critical value (Fig. 1.1c). In contrast, when the bombardment is performed at normal incidence, they observed a regular structure formed by randomly distributed dots with a diameter of about 40 nm (Fig. 1.1a). Since this discovery, ripples have been found on a large variety of materials, such as metals [2–4], semiconductors [5–11], and insulators [12, 13]. The universality of the formation process is evident.

Experimental parameters that determine the ripple features include incident angle, temperature, flux, fluence, and ion energy. A number of research groups have provided detailed quantitative results regarding the ripple formation.

As shown in Fig. 1.1, the first variable that is rather easy to change in sputtering is the angle of incidence of the incoming ions relative to the surface normal. It was

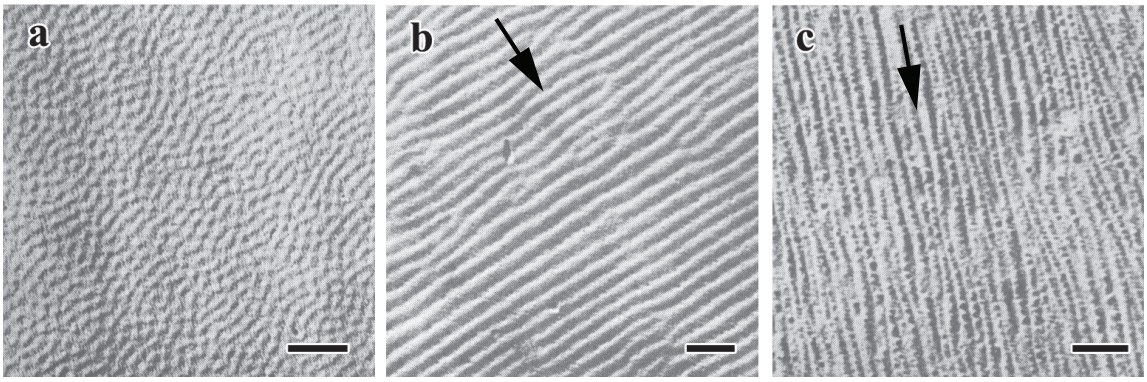


Figure 1.1: Experimental observations of ripple formation on a glass surface subjected to 4 keV ion bombardment at incidence of (a) 0, (b) 60°, and (c) 80°. Arrows show projected ion beam direction. Scale bar=250 nm [1].

shown that ripples are only formed for a limited range of incident angles, which, depending on materials and ions, typically vary between 30° and 70°. For example, Stevie *et al.* found that ripple can be induced only in the incident angles between 39° and 52° in experiments of 6 and 8 keV $O_2^+$ sputtering of Si and 8, 5.5 and 2.5 keV $O_2^+$ sputtering of GaAs [14]. Similarly, For Si bombarded by 10 keV $O_2^+$ ion, Wittmaack found that ripple formation occurs at incident angles between 32° and 58° [15]. In a more recent analysis of ripple wave vector rotation on Cu(110) surface under $Ar^+$ ion bombardment with 1 keV energy at a temperature in the range of 180∼450 K, Rusponi found two types of oriented ripples and shown that critical incident angle is around 65° [3, 4].

Temperature dependence of ripple formation has been also reported in references [16–18]. Two different behaviors have been observed: exponential dependence of the ripple wavelength on the temperature at high temperature, while at low temperature the wavelength keeps constant. For GaAs bombarded by 17.5 keV $Cs^+$ ions, Maclaren *et al.* found that ripple wavelength increased from 0.89 to 2.1 $\mu$m as the temperature increased from 45°C to 100°C while no ripple was observed above

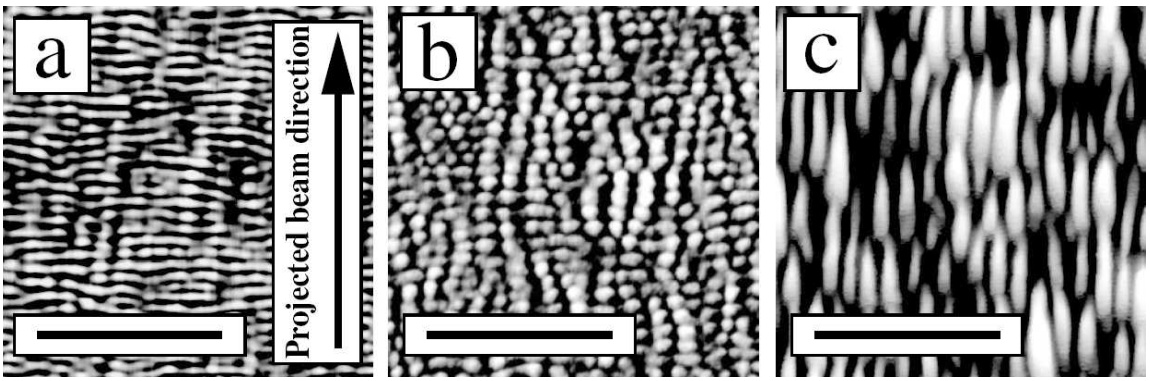


Figure 1.2: Dependence of ripple evolution on fluence at (a) $8.4\times10^{18}$ ions/cm$^2$, (b) $2.2\times10^{19}$ ions/cm$^2$, and (c) $4.8\times10^{19}$ ions/cm$^2$. Incident angle 60°, scale bar 5 $\mu$m, temperature 657°C, energy 500 eV [19].

100°C [16]. Umbach *et al.* have studied the effects of temperature on the ripple formation on the 2.0 keV $Ar^+$ eroded $SiO_2$ in the temperature ranging from room temperature to 800°C [17]. They found that for the temperature larger than 400°C the ripple wavelength increases exponentially while for the temperature less than 400°C the ripple wavelength is independent of temperature.

Recently, more effort has been devoted to the study of ripple evolution with fluence during ion bombardment. A variety of intriguing phenomena take place for a long time bombardment, including rotation of tipple [19–21], roughening [20], coarsening [19, 22], and propagation [13, 23]. Brown *et al.* have studied the surface development of Si(111) under high fluence ion bombardment with ion energy of 500 eV at temperature from 600°C to 750° [19]. A superposition of ripples oriented with the wave vector parallel to and perpendicular to ion beam was found (Fig. 1.2). For Si(111) bombarded by 30 keV Ga ions, Habenicht *et al.* found that the propagation direction of ripples on Si by ion bombardment is opposite to that predicted by current models [13]. The same result has been reported by Alkemade on the ion bombardment of $SiO_2$ [23]. On the other hand, it was also found that ordering can

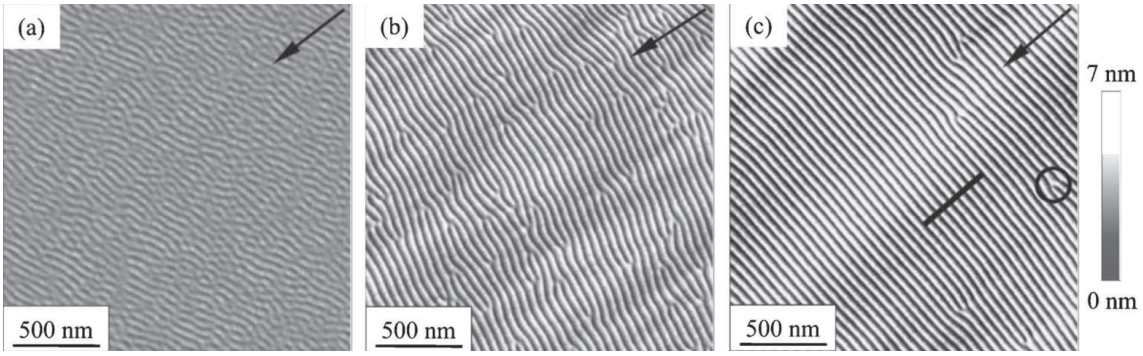


Figure 1.3: Highly ordered ripples were created at high fluence. (a) $3.36\times10^{17}$ ions/cm$^2$, (b) $2.24\times10^{18}$ ions/cm$^2$, and (c) $1.34\times10^{19}$ ions/cm$^2$. Arrows show projected ion beam direction. Incident angle 15°, room temperature, energy 500 eV [24].

be improved for a long time bombardment. As shown in Fig. 1.3, highly ordered ripples were created on the surface of Si subject to 1.2 keV $Kr^+$ ions for the fluence up to $1.34\times10^{19}$ ions/cm$^2$ [24].

The effects of ion energy on the ripple wavelength were reported in [8,17,25]. The experiments indicate that the ripple wavelength increases linearly with increasing ion energy. The range of ion energy for ripple formation was also reported by Vajo *et al.* [8]. When $Ar^+$ ions was used on the Si(100) surface, it was found that ripples can not be induced for energy less than 1.5 keV or larger than 9 keV.

### 1.1.2 Dot formation

Under normal bombardment, it is well known that randomly distributed dots instead of ripples can be created as shown in Fig. 1.1a. Although this behavior was discovered in 1962, the ordered dots was reported more than 30 years later. As shown in Fig. 1.4, in 1999, Facsko *et al.* reported that quantum dots with 35 nanometers in diameter can be induced by ion sputtering under normal incidence on gallium antimonide surfaces [26]. In this experiment, a commercial ion-sputtering system with low-energy $Ar^+$ of 420 eV ions were used. The typical ion flux in the

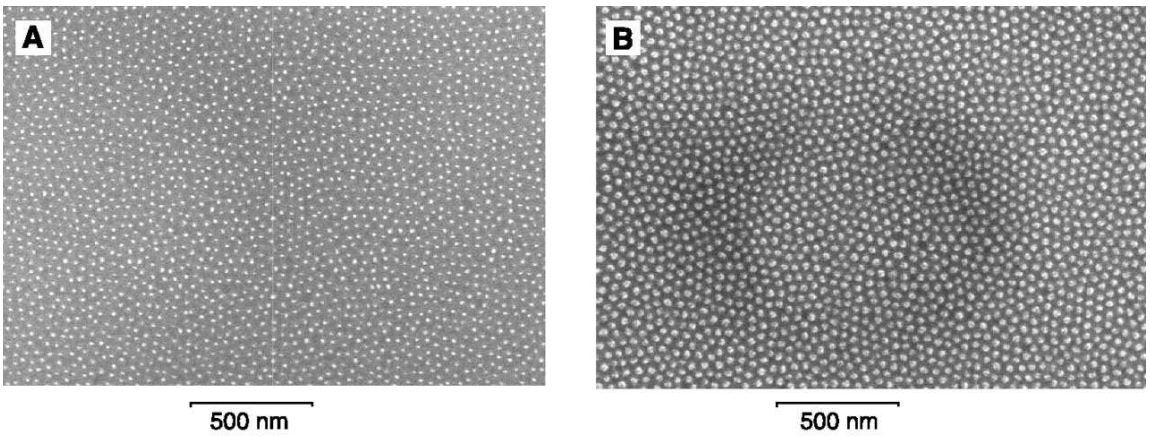


Figure 1.4: SEM images of highly ordered cones on a GaSb(100) surface show the temporal evolution of dot formation during ion sputtering at (A) $4\times10^{17}$ cm$^{-2}$ (40 s), (B) $2\times10^{18}$ cm$^{-2}$ (200 s) [26].

experiments was $1 \times 10^{16}$cm$^{-2}$s$^{-1}$. It was found that size and shape of regular pattern of dots depend on the ion fluence (Fig. 1.4). The ripple formation mechanism was employed by Fracsko *et al.* to explain the dot formation.

Another condition for dot formation is off-normal bombardment with simultaneous sample rotation [24, 27–32]. Frost et al. first reported that for rotated InP target under oblique ion incidence well ordered quantum dots can be formed (Fig. 1.5) [27]. The samples used in their work were commercially available epi-polished semi-insulating (100) InP substrates. InP surfaces were simultaneously rotated and sputtered at an incidence angle 40°, ion energy 500 eV, and ion flux 150 $\mu$Acm$^{-2}$. As shown in Fig. 1.5, immediately after the start of sputtering mound-like or cone-like structures begin to appear, their lateral size and height become larger as the sputtering proceeds. For longer sputter times, the lateral size of the mound saturates and the topography changes from a more irregular to a highly regular hexagonal pattern of mounds (Fig. 1.5c). The relationship between dot structure and incident angle was also studied. Up to incidence 50°, the close-packed hexagonal

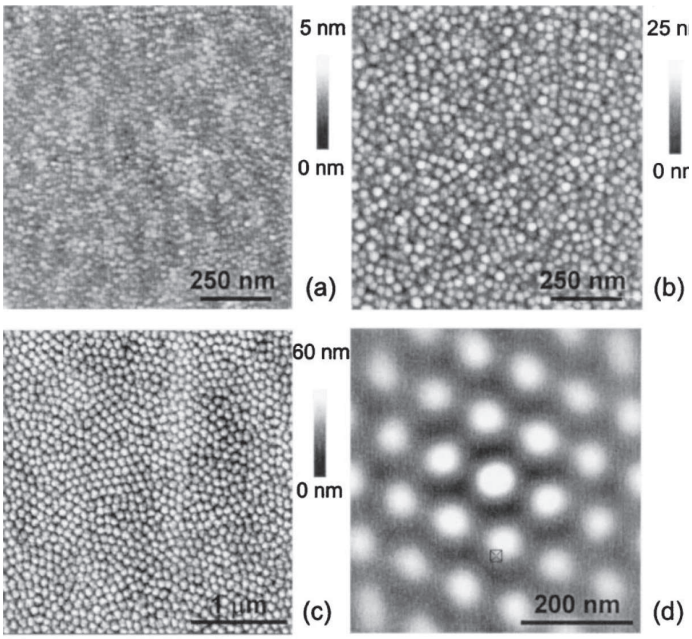


Figure 1.5: AFM images showing a sequence of the evolution of InP surface topography with increasing sputter time at (a) 10 s, (b) 40 s, and (c) 9600 s. (d) Represents the two-dimensional autocorrelation function calculated from a magnified area of image (c) [27].

mound pattern is conserved; for further increasing of incidence the periodic pattern vanishes. Last, at incidence 80° mound formation again appears, but with a smaller mound size as for incidence 50°. Furthermore, the observed conelike structures are oriented toward the direction of the ion beam incidence.

Recently, Zebri *et al.* shown that under off-normal bombardment without sample rotation both ordered ripple and dot are formed during 2 keV $Xe^+$ ion beam erosion of Si surfaces at room temperature [33]. The transition from ripple to dots was observed when increasing incident angle (Fig. 1.6). The conditions for different feature formations are summarized in Fig. 1.7. At near normal ion incidence angle of 5°, ion-induced ripples with the wave vector parallel to the projected ion beam direction evolve on the surface (Fig. 1.6a). This topography is maintained up to incidence of 23°. With further increase of the ion incidence angle, a rotated ripple with a ripple wave vector no longer perpendicular to the projection of the ion beam

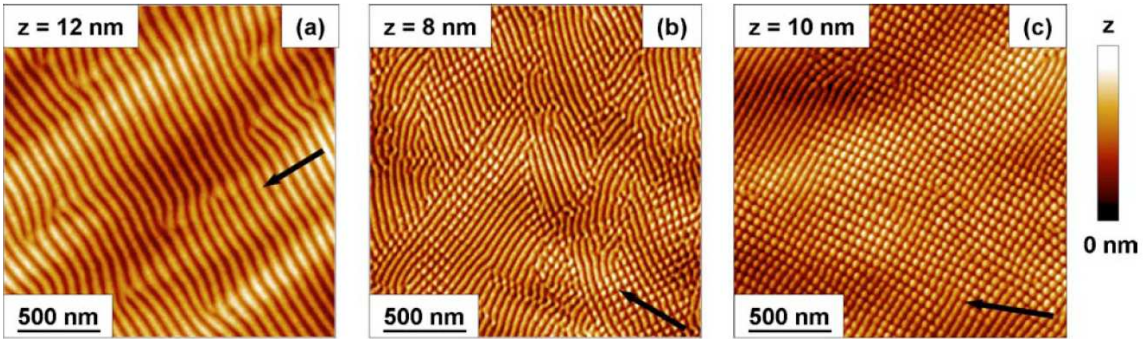


Figure 1.6: AFM images of 2 keV $Xe^+$ ion beam eroded Si surfaces at different ion incidence angles: (a) 5°, (b) 25°, and (c) 26°. Ion fluence =$5.8 \times 10^{18}$ $cm^{-2}$ [33].

appears (Fig. 1.6b). Another interesting observation is that ripples start to transform into dots ordered along previously existing ripples. By increasing the ion incidence angle to 26°, the topography is dominated by dot structures, appearing along and perpendicular to rotated ripples, respectively (Fig. 1.6c). An almost perfect square array of dots was formed. These important observations are contrary to the up to date experiments and theoretical models. Furthermore, the whole process of ripple-dot pattern transition is not predicted by the theory and not observed up to now in the experiments.

Similar results have also been obtained by Zebri *et al.* on ion eroded Ge target (Fig. 1.8) [30]. Without rotation, the ordered dots are observed at the incident angle of 20° on Ge surfaces during energy 2 keV $Xe^+$ ion beam erosion at room temperature. For normal ion incidence, nanoscale dot structures are formed while for slightly off normal incidence these dots transform into a highly ordered ripple pattern. For more large ion incidence $15 \sim 20°$, a dot pattern develops, showing a hexagonal ordering of the individual dots. Finally, for incidence angles greater than 25° the dot pattern transforms into smooth surfaces with some stochastic variations. It was suggested that an anisotropically generalized version of a damped nonlocal

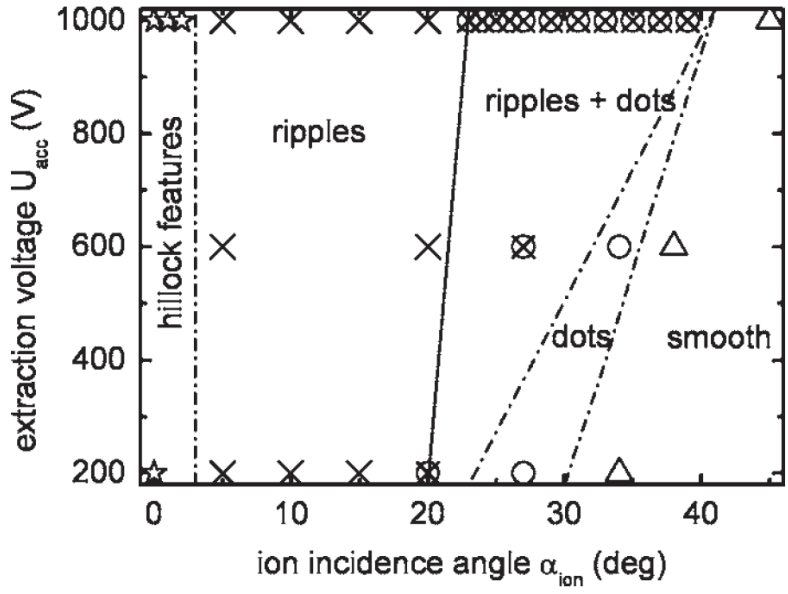


Figure 1.7: Topography diagram for 2 keV $Xe^+$ ion beam erosion of Si surfaces for different acceleration voltages and ion incidence angles. The symbols denote different patterns obtained for different pairs of energy and incident angle: $\star$, hillock structures; $\times$, parallel mode ripples; $\otimes$, co-existing ripples and dots; $\bigcirc$, dots; $\triangle$, smooth surfaces [33].

Kuramoto-Sivashinsky equation could be used to model ion beam erosion under normal and oblique incidences.

Within a few years following the discovery of ion-induced dot formation in GaSb, researchers determined that ordered arrays of dots could be formed under certain conditions. Subsequently, it was also find that ordered arrays of dots can be formed in many semiconductors. Table. 1.1 shows the summary of the experimental observations of ordered dot formation in semiconductors. Because the size of dots is the function of fluence, we show the typical size and corresponding fluence in the table.

### 1.1.3 Void/bubble formation

Under high energy ion bombardment, the defects are mainly induced inside the target by displacement of target atoms from their regular lattice sites. Three dimensional ordered patterns, including void lattice [41–43], bubble lattice [44–46],

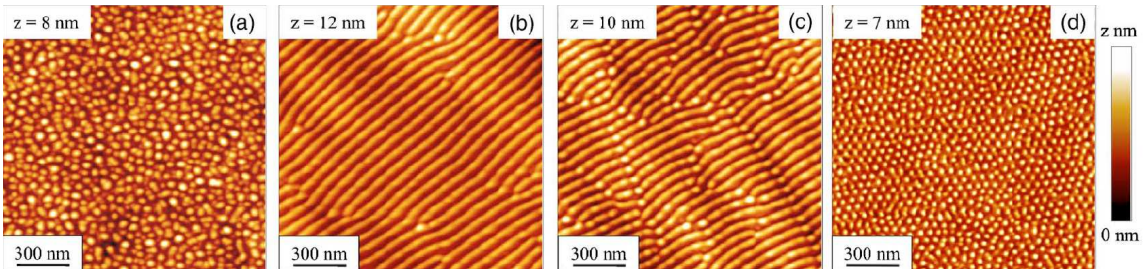


Figure 1.8: AFM images of $Xe^+$ ion beam eroded Ge surfaces for different ion incidence angles: (a) 0, (b) 5°, (c) 10°, and (d) 20°. Ion energy=2 keV, flux=$2 \times 10^{11}$ $s^{-1}cm^{-2}$, and fluence = $6.7 \times 10^{18}$ $cm^{-2}$ [31].

Table 1.1: Summary of quantum dot observations in ion irradiated semiconductors

| Target | Ion | Energy (keV) | Flux $10^{14}(cm^{-2}s^{-1})$ | Temperature (°C) | Fluence $10^{18}(cm^{-2})$ | Diameter (nm) | Incidence |
|---|---|---|---|---|---|---|---|
| GaSb [26] | Ar | 0.42 | 1 | 25 | 4 | 35 | normal |
| InP [27] | Ar | 0.5 | 0.9 | 12 | 9 | 35 | 10° ∼ 80°+rotate |
| GaSb [34] | Ar | 0.5 | 0.5 | 90 | 3 | 40 | normal |
| Si [33] | Xe | 2 | 16 | 25 | 5.8 | 25 | 26° |
| Ge [30] | Xe | 2 | 18.7 | 25 | 6.7 | 25 | normal and 25° |
| Si [35] | Ar | 1.2 | 15 | 25 | 0.09∼81 | 40∼50 | normal |
| Si [36] | Ar | 1 | | 0∼352 | 0.9 | 25∼10 | normal |
| Si [31] | Ne,Kr,Xe | ≤2 | 1.87 | 25 | 0.1∼13.4 | ∼35 | 75°+rotate |
| InP [37] | Ar | 0.5∼2 | | -173∼77 | 0.11∼280 | 30∼60 | normal |
| GaSb [38] | Ar | 3 | 0.065 | 25 | 0.3∼4 | 40∼60 | ≤10° |
| Si [39] | Ar | 0.1∼0.5 | 4 | 55∼70 | 0.52 | 20∼50 | normal |
| Si [40] | Ar | 1 | 1.25 | 25 | 5.6 | Mo-seeded | normal |

precipitate ordering [47, 48], defect walls and vacancy loop ordering [49–51] can be formed depending on the systems of ion-targets and irradiation conditions. It is well known that preferential absorption of self-interstitial atoms by dislocations leads to a bias in the defects fluxes to the sinks. The resulting excess vacancy concentration can lead to nucleation and growth of voids which cause volume swelling of the irradiated materials.

In 1967, Cawthorne and Fulton first reported the experimental observation on irradiated-induced voids [52]. In this work, spherical or polyhedral cavities are observed on the specimens irradiated by neutron doses greater than $1 \times 10^{22}$ $cm^{-2}$ at temperature range of 400°C∼ 610°C. In 1971, the ordered void array or void lattice inside Mo during 3.2 MeV $N^+$ ion bombardment at temperature of 870°C up to a

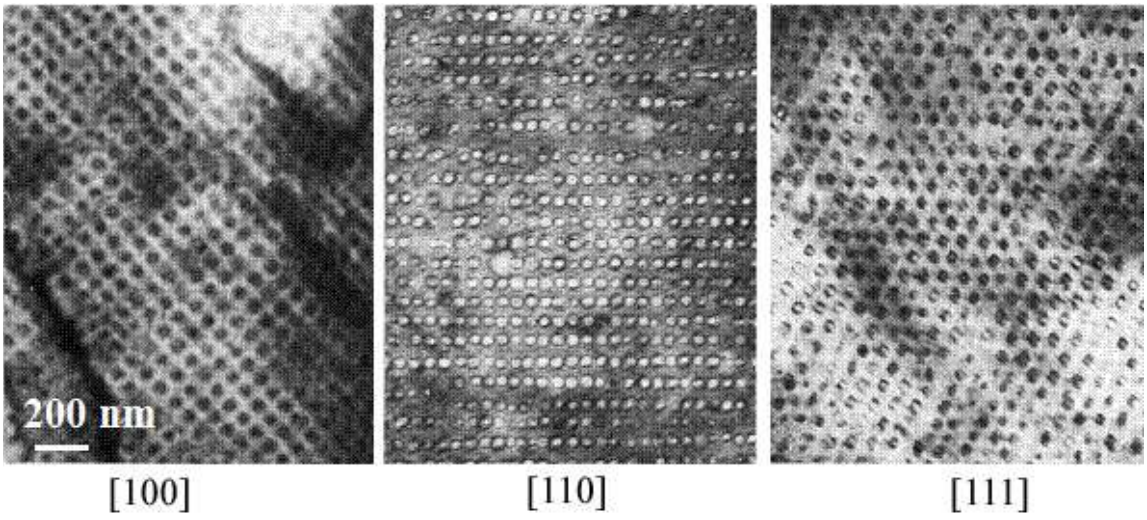


Figure 1.9: TEM micrographs of void lattice in 3.2 MeV $N^+$ eroded Nb viewed in the [100], [110] and [111] crystalline axis directions [53].

dose of $7 \times 10^{17}$ $cm^{-2}$ was discovered by Evens [41]. The molybdenum specimens were single crystal disks produced from electron beam zone refined materials, subsequently annealed near the melting point in high temperature. Three dimensional arrays are confirmed by viewing from three directions. Fig. 1.9 shows a typical experimental observation of 3-D void lattice on the 3.2 MeV $N^+$ ion bombardment of Nb at temperature of 870°C [53].

Fully developed void superlattices have been observed in irradiated BCC metals after dose levels of 30 dpa. In contrast, the development of void superlattices in FCC metals apparently requires considerably higher damage levels of $100 \sim 400$ dpa. There has been only one set of observations of a fully developed void superlattice in an FCC metal, namely pure nickel specimens which were irradiated to damage levels of 400 dpa [42]. Imperfect FCC void lattices have also been reported for irradiated Al [46, 54], Ni-Al alloys [55], stainless steel [56] and Cu-Ni [57] specimens to damage levels of $10 \sim 80$ dpa.

The experimental observations suggest that void superlattice can be formed over a wide temperature range. The void lattice parameter has been reported to initially decrease with increasing dose as the superlattice is being formed, and then attains a constant value once the superlattice is fully developed [53]. The void lattice parameter decreases slightly with increasing damage rate. It is likely that the actual irradiation temperature in the original studies on Mo may have been significantly higher than environment temperature due to beam heating [45]. Table 1.2 summarizes the experimental observations of void lattice induced by ions in metals.

Table 1.2: Selection of irradiation conditions and structure data of void lattice in metals [51, 58]

| Target | Ion | Energy (MeV) | Fluence dpa | Temperature (°C) | Diameter (nm) | superlattice constant (nm) |
|---|---|---|---|---|---|---|
| Al | $Al^+$ | 0.4 | 40 | 50 | 10 | 60 |
| Al | n | >0.1 | 6 | 55 | 65 | 250 |
| Ni | $Ni^+$ | 5 | 360 | 527 | 25 | 66 |
| Ni | $Se^+$ | 6 | 400 | 525 | 18 | 66 |
| Ni-%2Al | $N^+$ | 0.4 | 70 | 500 | 14 | 65 |
| Mo | $N^+$ | 2 | 100 | 870 | 4 | 22 |
| Mo | $Ta^+$ | 7.5 | 130, 150, 40 | 900 | 6, 15, 5.8 | 31, 46, 37 |
| Mo | $Ta^+$ | 7.5 | 7.5, 18, 40 | 450 | 2.5, 4.5, 4 | 22, 22, 22 |
| Mo | $Ta^+$ | 7.5 | 40 | 715 | 5.7 | 32.8 |
| Mo | n | >0.1 | 5 | 430, 580, 600 | | 21, 27, 30.5 |
| Mo | n | >0.1 | 5 | 800, 900, 1050 | | 40, 47, 66 |
| Mo-5%Ti-0.1%Zr | $N^+$ | 2 | 300 | 870 | 6 | 22 |
| Mo-0.5%Ti | n | >0.1 | 36 | 585, 790 | 6.9, 7.2 | 21.5, 31.5 |
| W | n | >0.1 | 2 | 580, 680 | 3, - | 19.5, 20 |
| W | n | >0.1 | 2 | 800, 900, 1050 | -, 4, - | 21, 25, 30 |
| Nb | $Ni^+$ | 5 | 5 | 800 | 4.5 | 35 |
| Nb | $Ta^+$ | 7.5 | 140, 290 | 800 | 12.5, 11 | 34, 38 |
| Nb | $Ta^+$ | 7.5 | 300 | 900 | 25 | 75 |
| Nb | $Ni^+$ or $V^+$ | 3.2 | 30∼140 | 650 | 1.6 | 10 |
| Nb-1%Zr | $Ni^+$ or $V^+$ | 3.2 | 30∼140 | 780, 805 | 7.5, 14 | 25, 35 |
| Nb-1%Zr | $Ni^+$ or $V^+$ | 3.2 | 30∼140 | 850, 925, 1010 | 10, 25, 78 | 34, 61, 145 |
| Nb | n | >0.1 | 34 | 790 | 18.6 | 66.5 |
| Ta | n | >0.1 | 36 | 585 | 6.1 | 20.5 |
| Cb | $Ta^+$ | 7.5 | 140, 290 | 620 | 12.5, 11 | 34, 38 |
| Cb | $Ta^+$ | 7.5 | 300 | 680 | 25 | 75 |
| Cb | $Ni^+$ | 5 | 5 | 620 | 4.5 | 35 |
| Cb | n | >0.1 | 34 | 617 | 18.6 | 66.5 |

The void lattice parameter is typically about two orders of magnitude larger than the atomic lattice parameter, and about four times larger than the void diameter in fully-developed void superlattices. The ratio of the void lattice parameter to the void diameter tends to approach a value of 10 once the superlattice is fully

developed [42, 53].

In addition to void lattice, three-dimension arrays of other irradiation-induced nanoscale defect clusters (e.g., inert gas bubbles, dislocation loops, stacking fault tetrahedral and secondary phase precipitates) have also been reported [51, 58]. Table 1.3 summarizes the experimental observations of gas bubble superlattices in irradiated BCC and FCC materials [58].

Table 1.3: Selection of irradiation conditions and structure data of bubble lattice in metals [51,58]

| Target | Ion | Energy (keV) | Fluence $10^{21}(cm^{-2}s^{-1})$ | Temperature (°C) | Diameter (nm) | superlattice constant (nm) |
|---|---|---|---|---|---|---|
| Ni | $He^+$ | 30 | 4 | 25 | 2 | 6.6 |
| Ni | $He^+$ | 0.25∼8 | 1 | 25 | 2 | 8.1 |
| Cu | $He^+$ | 30 | 4 | 25 | 2 | 7.6 |
| Cu | $H^+$ | 16 | 130 | 25 | 2 | 12 |
| Fe | $He^+$ | 50 | 3 | 25 | 2.5 | 6 |
| Au | $He^+$ | 160 | 10 | 5 | 2 | 8 |
| W | $He^+$ | 50 | 1.5 | 500 | 2 | 6.2 |
| 316SS | $He^+$ | 30 | 4 | 25 | 2 | 6.5 |
| 321SS | $He^+$ | 30 | 4 | 25 | 2 | 6.4 |
| Ta | $He^+$ | 30 | 5 | 300 | 2.3 | 6.4 |
| Cr | $He^+$ | 40 | 3 | 25 | 2.4 | 5.1 |
| Mo | $He^+$ | 36 | 1 | 25 | 2.4 | 5.2 |
| Mo | $He^+$ | 36 | 1 | 25, 700 | 2.4, 2.4 | 5.2, 5 |
| Mo | $He^+$ | 40 | 5 | 500 | 2.4 | 5.4 |
| Mo | $He^+$ | 40∼60 | 8 | 400 | 2.2 | 6.2 |
| Mo | $He^+$ | 100 | 1 | 550 | | 5.1 |

It has been reported that the helium bubble lattice can be induced in different metals with parameter ranges from 4 to 8 nm [45,58,59]. The FCC noble metals (Cu, Au) have the largest bubble lattice parameter, whereas a BCC metal (vanadium) has the smallest bubble lattice parameter. The bubble lattice parameter is about three times the mean bubble diameter [58]. Fig. 1.10 shows TEM observations of helium bubble lattice, formed by irradiating Au with 30 keV helium at room temperature to an ion fluence of $4 \times 10^{21} cm^{-2}$ [59]. A microscale helium bubble superlattice (70 nm bubble diameter, 105 nm bubble lattice parameter, Fig. 1.10b) has been observed to coexist with the usual (nanoscale) bubble superlattice (Fig. 1.10a) in He implanted Au at relatively high fluence [59].

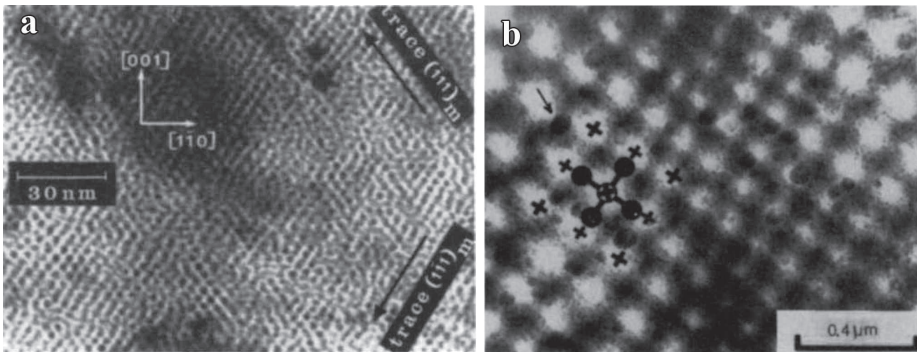


Figure 1.10: (a) TEM micrographs of He bubble formation in copper. The experiment was performed with 160 keV He at 300 K up to dose of $4 \times 10^{17}$ cm$^{-2}$. (b) He bubble formation in 160 keV He eroded Au at 280 K at dose of $1 \times 10^{18}$ cm$^{-2}$ [59].

Defect cluster pattern formation has also been observed in copper specimens exposed to 3 MeV protons. The dislocation loop microstructure revealed by TEM observations is shown in Fig. 1.11 [51,60]. The single-crystalline Cu was used in this experiment. Specimen was irradiated to 0.65 dpa and 2 dpa at temperature of 370 K. The wall arrangement shows a typical periodicity length of 60 nm and the walls are separated from each other by regions free of visible defects.

## 1.2 Theory for Ion-induced Self-assembly

Formation of these nanoscale structures has been classified as a self-organization (or self-assembly) phenomenon by non-linear dissipative processes in system far from equilibrium [61–63]. It shows that the process has a driving force that is intrinsic to the crystalline materials. Understanding this driving force is fundamentally important for the development of nanostructures with periodic arrays. Several models of structure evolution based on the continuum dynamical equations have been proposed and studied analytically and numerically [18, 23, 63–69]. This part will focus on reviewing the current understanding of the underlying physical mechanisms and the comparison between theories and experiments.

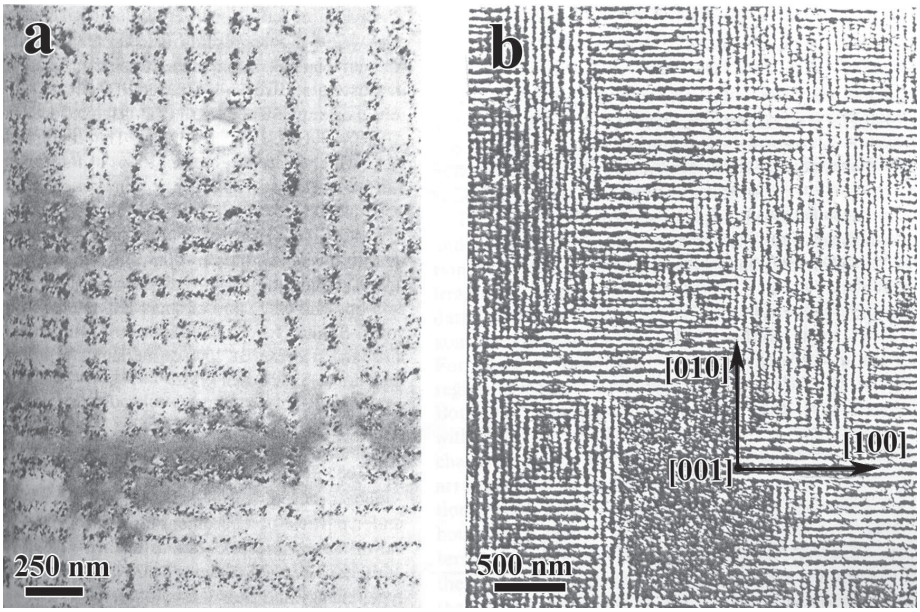


Figure 1.11: Periodic arrays of planar walls of defects in Cu irradiated with protons up to 0.65 dpa (a) and 2 dpa (b) [51,60].

### 1.2.1 Sigmund's theory of sputtering

During ion sputtering the first mechanism we should consider is the erosion rate of ion bombardment characterized by sputtering yield: the average number of atoms leaving the surface of a solid per incident particle. The composition of the target, the parameters of the incident ion beam, and experimental geometry contribute to the sputtering yield [70]. In the process of sputtering, the incident ions penetrate into target and transfer their kinetic energy to the target atom by creating cascade of collisions among the substrate atoms or through other processes such as electronic excitations. Most of these atoms will come back to their original locations but some of them, especially those on the surface which obtained energy larger than the surface binding, will be permanently removed from substrate. The sputtering yield was derived on the basis of a linear Boltzmann transport equation under the assumption of random slowing down in an infinite medium. For amorphous and

polycrystalline targets, Sigmund revealed that the sputtering yield is proportional to the energy accumulated by ions. More importantly, Sigmund proved that sputtering yield is larger for troughs than for crests [71]. Many surface features induced by ion bombardment, including ripple and nanodot formation are based on this theory [26, 32, 63, 64, 72–76].

For amorphous and polycrystalline targets, sputtering yield is given by [77]

$$Y = \Lambda F(E, \eta) \tag{1.1}$$

where $\Lambda$ is the materials factor given by

$$\Lambda = \frac{3}{4\pi^2} \frac{1}{N U_0 C_0} \tag{1.2}$$

where $N$ is the atomic density of targets, $U_0$ the surface binding energy, and $C_0$ ($\approx 1.808\text{Å}^2$) is the constant coefficient in the power approximation of the Thomas-Fermi cross section [71], $F(E, \eta)$ is the deposited energy distribution, $\eta$ is the cosine of incident angle. For perpendicular incidence, Sigmund assumed that energy deposited at surface can be expressed as [71, 77–79]

$$F(E, 1) = \alpha N S_n(E) \tag{1.3}$$

where $N$ is the atomic density of target atoms, $S_n$ is the nuclear stopping cross-section at energy $E$, and $NS_n = dE/dx\ |_n$, the nuclear energy-loss rate, and $\alpha$ is a factor that depends on $M_2/M_1$ ($M_1$ is the mass of ion and $M_2$ is the mass of target atom). Thus the sputtering yields for normal incidence can be determined by the nuclear stopping cross-section. Several nuclear stopping cross-sections are proposed, such as power approximation of the Thomas-Fermi cross section [77], ZBL universal function [80] and Lindhard's expression [71].

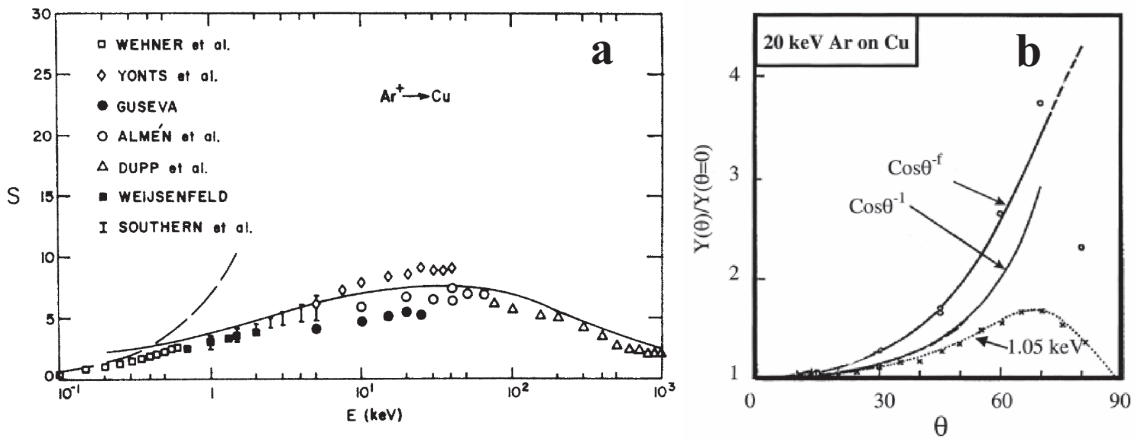


Figure 1.12: Comparison of Sigmund's theory with experimental observations. (a) Energy dependent [77]. (b) Incidence dependent [81].

Eq. 1.1 can be rewritten in an integral form [78]

$$N(\mathbf{r}, \varepsilon, \theta) = \Lambda \int \int_{\mathbf{S}} \phi(\mathbf{r}') F(\mathbf{r} - \mathbf{r}') dA' \tag{1.4}$$

where the integral is evaluated over the area $\mathbf{S}$, $\phi(\mathbf{r}')$ is a correction to the uniform flux $f$, $\phi(\mathbf{r}')dA'$ is the number of ions hitting on an area $dA'$, $F(\mathbf{r} - \mathbf{r}')$ denotes the sputtered atoms at position $\mathbf{r}$ generated by an ion hitting the surface in a point $\mathbf{r}'$. The gaussian distribution was assumed for energy distribution. If we let ion beam be parallel to $z$ axis, the energy distribution is given by [71, 77–79]

$$F(\mathbf{r}) = \frac{\epsilon}{(2\pi)^{3/2}\alpha\beta^2} \exp\left(-\frac{(z-a)^2}{2\sigma^2} - \frac{x^2}{2\beta^2} - \frac{y^2}{2\beta^2}\right) \tag{1.5}$$

where $a$ is average penetration depth, $\alpha$ and $\beta$ are the energy range straggling along $y$ and $z$ directions, respectively. This equation was widely used later for quantitative explanation of many features induced during ion sputtering [26, 32, 63, 64, 72–76].

Fig. 1.12 shows the comparison of Sigmund theory with experimental observations. It can be seen that this theory can be used successfully to predict energy-dependent sputtering yields for a wide range of energy and a variety of ion-target combinations

[81–86]. However, one challenging problem associated in this model is the angle-dependent sputtering (Fig. 1.12b). It can not predict peak position of sputtering yield related to incident angle. Sigmund pointed out that this maximum sputtering yield at a certain glancing angle can not be explained on the basis of the assumption of an infinite medium [77].

### 1.2.2 Ripple and dot formation

To date the rather successful theoretical model for the ripple formation was developed by Bradly and Harper (BH model) [64]. The linear partial differential equation (PDE) describing kinetic behavior of species on the surface was derived on the basis of Sigmund's theory. A prescribed special profile was assumed and sputtering yield in integral form (Eq. 1.4) was used. For simplicity, small approximation (expending surface profile to the first order of slope) was also assumed. Because of only using the curvatures to present the surface morphology, this model is regarded as curvature-dependent sputtering. By adding thermally induced surface diffusion to the initial equation derived on the Sigmund theory, the wavelength and critical angle can well be predicted by this model. Now it is widely accepted that ripple formation is attributed to the roughening process due to sputtering and smoothing process due to diffusion. This model was valid at the very beginning of ripple formation because of small slope approximation. The new features induced with increasing bombardment time, such as roughening, coarsening, and rotation can not be predicted by this model. It was found that these properties are the results of nonlinear effects which is not included in BH model. Later, Cuerno and Barabási developed a nonlinear equation to explain the ripple evolution during long time limit by extending the surface profile to second order of slope [63, 65]. The redeposition and viscous flow were also considered [66, 87] and the same form as damped Kuramoto-Sivashinsky (DKS)

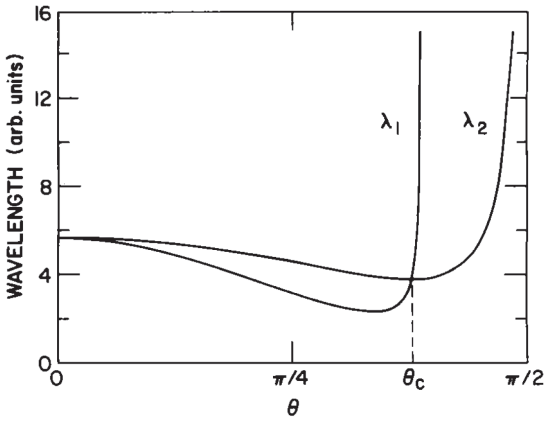


Figure 1.13: Plot of wavelength ($\lambda_1$ and $\lambda_2$ vs incident angle $\theta$ for $\alpha = \beta = a/2$). The selected wavelength $\lambda$ for a given $\theta$ is the small of $\lambda_1(\theta)$ and $\lambda_2(\theta)$ [64].

growth model was derived. By changing the parameters of DKS equation, not only ripples but also dots can well be predicted [88, 89].

In BH model, surface profile was summed as

$$z = \frac{x^2}{2R_1} + \frac{y^2}{2R_2} \tag{1.6}$$

where $1/R_1$ and $1/R_2$ are the principle curvatures. substituting Eqs. 1.6 and 1.5 into 1.4, Bradly and Harper derived a lineae equation for surface morphology evolution

$$\frac{\partial h(x,y,t)}{\partial t} = \nu_x \nabla_x^2 h + \nu_y \nabla_y^2 h - K \nabla^4 h \tag{1.7}$$

where $h(x, y, t)$ is the height of the bombarded surface described by coordination $x$ and $y$, $\upsilon_x$ and $\nu_y$ are the effective surface tensions generated by the erosion process, dependent on the angle of incidence of the ions, $K$ is the relaxation rate due to surface diffusion [90]. Using a linear analysis, Eq. 1.7 gives wavelength

$$\lambda = 2\pi \sqrt{\frac{2K}{|\nu|}} \sim (fT)^{-1/2} \exp\left(\frac{-\triangle E}{k_b T}\right) \tag{1.8}$$

where $\nu$ is the largest in absolute value of the two effective surface tension coefficients, $\nu_x$ and $\nu_y$, $f$ is the ion flux, $T$ is temperature, $k_b$ is Boltzmann constant, $\Delta E$ is the

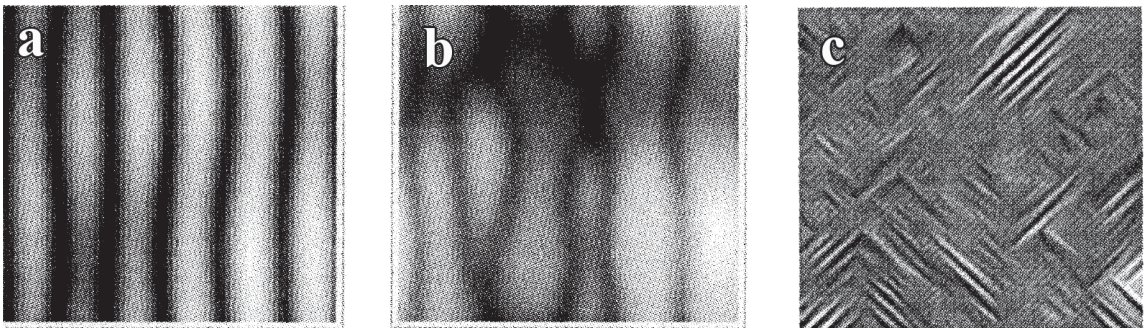


Figure 1.14: Computer simulation showing (a) ripple formation at an early time, (b) coarsening occurs at a later time and (c) rotation of ripples at later time [91].

activation energy for surface diffusion. The calculation also predicts that the ripple direction is a function of the angle of incidence (Fig. 1.13).

Eq. 1.7 is linear, valid for the ripple formation at the very beginning of bombardment. This model predicts unbounded exponential growth of the ripple amplitude. Thus it cannot account for the stabilization of the ripples and for kinetic roughening, both phenomena being strongly supported by experiments. Furthermore, the BH model cannot account for low temperature ripple formation since no smoothing mechanism takes place. Despite these shortcomings, the BH theory represents a major step in understanding the mechanism of surface evolution in ion sputtering.

Following the approach in BH model, Cuerno and Barabási derived a nonlinear equation [63, 65]

$$\frac{\partial h(x,y,t)}{\partial t} = \nu_x \frac{\partial^2 h}{\partial x^2} + \nu_y \frac{\partial^2 h}{\partial y^2} + \frac{\kappa_x}{2}\left(\frac{\partial h}{\partial x}\right)^2 + \frac{\kappa_y}{2}\left(\frac{\partial h}{\partial y}\right)^2 + K\nabla^2(\nabla^2 h) + \eta \quad (1.9)$$

where $\upsilon_x$ and $\nu_y$ are the same meaning as those in BH model (Eq. 1.7), $\lambda_x$ and $\lambda_y$ describe the slope dependent sputtering, $\eta$ is noise. By computer simulation (Fig.1.14), rotation of ripple, coarsening, and roughening can well be predicted by Eq. 1.9 [91].

Recently a generalization of theory has been successfully introduced to account

for the redeposition [88, 92], viscous flow [23] and anisotropic surface diffusion [2–4]. This new equation has the same form as DKS growth model given by

$$\frac{\partial h}{\partial t} = -(\alpha + \nu\nabla^2 + D\nabla^4)h - \lambda(\nabla h)^2 + \eta \tag{1.10}$$

where $\nu$ is effective surface tension generated by the erosion process due to surface curvature or viscous flow due to surface stress, $D$ is effective diffusion coefficient from thermal diffusion, radiation induced diffusion, and viscous flow, $\lambda$ describes the tilt-dependent sputtering yield, $\eta$ is a Gaussian white noise resulting from the stochastic nature of erosion process, a damping term $-\alpha h$ accounts for the redeposition of sputtered species on the surface.

Numerical simulation shows that predictions from Eq. 1.10 are in good agreement with experimental observations [88]. Facsko *et al.* performed the numerical integration of DKS equation on an equally spaced two dimensional mesh (Fig. 1.15). Eulers method is applied for the time derivative and an isotropic form of the Laplace operator is applied. For the numerical integration the following values for the coefficients were used: a mesh size of 400×400 points, a spatial step width $dx = 0.5$, time steps $dt = 0.01$.

### 1.2.3 Void and bubble formation

A number of theories have been given for the stability and for motion of void/bubble lattices in metals, including elastic interaction, phase instability model, cavity and interstitial loop interaction, and anisotropic self-interstitial-atom (SIA) diffusion. Amongst these the most favored is the model proposed by Foremen [93] and its further development by Evans [48, 94, 95] and Woo [96–98]. In this theory, crystallographic anisotropic diffusion of self-interstitial atoms (SIAs) in host materials is proposed to interpret the void lattice formation. This model is based on the shad-

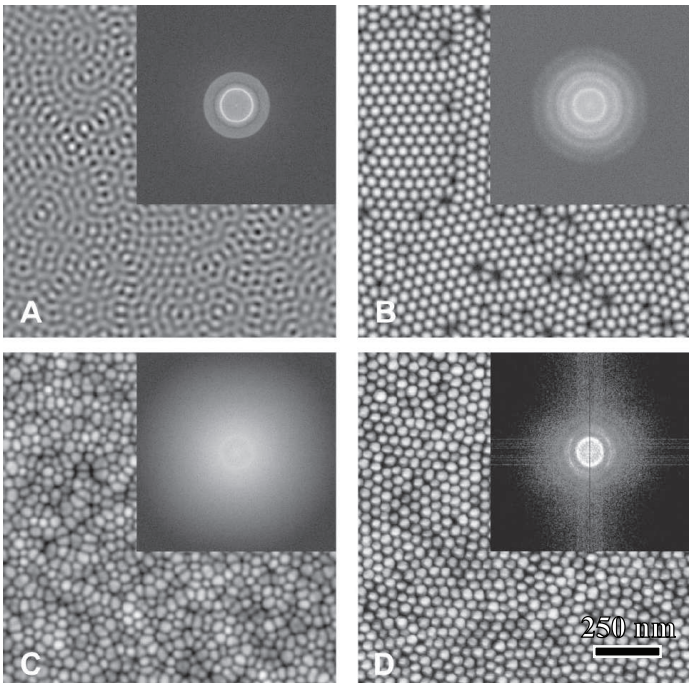


Figure 1.15: Pattern formation calculated from Eq. 1.10: (A) pattern at early time, (B) ordered patterns in the later time, (C) chaotic patterns in the later time for different parameters. (D) AFM image of GaSb after sputtering with 500 eV $Ar^+$ ions at $6 \times 10^{18} cm^{-2}$ ion dose. Insets show FFT spectra [88].

owing effects due to voids in the propagation of interstitial by crowdions.

**Elastic interaction**

The first suggestion of explanation of void lattice formation using void-void elastic interaction is proposed by Malen and Bullough [99]. This model and its further development by Stoneham [100] and Tewary and Bullough [101], applying the energy minimum, successfully gave the order of magnitude for the ratio of void lattice parameter to void radius. These explanations highlight the significant role of elastic anisotropy in the void/bubble lattice formation. However, the formation of void/bubble superlattices in isotropic material remains unanswered. The prior assumption of void shape and lattice type precludes many possible patterns. Furthermore, this model does not involve the radiation damage and kinetics of species induced by ion irradiation. Theoretical study of the metallic colloid formation [102],

however, demonstrated that elasticity interactions in the dynamic ordering process provide the basis for understanding of pattern formation.

**Phase instability model**

Martin and co-authors [100, 103, 104] first established the phase instability theory using a set of rate functions describing the dynamics of defect combination and migration. Based on the continuum model, Martin proposed an effective free-energy function which is minimum at steady state. At the same time, Bullough, Eyre and Krishan [105, 106] also provided a set of equations for understanding and correlating the void growth, which, lately used to analyze the lattice formation, are called BEK model. Recently, more complicated partial differential equations (rate functions) are established by Walgreaf and co-workers [62, 68, 69] by considering more defect species including vacancies, interstitial atoms, voids, vacancy and interstitial clusters, vacancy and interstitial loops, dislocations and network dislocations. In these models, the conventional non-equilibrium approach was used to give the criteria under which the system becomes instability and selects the void patterns. One problem of these models is that they can not predict the crystallography of the void lattice which has the same symmetry as the host lattice.

By taking into account of dynamical equations for two mobile atomic species (vacancies and interstitial atoms) [105–107], the simple rate equation describing the behavior and interstitial is given by

$$\begin{aligned}\frac{\partial C_i}{\partial t} &= P(1-\varepsilon_i) - \alpha C_i C_v + D_i \nabla^2 C_i - D_i C_i (Z_{iN} + Z_{iv}\rho_v + Z_{iI}\rho_I \\ &\quad + Z_{iC}\rho_C) \qquad (1.11)\\ \frac{\partial C_v}{\partial t} &= P(1-\varepsilon_v) - \alpha C_i C_v + D_v \nabla^2 C_v - D_v (Z_{vN}(C_v - \bar{C}_{vN})\rho_N \\ &\quad + Z_{vV}(C_v - \bar{C}_{vV})\rho_V + Z_{vI}(C_v - \bar{C}_{vI})\rho_I + Z_{vC}(C_v - \bar{C}_{vC})\rho_C) \qquad (1.12)\end{aligned}$$

where $C_v$ corresponds to the concentration of vacancies and $C_i$ to interstitials, $\rho_N$ is the network dislocation density, $\rho_V$ the vacancy loop density, $\rho_I$ the interstitial loop density and $\rho_C$ the void sink density, $P$ is the displacement damage rate, $\varepsilon_i P$ the in-cascade interstitial loop production rate and $\varepsilon_v$the cascade collapse efficiency of vacancy loops, $\alpha$ is the recombination coefficient, Zs are the bias factors (which may usually be approximated by $Z_{iN} = Z_{iI} = Z_{iV} = 1 + B$ and $Z_{vI} = Z_{vN} = Z_{vV} = Z_{vC} = Z_{iC} = 1$, $B$ being the excess network bias). $\bar{C}_{vN}$, $\bar{C}_{vV}$, $\bar{C}_{vI}$, and $\bar{C}_{vC}$ are the concentrations of thermally emitted vacancies from network dislocations, vacancy and interstitial loops, and voids, respectively. Equations for dislocation loops, void evolution, the void number density, and the sink density are given in terms of structure of voids. Pattern formation and selection are determined by instability analysis from above equations. Similar to Cahn and Hilliard's description of thermal diffusion in a binary mixture, Martin proposed a mean-field description of solid solution in the present of irradiation-induced atomic mixing [103, 104, 108]. This model is based on the two separate dynamics: vacancy assisted thermal exchanges that drive the system to thermodynamical equilibrium, and irradiation-induced random interchanges of atomic positions. The competition between the irradiation-induced mixing and irradiation-enhanced diffusion to low-energy configurations is responsible for the pattern formation.

Fig.1.16 shows a simulation result describing the dynamic formation and pattern evolution of voids in molybdenum based on a phase-field model which incorporates the free energy of mixing, interfacial energy and elastic energy [109]. A Cahn-Hilliard type nonlinear diffusion equation was used for vacancy diffusion. This work highlights the importance of elastic interaction and elastic anisotropy to this 3-D pattern formation process.

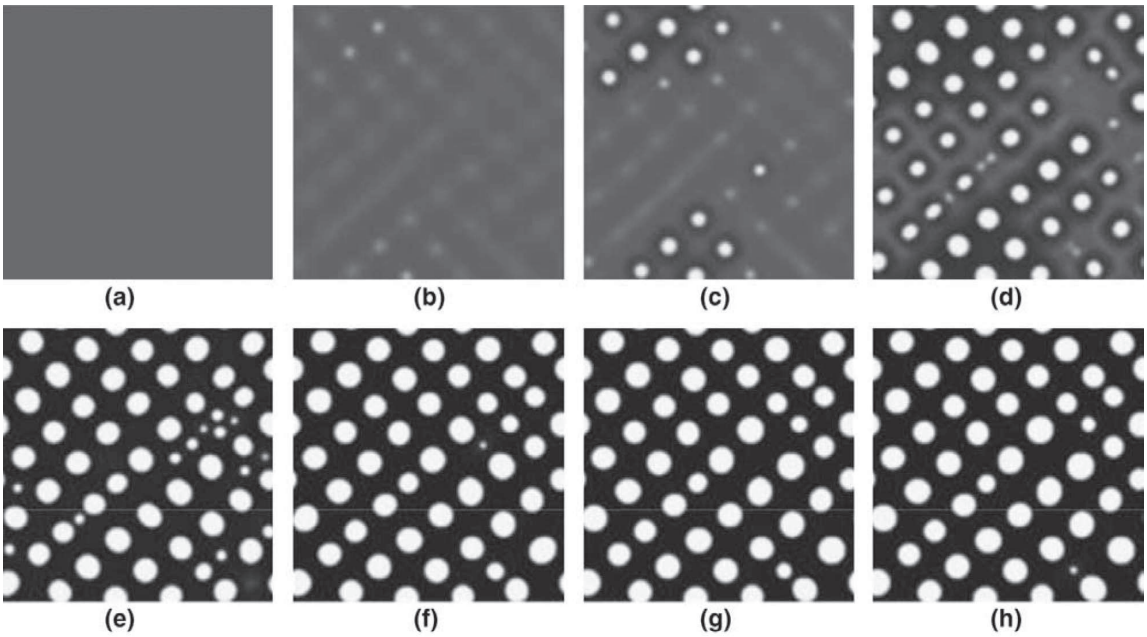


Figure 1.16: Computer simulated formation and pattern evolution of voids in molybdenum for different times: (a) t= 0, (b) t= 799.92, (c) t= 823.68,(d) t= 850.08, (e) t= 892.32, (f) t= 1016.40, (g) t= 1201.20, and (h) t= 1440.12 [109].

### Cavity and interstitial loop interaction

Dubinko et al. [110] have proposed the theory involving interaction between cavities and interstitial loops to explain both bubble and void lattice. For bubble lattice, this model assumed that loop glide along the crystal close-packed direction can cause an effective repulsion between two bubbles in the glide direction and balance a diffusive attraction between adjacent bubbles. It is suggested that interstitial loops (dislocations) are punched out (or absorbed) due to the exerting pressure by the entrapped gas inside bubbles (or the surface tension of void surfaces) according to Greenwood's loop punching mechanism [111]. For void lattice, it is formed by the anisotropic diffusion of interstitial loops. The interstitial loops are attracted toward voids along the crystal close-packed directions, forming loop supply cylinders (LSC). When LSCs of two voids overlap, the supply of interstitial loops toward each void

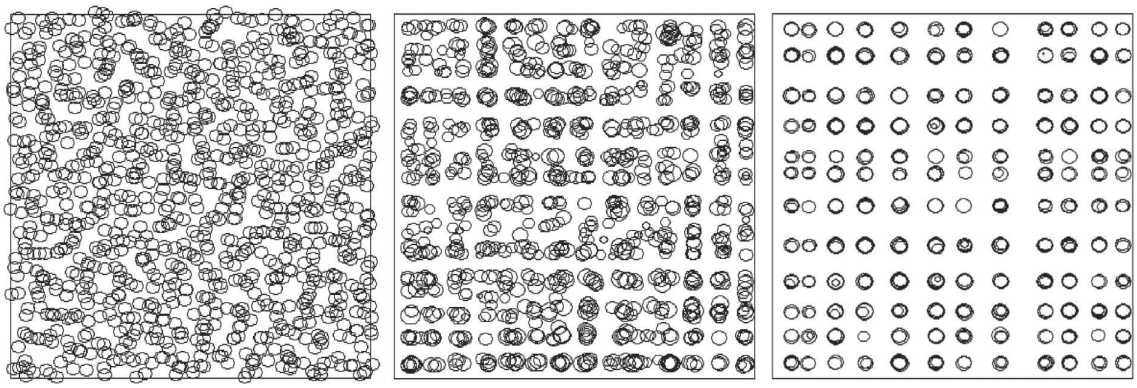

Figure 1.17: Computer simulation based on anisotropic self-interstitial-atom (SIA) diffusion. (a) Start, (b) 0.28 dpa, and (c) 0.84 dpa [95].

drops drastically. On the other hand, those disordered voids keep absorbing interstitial loops and shrink. Eventually only ordered voids survive. This model, from basic physical mechanism is the anisotropic diffusion model as shown below.

**Anisotropic self-interstitial-atom (SIA) diffusion**

This model is based on the concept of crystallographic anisotropic diffusion of self-interstitial atoms (SIAs) in host materials. The model builds up on a series of work of Foreman [93], Evans [41,47,48,94,95], Woo and Frank [96–98]. These models have shown that SIA moving in one or two directions would tend to order voids along these directions. It has been proved that unaligned voids will always receive a larger flux of SIA than voids which are aligned. The reason is that these aligned atoms are shadowed and isolated atoms are unshadowed if assuming that interstitial atoms are moving along a particularly direction. In a metal, the most probable direction for interstitial atom moving is the close packed direction. As a result this model gives a reasonable explanation for the coincidence of structure of the void and bubble lattice with the parent fcc and bcc metals. The simulation based on this assumption has been performed by Evans (Fig. 1.17) [95].

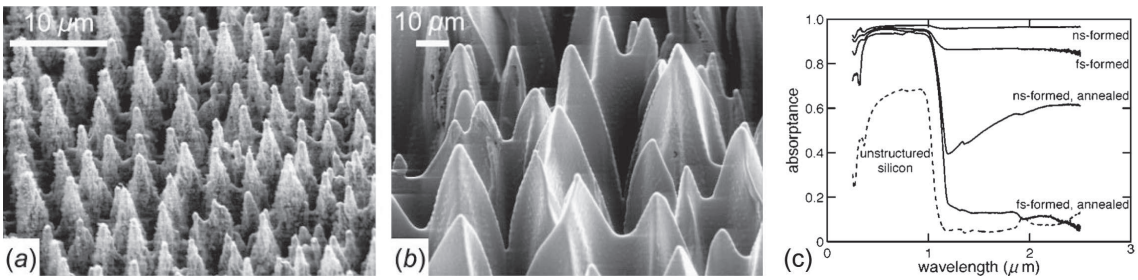


Figure 1.18: SEM image showing surface structure of Si formed by (a) femtosecond laser pulses in Mazur lab and (b) nanosecond laser pulses in Aziz lab. (c) Optical properties of structured Si before and after thermal annealing at 875 K for 45 min [115].

## 1.3 Potential Application

The ion-induced nanostructures opens up a promising new approach to lithography free patterning of nano-scale arrays for various applications including, for example, nanoscale photonic and electronic devices. The ion induced structures also have potential applications in investigating fundamental physical phenomena, such as sputtering effect on the deposition, diffusion and aggregation. It is well known that nanoscale structures, which are the building blocks of future technologies, are exceedingly difficult to fabricate by conventional materials processing methods and are often much less stable than their macroscopic counterparts. Significant effort has been devoted to developing new effective techniques to fabricate small structures to satisfy the minimization requirements of the future devices. Ion irradiation technique, which has long been employed in the semiconductor industry as a highly controlled method of doping semiconductors, is one of these techniques that has ability to create small and stable structures [112, 113].

As an indirect band-gap material, silicon is a poor light emitter. Si cannot be used as an optoelectronic material at important infrared (IR) wavelengths, and Si solar cells fail to convert more than two thirds of the incident solar power into electricity.

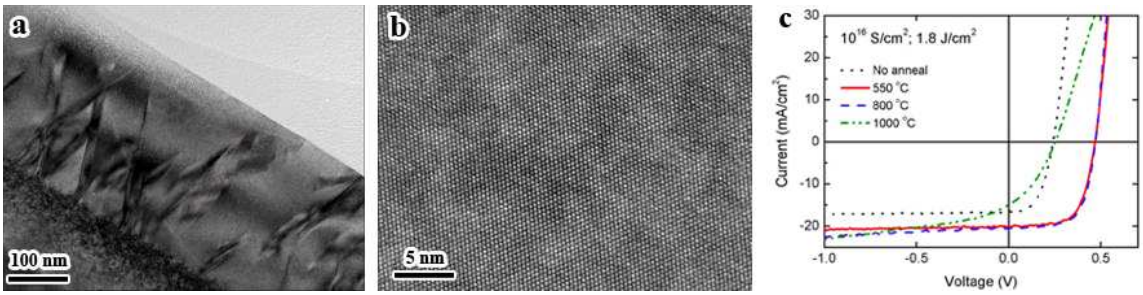


Figure 1.19: (a) Cross-sectional TEM image of n-Si(111) sample implanted to a dose of $1 \times 10^{16}$ $cm^{-2}$, (b) HRTEM image for same sample. (c) Dark I-V curves measured for p-Si(001) sample implanted at dose $1 \times 10^{16}$ $cm^{-2}$ and furnace annealed at different temperatures [113].

However, the low cost and simple integration with existing Si fabrication techniques drives researchers to find ways to extend its capabilities. For years, scientists have focused their efforts on altering Si so that it can be used as a light emitter. Investigated systems include porous Si, Si nanocrystals and nanoclusters, dislocations, superlattices, interface states, and impurities. However, despite many years of investigating these systems, none has emerged as a clear winner. Mazur group discovered a novel laser processing technique that alters the surface morphology and composition of Si, drastically changing the optical properties [114, 115]. By irradiating the surface of a Si wafer with femtosecond laser pulses in the presence of a sulfur-bearing gas, the originally shiny, flat surface is transformed into an array of pillars (Fig. 1.18a and b) [115]. The resulting surface has near-unity absorption from the near-ultraviolet to IR photon energies that are well below the 1.1 eV band gap (i.e. wavelengths longer than 1.1 microns). Because of the altered optical properties, this material holds great promise in producing a Si-based IR detecting, light emitting, or enhanced photovoltaic material. The early work on this silicon photodetectors has been spun out to a start-up company to make low-cost, high-performance IR imaging arrays.

Aiziz group have been investigating the optoelectronic behavior of ion implanted

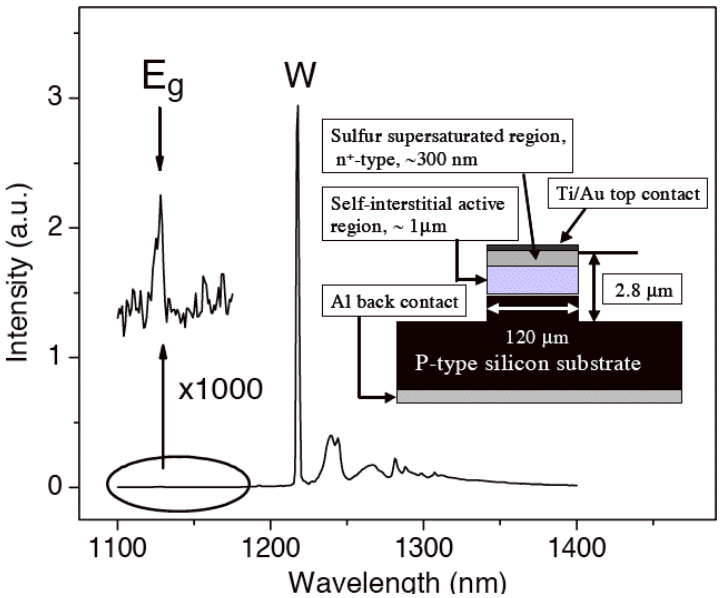


Figure 1.20: Bright luminescence peaked at 1218 nm, labeled W, is about three orders of magnitude greater than inter-band luminescence at band-gap energy labeled Eg. Inset is schematic of W-line LED [112].

Si. They showed that ion implanting a silicon wafer with sulfur and then irradiating with a single nanosecond laser pulse keeps the surface optically flat, which is supersaturated with sulfur and free of extended defects (Fig. 1.19a and b), and yet absorbs strongly in the sub-band gap region [113]. Simple p/n junctions out of this material have been made (Fig. 1.19c) and the first working light emitting devices (LED) out of this material was also fabricated (Fig. 1.20) [112].

## 1.4 Objectives

Since the discovery of one to three dimensional structures in irradiated materials [1,26,41], a variety of experiments and models have been performed to investigate this phenomenon. However, the underlying mechanisms are not well understood. It is unclear why experimentally observed typical parameter of patterns is so universal and weakly depends on the temperature and irradiation intensity. Sometimes the results cannot be repeated presumably due to small variations of the experimental

conditions that were thought unimportant before. Understanding the mechanism of pattern formation needs more experimental data on the kinetics of its formation in time and for different ion-target systems.

The patterns observed in radiated materials have much in common with these seen in lasers, interacting chemicals, convection fluids, etc. The central of them in the study of patterns, therefore, is to understand the rules determining behavior of patterns which may arise from a large class of physical system. There is also the possibility of technological payoffs from understanding patterns.

The overall objective of this research is to investigate the self-organized patterns under ion beam bombardment with emphasis on fabrication, characterization, modeling and application. The primary research interests in this area include the formation of nanostructures in a wide range of materials induced by non-equilibrium methods. Particular emphasis was focused on dynamic processes of the nanostructure formation, a fundamental understanding of ion-induced structures and the possibility of technological utilization. A detailed study of pattern formation was conducted via FIB implantation, TEM and AFM observation, optical measurement, and modeling. Numerical simulations was performed to establish the critical link between the self-organized nanostructures and the experimental conditions. The common features of mechanism underlying one to three dimensional pattern formation were explored.

# CHAPTER II

# Sputtering Yield of Amorphous and Polycrystalline Materials

## 2.1 Angular Dependence of Sputtering Yield

Ion-induced sputtering is a subject of constant research by many scientists over the last few decades due to its wide applications in semiconductor industry, surface analysis, and deposition. The understanding of this phenomena lies in the framework of Sigmund's theory [77]. This theory was derived on the basis of a linear Boltzmann transport equation under the assumption of random slowing down in an infinite medium. For amorphous and polycrystalline targets, Sigmund revealed that the sputtering yield is proportional to the energy accumulated by ions on the surface. It was shown that this theory can be used successfully to predict energy-dependent sputtering yields for a wide range of energies and a variety of ion-target combinations [82–86]. Many surface features induced by ion bombardment, including ripple and nanodot formation are based on this theory [26, 32, 63, 64, 72–76]. However, one challenging problem associated with this process is the angle-dependent sputtering yield. According to Sigmund's theory, the evolution of sputtering yield with ion energy $E$ and incident angle $\theta$ measured from the surface normal is given by Eq. 1.1. This equation can be understood as the production of sputtered atom density (in unit of atoms per length) per bombarding ion and depth from which sputtered atoms

come [77, 116]. By solving linear Boltzmann's equation under assumption of infinite medium using Thomas-Fermi cross section $d\sigma = C_m E^{-m} T^{-1-m} dT$ with $m = 0$ and $C_0 = \frac{1}{2}\pi\lambda_0 a^2$, where $\lambda_0 = 24$ and $a = 0.219$, Sigmund obtained incidence dependent sputtered atom density $F(E,\eta)/(\pi^2 U_0)$ and incidence independent depth $3/(4NC_0)$ [77, 116]. The production of these two terms determines the sputtering yield (Eq. 1.1). Assuming Gaussian distribution of deposited energy distribution $F(E,\eta)$, where $\eta = \cos\theta$, from Eq. 1.1 the normalized sputtering yield can be approximated as

$$\frac{Y(E,\eta)}{Y(E,\eta=1)} = (\cos\theta)^{-f_s} \tag{2.1}$$

where the exponent $f_s \approx 1 \sim 2$, depending on the mass of ion and atom [77,85]. This means that sputtering yield increases with the incidence angle and goes to infinite for grazing incidence. It is well known from experiment that the sputtering yield reaches a maximum at an oblique incidence about 70° and then approaches zero at $\theta = 90°$ (Fig. 1.12). Sigmund pointed out that this maximum sputtering yield at a certain glancing angle can not be explained on the basis of the assumption of an infinite medium [77]. Although this subject is mostly of applied interest and has been intensively investigated over several decades [82, 117–120], angular dependence of sputtering yield is still not well understood.

Starting with the recoil atom density [77, 116, 121], it was found that sputtered atom depth is proportional to the cosine of incident angle. The peak of sputtering yield can be attributed to a balance between two competitive effects: one is the deposited energy $F(E,\eta)$ which increases with incident angle and thus enhances the sputtering yield, and another is the sputtered atom depth which decreases with incident angle and thus reduces the sputtering yield.

According to Sigmund's theory [116, 121], the average number of recoil atoms

passing through the surface plane with energy $(E_1, dE_1)$ in the solid angle $(\mathbf{\Omega_1}, d\Omega_1)$ per incident ion is given by [121]

$$Y = \int \int J(E_1, \Omega_1) dE_1 d^2\Omega_1 \tag{2.2}$$

where $J(E_1, \mathbf{\Omega_1})$ is the number of recoil atoms per unit energy and unit solid angle. Eq. 2.2 gives sputtering yield if we integrated over $E_1 \cos^2\theta_1 > U$, where $\theta_1$ is the angle between $\mathbf{\Omega_1}$ and the outward surface normal, $U/\cos^2\theta_1$ is the surface binding energy. Following approach suggested by Falcons and Sigmund [121], using power cross section with $m = 0$, $J(E_1, \mathbf{\Omega_1})$ is given by

$$J(E_1, \Omega_1) = \frac{3F(E,\eta)}{2\pi^3} \int_0^\infty \frac{dE_0}{E_0^2} \int_0^\infty dx \delta(E_1 - f(E_0, x, \mathbf{\Omega_1})) \tag{2.3}$$

where $F(E, \eta)$ is deposited energy density on the surface, $E_0$ is initial energy of recoil energy, $\delta$ is Dirac delta function, $f(E_0, x, \mathbf{\Omega_1})$ is the energy of recoil atom with initial energy $E_0$ after traveling from $x$ to the surface in direction $\mathbf{\Omega_1}$. In order to integrate Eq. 2.3, we need to know the relationship between energy $E_1$ and initial energy $E_0$ at depth $x$ for recoil atoms.

Energy loss for both ion and recoil atom has the form [121]

$$\frac{dE}{dR} = -CE^\gamma \tag{2.4}$$

where R is the traveled path length and $C$ and $\gamma$ are constants. For power approximation of cross section, $\gamma = 1 - 2m$. If we assume $m = 0$, according to Sigmund's assumption [77], $C = NC_0$, where $N$ is target atomic density.

For an incident ion with initial energy $E_i$ and incidence $\theta$, the energy $E_0$ at depth $x$ from surface is given by (integrating Eq. 2.4 under $m = 0$ for incident ion)

$$E_0 = E_i \exp\left(-\frac{Cx}{\eta}\right) \tag{2.5}$$

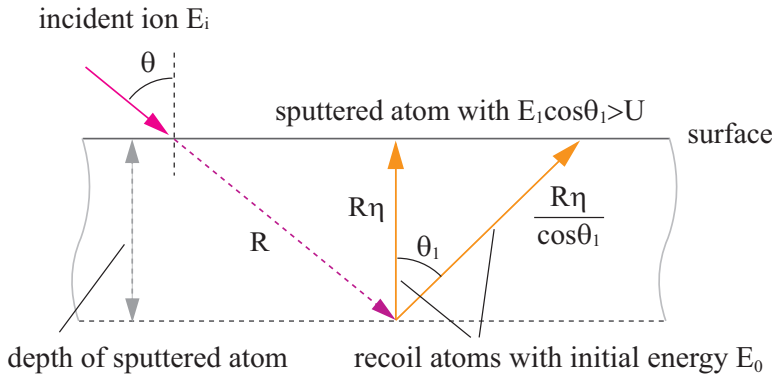


Figure 2.1: Schematic illustration of the variation of sputtered atom depth with incident angle. Recoil atoms with initial energy $E_0$, after traveling depth $R\eta/\cos\theta_1$, reach surface with energy $E_1$. Sputtered atoms satisfy $E_1\cos\theta_1 > U$ (surface binding is given by $U/\cos^2\theta_1$).

This equation shows the depth of an incident ion that has the energy $E_0$ under off-normal bombardment is equal to the cosine of incident angle times the depth of incident ion with the same energy under normal bombardment (Fig. 2.1). Because this energy will be transferred to recoil atom, for a given energy $E_0$, the depth of recoil atom has the same relationship between normal and off-normal bombardment. Thus the energy $E_1$ of a recoil atom with initial energy $E_0$ at depth $x$ from surface is given by (integrating Eq. 2.4 under $m = 0$ for recoil atom)

$$E_1 = E_0 \exp\left(-\frac{Cx}{\eta\cos\theta_0}\right) \tag{2.6}$$

where $\theta_0$ is the angle between $\mathbf{\Omega_0}$ and the outward surface normal. This equation is different from that derived by Falcons and Sigmund [121] by a parameter of $\eta$ on the right hand of Eq. 2.6. This reduced depth at off-normal bombardment shows that more recoil atom can easily escape from surface without inducing further recoil atoms, and then lead to the decrease of sputtering yield. The schematic explanation of this difference is shown in Fig. 2.1. Submitting Eqs. 2.6 and 2.3 into Eq. 2.2 yields

$$Y(E,\eta) = \eta\Lambda F(E,\eta) \tag{2.7}$$

where power approximation of Thomas-Fermi cross section with $m = 0$ is used. At normal bombardment, this equation reduces to the Sigmund's result. At off-normal bombardment with increasing incident angle, $\eta$ decreases and $F(E, \eta)$ increases. When the incident angle is equal to 90°, because the depth of sputtered atoms is zero, the sputtering yield reaches zero. Deposited energy distribution $F(E, \eta)$ on the surface can be approximated as Gaussian distribution set up in terms of the moments [77]

$$F(E, \eta) = \frac{E_i}{(2\pi)^{1/2} A} \exp\left(-\frac{\eta^2 a^2}{2A^2}\right) \tag{2.8}$$

where $a$ is the projected energy range, $A^2 = \eta^2\alpha^2 + \eta'^2\beta^2$, $\alpha$ and $\beta$ are the energy range straggling along longitudinal and lateral directions respectively, $\eta' = \sqrt{1-\eta^2}$. With increasing incident angle, deposited energy increases through exponential term while corresponding depth of sputtered atoms decreases through cosine term. A balance between these two terms gives rise to the peak position of sputtering yield (Fig. 2.2).

Substituting Eq. 2.8 into Eq. 2.7 and letting the derivative of Eq. 2.7 in terms of $\eta$ be zero, we have the incident angle $\theta_{max}$ in which the sputtering yield achieves its maximum value. For simplicity, we assume symmetric case $\alpha = \beta$.

$$\cos\theta_{max} = \frac{\alpha}{a} \tag{2.9}$$

which means the maximum sputtering yield only depends on the energy range and straggling (deposited energy distribution). For deposited energy, if we assume $a \approx 2.5\alpha$, Eq. 2.9 shows the maximum sputtering yield will appear at $\theta_{max} = 66°$ (Fig. 2.2). This is in good agreement with the experimental observation showing the maximum sputtering yield takes place around $\theta = 70°$. From Eq. 2.7, under assumption of Gaussian distribution and symmetry case (Eq. 2.8), the normalized

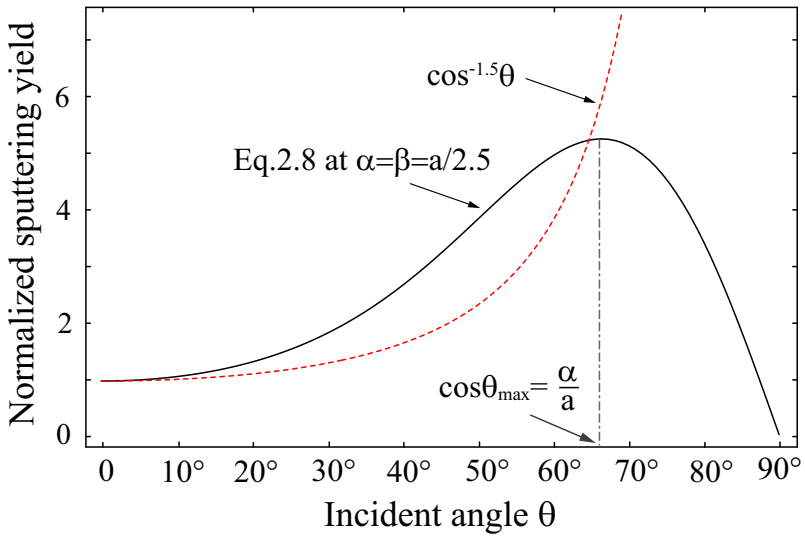


Figure 2.2: Normalized sputtering yield as a function of incident angle from our model. Sigmund's theory (dashed curve) was given for comparison.

sputtering yield is

$$\frac{Y(E,\theta)}{Y(E,\theta=0)} = \cos\theta \exp\left(\frac{a^2 \sin^2\theta}{2\alpha^2}\right) \tag{2.10}$$

where we replace $\eta$ by $\cos\theta$.

The variation of sputtering yield with energy range and straggling is shown in Fig. 2.3. With increasing ratio of projected range to struggling, maximum value of sputtering yield moves to larger incident angle. For higher energy and lighter ion, $a/\alpha$ becomes larger and peak tends to move to higher incidence. This prediction is consistent with experimental results: the higher ion energy or lighter ion, the larger incident angle for maximum sputtering yield.

Fig. 2.4 shows the comparison of angle dependent sputtering yield predicted by Eq. 2.10 with the experimental results for different energies and different ion-targets systems [122–124]. The quantitative values of the coefficients $a, \alpha, \beta$ for energy distribution can be found using the theory of Winterbon *et al.* [125] from the corresponding

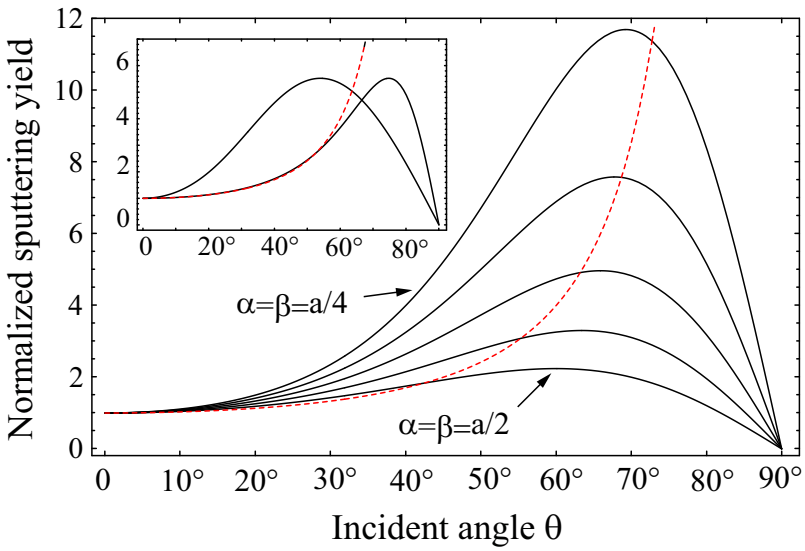


Figure 2.3: Angular dependence of sputtering yield on different ratio of energy range to straggling: from top to bottom (symmetry case $\alpha = \beta$), $a/\alpha = 4, 3.5, 3, 2.5, 2$. Insert shows the sputtering yield for asymmetry case: from left to right $a = 2.5\alpha = 1.5\beta, a = 2.5\alpha = 4\beta$. Dashed curve showing the Sigmund theory given by $\cos^{-2}\theta$.

values for the ion distribution using Monte-Carlo simulation code SRIM as shown in Table 2.1 [80]. We can observe that theoretical predictions in Eq. 2.10 compare fairly well with experimental data.

Table 2.1: Energy rang and straggling calculated from TRIM and Winterbon's theory [81,126]

| Target | Ion | Energy (keV) | a (nm) | $\alpha$ (nm) | $\beta$ (nm) |
|---|---|---|---|---|---|
| Diamond | Ar | 0.5 | 1.8 | 0.8 | 1 |
| Cu | Xe | 1.05 | 1.7 | 0.8 | 0.9 |
| Cu | Kr | 1.05 | 1.1 | 0.6 | 0.4 |
| Cu | Ne | 1.05 | 1.6 | 0.9 | 0.6 |
| Ag | Xe | 100 | 15.6 | 5.9 | 3.5 |

It is well known that average projected energy range is give by $\langle x_\theta \rangle = \eta \langle x_0 \rangle$ [125], where $\langle x_\theta \rangle$ and $\langle x_0 \rangle$ are average damage depth at off-normal and normal bombardment, respectively. This relationship was derived from linear Boltzmann's transport equation under the same assumptions as those in Sigmund's theory. For approximation with $m = 0$ in Thomas-Fermi cross section, the average projected energy range

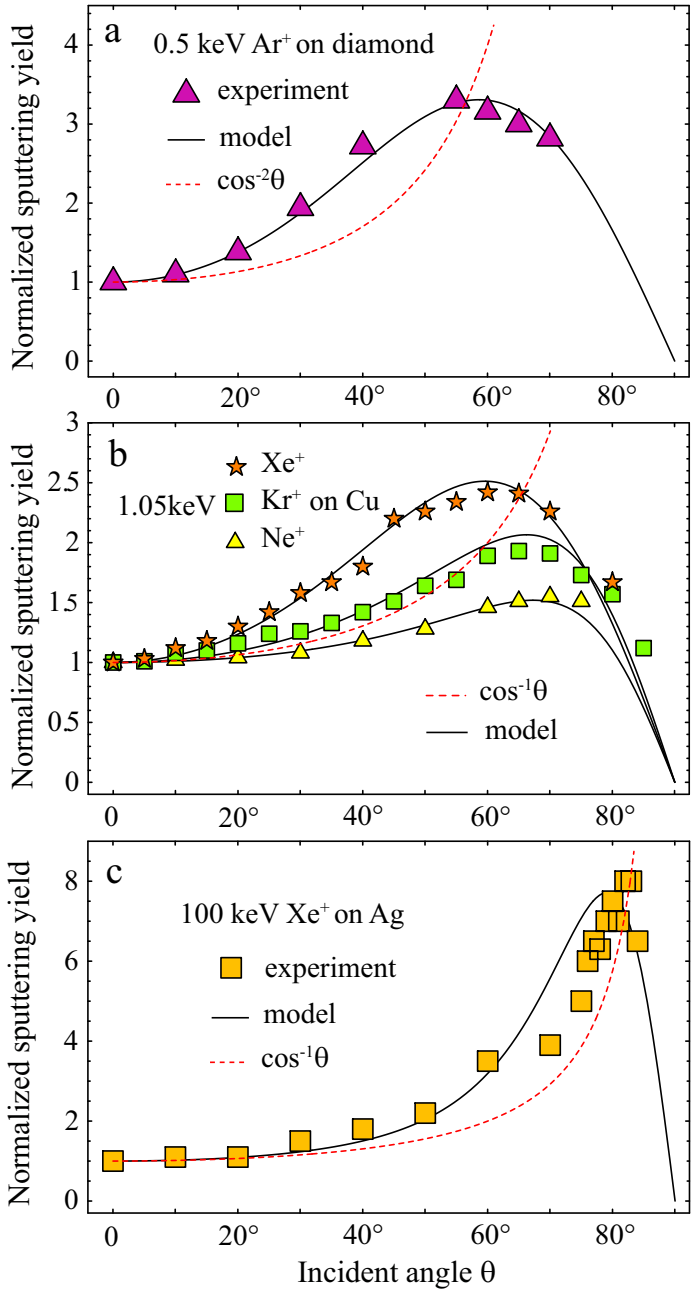


Figure 2.4: Comparison of angular dependence of sputtering yield predicted by the model with experimental results, (a) 0.5 keV Ar ion on diamond [122], $a = 18$Å$, \alpha = 8$Å$, \beta = 10$Å. (b) 1.05 keV Xe, Kr, and Ne ions on Cu [123], for Xe on Cu, $a = 17$Å$, \alpha = 8$Å$, \beta = 9$Å; for Kr on Cu, $a = 11$Å$, \alpha = 6$Å$, \beta = 4$Å; for Ne on Cu, $a = 16$Å$, \alpha = 9$Å$, \beta = 6$Å. (c) 100 keV Xe on Ag [124], $a = 156$Å$, \alpha = 59$Å$, \beta = 35$Å.

is energy independent [77, 121, 125]. This means the recoil atoms with different energies, including sputtered atoms at the surface which have energy larger than surface bonding, satisfy the same equation describing the relationship for the range between normal and off-normal bombardment. Therefore, we can assume the average depth of recoil atom is equal to the average depth of sputtered atoms. This can be confirmed by Eq. 2.6. The average depth of recoil atom is given by $2\eta/(\pi\lambda_0 N a^2)$, where $2/(\pi\lambda_0 N a^2)$ is average depth at normal bombardment which agrees very well with the estimate of sputtered atom depth $3/4 \cdot 2/(\pi\lambda_0 N a^2)$ given by Sigmund [77].

## 2.2 Influence of Surface Morphology on Sputtering Yields

This study analyzes the effect of surface morphology on sputtering yield using a specially prescribed surface shape. Compared to a flat surface, it was found that surface morphology can cause a decrease in the sputtering yield and an increase in the incident angle corresponding to the maximum sputtering yield. Based on Sigmund's theory, an analytical formula for morphology dependent sputtering yield was developed by averaging the curvature dependent sputtering yield. The predicted dependence of sputtering yield on surface morphology is in good agreement with experimental observations.

Curvature dependent sputtering is a primary mechanism contributing to the evolution of surface morphologies induced by ion beam [32, 63, 64, 72, 76, 77, 126]. The understanding of this mechanism lies in the framework of Sigmund's theory [77]. For amorphous and polycrystalline materials, Sigmund proposed that the sputtering yield is proportional to the energy accumulated on the surface. By introducing a discrete surface profile consisting of two intersecting planes, Sigmund found that the sputtering yield is smaller on top of the crest than on the bottom of the trough [78].

As a consequence, sharp cones appear to be more stable than flat surfaces. Extending this theory to take into account a continuum surface profile, Bradly and Harper (BH model) derived a linear partial differential equation for explaining ion-induced ripple formation [64]. Cuerno and Barabási developed a nonlinear partial differential equation to interpret the evolution of ripples for a long bombardment [63]. Although Sigmund's theory is focusing on the planar surface, it was shown that, with the appropriate assumption of surface geometry, Sigmund's theory can be used successfully to predict surface features induced by ion beam [63, 64, 82–86]. Compared to Sigmund's theory which is based on transport model and is valid at energies sufficiently above the threshold energy, Monte-Carlo simulation can predict sputtering behavior in very details of energy and incidence [127]. Based on this simulation, the effects of roughness on sputtering yield has been pursued by assuming fractal surface topography and measured surface topography [128, 129].

Sputtering yield dependence on surface curvature was derived in the BH model. In this model, curvature dependent sputtering yield appeared in a complex differential equation in which curvature was represented by a second derivative of surface height under the small slope approximation [64]. Following this approach, the effects of morphology on sputtering yield have been investigated in recent years [130, 131]. In order to achieve analytical results, all these studies use a prescribed undulated shape of the surface. Therefore, the derived sputtering yield is curvature dependent for a specially assumed shape rather than morphology dependent. The real surface geometry is sufficiently complicated that a finite number of parameters cannot provide a full description. However, because the sign and value of curvature change at different locations, if we assume the same amount of positive and negative curvatures, based on the previous studies, the simple equation for morphology dependent sputtering

yield can be derived by averaging the curvature dependent sputtering yield. In this chapter, a formula characterizing the influence of surface morphology on evolution of sputtering yield is developed. It is shown that surface morphologies induced by the ion bombardment can give rise to a decrease in sputtering yield and a shift of the incident angle at which sputtering yield is maximized.

## 2.3 Model

### 2.3.1 Ion energy distribution and local flux

**Ion energy distribution**

Since the pioneering work of Bradley and Harper (BH model) [64], the theory for ripple formation induced by ion beam on the surface of materials has been intensively investigated. One assumption of BH model is the Gaussian distribution of energy which makes integration possible under small slope approximation [64,65,76]. According to Sigmund's theory [77], in the elastic collision region where electronic stopping is not dominating, the energy distribution $F(x)$ can be set up in terms of the moments $\langle x^n \rangle$ by the following equation

$$F(x) = \frac{\epsilon}{\langle \Delta x^2 \rangle^{1/2}} [\varphi_0(\xi) - \frac{\Gamma_1}{6}\varphi_3(\xi) + \left(\frac{\Gamma_2}{24}\varphi_4(\xi) + \frac{\Gamma_1^2}{72}\varphi_6(\xi)\right) + \cdots] \tag{2.11}$$

where $\epsilon$ is the energy of ion, $n$ is the order of moments, and

$$\langle \Delta x^n \rangle = \langle (x - \langle x \rangle)^n \rangle \qquad n = 2, 3, \cdots \tag{2.12}$$

$$\varphi_n(\xi) = \left(d^n / d\xi^n\right) (2\pi)^{-1/2} e^{-\xi^2/2} \qquad n = 0, 1, 2, \cdots \tag{2.13}$$

$$\xi = (x - \langle x \rangle) / \langle \Delta x^2 \rangle^{1/2} \tag{2.14}$$

$$\Gamma_1 = \langle \Delta x^3 \rangle / \langle \Delta x^2 \rangle^{3/2} \tag{2.15}$$

$$\Gamma_2 = \langle \Delta x^4 \rangle / \langle \Delta x^2 \rangle^2 - 3 \tag{2.16}$$

Gaussian distribution is obtained by taking into account the first term in the large square brackets. The corresponding coordinations are build as the $x$ axis along

the beam direction (local coordination system). At normal bombardment, Eq. 1.5 can be obtained from Eq. 2.11. When off-normal ion beam bombards the target, we always assume that Eq. 1.5 does not change if we make the $x$ axis along the beam direction. Therefore, due to the surface curvature is functioned on laboratory reference frame, there is a rotation angle (incident angle $\theta$ ) between two systems (Fig. 2.1). Coordination transformation is needed. The values in Eq. 2.11 should be calculated again under the laboratory coordination for spatial energy distribution through the transition of local system [77]. The spatial moments are given by

$$M_{hkm}(\epsilon,\theta) = \int_{-\infty}^{+\infty}\int_{-\infty}^{+\infty}\int_{-\infty}^{+\infty} x^h y^k z^m F(x,y,z)dxdydz \tag{2.17}$$

here $p$ is the energy distribution, $\theta$ is the angle between the initial direction of motion of the incident ions and the axis of the laboratory system. If we place the ion direction parallel to the negative direction of $x$ axis in local system, the moments in the laboratory system is given by substituting coordination rotation

$$x = \eta x' - \eta' y' \tag{2.18}$$

$$y = \eta' x' + \eta y' \tag{2.19}$$

$$z = z' \tag{2.20}$$

$$\eta = \cos\theta \tag{2.21}$$

$$\eta' = (1-\eta^2)^{1/2} \tag{2.22}$$

into Eq. 2.17. Thus the moments under the laboratory system are

$$M_{hkm} = \int_{-\infty}^{+\infty}\int_{-\infty}^{+\infty}\int_{-\infty}^{+\infty} (\eta x' - \eta' y')^h (\eta' x' + \eta y')^k z^m p dx' dy' dz' \tag{2.23}$$

Substituting the moments in Eq. 2.23 into Eq. 2.11, The Gaussian approximation for spatial distribution under laboratory coordination is

$$F(r) = \frac{\epsilon}{(2\pi)^{3/2}\sqrt{AB}\beta}\exp\left(-\frac{(x-\eta a)^2}{2A^2} - \frac{(y-\eta' a)^2}{2B^2} - \frac{z^2}{2\beta^2}\right) \tag{2.24}$$

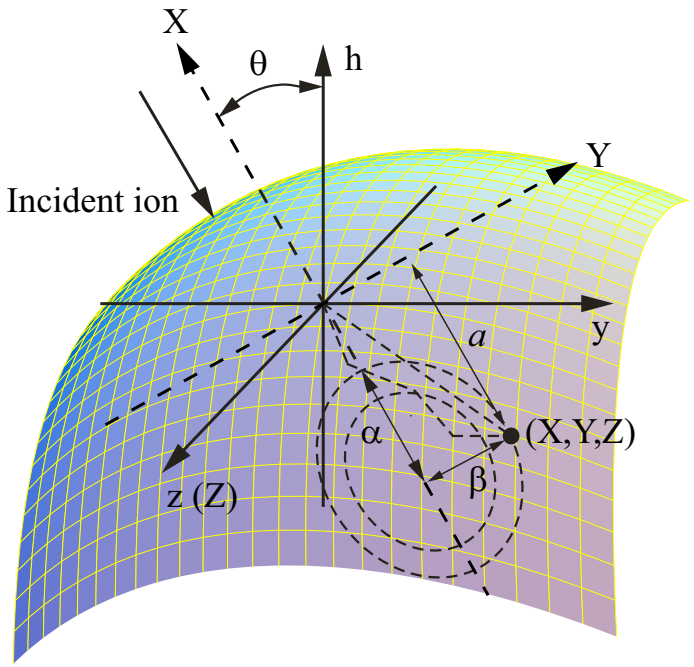


Figure 2.5: Schematic illustration of the two reference systems, local coordination $(X, Y, Z)$ and laboratory coordination $(h, x, y)$, and the definition of projected range $a$ , straggling $\alpha$ and $\beta$, and incident angle $\theta$. The dashed curve denotes the equal energy contour.

where

$$A^2 = \eta^2\alpha^2 + \eta'^2\beta^2 \tag{2.25}$$

$$B^2 = \eta'^2\alpha^2 + \eta^2\beta^2 \tag{2.26}$$

Eq. 2.24 gives the average energy deposited per unit volume at a point with coordinates $(x, y, z)$ (energy density distribution) in terms of the projected range and incident angle.

**Local flux**

When evaluating surface integral, flux as a function of surface profile is needed (local flux compared to the flux determined by equipment). For three-dimension, the simple way to calculate local flux is to use vector-valued functions. Similar to calculation of the flow of a fluid through a surface, we can assume both ion flux and surface have orientations. If we let projected ion beam direction be parallel to

negative $h$ axis, the flux can be represented by

$$\mathbf{F} = -f\cos\theta\mathbf{i} + f\sin\theta\mathbf{j} \tag{2.27}$$

where f is a value of flux, $\mathbf{i}$ and $\mathbf{j}$ are unit vector along positive $x$ and $y$ axes. Normal direction of a surface $z = h(x, y)$ in a vector form is given by

$$\mathbf{n} = \frac{-1}{\sqrt{1+\nabla_x^2 h+\nabla_y^2 h}}\mathbf{i} + \frac{\nabla_x h}{\sqrt{1+\nabla_x^2 h+\nabla_z^2 h}}\mathbf{j} + \frac{\nabla_y h}{\sqrt{1+\nabla_x^2 h+\nabla_y^2 h}}\mathbf{k} \tag{2.28}$$

where $\mathbf{k}$ is unit vector along positive $z$ axis. Thus the local flux is given by

$$\phi(r) = \mathbf{F}\cdot\mathbf{h(x,y,z)} \tag{2.29}$$

$$= \frac{f\cos\theta}{\sqrt{1+\nabla_x^2 h+\nabla_y^2 h}} + \frac{f\sin\theta\nabla_y h}{\sqrt{1+\nabla_x^2 h+\nabla_y^2 h}} \tag{2.30}$$

At normal bombardment, Eq. 2.30 is

$$\phi(r) = \frac{f}{\sqrt{1+\nabla_x^2 h+\nabla_y^2 h}} \tag{2.31}$$

At off-normal bombardment for two dimension, Eq. 2.30 reduces to

$$\phi(r) = \frac{f\cos\theta}{\sqrt{1+\nabla_y^2 h}} + \frac{f\sin\theta\nabla_x h}{\sqrt{1+\nabla_y^2 h}} \tag{2.32}$$

For two dimension, the average flux can be written as

$$\langle\phi(r)\rangle = \frac{1}{\int_l dl}\int_l \boldsymbol{\phi}(r)dl \tag{2.33}$$

where $\mathbf{l}$ is a curve with period $\lambda$, given by

$$dl = \sqrt{1+(\nabla_y x)^2}dy \tag{2.34}$$

Substituting Eqs. 2.32 and 2.34 into Eq. 2.31 gives

$$\langle\phi(r)\rangle = f\lambda/l\cos\theta + \frac{f\sin\theta}{\int_l dl}\int_{-\lambda/2}^{\lambda/2}\nabla_y x dy \tag{2.35}$$

$$= f\lambda/l\cos\theta \tag{2.36}$$

where $l$ is curve length in one period. Because $x$ is a periodic function of $y$ with period $\lambda$, the second term on the right hand of Eq. 4.16 is zero. This can be understood in the following way: in one period $\lambda$, the total ions on the surface is $f\lambda\cos\theta$, and length of curve in period $\lambda$ is $l$. Thus the average flux on the surface is ratio of these two terms. e.g. Eq. 2.36. Here we did not consider shadowing effects.

### 2.3.2 Sputtering yield on a rough surface

According to Sigmund's theory [77, 78], the sputtering yield can be expressed by

$$Y = \frac{\iint_{\Re} N(\mathbf{r}, \varepsilon, \theta) \cdot d\mathbf{S}}{\iint_{\Re} \phi(\mathbf{r}) \cdot d\mathbf{S}} \tag{2.37}$$

where $N(\mathbf{r}, \varepsilon, \theta)$ is the number of sputtered atoms per unit area per unit time at position $\mathbf{r}$, ion energy $\varepsilon$ and incident angle $\theta$, $\phi(\mathbf{r}')$ is local flux of ion at $\mathbf{r}$, and $\mathbf{S}$ is the surface area over the integrated range $\Re$. Here we evaluate the total number of sputtered atoms on a well defined surface, and calculate the total ions hitting on the same surface. The sputtering yield can be defined as the ratio of these two terms. $N(\mathbf{r}, \varepsilon, \theta)$ is given by

$$N(\mathbf{r}, \varepsilon, \theta) = \Lambda \iint_{\Re} F(\mathbf{r} - \mathbf{r}')\phi(\mathbf{r}') \cdot d\mathbf{A}' \tag{2.38}$$

where the integral is evaluated over the area $\Re$, $\Lambda$ is a parameter characterizing the properties of target materials (Eq. 1.2), $\phi(\mathbf{r}') \cdot d\mathbf{A}'$ is the number of ions hitting on an area $d\mathbf{A}'$, $F(\mathbf{r} - \mathbf{r}')$ denotes energy density at position $\mathbf{r}$ generated by an ion hitting the surface in a point $\mathbf{r}'$. To evaluate Eq. 2.38, we need to know the surface profile. Following BH model, we can assume that surface height is given by

$$h = -\frac{y^2}{2R_1} - \frac{x^2}{2R_2} \tag{2.39}$$

where $R_1$ and $R_2$ are two principle radii of curvature, and we place the ion beam in the plane formed by the $h$ and $y$ axes and let projected ion beam direction be parallel

to $h$ axis (Fig. 2.5). The energy density $F(\mathbf{r})$ can be approximated as Gaussian distribution (Eq. 2.24). We assume further that the surface varies smoothly enough so that the product of derivatives of $h$ can be neglected, and $R_1$ and $R_2$ are much larger than $a$ for the purpose of neglect of second or higher order in $a/R_1$ and $a/R_2$ in Eq. 2.38. Because the dominant contribution to this equation comes from $y/a$ and $x/a$ of order 1, rational approximation can be made by assuming the integral of Eq. 2.38 is over the infinite range in order to eliminate the error function [63, 64].

For real surface morphology, only average of curvature dependent sputtering yield can well describe morphology effects. For simplicity, considering changes of sign and value of curvature, we assume the same amount of positive and negative curvatures. However, it can be proved that average flux over any smooth surface (symmetry profile, no shadowing effects) is $f\cos\theta$ and average sputtered atoms are $fY_\theta\cos\theta$, where $Y_\theta$ is sputtering yield on flat surface at incident $\theta$ [119], Therefore sputtering yield at off-normal bombardment on curved surface is $Y_\theta$, the same as that on the planar surface. The problem here is the symmetry profile assumption. It was found, with bombardment proceeding, that asymmetry profile can form in which one side of profile is larger than the other (Fig. 2.6) [33, 119, 132, 133]. This asymmetry structure can give rise to extra flux and sputtered atoms which depend on the surface morphology. Under these conditions, we need to calculate the sputtering yield again on a single surface shape and then make average. We can assume that $h$ varies slowly from $h_1$ to $h_2$ and corresponding $y$ and $x$ from $-\sqrt{2h_1R_{1,2}}$ to $\sqrt{2h_2R_{1,2}}$, where only radiation ions over the interval $-\sqrt{2h_1R_{1,2}} \le y, x \le \sqrt{2h_2R_{1,2}}$ have the contributions to the sputtering (Fig. 2.6). The integrating shows

$$Y(R,\eta) = \left[\frac{\eta - \frac{a\eta^2}{2A^2}\left(\frac{B^2}{R_1}+\frac{\beta^2}{R_2}\right) - \frac{a\eta'^2}{R_1}\left(\frac{\eta^2a^2}{2A^2}-1\right) + \eta'\gamma\left(1-\frac{\eta^2a^2}{A^2}\right)}{\eta+\gamma\eta'}\right]Y_\theta \qquad (2.40)$$

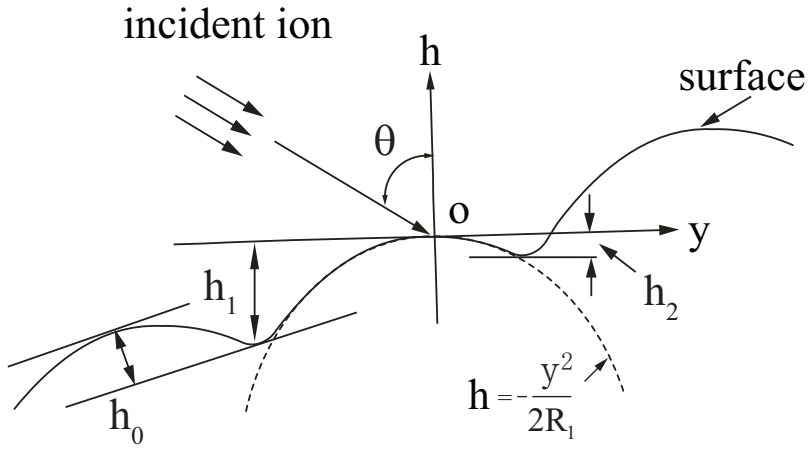


Figure 2.6: Side view normal to x axis showing asymmetry profile at oblique incidence. Dashed curve showing the assumed symmetry profile. The integration is over the range of $-\sqrt{\mid 2h_1R_1 \mid} \leq y \leq \sqrt{\mid 2h_2R_1 \mid}$.

where $Y_\theta$ is sputtering yield at incident angle $\theta$ given by [134]

$$Y_\theta = \eta\Lambda\epsilon/(\sqrt{2\pi}A)\exp(-\eta^2a^2/(2A^2)) \tag{2.41}$$

$\gamma$ is a positive parameter, depending on surface roughness, given by

$$\gamma = \sqrt{\mid \frac{h_1}{2R_1} \mid} - \sqrt{\mid \frac{h_2}{2R_1} \mid} \propto \sqrt{\mid \frac{h_0}{2R_1} \mid} \tag{2.42}$$

where $h_0$ can be considered as roughness height. $\gamma$ is a new parameter we introduced in our model, depending on both surface roughness and curvature. No available data from theory or experiment can be obtained for $\gamma$. In order to make comparison, the value of $\gamma$ is determined by fitting experimental data for sputtering yield after other parameters $(a, \alpha, \beta)$ are computed by simulation.

Eq. 2.40 gives curvature dependent sputtering yield. If we assume the same amount of positive and negative curvatures in Eq. 2.40 and calculate the average sputtered atoms and average ions respectively, the simple equation can be obtained by neglecting terms including $1/R$ in Eq. 2.40. The sputtering yield can be approx-

imated as

$$Y(R,\theta) \approx \frac{1+\bar{\gamma}\tan\theta(1-\frac{\cos^2\theta a^2}{A^2})}{1+\bar{\gamma}\tan\theta} Y_\theta \tag{2.43}$$

where $\bar{\gamma} \propto \frac{1}{n}\sum_{i=1}^{n}\sqrt{|\frac{h_i}{2R_i}|}$, an additional term showing surface morphology effects on sputtering yield. Fig. 2.7 shows the relationship between sputtering yield and incident angle given by Eq. 2.43 with different surface morphologies and energy ranges. It can be seen that the peak of sputtering yield appears around $65^\circ \sim 80^\circ$ depending on the energy ranges and surface morphologies. The peak position of sputtering yield comes closer to $90^\circ$ with increasing ion energy ($a/\alpha$ increases) or increasing surface roughness ($\bar{\gamma}$ increases). At angle smaller than $60^\circ$, the trend of sputtering yield predicted by our model is very similar to that proposed by Sigmund. At high angle, sputtering yield goes through maximum value and then decreases dramatically to zero. These predictions are in good agreement with the experimental observations in which surface features generated by the ion bombardment can lead to a reduction in the sputtering yield [15, 128, 129, 135–137].

### 2.3.3 Special cases

At normal bombardment, for a single surface given by Eq. 2.39, under symmetric case $\alpha = \beta$, combination of Eqs. 2.37-2.44 gives

$$Y(R,0) = \left[1 - \frac{a}{2}\left(\frac{1}{R_1} + \frac{1}{R_2}\right)\right] Y_0 \tag{2.44}$$

where $Y_0$ is the sputtering yield for planar surface at normal bombardment, given by $Y_0 = \Lambda\epsilon/(\sqrt{2\pi}\alpha)\exp(-a^2/(2\alpha^2))$ [77, 78, 138]. If we replace $\frac{1}{R_1}$ and $\frac{1}{R_2}$ by the second derivatives of height in terms of $y$ and $x$, under the symmetry case ($\alpha = \beta$) and normal bombardment, the same equation can be found in BH model [64]. If we assume $R_1 = R_2 = R$, Eq. 2.44 gives the simple equation describing sputtering yield

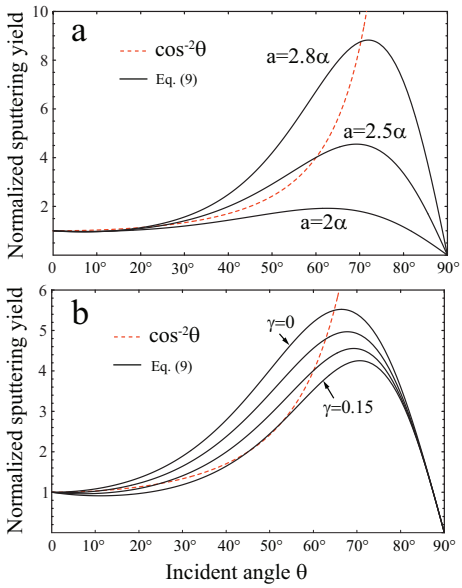


Figure 2.7: Angular dependence of sputtering yield with (a) energy ranges at $\gamma = 0.1$ and (b) surface morphologies at $a/\alpha = 2.5$, from top to bottom, $\gamma = 0, 0.05, 0.1, 0.15$. Curves ($\cos^{-2}\theta$) from Sigmund's theory were given for comparison.

as a function of radius $R$.

$$Y(R,0) = \left(1 - \frac{a}{R}\right) Y_0 \tag{2.45}$$

This equation reveals a unique property of sputtering: the sputtering yield increases from crests (positive $R$) to planar surface ($R = \infty$) and has maximum value for the trenches (negative $R$). Many features induced by ion bombardment, including ripple formation are based on this mechanism [63, 64]. For spherical particles ($R > 0$), Eq. 2.45 shows that the sputtering yield increases with increasing particle size. This result can explain why the uniform particles can be obtained for ion beam assisted deposition.

### 2.3.4 Comparison with experiment

Fig. 2.8 shows the comparison of angle dependent sputtering yield predicted by Eq. 2.43 with the experimental results [123, 139, 140] for different ion energies and different ion-target systems. Values of parameters used for numerical estimation of

sputtering yield in Eq. 2.43 under the experimental conditions are listed in Table 2.2. We can observe that theoretical predictions in Eq. 2.43 compare fairly well with experimental data. In Fig. 2.3c, three fitting parameters $\gamma$ are given. It can be seen that for small incident angle the morphology effects can be negligible, while at high incident angle, the morphology effects play an important role on the value and position of maximum sputtering yield. The quantitative values of the coefficients $a$, $\alpha$, $\beta$ for energy distribution can be evaluated from the corresponding values for the ion distribution using the theory of Winterbon *et al* [125]. We use Monte-Carlo simulation code SRIM to generate ion distribution parameters [80].

Table 2.2: Parameters used for numerical estimation of sputtering yield [80,125]

| Target | Ion | Energy (keV) | a (nm) | $\alpha$ (nm) | $\beta$ (nm) | fitting parameter $\bar{\gamma}$ |
|---|---|---|---|---|---|---|
| Ni | Ar | 200 | 66 | 25 | 11 | 0.02 |
| Cu | Ar | 1.05 | 2.7 | 1.3 | 0.8 | 0.01 |
| Ta | Ar | 1.05 | 1.5 | 0.8 | 0.6 | 0.01 |
| Ag | Ar | 1.05 | 1.5 | 0.9 | 0.7 | 0.01 |
| Ni | H | 1 | 10 | 4 | 3 | 0.1 |

We neglect redeposition and shadow effects in our model. In order to get analytical resolution, small slope approximation was assumed. This condition is only valid at the beginning of bombardment where shadow and redeposition can be neglected. However, for a long bombardment, with increasing of roughness and slope, these two effects should be taken into account [128].

## 2.4 Conclusion

In summary, an expression for interpreting the evolution of sputtering yield as a function of incident angle based on Sigmund's theory has been derived. It was found that the peak of angular dependence of sputtering yield results from two competitive effects: increased energy deposited on the surface by incident ion and decreased

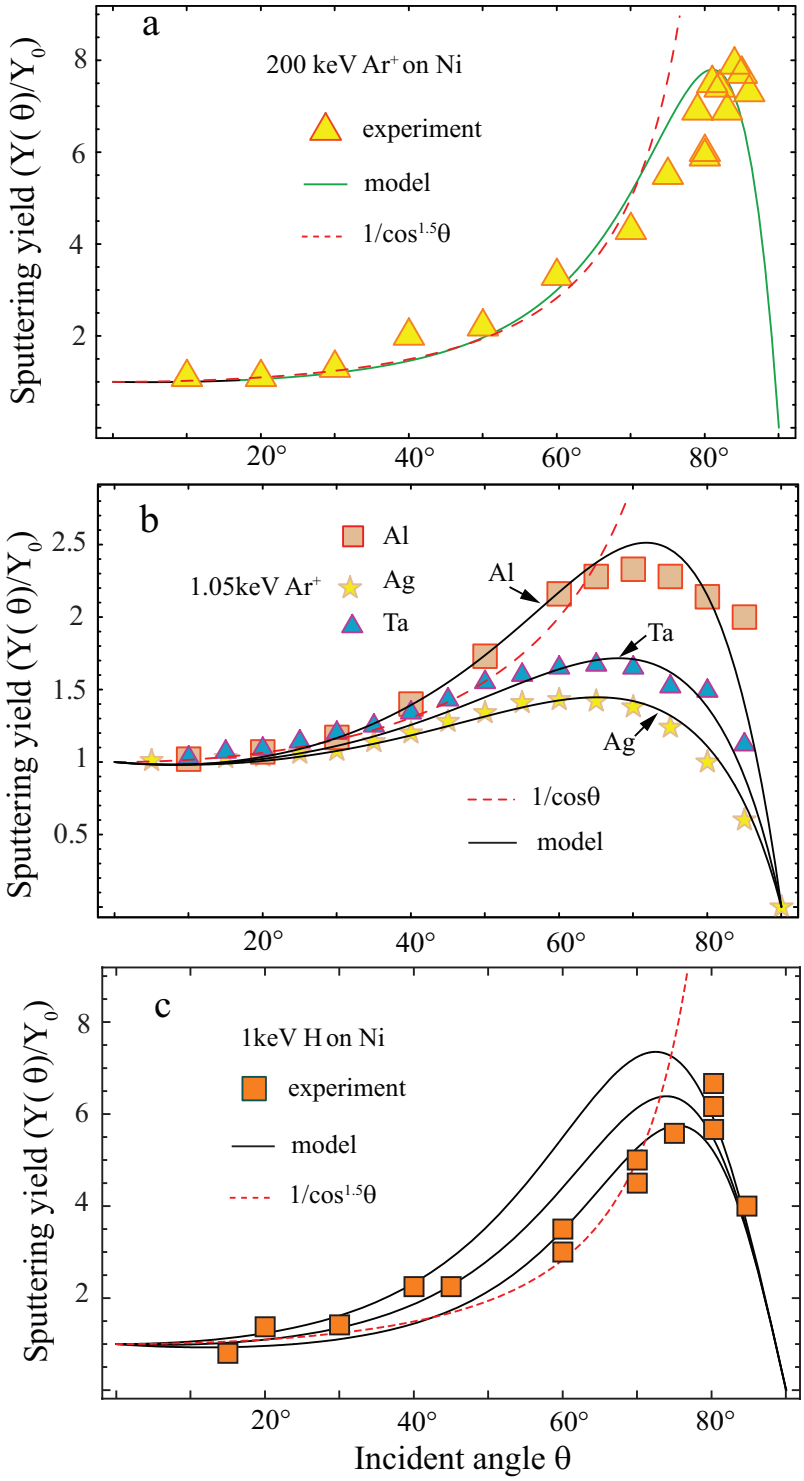


Figure 2.8: Comparison of angular dependence of sputtering yield predicted by the model with experimental results, (a) 200 keV Ar ion on Ni [138], $\gamma = 0.02$, (b) 1.05 keV Ar ion on Al, Ta and Ag [123], $\gamma = 0.01$, (c) 1 keV H on Ni [139], from top to bottom: $\gamma = 0$, $\gamma = 0.05$, $\gamma = 0.1$.

depth traveled by sputtered atom. In addition, a continuum model for morphology dependent sputtering yield has been introduced. For a particular surface geometry, curvature dependent sputtering yield was derived following the approach given in BH model. In particular, we shown that large particles have higher sputtering yield than small particles. For surface morphology effect, due to the asymmetry surface profile induced by ion beam, the averaged sputtered atoms which are different from planar surface are generated and thus the morphology dependent sputtering yield was derived by averaging curvature dependent sputtering yield. It was found that, within the small slope approximation, with the development of surface morphology by ion bombardment, the sputtering yield decreases and the incident angle at which sputtering yield is maximum increases. The predicted results are in agreement with experimental observations.

# CHAPTER III

# One Dimensional Pattern Formation under Ion Bombardment

## 3.1 Propagations of Ripples on Pyrochlore Induced by Ion Beam Bombardment

The morphological evolution of ion-beam induced ripples has been extensively investigated in recent years due to both experimental and theoretical interests. Several models of ripple growth based on the continuum dynamical equations for the height of the interface have been proposed and studied analytically and numerically, revealing a rich variety of interesting phenomena [18, 23, 63–67, 141]. Up to now, four main mechanisms are considered for ripple formation: sputtering, surface diffusion, redeposition, and viscous flow [23, 63–65]. For simplicity, small slope approximation was assumed for establishment of continuous kinetic equations. At the beginning of ripple formation, the linear partial differential equation was developed in which only the first order in slope was included. In this regime, the driving mechanism is the dependence of the sputtering yield on the local surface curvature. The orientation and wavelength of ripples can be described by the Bradley and Harper (BH) model [64]. With increasing of ripple slope for further bombardment, the second order in slope was added and thus nonlinear partial differential equation was developed [63, 65, 66]. In this nonlinear regime, nonlinear terms dominate and give rise to other surface

morphologies such as roughening, coarsening, and saturation of ripples by either destroying the ripples or generating a new rotated ripple structure [21, 63]. Now most features induced by ion bombardment are discussed based on this nonlinear equation. Ion incidence dependent orientation, fluence dependent rotation, coarsening and roughening can be successfully predicted by this model. However, recent experimental observations show that these existing models can only partially describe or even contradicts the observed propagation of ripples. For example, for Si(111) bombarded by 30 eV Ga ions, Habenicht *et al.* found that the propagation direction of ripples on Si by ion bombardment is opposite to that predicted by current models [13]. The same result has been reported by Alkemade on the ion bombardment of $SiO_2$ [23]. Additionally, Datta *et al.* found no shift of ripple on ion bombardment of diamond [22]. Ripple propagation is an important phenomenon for understanding of ripple growth but only a few efforts are made on this study.

It is well known that a common feature of most models for ripple formation is their assumption of a smooth surface profile [142]. Under this assumption, surface can be described in powers of derivatives of height and thus analytical results can be obtained based on Sigmund's theory [63–65, 77]. This implies that these models are only restricted to small slopes including nonlinear regime. The investigation of ion-induced features with large slope has been reported [143–146]. Barber *et al.* proposed a geometrical construction to predict morphological evolution during ion bombardment by employing the approach used in chemical etching [146]. Nobes and Carter established a shock wave equation which was derived from the fact that different erosion by ion beam along the curvature can lead to the slope change under the assumption that surface erosion is caused only by sputtering [143–145]. Based on this model, they successfully predict many features induced by ion beam, such as

cone formation, apex angle of cone and evolution of hemispherical trough. In a more recent analysis of ion sputtering of steep surface features, Chen *et al.* developed a shock wave equation by making using of the classical theory of sputtering yield without small slope approximation based on Sigmund's theory [76]. By considering thermal diffusion, Chen *et al.* found a stable slope for a long time bombardment, in consistent with that predicted by Barber, Nobes and Carter.

Pyrochlore ($A_2B_2O_7$, space group Fd3m) is a cubic, anion deficient derivative of the fluorite structure ($AX_2$), two types of cations ordered at the A-site and B-site and one-eighth of the anions missing (Fig. 3.1). As in the fluorite structure, the cations, A and B, form a face centered cubic array, and the anions are located in the tetrahedral interstices of the cations array. The face centered A site and B site cations are ordered in alternate [110] rows. Ideal pyrochlore consists of cubic coordinated A-site cations ($AO_8$) and octahedrally coordinated B-site ($BO_6$). The smaller B cations form a continuous, slightly distorted corner sharing network, in which the larger A cations occupy channels within the octahedral network (Fig. 3.1). Pyrochlore compounds display an unusual variety of physical, chemical, and electronic properties due to the remarkable range of compositions and extensive cation substitutions at both the A and B sites. They are important in numerous technological applications that encompass catalysts, piezoelectric materials, ferro- and ferrimagnetism, luminescent compounds, giant magnetoresistant materials, and as a solid electrolyte in solid oxide fuel cells. Importantly, the properties of pyrochlore, e.g., the ionic conductivity, can be manipulated on a nanometer scale by the use of ion-beam irradiation or implantation techniques, and numerous nanostructures, including nanodots and nanodomains, one-dimensional nanowires, and two-dimensional nanolayers, have been created by ion beam techniques in pyrochlore materials [147, 148].

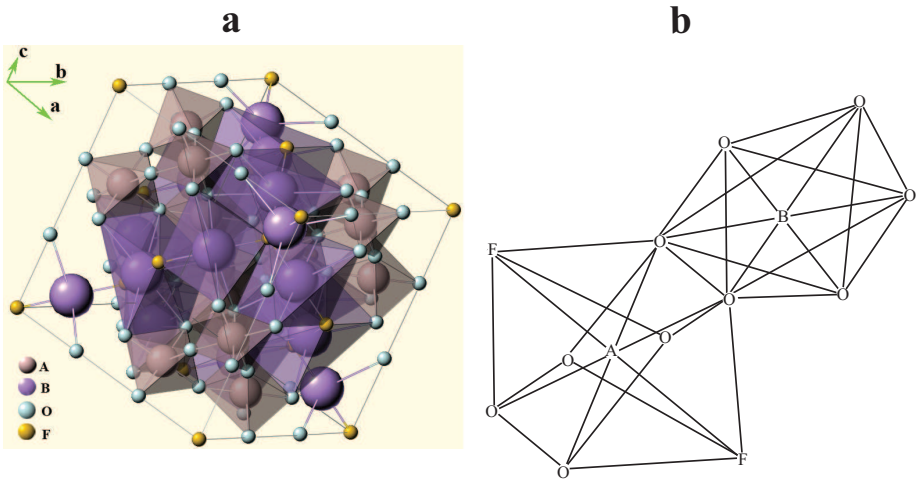


Figure 3.1: Pyrochlore structure. (a) Schematic illustration of Pyrochlore structure with formula $A_2B_2O_6F$. (b) The coordination geometries of adjacent A and B site cations.

In this chapter, the morphological evolution of ion-beam induced ripples on $Cd_2Nb_2O_7$ pyrochlore has been studied. Through *in situ* experiments, it was found terrace-like ripples consisting of sufficiently steep slopes which are far away from smooth. The slope and velocity of terrace only depend on the incident angle, independent of the details of the bombardment process. Following approaches given by Nobes and Carter [143–145], a partial differential equation for arbitrarily large slopes in which the shock wave was found was established. The terrace ripple can thus be understood as the propagation of a shock front that self-selects a stable slope.

### 3.1.1 Experiment and results

Our experiments were carried out using a focused ion beam (FIB) in a dual-beam instrument (FEI Nova 200 NanoLab). Single crystal of $Cd_2Nb_2O_7$ pyrochlore was irradiated in a vacuum of $2 \times 10^{-7}$ mbar at room temperature. The 30 keV focused $Ga^+$ beam with a current 5 nA were used for all of the ion beam experiments. Incident angle was varied from 35° to 65° to measure the relationship between propagation velocity and incident angles. Ion fluence up to $1 \times 10^{18}$ cm$^{-2}$ was chosen for a long

time limit. The spot size of 30 keV $Ga^+$ ion beam was 50 nm with the overlap of 50%. Each spot size was bombarded during 1 $\mu$s with repetition time of 100 ms. The surface morphology was characterized by *in situ* scanning electron microscopy (SEM) and *ex situ* atomic force microscopy (AFM). AFM measurements were carried out in tapping mode under ambient condition using phosphorus-doped Si cantilevers (Nanoscope IV).

In order to eliminate the effects of sample shift on the propagation of ripples, we first performed bombardment on one area of $30\times30$ $\mu m^2$ for 5 minutes, corresponding to an ion flux $3.5 \times 10^{15}$ $s^{-1}cm^{-2}$, then cover 1/6 of the area and let the ion beam hit the rest of this area for an additional 3 minutes with the same flux, and next covered 2/6 area and kept bombarding the rest area. We repeated this step until we had five regions, each of which with a higher fluence ($6.24 \times 10^{17} cm^{-2}$) than the previous one (Fig. 3.2). Thus we can accurately obtain the relative movement of ripples with the increase of ion fluence in a single picture. For incidences ranging from 30° to 65° in our experiments, the propagation direction is along the projected ion beam direction. This is in accordance with the observations by Alkemade [23] and Habenicht [13] but opposite to that predicted by current model.

Most common features of ripple evolution with variation of fluence observed by other authors for different materials previously are included in Fig. 3.2: coarsening with the increase of wavelength that small ripples are eliminated by merging together [19, 22]; transition from the perpendicular model (wave vector perpendicular to the projected ion beam direction) to a parallel mode at fixed incident angle (Fig. 3.2d) [19–21]; traveling of propagation along the projected ion beam direction regardless of incident angle [13, 23]; and roughening [18, 119, 149]. As shown by dashed lines (Fig. 3.2) the propagation direction is always along the projected ion

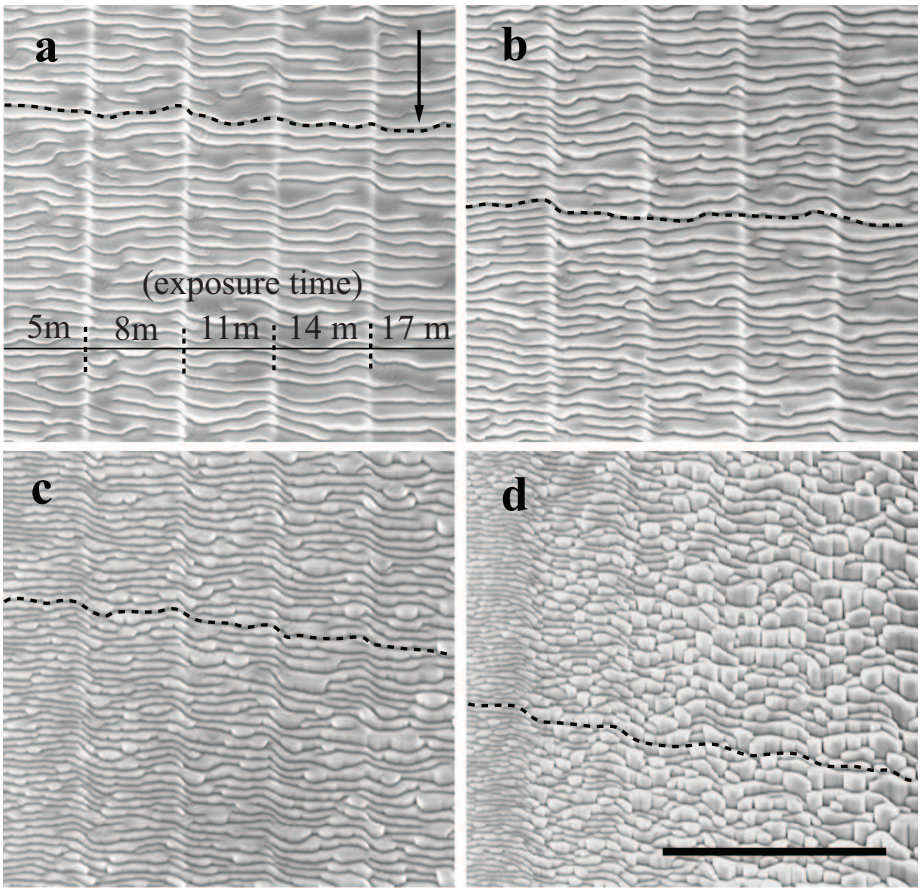


Figure 3.2: SEM images showing the propagation of ripples with the fluence at different incident angles. Five regions are shown in each image, the fluence is $1.04 \times 10^{18}$ cm$^{-2}$ for the left region (5 min) and increases by $6.24 \times 10^{17}$ cm$^{-2}$ (3min) per region from the left to right of each image. Dashed lines indicate the propagation of ripples, and the arrow is the projected ion beam direction. Incident angles are (a) 35°, (b) 40°, (c) 50°, and (d) 60°. Scale bar is 10$\mu$m. The ripple shifts along projected ion beam direction with increasing fluence.

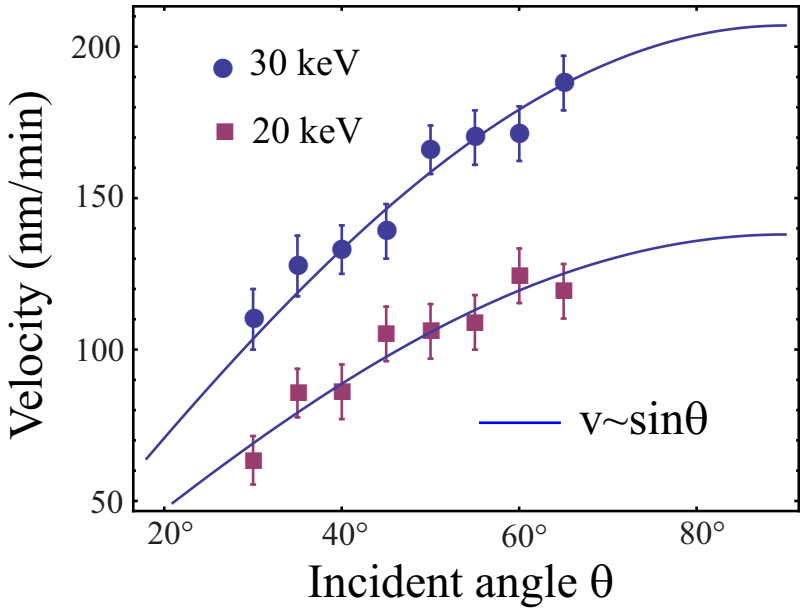


Figure 3.3: Dependence of the propagation velocity on incident angle at energy 30 keV and 20 keV. Flux $3.5 \times 10^{15}$ $s^{-1}cm^{-2}$.

beam direction although at low incidence the shift of ripple is small.

Table 3.1: Propagation velocity observed at different incident angle and ion energy (nm/min)

| Incident angle (deg.) | ≤25 | 30 | 35 | 40 | 45 | 50 | 55 | 60 | 65 |
|---|---|---|---|---|---|---|---|---|---|
| Energy (30 keV) | no ripple | 103 | 118 | 133 | 146 | 159 | 170 | 180 | 188 |
| Energy (20 keV) | no ripple | 50 | 83 | 83 | 100 | 100 | 110 | 120 | 115 |

Table 3.1 summarizes the propagation velocities observed at different incident angles and ion energies. Fig. 3.3 shows the relationship of propagation of ripples and incident angles obtained from Fig. 3.2. At fixed flux, the velocity is stable with rising of bombardment time but increases with increasing of incident angle. It can be seen that propagation velocity is proportional to the sine of incident angle. In order to study flux and energy effects, we performed experiments at different fluxes and energies. We found that if fluence is large enough (larger than $1 \times 10^{17} cm^{-2}$), this relationship can be observed.

As mentioned, most studies have focused on the dynamic equations and ascribed

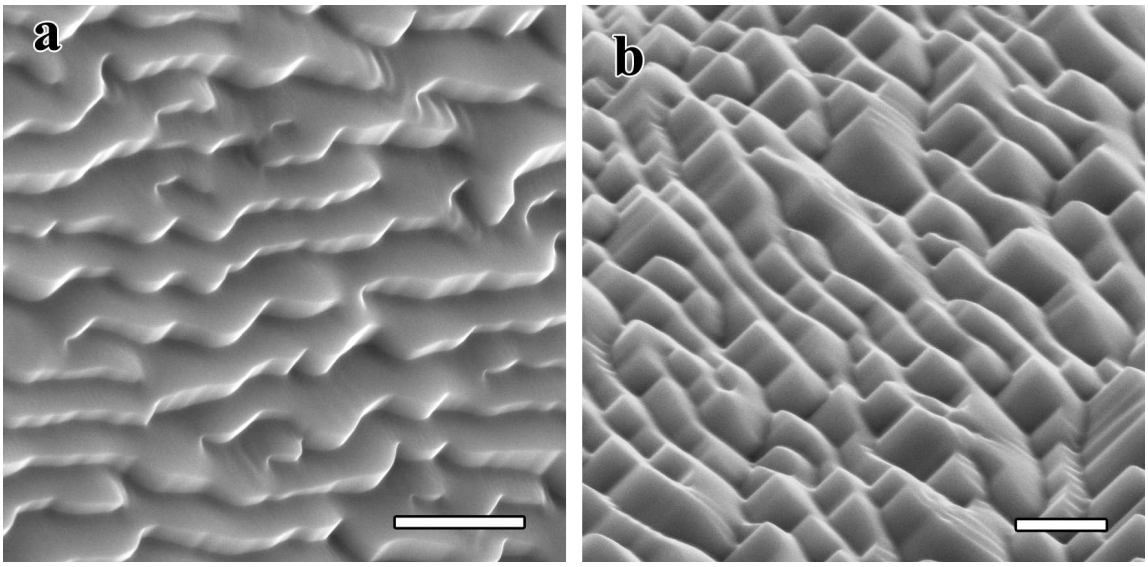


Figure 3.4: SEM images showing the terrace-like ripples induced at incident angles of (a) 45° and (b) 60°. The view directions are (a) tilt 20° relative to surface normal and (b) rotate 40° and tilt 30° relative to normal. Fluence is $6 \times 10^{17} \mathrm{cm}^{-2}$. Projected ion beam before rotation and tilt is from top to bottom. Scale bar is $1\mu$m.

these phenomena to the evolution of nonlinear terms. The microscopic details of ripple profile have been overlooked and assumed as smooth curve (no facets) with small slope [63, 64]. If we take high-magnification images in various viewing directions (Fig. 3.4), we find that terrace structures with steep slopes are generated with increasing fluence. By rotating and tilting the sample (Figs. 3.4a and 3.4b), such a characteristic structure can be identified, which is different from the images viewed at low magnification (Fig. 3.2). Moreover, If we study the orientation of terrace, we found one surface of terrace is parallel to the ion beam and the other is nearly perpendicular to the ion beam (Fig. 3.5). Fig. 3.5a is viewed along the beam direction. Because one side can not be observed along this direction, it should be parallel to the ion beam. If shadow area exists, as shown by Carter [119], sawtooth-like ripples will develop in which one side of sawtooth is nearly parallel to the ion beam. When we viewed from direction perpendicular to ion beam (Fig. 3.5b), the other side, which

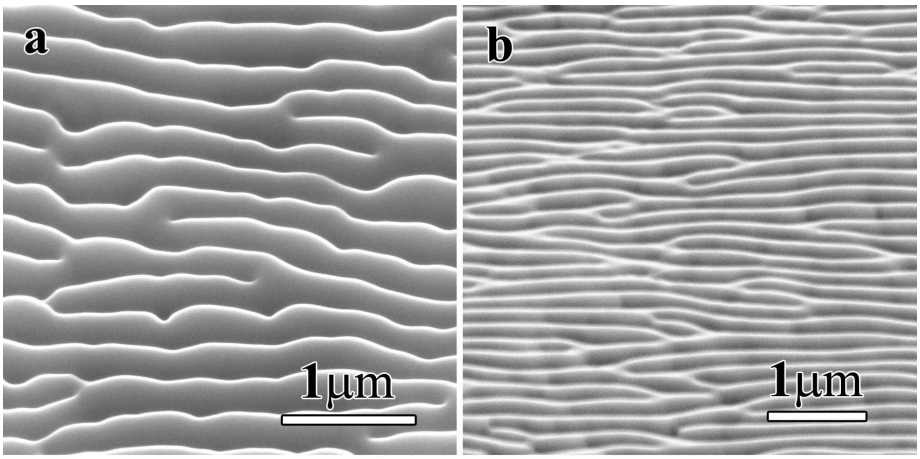


Figure 3.5: SEM images showing orientation of ripples related to ion beam direction viewed from (a) parallel to ion beam and (b) perpendicular to ion beam. Energy 30 keV, fluence $6 \times 10^{17}\text{cm}^{-2}$, incident angle 45°.

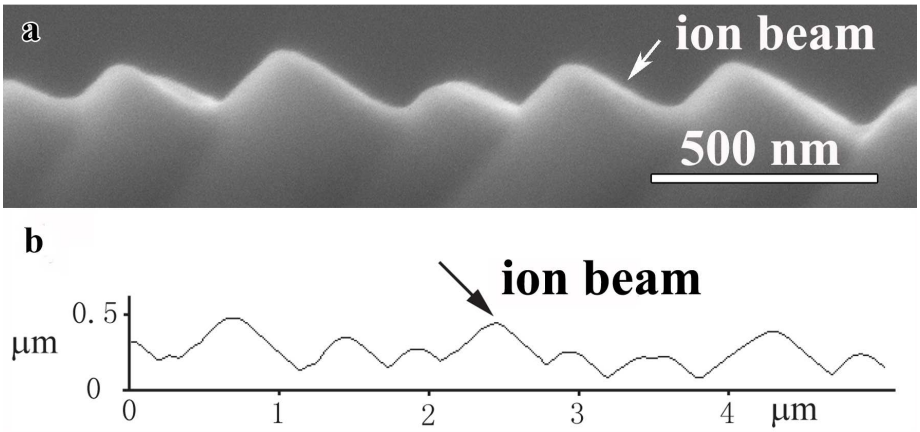


Figure 3.6: (a) Cross-sectional SEM image. (b) AFM cross-section profile. Energy 30 keV, fluence $6 \times 10^{17}\text{cm}^{-2}$, incident angle 45°.

is nearly perpendicular to ion beam can be found. This relationship can also be confirmed by cross-sectional SEM image (Fig. 3.6a) and AFM cross-sectional profile (Fig. 3.6b). It was found that this terrace structure propagates over a large distance while preserving or even sharpening the steep slopes.

Fig. 3.7 shows the transition area between the different fluences. Compared with Fig. 3.2, enlarged images show more details about ripple growth. It can be seen that only perpendicular side of ripples recedes while the other parallel side does not

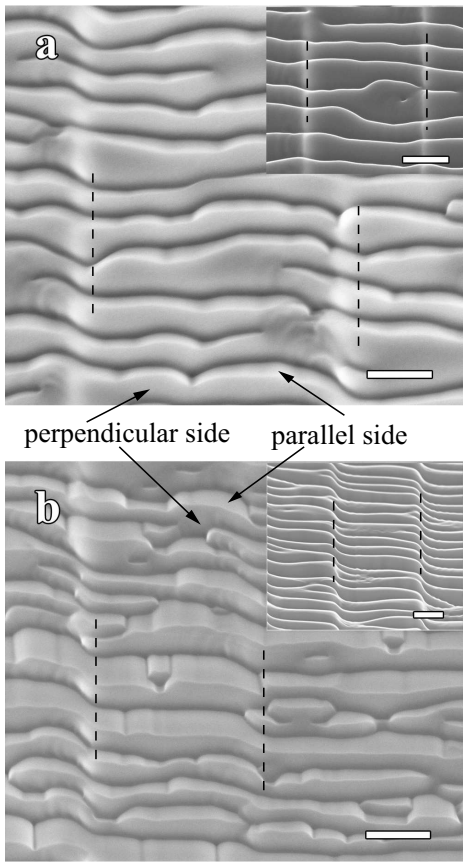


Figure 3.7: Ripple evolution at different ion fluences (SEM images). High magnification image at incident angle (a) 40° and (b) 60°. Insets show SEM images viewed from direction (a) along ion beam direction and (b) perpendicular to ion beam direction. Only the perpendicular side is sputtered and recedes but the parallel side does not shift for different fluences. Dashed lines shows different fluence regions. From right to left the fluence increases by $6.24 \times 10^{17}\text{cm}^{-2}$. Scale bar is 1 $\mu$m.

shift. This is because the sputtering yield is close to zero for parallel side and only perpendicular sides are sputtered. Further support can be obtained from images viewed from direction perpendicular to ion beam and parallel to ion beam (insets in Figs. 3.7a and b).

Fig. 3.8 shows overlap ripples: small wavelength ripples grow on the sides of terrace-like ripples. The wavelength of small ripple is two order less than large ripple. According to BH model, the small ripple can be contributed to the ion-solid interaction on the sides of terrace.

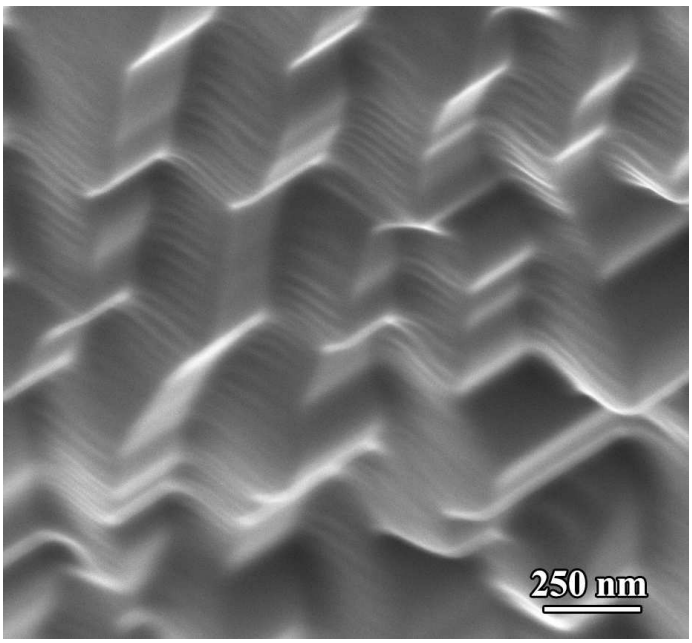


Figure 3.8: SEM image showing small wavelength ripples embedded in large wavelength ripples. Energy 30 keV, fluence $6 \times 10^{17}$ cm$^{-2}$, incident angle 45°.

### 3.1.2 Discussion

**Ripple formation**

Since the pioneering work of Bradley and Harper (BH) [64], the theory for ripple formation induced by ion beam on the surface of materials has been intensively investigated. A common feature of most studies is that ripple formation depends on the curvature dependent sputtering [64]. Though nonlinear terms were added to the BH's equations and discussed in detail by considering roughening mechanism, redeposition and viscous flow [23, 63, 65, 66, 92, 150–153], this basic curvature dependent feature remains. Based on Navier-Stokes equations for viscous flow, Rudy and Smirnov put forward a model for explanation of ripple formation by assuming that amorphous layer can be considered as Newtonian fluid [152], and Alkemade proposed the mechanism for the propagation of ripples [154]. One assumption of BH model is that initial surface curvature doses not change when making integration for the

continuous irradiation by using Gaussian distribution of energy, and after calculation this constant is replaced by the second derivative of height in terms of local coordinations [64, 65, 76].

In contrast to BH model and CB model, we assume that surface height $z = h(x, y)$ in the laboratory system can be expanded in two dimensions in powers of derivatives of $h(x, y)$

$$h(x, y) = h_0 + b_x x + b_y y + \frac{x^2}{2R_x} + \frac{y^2}{2R_y} + \cdots \tag{3.1}$$

where $b_x$ and $b_y$ are the slops, and $1/R_x$ and $1/R_y$ are the second derivatives. Here the surface height is represented as local space derivatives, and we assume the slope is small enough and curvature is large enough that the only first order is needed as in previous studies. Using Eqs. 1.4, 2.24, and 2.30, setting $\mathbf{r} = 0$, we obtain

$$\begin{aligned} N(x, y, b_x, b_y, R_x, R_y, \theta) &= \frac{G}{2\pi A\beta} \int_{-\infty}^{+\infty} \int_{-\infty}^{+\infty} dxdy \left( c + sb_y + s\frac{y}{R_y} \right) \\ &\quad \times \exp\left( -\frac{x^2}{2\beta^2} - \frac{(y + sa)^2}{2A^2} \right) \\ &\quad \times \exp\left\{ -\frac{1}{2B^2} \left[ (h(x, y))^2 - 2cah(x, y) \right] \right\} \end{aligned} \tag{3.2}$$

where

$$G = \frac{\Lambda \epsilon f}{\sqrt{2\pi} B} \exp\left( -\frac{c^2 a^2}{2B^2} \right) \tag{3.3}$$

The last exponential term in the integral is a function of slopes and second derivatives of height. If we assume the height varies slowly enough that $R$ is much larger than $a$ and slope is much smaller than $a$, we can neglect higher derivative terms in the Taylor expansion of $h(x, y)$. Here, in order to obtain the nonlinear terms in final partial differential equations, we expand this term to first order in $a/R_x$ and $a/R_y$

and second order in $ab_x$ and $ab_y$. Let the original height ($h_0$) be zero, we have

$$\begin{aligned} N(b_x, b_y, R_x, R_y, \theta) &= \frac{G}{2\pi A\beta}\int_{-\infty}^{+\infty}\int_{-\infty}^{+\infty} d\zeta_x d\zeta_y \exp\left(-\frac{(a\zeta_y + sa)^2}{2A^2} - \frac{a^2\zeta_x^2}{2\beta^2}\right) \\ &\times\left\{c + sb_y + s\frac{a\zeta_y}{R_y} - \frac{ca^2}{2B^2}\left[\zeta_x^2 b_x^2 + \zeta_y^2 b_y^2 - 2c\zeta_x b_x - 2c\zeta_y b_y\right.\right. \\ &\left.\left. -c\zeta^2\frac{a}{R_x} - c\zeta^2\frac{a}{R_y} - 2s\zeta_y b_y^2\right] + \frac{c^3a^4}{2B^4}(\zeta_x^2 b_x^2 + \zeta_y^2 b_y^2)\right\} \end{aligned} \tag{3.4}$$

where $x = a\zeta_x$ and $y = a\zeta_y$. This slope and curvature dependent sputtered atoms per unit area per unit time, which determines the time evolution of height is along the normal direction of surface. Using the assumption of normal direction mentioned before, we obtain

$$\frac{\partial h(x,y,t)}{\partial t} = -\Omega N(b_x, b_y, R_x, R_y, \theta)\sqrt{1 + (\nabla_x h)^2 + (\nabla_y h)^2} \tag{3.5}$$

where $\Omega$ is the volume of atom. By considering the surface diffusion and noise, evaluating this integral yields

$$\frac{\partial h(x,y,t)}{\partial t} = -\nu_0 + \gamma\nabla_y h + \nu_x\nabla_x^2 h + \nu_y\nabla_y^2 h + \lambda_x(\nabla_x h)^2 + \lambda_y(\nabla_y h)^2 - K\nabla^4 h + \eta \tag{3.6}$$

here

$$\nu_0 = \Omega G c \tag{3.7}$$

$$\gamma = \Omega G c\left(\frac{a^2c^2}{B^2} - 1\right) \tag{3.8}$$

$$\nu_x = -\frac{\Omega G c^2 a\beta^2}{2B^2} \tag{3.9}$$

$$\nu_y = \Omega G a\left(s^2 - \frac{c^2}{2B^2}(A^2 + s^2a^2)\right) \tag{3.10}$$

$$\lambda_x = \Omega G c\left(\frac{\beta^2}{2B^2} - \frac{1}{2} - \frac{c^2a^2\beta^2}{2B^4}\right) \tag{3.11}$$

$$\lambda_y = \Omega G c\left(\frac{\beta^2 + 3cs^2a^2}{2B^2} - \frac{1}{2} - \frac{c^2a^2(A^2 + s^2a^2)}{2B^4}\right) \tag{3.12}$$

$$K = \frac{D_s\gamma\nu\Omega^2}{k_BT} \tag{3.13}$$

The main difference between former models and our present model, is that, we made integral after rotation of coordinations while rotation was considered during integral in previous models. At symmetry case ($\alpha = \beta$), the same results are achieved [63–65, 76].

**Steady state topography induced by ion sputtering**

At the beginning of ripple formation, the surface varies smoothly enough that the condition for BH model is satisfied. The ripple formation can then be described by linear equation. The corresponding orientation and wavelength can be calculated by linear analysis. As the sputtering proceeds, due to curvature dependent sputtering where crest is eroded less than trough, the steep slopes are generated. Hence the model resulting from an expansion in gradients of the height breaks down.

The same behavior has been found in cone structure induced by ion beam bombardment. Nobles and Carter developed a partial differential equation to explain the corn formation [143–145]. Following their approach. we can derive an equation for the profile of ripple growth. Here we assume that sputtering yield is only dependent on incident angle, and redeposition, viscous flow and thermal diffusion are neglected. As shown in Fig. 3.9, we set up coordination as h axis parallel to the ion beam. For a two-dimension, slope rate can be determined by the sputtering yield. At normal bombardment, the sputtering rate occurs in a direction locally normal to the surface. The incident angle $\theta$ is the angle measured from the ion beam to the surface normal. When surface is removed by ion beam with velocity $v$ at time $t$, the decrease along $h$ axis is

$$\frac{\partial h}{\partial t} = -v\sqrt{1+p^2} \tag{3.14}$$

where $p$ is slope given by $p = \partial h/\partial x$. If we only consider sputtering yield, $v$ is given

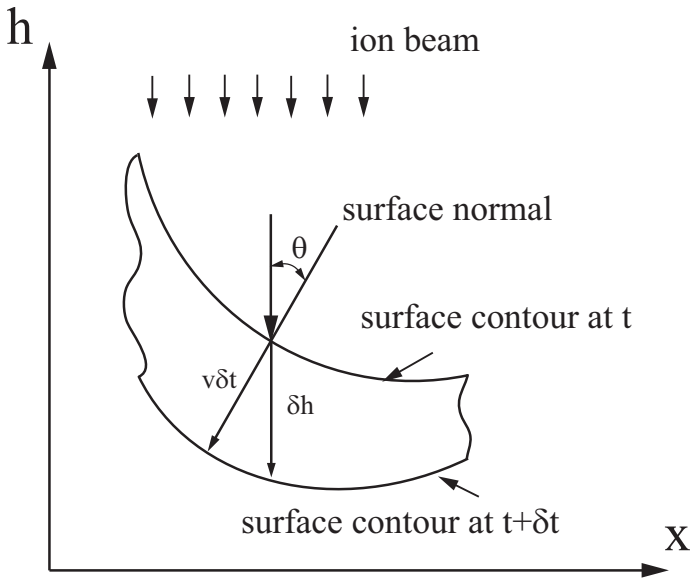


Figure 3.9: Evolution of surface bombarded by ion beam. Ion sputtering rate direction is along the surface normal.

by

$$v = \Omega I(\theta) Y(\theta) \tag{3.15}$$

where $\Omega$ is atomic volume, $I(\theta)$ is local ion flux, and $Y(\theta)$ is sputtering yield. The latter two terms are surface slope dependent. At normal bombardment $I(\theta)$ is given by

$$I(\theta) = \frac{I}{\sqrt{1+p^2}} \tag{3.16}$$

where $I$ is ion flux. Combination of Eqs.3.14 to 3.16 gives

$$\frac{\partial h}{\partial t} = -\Omega I Y(\theta) \tag{3.17}$$

If we make derivative of Eq. 3.17 in terms of $x$, we have

$$\frac{\partial p}{\partial t} = -\Omega I \frac{\partial Y(\theta)}{\partial \theta} \cdot \frac{\partial \theta}{\partial x} \tag{3.18}$$

The same equation has been derived by Nobles and Carter by different approaches. Using this equation they explained the sharp cone formation and derived that apex

angle of cone is $\pi - 2\theta_c$ where $\theta_c$ is critical angle in which sputtering is maximum [143–146]. Eq. 3.18 shows the change of slope in terms of time depends on two terms: change of sputtering yield in term of incident angle and change of incident angle in terms of coordinate. For sputtering yield, as shown in Fig.3.10a [134], it is well known that sputtering yield increases slowly from 0 to around 70° and then decrease abruptly to zero at 90°. There is a maximum value of sputtering yield in which $\partial Y(\theta)/\partial\theta = 0$. For change of incident angle, it can be given from the local surface normal. Here we assume the initial surface is sinusoidal curve and change of local incidence with coordinate is shown in Figs. 3.10b and c. Because signs of $\partial Y(\theta)/\partial\theta$ and $\partial\theta/\partial x$ are known for a given curve, we can determine the slope change during bombardment.

At steady state $\partial p/\partial t = 0$, we have $\theta = 0$, $\theta = \pi/2$, or $\theta = \theta_c$. Hence, for a long time limit, combination of three slopes can be obtained as shown by Nobles and Carter [143–145]. If local incident angle $\theta < \theta_c$, which means $\partial Y(\theta)/\partial\theta > 0$, two conditions can be found: for $\partial\theta/\partial x > 0$, slope $p$ will decrease and consequently we have $\theta \to 0$; another condition is $\theta \to \theta_c$ for $\partial\theta/\partial x < 0$. If local incident angle $\theta > \theta_c$, which means $\partial Y(\theta)/\partial\theta < 0$, there are also two conditions: $\theta \to \pi/2$ when $\partial\theta/\partial x < 0$ and $\theta \to \theta_c$ when $\partial\theta/\partial x > 0$. At off-normal incidence, for simplicity, we rotate coordinates and let $h$ be parallel to ion beam direction. Under this condition, Eq. 3.18 does not change but slope should be evaluated in the rotated coordinates. At low incident angle (Fig. 3.10b), condition $\theta < \theta_c$ is satisfied along the whole surface. We have steep surface with incidence $\theta = 0$ for $\partial\theta/\partial x < 0$ and $\theta = \theta_c$ for $\partial\theta/\partial x > 0$. At high incidence (Fig. 3.10c), there exist points at which off-normal beam is tangent to the curve on the surface, which means no motion perpendicular to ion beam can be induced by the ion beam, only planes, either parallel or perpendicular to the ion

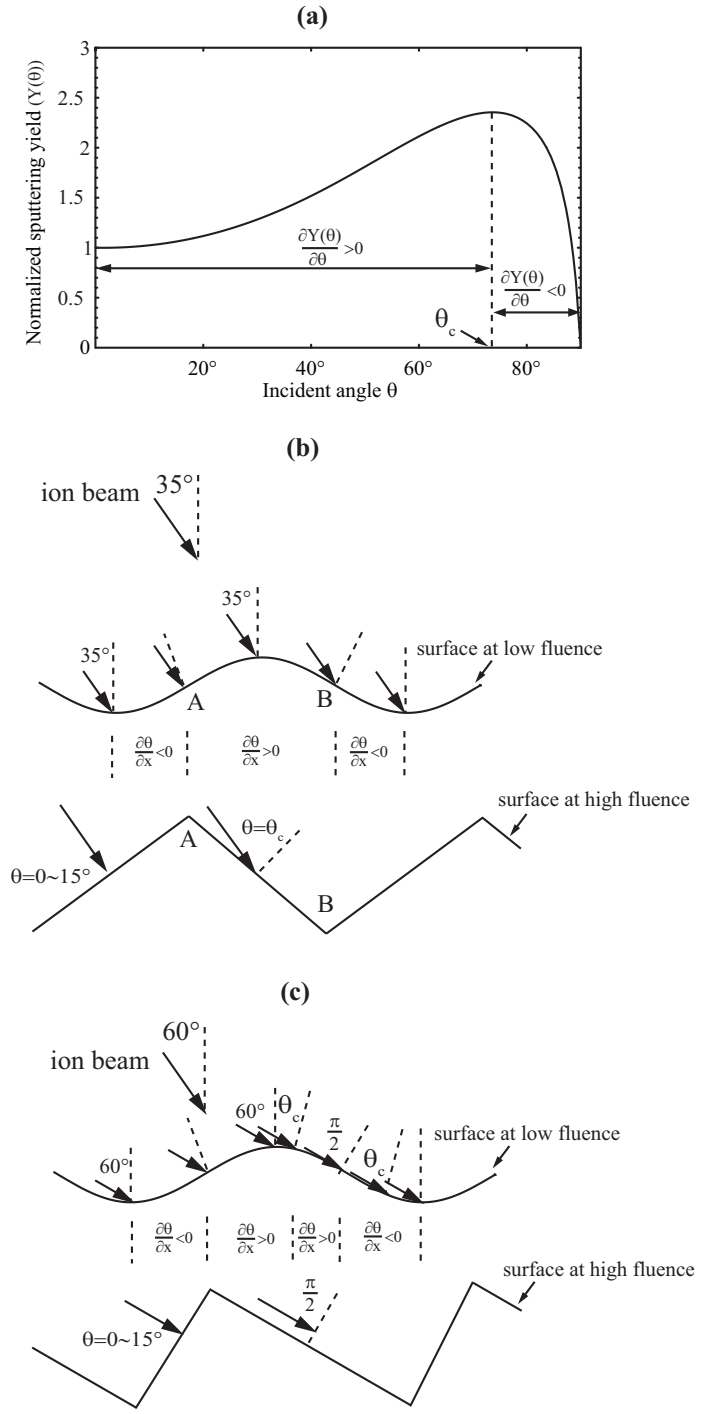


Figure 3.10: Schematic illustration of the process for terrace like ripple formation. (a) The dependence of sputtering yield on incident angle. Terrace-like ripple formation with increasing of fluence at (b) 35° and (c) 60°. In (b), A shows smallest incident angle and B shows largest incident angle. In (c) critical incident angle ($\theta_c$) and shadow area (starting at incident angle $\pi/2$) appear. Dashed lines show surface normal.

incidence can be formed on the surface under long time limit. It can be seen that for low incident angle, the length of perpendicular surface is shorter than that of parallel surface while for high incident angle it is inverse. These results are in good agreement with experimental observations. The discontinuous points (for example A and B in Fig. 3.10b) can be understood from the different sputtering yield: a peak position appears at point A because the sputtering yield is minimum compared with neighbors due to the smallest incident angle, while at point B the sputtering is maximum (largest incident angle) and the trough can be generated. Because the curve of sputtering yield related to incident angle (Fig. 3.10a) is so flat around $0 \sim 15^\circ$ that incidences on perpendicular side of terrace at steady state can be varied in a range of $\theta = 0 \sim 15^\circ$.

The ripple propagation velocity can be explained from this particular shape. At low incidence ($\theta < 45$), the maximum sputtering yield is on the slope (down slope) that is opposite to the ion beam (Fig. 3.10b). As shown in Fig. 3.11, for the slope (up slope) that faces the ion beam, incident angle $\theta = 0$, the flux is $I$, sputtering yield is $Y$ (sputtering yield at $\theta = 0$), and projected velocity along $x$ axis is $v_x = \Omega I Y \sin\theta_0$, where $\theta_0$ is the angle between ion beam and h axis. For the slope that opposes the ion beam, the flux is $I\cos\theta_c$, sputtering yield is $Y(\theta_c)$, and projected velocity along $x$ axis is $v_x = -\Omega I Y(\theta_c)\sin(\theta_C - \theta_0)\cos\theta_c$. Therefore, the observed velocity is

$$v_p = \Omega I Y(\sin\theta_0 - Y\theta_c \sin(\theta_c - \theta_0)\cos\theta_c / Y) \tag{3.19}$$

If we use Sigmund's theory $Y(\theta) = Y\cos^{-1}\theta$, which is valid at incident angle $\theta < 60^\circ$ [64, 77], we have positive propagation velocity at $\theta > 35^\circ$ by assuming $\theta_c = 70^\circ$. However, value of velocity predicted by this model at low incidence is small compared with our experimental observations. Here we do not consider viscous flow. It has been reported that viscous flow can enhance the propagation along the projected ion

beam direction [23].

At high incident angle ($\theta > 45$), we should consider the shadow effects (Fig. 3.10c). Under these conditions, the sides of terrace are either perpendicular or parallel to the ion beam. The velocity is

$$v_p = Y \sin\theta \tag{3.20}$$

This result is in good agreement with our experimental observations. Therefore, we can draw a conclusion that sputtering is a dominant mechanism in terrace ripple propagation at high incidence.

It should be noted from our experiment that the value of velocity at low incidence also satisfies Eq. 3.20 (Fig. 3.3), and the incident angle on slope that is opposite to the ion beam is close to $\pi/2$ (Fig. 3.7). In real surface, because viscous flow happens in the amorphous layer on the surface, it can be expected that this effect can cause the top of curve to move fast and form shadow area, leading to the parallel side of terrace [119]. Additionally, incident angle 35° is the minimum angle for ripple formation. For the slope equal to 1 (small slope approximation is valid at slope less than 1), at incident angle 35° the local maximum incident angle can reach close to 80°. Hence, for large slope (larger than 1) we considered here, it is reasonable to assume tangent profile of ripple and even shadow area can be formed at low incident angle.

**Shocks in ripple**

Because $p = \tan\theta$, Eq. 3.18 can be rewritten as

$$\frac{\partial\theta}{\partial t} + C(\theta)\frac{\partial\theta}{\partial x} = 0 \tag{3.21}$$

where $C(\theta) = \Omega I \cos^2\theta \partial Y(\theta)/\partial\theta$. The form of this equation is found in many physical phenomena and typically results in discontinuities due to interference between

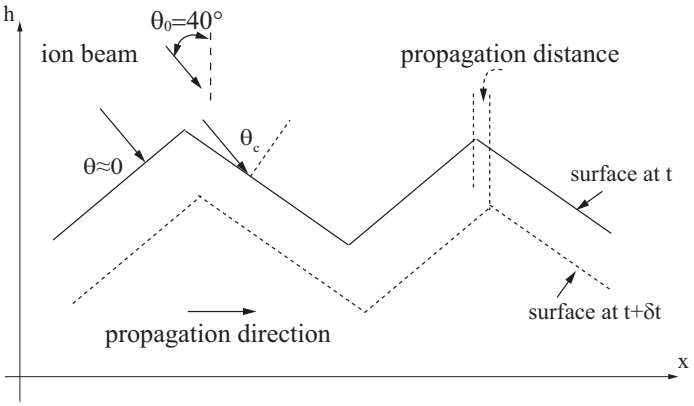


Figure 3.11: Schematic illustration of the propagation of terrace like ripples. The competitive of local flux and sputtering yield leads to the propagation of ripples along projected ion beam direction.

waves. Shocks or rarefaction waves are called when these discontinuities occurs. Similar to chemical etching, Barber has employed properties of shock wave to develop geometrical approach to predict surface morphologies induced by ion beam [146]. Later Nobles and Carter have derived nonlinear equation confirming that the ion bombardment can give rise to the shock waves and thus lead to edge formation [143–145]. In a recent analysis of surface morphology development induced by ion beam, a kinematic shock wave has also been derived by Chen to interpret the steep slope development [76]. It is now believed that formation of large slope surface morphology during ion etching could be well understood in terms of the propagation of a shock front. The shock wave can be understood from Fig. 3.12. When a wave front propagate, if velocity is the same for all the parts of front, after a time, this wave will keep the original shape Fig. 3.12b. However, if velocity is different for different parts of front, the shock wave will take place and discontinuity will be created Fig. 3.12b.

In order to understand step formation in ripples, we apply the geometrical construction to a sinusoidal surface at various incidences. This approach is based on the fact that surface development during bombardment can be described by the shock

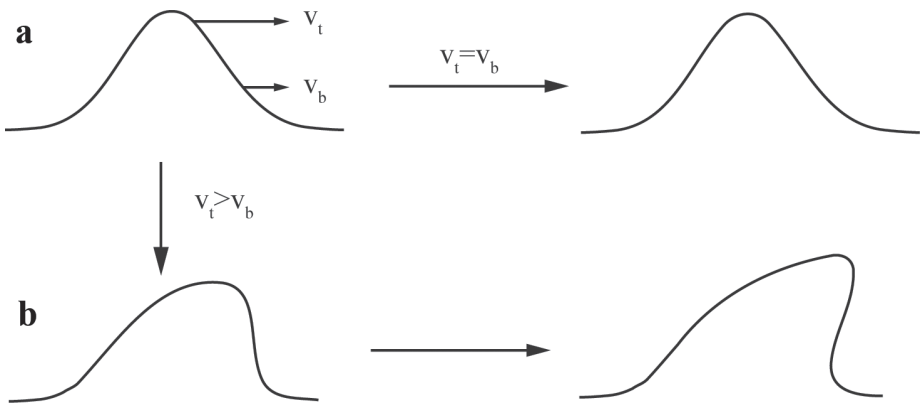


Figure 3.12: Schematic illustration of shock wave. (a) Normal propagation of wave with the same velocity. (b) Shock wave occurs due to different propagation velocity.

wave in which the orientation of ion etching trajectories can be well defined by the velocity of the surface in the normal direction. The same form as Eq. 3.21 with surface derivatives has been proposed [155, 156]. The analytical solution to this shock wave equation is quite difficult but the development of surface can be constructed from this equation by plotting trajectories as well as the etching depth defined by sputtering yield [143–146]. The computer was performed to draw trajectories from 100 equally spaced points on the initial sinusoidal surface according to the slope and local incident angle which is a function of coordinates. The slope of trajectories is derived by Carter [145]

$$\frac{dh}{dx} = \frac{\sin\theta\cos\theta(dY(\theta)/d\theta) - Y(\theta)}{\cos^2\theta(dY(\theta)/d\theta)} \tag{3.22}$$

The continuous equation for sputtering yield as a function of incident angle should be known. Here we use formula given by [134]

$$Y(\theta) = \cos\theta\exp(-\frac{a^2}{2\alpha^2}\cos^2\theta) \tag{3.23}$$

where $a$ is average ion energy depth and $\alpha$ is ion energy straggling. $a^2/2\alpha^2 = 3.5$ was used in computer calculation. For initial curve $h = \sin x$, at off-normal incidence $\theta_0$, we have $\theta = |-\theta_0 + \pi + \arctan(\cos x)|$. Fig. 3.13 shows profiles for the sputtering of

a sinusoidal surface at different incidences. When two trajectories meet in space, an edge is produced and the lines beyond the meeting point are erased. The depth of each trajectory can be obtained from sputtering yield [119,143,146]. Facet structure is evident for long time bombardment. Incident angles of about 0 and 75° on two sides of terrace are developed. Velocity of propagation is along the projected ion beam direction at high and low incidence. The perpendicular side is larger at low incidence than high incidence. All these features are consistent with predictions from Eq. 3.17. Due to neglecting other effects such as viscous flow and redeposition, the parallel surface can not be predicted.

Alternative explanation for ripple evolution is based on earlier work by BH linear model and extended nonlinear models by considering four mechanisms: curvature-dependent sputtering, redeposition, thermal diffusion and viscous flow. Using Sigmund's theory [77,78], the total number of sputtered atoms per unit area per unit time can be estimated by integrating Gaussian distribution of energy on a prescribed shape of the surface. Eq. 3.15 is replaced by [63,77]

$$v = \Omega \int_{\Re} I(\mathbf{r}) Y(\mathbf{r}) d\mathbf{A} \tag{3.24}$$

where $I(\mathbf{r})$ is a local flux, $I(\mathbf{r})d\mathbf{A}$ is the number of ions hitting on an area $d\mathbf{A}$, $Y(\mathbf{r})$ denotes the sputtered atoms at original position $r = 0$ generated by an ion hitting the surface in a point $\mathbf{r}$. The integral is evaluated over the area $\Re$. This equation computes the sputtered atoms induced by the accumulated energy from different positions, i.e. curvature-dependent sputtering. Eq. 3.15 only describes single ion effects without consideration of neighbor ion contributions, valid for large slope dependent sputtering and small curvature approximation. By assuming surface profile and expanding to second order in slope, the nonlinear equation was established [21,63]. In our case, due to step ripple formation, this continuous equation can not interpret

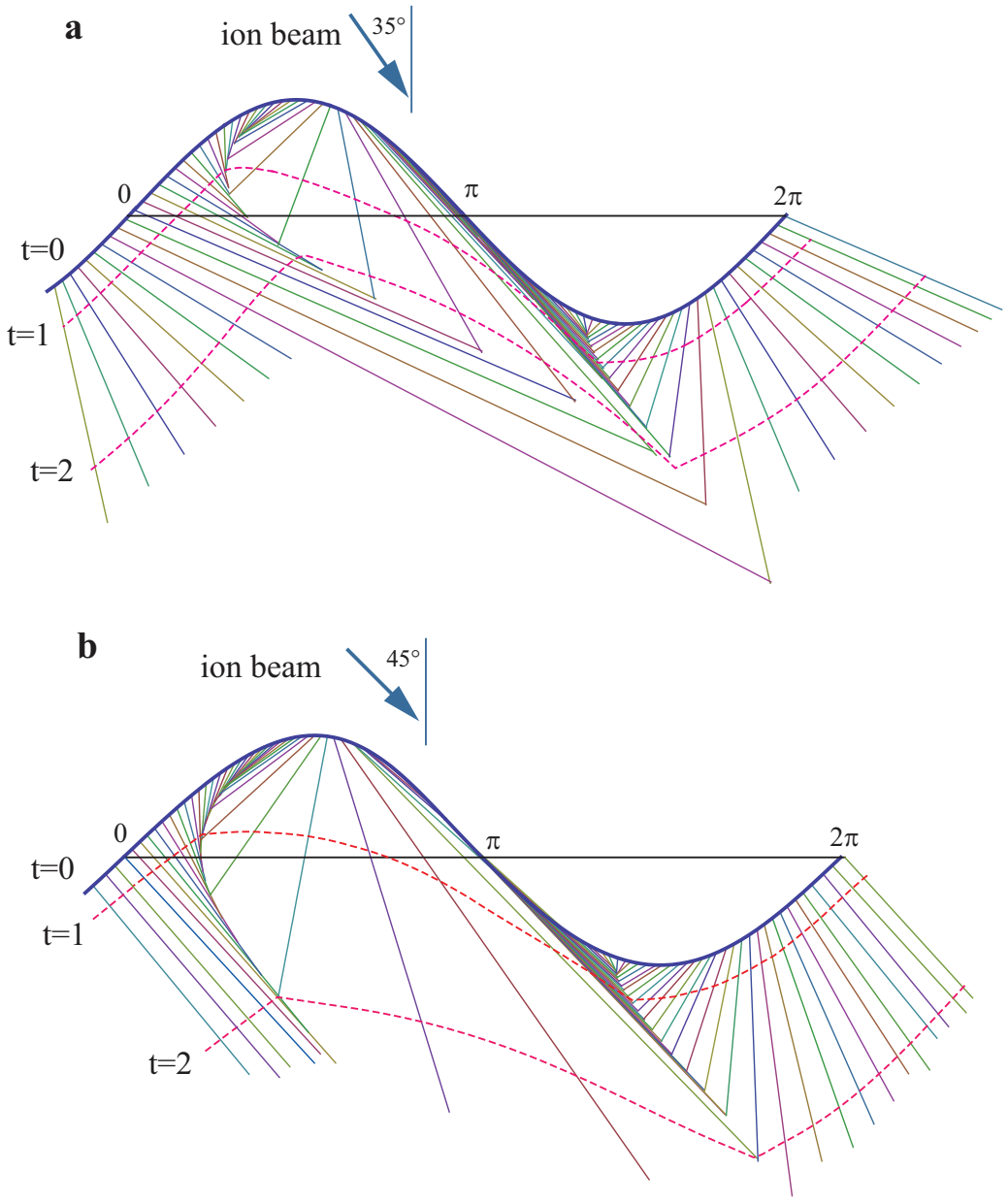


Figure 3.13: Geometrical construction of surface development subject to a uniform ion flux at incident angles (a) 35° and (b) 45°. Initial surface at time $t = 0$ is sinusoidal. Dashed curves show the surface morphology after time $t = 1$ and 2. Fine lines show the orientations of ion etching trajectories. Facet structure forms due to the discontinuous slope.

our experimental results.

Using Eq. 3.24 but without small slope approximation, Chen *et al.* derived a partial differential equation and found that steep slope with incident angle of 76° can be induced by ion beam, consistent with our studies [76]. It was shown that curvature-dependent sputtering can be ignored without significant error and the surface diffusion does not affect slope and velocity [76]. Recently, redeposition and viscous flow have been highlighted in evolution of surface morphology induced by ion beam [23, 72, 87, 88, 157]. But the analytical equation for these two effects is not well established [32, 87]. Viscous flow has been included in nonlinear equations to explain velocity of ripple propagation in which redeposition is not considered [23]. In our case, if we define redeposition as a damping term as shown by Facsko, *et al.* [88] $\partial h/\partial t = -ch$, where $h$ is surface hight and $c$ is a constant, in some cases, discontinuity can not occurs [156]. This means that redeposition tends to smooth the surface. In our experiment, the step structure can always be formed for long time limit and thus this term is not dominant. This can be due to the high vacuum conditions which can lead to small redeposition. Viscous flow, on the other hand, can contribute to formation of parallel surface of terrace-like ripples.

### 3.1.3 Conclusion

In conclusion, it was shown that terrace-like ripples can be induced by ion beam for a long time bombardment. The sides of terrace are either parallel to or perpendicular to the ion beam direction. The explanation is based on the slop-dependent sputtering rather than curvature-dependent sputtering yield which was widely used for description of ripple formation. The velocity is measured and found that velocity is proportional to the sine of incident angle. The mechanism of formation for such special shape is briefly discussed by considering the slope-dependent sputter-

ing. Shock wave was introduced to explain the terrace structure formation. Although this analysis is oversimplified in several respects, there is an encouraging qualitative agreement between model predictions and experiments.

## 3.2 Morphological Instability of Cu Nanowires Induced by $Ga^+$-ion Bombardment

Bombardment of solid surfaces by ions with intermediate energy can generate a rich variety of interesting patterns. Ripples and quantum dots are two examples which have been intensively studied both experimentally and theoretically [19, 23, 27, 32, 33, 63, 64, 87, 119, 158]. This self-organized structure has received particular interest recently as a promising candidate for an easy, inexpensive and large area fabrication of patterns [67]. A common feature of most studies is on the patterns which are induced on two-dimensional surface. A systematic analytic treatment of the evolution of morphologies for one dimensional materials subjected to ion bombardment, such as lines, has been lacking so far. Recently, it has been reported that ion sputtered nanolines can self-assemble into chains of ordered nanoparticles like the droplets in liquid. Lian *et al.* [74] demonstrated that focused ion beam (FIB) induced Co nanolines can form nanoparticles with the wavelength of 256 nm and diameter of 58 nm. Similarly, Zhao *et al.* [75] reported that Pt and Au nanolines can also form linear arrays of dots induced by focused 30 keV $Ga^+$ ion beam and 1 MeV Kr ion beam. They employed the Rayleigh instability [159] to explain the formation of nanoparticles. However, The classical Rayleigh instability describes the break-up of the cylindrical liquid jet under surface tension in which the volume is conservative. In their cases, due to the sputtering yield, the volume of lines decreases with the bombardment. For a solid rod with conservative volume at high temperature, the stability was originally discussed by Nichols and Mullins [160]. By linear anal-

ysis of surface diffusion, they found that solid cylinder was unstable for wavelength exceeding the circumference of the cylinder, in agreement with Rayleigh instability.

In this chapter, the experimental observation and theoretical modeling on morphological instability of Cu nanowlines induced by focused ion beam has been studied. A detailed description of evolution of lines under ion beam etching at normal incidence with various flux and temperature is shown. Following the pioneering work for ripple formation given by Bradly and Harper (BH model) [64], a partial differential equation based on the Sigmund theory [71, 77] and Nichols and Mullins approach [160] was derived. By linear analysis, a critical radius is found for the instability of nanolines, below which a wave vector along the longitudinal direction develops, giving rise to the formation of periodic dots.

### 3.2.1 Experiment and results

The nanowires used in our work were created via FIB direct writing on Cu thin films (thickness $\sim$ 80 nm and $\sim$ 120 nm) with different widths. This thin film was fabricated by deposition of Cu on Si (100) substrates with a native oxide at room temperature in a high vacuum magnetron sputtering chamber ($10^{-9}$ Torr). The ion bombardment experiments were performed in a dual-beam (FIB+SEM) instrument (FEI Nova 200 Nanolab) at the vacuum of $10^{-7}$ Torr. Focused $Ga^{+}$ ions beam with energy 10 keV at normal incidence were used to sputter the thin film surface for all ion beam experiments. The scanned area $15\times5$ $\mu m^2$ was kept constant. Wavelength and size of nanoparticles are monitored *in situ* by scanning electron microscopy (SEM). The current of ion beam and substrate temperature were varied. The spot size of 10 keV $Ga^{+}$ ion beam is 50 nm with the overlap of 50%. Each spot size was bombarded during 1 $\mu$s with repetition time of 100 ms. The topography of patterned structures was also measured using atomic force microscopy (AFM) operated at a taping mode.

Table 3.2: Experimental conditions and results. Instability occurs at a critical width for different initial lines

| Target | Width (nm) | Ion | Energy (keV) | Flux $10^{14}(\mathrm{cm}^{-2}\mathrm{s}^{-1})$ | Temperature (°C) | Fluence $10^{16}(\mathrm{cm}^{-2})$ | Critical width (nm) | Wavelength (nm) |
|---|---|---|---|---|---|---|---|---|
| Cu | 100 | $Ga^+$ | 10 | 4.2 | 25 | 1.5 | 100 | 315 |
| Cu | 200 | $Ga^+$ | 10 | 4.2 | 25 | 2.92 | 110 | 325 |
| Cu | 400 | $Ga^+$ | 10 | 4.2 | 25 | 6 | 95 | 310 |
| Cu | 600 | $Ga^+$ | 10 | 4.2 | 25 | 9 | 105 | 330 |

The evolution of nanolines subjected to ion bombardment has been reported by Lian and Zhao [74, 75]. Following their experimental procedure, four Cu lines with different widths (600 nm, 400 nm, 200 nm, 100 nm) were created by FIB direct writing (Fig. 3.14(a)). The experimental conditions and results are summarized in Table 3.2. After exposure time of about 100 s, the lines self-assemble into chains of periodic nanodots (Fig. 3.14(b)). Combining with previous studies, the main experimental features can be briefly summarized as: (1) widths of lines decrease linearly at the beginning of bombardment; (2) when widths of lines reach a critical value, periodic patterns start to form; (3) the line with larger width can develop into two lines and these two lines can evolve into periodic nanodots individually; (4) the pattern formation is within several minutes; (5) wavelength is nearly the same for different width lines.

A detailed study of the morphological evolution of Cu lines subjected to FIB bombardment at the room temperature for different exposure time is shown in Fig. 3.15. A Cu line with the square cross section of $120 \times 120$ nm$^2$ was created via FIB direct-writing (Fig. 3.15(a)). At the beginning of bombardment, no periodic patterns were found while the width of line decreases linearly. After a sputtering time $\sim 60$ s, corresponding to a fluence of $\sim 2.92 \times 10^{16}$ cm$^{-2}$, a periodic morphology with the wavelength of $\sim 320$ nm starts to appear (Fig. 3.15(b)), in which the average width of nanoline reduces to $\sim 100$ nm. With increasing bombardment time, the chain

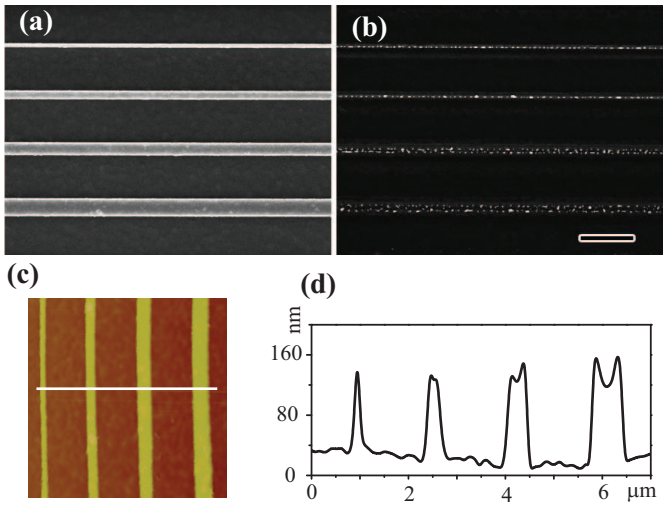


Figure 3.14: SEM images of chains of nanoparticle formation. (a) Cu lines with four different initial widths cut from a continuse 80 nm thick film using FIB before irradiation. (b) Bombardment up to fluence $5 \times 10^{16}$ cm$^{-2}$. Ion beam Energy $\varepsilon = 10$ keV, flux $f = 4.2 \times 10^{14}$ cm$^{-2}$s$^{-1}$, temperature T=300 K. (c) and (d) AFM image and cross-section profile showing the morphology variation for Cu lines. The scanning area of (c) is 7 $\mu$m by 7 $\mu$m. Scale bar is 2 $\mu$m.

of nanoparticles begins to form at time $\sim$ 90 s with the spacing equal to the same wavelength (Fig. 3.15(c)). These nanoparticles become smaller and eventually are sputtered away upon further milling (Fig. 3.15(d)). Due to redeposition and surface tension, the doughnut-shaped rims on the edges of line are generated during the ion bombardment process (Figs. 3.15(a) and (e) and AFM imgae in Figs. 3.14 (c) and (d)). This is a characteristic feature of the dewetting process [74, 75, 161]. With the increase of width of lines, this rim would grow up to a curved cylinder and would therefore break up into a chain of nanoparticles (Fig. 3.14 for 400 nm and 600 nm lines). This morphology is similar to the shape on the edge of plate discussed by Nichols and Mullins [160].

In order to investigate the development of rim, we made another experiment on the width of lines with the cross section of 500 (width)$\times$80 (thickness) nm$^2$ (Fig. 3.16). After ion etching with energy of 10 keV and flux of $4.2 \times 10^{14}$ cm$^{-2}$s$^{-1}$ for $\sim$ 180

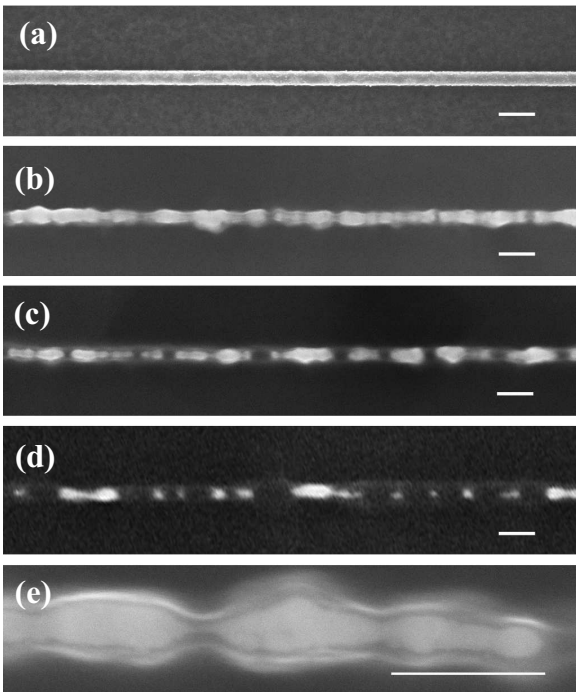


Figure 3.15: SEM images showing the temporal development of instability of a copper line with square cross section of $120 \times 120$ nm$^2$ at (a) $t = 0$ s, (b) $t = 60$ s, (c) $t = 90$ s, and (d) $t = 120$ s. (e) High magnification image of (b). Flux $f = 4.2 \times 10^{14}$ cm$^{-2}$s$^{-1}$, energy $\varepsilon = 10$ keV. Scale bar=300 nm.

s, with the decrease of both width and thickness, the craters or holes are formed, randomly distributed along the line (Fig. 3.16(b)). As the sputtering proceeds, this randomly distributed dots evolutes into two chains of regularly arranged patterns, parallel to the axis of wire (Fig. 3.16(c)). The degree of ordering is improved for further bombardment (Fig. 3.16(d)). Sinusoid-like structure with the nanoparticles on the vertex can be identified by tilting the sample (Figs. 3.16(e) and (f)).

The evolution of nanopartilces as a function of flux is shown in Fig. 3.17 at fixed energy, ion fluence, bombarded area and temperature. The experimental conditions are shown in Table 3.3. We found that wavelength is independent of the ion flux at temperatures 300 K and 350 K (Fig. 3.17). The same behavior has been reported on the Cu(100) surface for ripple formation [157, 162–165]. The explanation is based on the various species concentration on the surface with the temperatures.

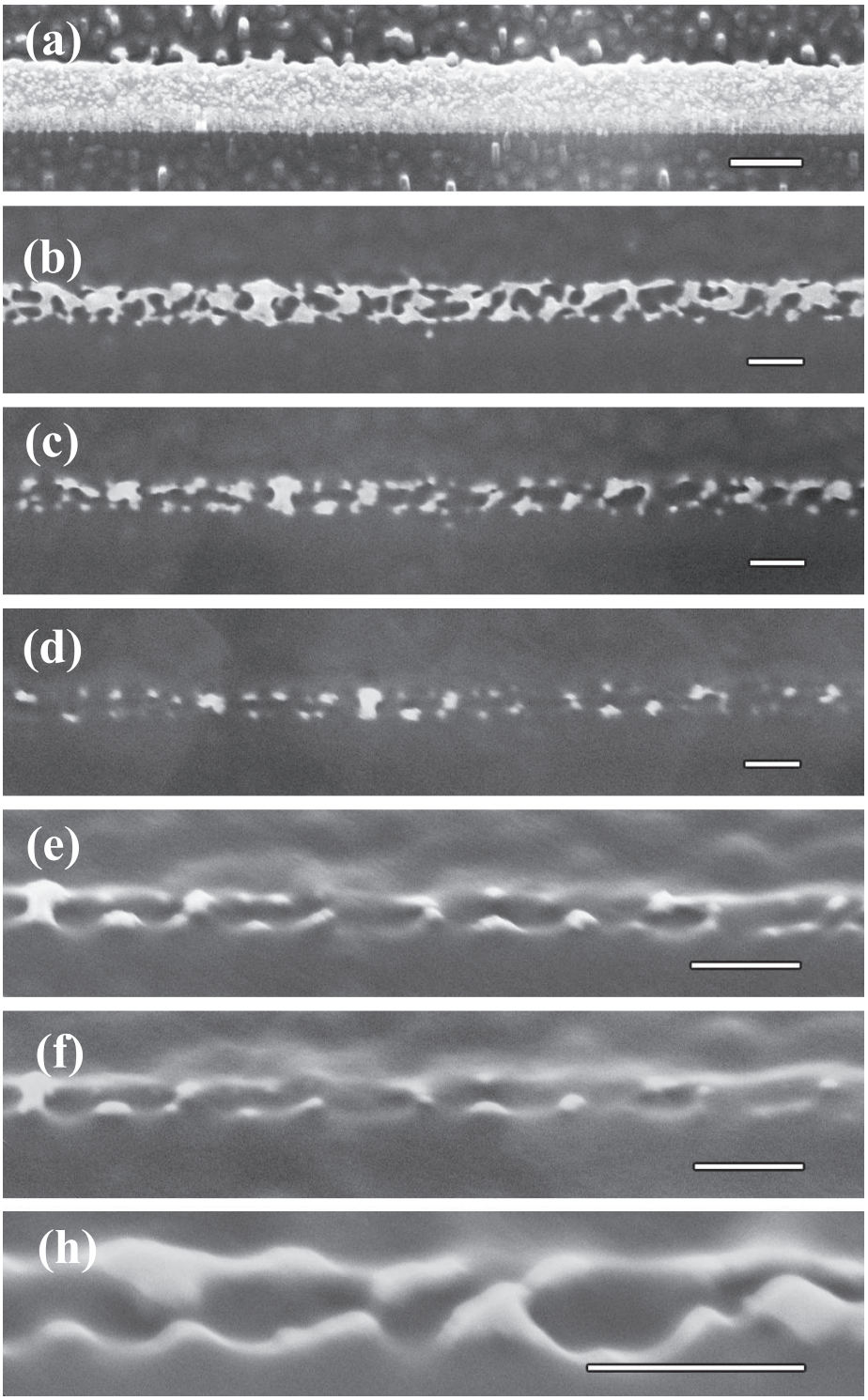


Figure 3.16: SEM images of morphological evolution of a copper line with rectangle cross section of $500 \times 80$ nm$^2$ at different bombardment time: (a) $t = 0$ s, (b) $t = 180$ s, (c) $t = 240$ s, and (d) $t = 300$ s. (a), (b), (c) and (d) are viewed from surface normal, while (e) and (f) are viewed from 52° relative to the surface normal of (c) and (d) respectively. (h) High magnification image of (e). Flux $f = 4.2 \times 10^{14}$ cm$^{-2}$s$^{-1}$, energy $\varepsilon = 10$ keV. Scale bar=500 nm.

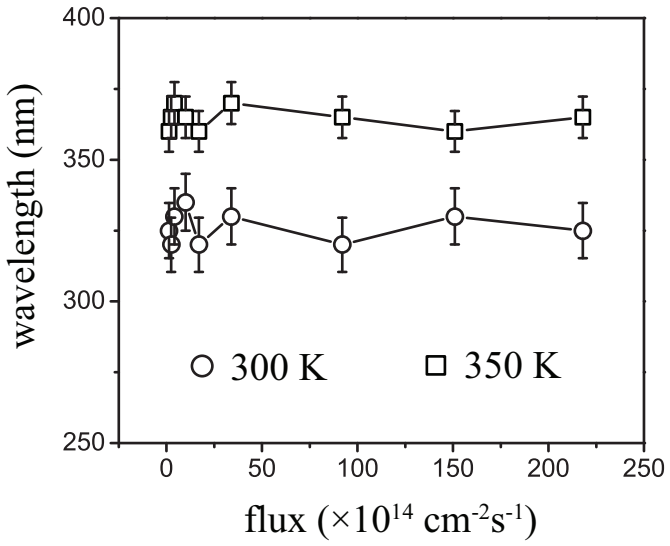


Figure 3.17: Wavelength as a function of flux at various temperatures. Within the limit of experimental error, the wavelength with respect to flux is constant.

Table 3.3: Flux effects on wavelength (nm/min) at different temperatures. Energy 10 keV

| Flux $10^{14}(\mathrm{cm}^{-2}\mathrm{s}^{-1})$ | 1.3 | 2.4 | 4.2 | 10 | 17 | 34 | 92 | 151 | 218 |
|---|---|---|---|---|---|---|---|---|---|
| Temperature (300 K) | 325 | 330 | 335 | 320 | 330 | 320 | 330 | 325 | 330 |
| Temperature (350 K) | 380 | 390 | 375 | 380 | 385 | 390 | 380 | 385 | 390 |

### 3.2.2 Model

The experimental results can be schematically described in Fig. 3.18. For small width lines, the cross section is ellipse (Fig. 3.14(c) and (d)). When the width reaches a critical value (Fig. 3.18(a)), periodic patterns start to develop until nanoparticles are formed. For larger width lines, due to dewetting effect [74, 75, 161] two rims on both edges of line are generated (Figs. 3.18(b) and 3.14(c) and (d)). According to Sigmund theory [77], the sputtering is higher in the middle of line than that on the rims. Thus original line breaks down to two lines, each of which evolve into periodic nanodots (Fig. 3.14 (a) and (b)). Next we will establish a linear partial differential equation based on roughening and smoothing mechanisms to show there exists a critical width for pattern formation.

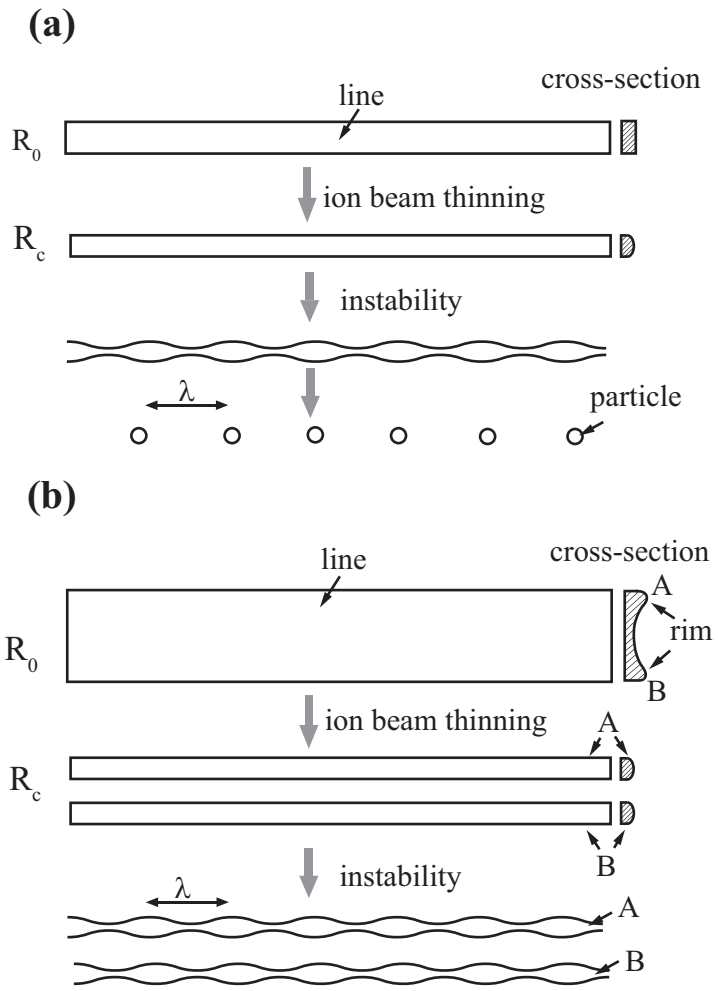


Figure 3.18: Schematic representation of particle formation. (a) Instability for a small size line (Fig. 3.15) and (b) instability for a large size line. $R_0$ is original size of line, $R_c$ is critical size at the beginning of pattern formation. Rim structure can be seen for the line with larger size (b).

**Ion induced roughening**

Theoretical approaches to surface erosion by ion bombardment typically used Sigmund's transport theory [71, 77] to calculate the sputtering yield at a point on an arbitrary surface function under the assumption of Gaussian distribution of deposited energy of ions [63–65]. According to Sigmund's theory [77], when the ion penetrates an average distance inside the solid it spreads their kinetic energy to the neighboring sites following Gaussian distribution. The sputtering yield at which material is ejected from a point is proportional to the energy accumulated there by all ions. For a homogeneous flux, the distribution of the total number of sputtered atoms per unit area per unit time along the outward normal surface is given by Eq. 1.4.

To evaluate Eq. (1.4), we need to know the surface profile. In our experiments, the cross sections of nanowlines in our experiment are square or rectangular. However, as shown by Lian and Zhao [74, 75], and in Fig. 3.14(d), when we reduce the sample with cross section up to less than $100 \times 100$ nm$^2$ from larger cross section by ion bombardment, due to redeposition, the surface diffusion and dewetting, such small cross section can be approximated as ellipse. Generally, the surface height $x = h(y, z)$ can be expanded into powers of derivatives of $h(y, z)$. For BH model [64], it was assumed that surface height can be expended as $h(y, z) = -y^2/2R_y - z^2/2R_z$, where $R_y$ and $R_z$ are the two principle radii of curvature. The integration reveals the negative surface tension. By combination of surface diffusion, they derived a linear partial different equation to explain the orientation and wavelength of ripple induced by ion beam. If expending surface profile into fourth power of height, Cuerno and Barabási [63, 65] proposed nonlinear equation to explain the morphology evolution of ripple for long time bombardment, such as roughening, coarsening, and rotation of ripple. In our case, due to shadow effects, only half of line can be bombarded by

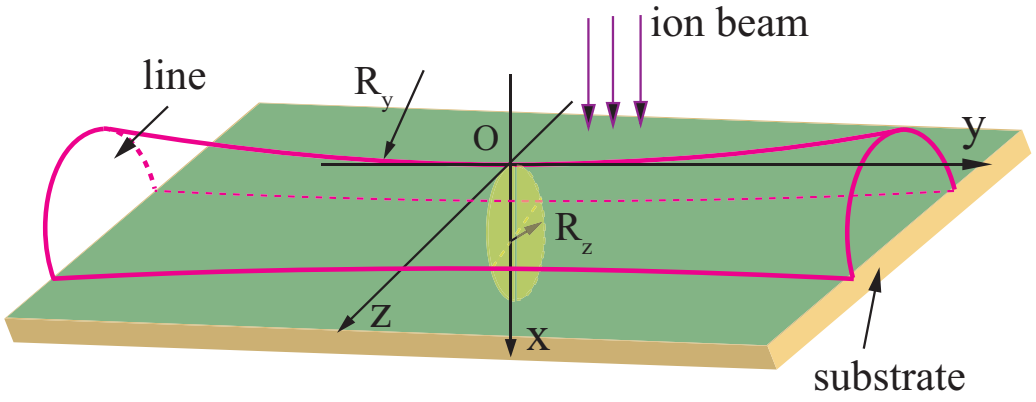


Figure 3.19: Schematic illustration of line and coordinate frame used to calculate the sputtering yield at point $O$. The ion beam direction is perpendicular to the wire axis. Two principle curvatures have opposite signs (we assume curvature is positive for convex surface).

the ion beam (Fig. 3.19). Thus we can assume that the surface function is

$$x = \frac{z^2}{2R_z} - \frac{y^2}{2R_y} \tag{3.25}$$

where $R_z$ and $R_y$ are two principal radii of curvature of surface at point $O$. Following ripple formation [63–65], we assume that the initial surface varies slowly enough that $R_z$ and $R_y$ are much larger than average penetration depth. Thus we can expand the exponential terms in Eq. (1.4) which include $1/R_y, 1/R_z$ to the first order and neglect second and higher orders.

According to Sigmund's theory, the deposited energy distribution is given by Eq. 1.5 and local flux for normal bombardment given by 2.31. Let $r = 0$ and the integral be over the range of $-\infty < y, z < +\infty$, we obtain the sputtered atoms at point $O$ contributed from all slowing down of ions inside materials. Combination of Eqs. 1.4,1.5,2.31, and 3.25 give

$$N(R_y, R_z) = \frac{\Lambda \epsilon f}{\sqrt{2\pi}\alpha} \exp\left(-\frac{a^2}{2\alpha^2}\right)\left(1 - \frac{a\beta^2}{2\alpha^2}\left[\frac{1}{R_z} - \frac{1}{R_y}\right]\right) \tag{3.26}$$

This can be understood as the flux of atoms outgoing from the wire along the surface

normal as a result of ion bombardment. For small slope approximation, we have

$$\frac{\partial R_z}{\partial t} = -\Omega N(R_y, R_z)\sqrt{1 + \nabla_y^2 x + \nabla_z^2 x} \approx -\Omega N(R_y, R_z) \tag{3.27}$$

where $\Omega$ is atomic volume. Substituting Eq. 3.26 into Eq. 3.27 gives

$$\frac{\partial R_z}{\partial t} = -v_0 + \eta K \tag{3.28}$$

where

$$\begin{aligned} v_0 &= \frac{\Omega \Lambda \epsilon f}{\sqrt{2\pi}\alpha} \exp\left(-\frac{a^2}{2\alpha^2}\right) \\ \eta &= \frac{\Omega \Lambda \epsilon f a \beta^2}{2\sqrt{2\pi}\alpha^3} \exp\left(-\frac{a^2}{2\alpha^2}\right) \\ K &= \frac{1}{R_z} - \frac{1}{R_y} \end{aligned} \tag{3.29}$$

where the ion beam is along the positive $x$ axis (Fig. 3.14), $K$ is the mean curvature of surface, $\eta$ can be considered as the ion beam induced surface tension.

**Ehrlich-Schwoebel roughening**

For a metal surface under its roughening temperature, an adatom willing to step down should go through a step edge where it has maximum potential energy (Ehrlich-Schwoebel barrier) [166, 167]. This barrier leads to a surface flux in the uphill direction and to an increase of slope. It has been reported that scaling law characterizing the time and spatial evolution of the ripples in the low temperature regime induced by low energetic ions satisfies a continuum model for deposition which includes an Ehrlich-Schwoebel barrier to the interlayer diffusion of surface defects [3,4,168]. Following references [3, 4, 67, 163, 165, 168, 169] we can introduce to Eq. 3.28 the term

$$\frac{\partial h}{\partial t} = \frac{f_s l_s l_d^2 \Omega}{2(l_s + l_d)a_0} K = SK \tag{3.30}$$

for Ehrlich-Schwoebel effect, where $S$ is roughening coefficient describing the effects of Ehrlich-Schwoebel barrier to interlayer diffusion, $f_s$ is the flux of mobile species on the

surface, $l_s$ and $l_d$ are the Schwoebel length and diffusion length respectively, $a_0$ is the lattice constant. The schwoebel length is defined as $a_0[exp(E_{ES}/kT)-1]$, where $E_{ES}$ is Ehrlich-Schwoebel barrier. In a surface growth model for deposition, diffusion and aggregation system, the diffusion length is determined by the competition between deposition and diffusion. The larger the flux, the less time is needed for deposited atoms to diffuse before meeting another atoms on the surface. The normalized flux $(f_s/D)^{-\psi}$ is typically used to describe the scaling property of mean diffusion length, where $D$ and $f$ are in unite of ML $s^{-1}$. The value of $\psi$ is 1$\sim$1/6, depending on the ratio of $f_s/D$, a higher flux corresponding to a larger value of $\psi$ [170]. Since both length $l_s$ and $l_d$ are exponential temperature dependence, Eq. 3.30 shows that $S$ has a maximum value at a certain temperature and dramatically decreases blow or beyond this temperature. Thus Ehrlich-Schwoebel barrier on the roughening plays an important role in a narrow range of temperature [165]. In principle, we can compare the value of two roughening coefficients $S$ in Eq. 3.30 and $\eta$ in Eq. 3.28 to determine the controlling mechanism. Because $\eta$ increases linearly with the increase of energy ($a/\alpha$ and $\beta/\alpha$ in Eq. 4.5are approximately constant) while $S$ is energy independent, and $\eta$ increases faster than $S$ with increasing flux, for high flux and energy, curvature dependent roughening becomes dominant [157, 165]. For Cu(001) system bombarded by 0.8 keV $Ar^+$ ion with $2.13\times10^{14}cm^{-2}s^{-1}$ flux and temperature from 393 to 473 K, Chason [162–164] showed that morphological evolution of Cu in the early stages can be well described by the predictions of the continuum theory in which Ehrlich-Schwoebel barrier is neglected. In our experiments, as shown in Fig. 3.20 for planar surface, no crystallographic features is induced by ion beam at normal bombardment, which is not consistent with the observations controlled by Ehrlich-Schwoebel barrier [2, 171–173]. Here we assume the mass transport do not

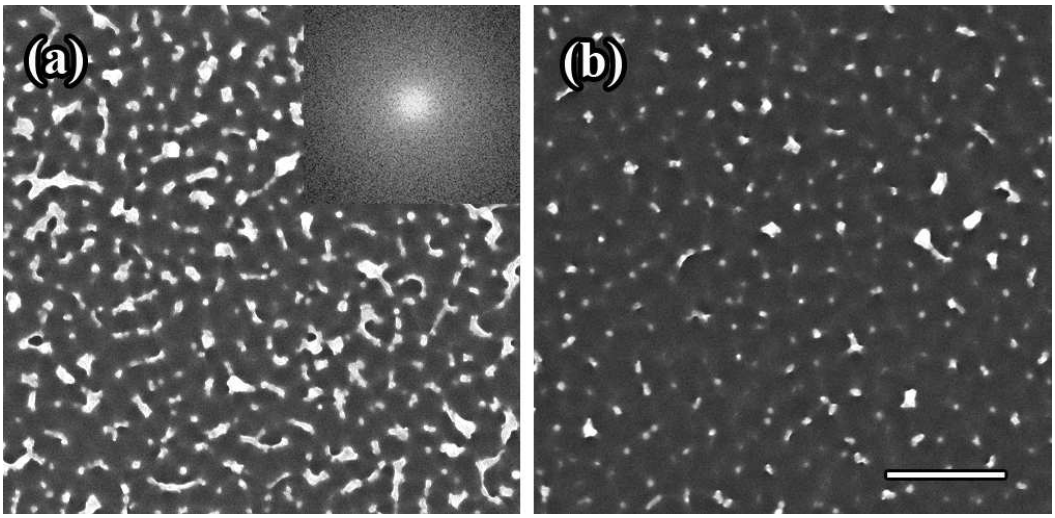


Figure 3.20: Evolution of thin film subjected to ion beam at normal incidence with various fluence: (a) fluence $8.5 \times 10^{16}$ cm$^{-2}$ and (b) fluence $1.6 \times 10^{17}$ cm$^{-2}$. Inset is FFT (Fast Fourier transformation) showing the isotropic property of pattern. Flux $f = 4.2 \times 10^{14}$ cm$^{-2}$s$^{-1}$, energy $\varepsilon = 10$ keV. Scale bar is 1 $\mu$m.

face Ehrich-Schwoebel barrier at step edges. This simplifying assumption enables us to make quantitative comparison of our model with experimental observations. However, as shown below this assumption does not change the general results of our model.

**Thermally induced smoothing**

The mobile species on the surface, biased by changes in surface energy, can smooth the surface by thermally induced diffusion. According to the classic work of Herring and Mullins [90, 174], for amorphous surfaces, a chemical potential energy is proportional to the surface curvature

$$\mu = K\gamma\Omega \tag{3.31}$$

where $\gamma$ is surface tension. Using Nernst-Einstein relation, a current of species on the surface is proportional to a gradient of the chemical potential

$$J = -\frac{D_s c}{kT}\nabla_s \mu \tag{3.32}$$

where $D_s$ is surface self-diffusion coefficient, $\nu$ is the number of diffusing atoms per unite surface area, $kT$ has its usual meaning. Divergence of $-J$ gives rise to the outward normal growth velocity [90, 160]

$$v_n = \frac{D_s \gamma \Omega^2 c}{kT} \nabla^2 K \equiv B \nabla_s^2 K \tag{3.33}$$

This equation does not take into account of anisotropic movement of species on a single crystal metal surface, As shown by Rusponi [3,4], the diffusion coefficient $D_s K$ can be replaced by two terms $D_{s,x} K_x + D_{s,Y} K_y$ to give the different rate along two axis.

**Ion-induced smoothing**

By expanding surface height into the fourth order, Makeev *et al* [65, 130] use Eq. 1.4 to obtain a term which is proportional to the fourth derivative of height. Since it is fully determined by the process of surface erosion and has a smoothing effect similar to the thermal diffusion, it is called ion induced surface diffusion. It has been reported that this term plays an important role at the low temperature in which the thermal diffusion is smaller [130, 162, 163, 175]. Combination of this term with thermal diffusion, the relationship between wavelength and flux is successfully explained [130, 162, 163, 175]. In our case, By expanding Eq. (3.25) into the fourth order, we also derived a nonlinear continuum equation including ion induced diffusion term. The result shows

$$\frac{\partial h}{\partial t} = \frac{a \beta \Lambda \epsilon f \Omega}{8\sqrt{2\pi}} \exp(-a^2/2\alpha^2) \nabla_s^2 K = \zeta \nabla_s^2 K \tag{3.34}$$

at normal bombardment. It can be seen that our expression is different from that derived in Refs [65, 130]. by atomic volume $\Omega$ used in the Eq. 3.27. This difference results in the small value compared with previous studies. Similar to smoothing

mechanism, we can make comparison of $\zeta$ and $B$ to determine which mechanism is dominate. As shown by Chason's group [162–164], if ion induced smoothing dominant, the wavelength is flux and temperature independent. If thermal smoothing dominant, the wavelength is the flux-independent but temperature dependent, depending on the mobility of surface defects. From experimental data we can find the smoothing mechanism.

Combining Eqs. (3.28), (3.31), (3.33), (3.34), we have linear equation for evolution of lines subjected to normal bombardment:

$$\frac{\partial R_z}{\partial t} = -v_0 + \Gamma K + D\nabla_s^2 K \tag{3.35}$$

where $\Gamma = \eta + S$, $D = B + \zeta$.

If we substitute the equations $\partial R_z/\partial t = -\partial x/\partial t$, $1/R_y = -\partial^2 x/\partial y^2$ and $1/R_z = \partial^2 x/\partial z^2$ into Eq. (3.26), we obtain the linear partial different equation which shows that the line is unstable with arbitrary wave vector due to the curvature dependent sputtering yield. It should be noted that the similar equations are derived in Refs. [64] and [9] for the ripple formation induced by the oblique ion beam on the two dimensional surface.

### 3.2.3 Analysis of stability

For an infinite long line and small amplitude perturbations, using cylinder coordination, the curvature can be expressed by

$$K = \frac{R_z^2 + 2\left(\frac{\partial R_z}{\partial \theta}\right)^2 - R_z\frac{\partial^2 R_z}{\partial \theta^2}}{\left[R_z^2 + \left(\frac{\partial R_z}{\partial \theta}\right)^2\right]^{3/2}} - \frac{\partial^2 R_z}{\partial y^2} \tag{3.36}$$

If we introduce an infinitesimal perturbation given by

$$R_z = R_0 + \delta(t)\exp(iky + in\theta) \tag{3.37}$$

where $R_0$ is initial radius of wire, $n = 0, 1, 2, 3 \cdots$, substituting Eqs. (3.36) and (3.37) into Eq. (3.26), and retaining only first order terms in $\delta(t)$ yield

$$\frac{\partial R_0}{\partial t} = -v_0 + \frac{\eta}{R_0} \tag{3.38}$$

and

$$\frac{\partial \delta(t)}{\partial t \delta(t)} = \left[\frac{1}{R_0^2} - \left(\frac{n^2}{R_0^2} + k^2\right)\right]\left[D\left(\frac{n^2}{R_0^2} + k^2\right) - \Gamma\right] \tag{3.39}$$

Eq. (3.38) expresses the shrinkage rate of the mean radius subjected to the ion beam. Since $R_0 \gg a$ and $\alpha \approx \beta$, we can neglect last term in Eq. (3.38) and obtain the evolution of radius with time

$$R_z = R_0 - v_0 t \tag{3.40}$$

This result is different from that given by Nichols and Mullins [160] in which the variance of the mean radius with time is zero. If we assume small slope, Eq. (3.40) is the direct result of bombardment.

Eq. (3.39) shows the dispersion relation of the fractional growth rates for various frequencies. If $\Gamma = 0$, the pure capillary effect is realized. It can be seen that any modes for $n \geq 1$ is stable. The instability occurs with wave vector along the axis of cylinder and wavelength of $\lambda = 8.89 R_0$, the identical results given by Nichols and Mullins [160]. If $D = 0$, it reduces to the pure irradiation effect. The surface is unstable with arbitrary wave vector, consistent with ripple formation for normal bombardment on the planar surface [63,64]. When both irradiation and capillary are present, the unstable modes can be determined under two conditions: if two terms on the right hand of Eq. (3.39) are all positive, we have

$$\begin{aligned} R_0 &< \sqrt{\frac{D}{\Gamma}} \\ \lambda &= \frac{8.89 R_0}{\sqrt{1 + \frac{\Gamma}{D} R_0^2}} \end{aligned} \tag{3.41}$$

with the wave vector parallel to the axis of line, and if two terms on the right hand of Eq. (3.39) are all negative, it shows that when $R_0 > \sqrt{D/\Gamma}$, and the arbitrary wave vector with $n^2/R_0^2 + k^2 > 1/R_0^2$ forms, which means we can not observe periodic structures on the surface of wire. Due to Eq. (3.40) is still valid, this process can be understood as only ion milling phenomenon. Once the radius of line satisfies the Eq. (3.41), the periodic waves parallel to line axis forms and then the line breaks into particles. Under this condition, we have

$$\begin{aligned} R_0 &> \sqrt{\frac{D}{\Gamma}} \\ \lambda &= 2\pi\sqrt{\frac{D}{\Gamma}} \end{aligned} \tag{3.42}$$

Thus, we obtain a critical width of line given by $R_c = \sqrt{D/\Gamma}$. If the width of line exceeds the critical value , although the unstable modes can occur, no ordered patterns can develop. Sputter etching gives rise to the decrease of width, leading to the maximum wavelength given by Eq. (3.42).

Compared with wavelength, $\lambda = 8.89R_0$, given by Nichols and Mullins [160] for solid cylinder (or Rayleigh instability [159] for an inviscid liquid) under the condition of conservation of volume, Eqs. (3.41) and (3.42) show that ion bombardment tends to suppress the instability induced by surface diffusion. The ratio of diffusion coefficient ($\Gamma$) induced by ion beam to the surface thermal coefficient ($D$) determines the correction to the Rayleigh instability. This is reasonable because the ion beam bombardment can reduce the radius of wire, thus leading to the decrease of wavelength. However, the relationship between the wavelength and radius of wire is not linear for ion bombardment. Eq. 3.42 shows if $R_0 \to \infty$, wavelength is independent of initial radius, and if the radius of wire is small and temperature is high enough that $\xi R_0^2 \ll 1$, Eq. 3.41 reduces to classical Rayleigh instability of a cylindrical rod. Therefore, for small radius and intermediate energy ions as shown in Lian [74] and

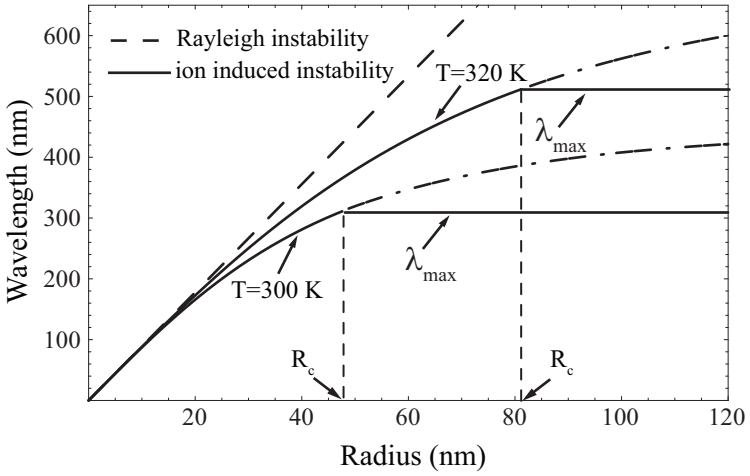


Figure 3.21: Dependence of the wavelength on the wire width from Eqs. (3.41) and (3.42). At $T = 300$ K, $R_c = \sqrt{D/\Gamma} = 48$ nm, at $T = 320$ K, $R_c = \sqrt{D/\Gamma} = 82$ nm. Rayleigh instability is given for comparison.

Zhao [75], Rayleigh instability can be used to approximately predict the experimental observations.

### 3.2.4 Comparison and discussion

**Comparison with Rayleigh instability and BH model**

Fig. 3.21 gives the comparison of our model with Rayleigh instability by assuming thermally induced smoothing mechanism and ion-induced roughening mechanism are dominate [63–65, 163, 164]. Under these assumptions the temperature dependence of wavelength is a simple Arrhenius equation, the same behavior as BH model [64]. The parameters we used in Fig. 3.21 are: energy $\varepsilon = 10$ keV, flux $f = 4.2 \times 10^{14}$ $\mathrm{cm}^{-2}\mathrm{s}^{-1}$, $kT = 4.14 \times 10^{-21}$ J, atomic volume $\Omega = 1.2 \times 10^{-23}\mathrm{cm}^3$, material factor $\Lambda = 1.4 \times 10^{-9}\mathrm{cm\ eV}^{-1}$ [77], penetration depth $a = 3.9$ nm [80,125], straggling $\alpha = 2$ nm, [80,125] and straggling $\beta = 1.2$ nm [80,125]. Since the surface tension, concentration of mobile defects, and diffusion coefficient are dependence of irradiation conditions and surface properties, for simplicity, we assume: surface tension $\gamma = 1.78 \times 10^{-4}$ J $\mathrm{cm}^{-2}$ [176], diffusion coefficient $D_s = 2.74 \times 10^{-12}$ $\mathrm{cm}^2\mathrm{s}^{-1}$ [177], and concentration

of mobile defects $\nu$ = surface atomic density = $1.9 \times 10^{15}$ cm$^{-2}$. Substituting these values into Eqs. 4.5 and 3.33 gives $B = 3.3 \times 10^{-26}$ cm$^4$s$^{-1}$, $\eta = 1.4 \times 10^{-15}$ cm$^2$s$^{-1}$ and $v_0 = 0.21$ nm s$^{-1}$. Rough theoretical estimate of the critical radius and wavelength for a Cu wire is $R_c = 48$ nm, $\lambda = 300$ nm for any $R_0 > R_c$, and $\lambda = 8.89R_0/\sqrt{1 + 4.4 \times 10^{-4}R_0^2}$ (in unit of nm) for $R_0 < R_c$. It should be noted that Arrhenius behavior is very sensitive to temperature and energy, a small temperature or energy change can result in a significant different outcome, which can differ by an order of magnitude or more. For example, if temperature change from 300 K to 320 K, the critical radius calculated from above assuming values can increase from 48 nm to 82 nm as shown in Fig. 3.21. However, It is well known that the temperature dependent wavelength can not be described by a simple Arrhenius behavior. Surface tension and concentration of mobile defects are not only dependent of temperature but also dependent of slope [165].

Fragmentation of Cu nanowire driven by Rayleigh instability at various temperatures has been reported [178]. Since the breakup time is proportional to $R_0^4$ according to Nichols and Mullins instability [160], nanowire with 55 nm radius exhibits no changes after annealing at 400°C during 20 min. In our experiments, however, within 1 minute, the same size nanolines can undergo significant changes at room temperature (Fig. 3.14). It can be drawn a conclusion that the interaction between ion and nanowire is the main reason for the fragmentation of nanowire.

According to the linear equation for ripple formation [64], with normal bombardment on the amorphous surface, no ordered ripple forms although the surface is unstable. For single crystal surface, the ripple can be induced by the surface anisotropy diffusion at normal bombardment. In our case , However, the ordered patterns can be formed at normal bombardment although we show that surface effects can be neg-

ligible. This is because of a relationship between two principle curvatures (Eq. 3.36). The critical radius seems to provide a criterion for distinguishing between plane and cylinder. When the radius exceeds the critical value, the behavior of cylinder is similar to the planar surface described by linear analysis in BH model [64]. For BH model [64] the smoothing terms induced by sputtering and surface tension are competitive with the roughening terms induced by sputtering etching and ES barrier, while for the wire, both smoothing and roughening terms make the wire unstable. The role of smoothing is to select one unstable mode for the radius less than critical value.

**Flux dependence of nanoparticles**

The flux independence in our experiment means that surface has sufficient time, between an ion hit and the following, to rearrange it via the diffusion process. The understanding of flux dependence of ripple wavelength has been extensively studied [9, 12, 163–165], focusing on the variation of concentration with the energy and flux. Their approach can be extended to our model although not the current one specifically. If we neglect cluster formation, the concentration of mobile defects on the surface, depending on the production and annihilation rates, satisfies the mass conservation equations [58, 107, 179]

$$\frac{\partial C_v}{\partial t} = D_v \nabla^2 C_v + K_d - K_{iv} C_i C_v - \sum_s K_{sv} C_s C_v \tag{3.43a}$$

$$\frac{\partial C_i}{\partial t} = D_i \nabla^2 C_i + K_d - Y f - K_{iv} C_i C_v - \sum_s K_{si} C_s C_i \tag{3.43b}$$

where $D_i$ and $D_v$ are the defect diffusion coefficients, $K_d$ is the defect generation rate, $C_i$ and $C_v$ are the defect concentration, $C_s$ are the sink densities and $K_{si}$ and $K_{sv}$ are the sink reaction rates, $K_d = f\sigma_d/N$, where $\sigma$ is displacement cross section in units of displacements/ion/Å [80], $N$ is atomic density of target. In special cases

where the spatial distribution of defects is important, The Eq. 3.43 can be solved in their spatially dependent form (third and fourth terms in Eq. 3.43 are zero) [163], In most cases where the defect separation is larger than the distance between extended sinks, this equation is used in its spatially independent form [9, 12, 164]. Because two equations are coupled in a nonlinear form, they have no analytical solution, and are normally solved numerically. Depending on the irradiation temperature, the microstructure of materials, the damage rate, two types of processes can be identified in spatially independent form: for high mobility of defects, high sink density and low displacement rate, defects absorption at sinks limits the accumulation, and we have sink-dominated regime, whereas for low temperature, high displacement rate and low sink density microstructures, recombination limits accumulation, giving rise to a recombination-dominated regime. At steady state, in sink dominated regime, the first and third terms on the right hand of Eq. 3.43 can be assumed to be zero, thus $C_v \propto f$ and $C_i \propto f$, and then $B \sim f$. From Eqs. 3.41 and 3.42, we know that wavelength is independent of flux. In recombination dominated regime, the first and fourth terms on the right hand of Eq. 3.43 are zero, we have $C_v \propto f^{1/2}$ and $C_i \propto f^{1/2}$, and then $B \sim f^{1/2}$. Therefore, under this condition wavelength is flux dependent. If we further assume that $\zeta \ll B$, we have $\lambda \propto f^{-1/4}$. In our experiments, ion flux is high ($f = 4.2 \times 10^{14}$ cm$^{-2}$s$^{-1}$). We should consider the implantation of Ga atoms on the surface. Because the sputtering removes both target and implanted atoms, with the receding of the sample surface, the initial Gaussian shaped distribution of implanted atoms overlap, leading to an increase of concentration of implanted atoms at the surface. The Ga atom fraction on the surface at steady state is $C_{Ga} = 1/Y_m$ [180], where $Y_M$ is the sputtering yield per implanted ion. For 10 keV Ga ion on Cu surface, $C_{Ga} \approx 25\%$. The result of these Ga atoms on the Cu surface can create high

sinks for mobile species. Considering steps and mobilities in metals, we believe our experiment condition belongs to sink-dominated regime, in which the wavelength is flux independent.

**Temperature dependence of nanoparticles**

The thermal equilibrium concentration of defects is small compared with the ion induced defect concentration in our experimental conditions. We neglect this effect in Eq. 3.43. But at high temperature, the defects have high mobility and thus the irradiation induced defects are lost quickly. The thermal equilibrium defects are dominate. We need to use thermal defect creation rate to replace $K_d$ in Eq. 3.43. As a result, we have $\lambda \propto f^{-1/2}$ [163]. At intermediate temperatures, where $k_d$, the rate of defects induced by ion beam begin to dominate diffusion process, if the density of fixed sinks is not extremely low, corresponding to the sink-dominated regime, wavelength is independent of flux. At still lower temperature and low sink densities, the concentration of defects induced by the beam becomes high enough that recombination starts to dominate. This situation corresponds to a recombination-dominated regime in which $\lambda \propto f^{-1/4}$.

During bombardment, The slowing down of the incident ions in the target materials initiates displacement cascades. Except a small fraction of kinetic energy is emitted by sputtered atoms or stored as defects, almost all of the kinetic energy is converted to heat. Assuming that a local thermal equilibrium is established within a cascade volume, it has been reported that temperature at local site can reach up to 39000 K for 10 keV Bi ion on Ge [70] and exists for several picoseconds before being quenched to ambient temperature. Once a dynamic equilibrium is established, the concept of local heating and temperature become reasonable. Under conditions that sample well contacts to a heat reservoir, a finite steady-state temperature increase

is given by $T_i = P/(\pi r_i \kappa_i)$ [180, 181], where $P$ is beam power, $r_i$ is beam size, $\kappa_i$ is sample thermal conductivity. In our case, Cu line on the surface of Si substrate, $T < 1°$C. Therefore, in our experiment, it is reasonable to assume that temperature is the heat reservoir temperature.

If ion-induced smooth mechanism and ion-induced roughening mechanism are dominate at low temperature [65,163,164,175], from Eqs. 3.42, 3.34 and 3.28, we have $\lambda = 2\pi\sqrt{\zeta/\eta} = \alpha/2$ for $\alpha = \beta$, independence of flux and temperature. This value is two orders of magnitude smaller than the experimental data. The similar results have been reported for the ripple formation on silicon surface by low-energy noble gas ion beam erosion at room temperature [33]. Because $\alpha$ is around several nanometers for the ion energy less than 10 keV, these observation means only ion-induced smoothing mechanism can not explain the pattern formation even at low temperature. On the other hand, if thermally induced smoothing mechanism and ion-induced roughening mechanism are dominate [63–65, 163, 164], from Eqs. 3.42, 3.33 and 3.28 we obtain the wavelength which is a function of diffusivity, concentration of mobile species on the surface and temperature. It is known these parameters depend on the radiation conditions and target properties as simply described by Eq. 3.43.

In this model, the effects of redepositon and viscous flow on the instability of nanolines was not considered. The first effect can lead to the non-linear terms which has little effects on the growth of a small disturbance for linear stability analysis [21]. Viscous flow is another important relaxation mechanism in amorphous systems as pointed out by a number of group [10, 12, 182, 183]. In this case, because the surface remains crystalline during bombardment, this effect is neglected in our model.

### 3.2.5 Conclusion

In conclusion, the morphological evolution of ion induced nanoparticle formation on Cu wire both experimentally and theoretically have been studied. The experimental data shows that when the radius reaches a certain value, longitudinal mode can develop until the wire breaks up to a line of particles with periodic spacing. Sigmund's theory [71, 77] and Nichols and Mullins [160] approach were combined to develop a new model to interpret the experimental observations. Linear-stability analysis shows that there is a critical radius for particle formation. The radius larger than this value will eventually reach this value by ion etching and one wave parallel to the axis of wire forms, leading to the periodic particle formation.

## 3.3 Ordered Nanocrystals on Argon Ion Sputtered Polymer Film

Bombardment of solid surfaces with low energetic ions is under intensive investigations due to its self-assembly into well-ordered periodic structure. A variety of topographies can result from surface erosion depending on sputtering conditions and material properties [27, 64, 78, 158]. Ripples, bumps, cones and fingerprint-like structures are the typical morphologies with the wavelength scales of the order of 10-1000 nm. Low energy ion bombardment is regarded as an alternative process for the fabrication of various nanostructured surface or interfaces besides common applications such as ion beam assisted deposition, reactive etching, sputter etching, and plasma assisted chemical vapor deposition [184]. Recently, it has been reported that hexagonal ordering quantum dots can be generated by $Ar^+$ ion sputtering under normal incidence on the GaSb and oblique ion incidence sputtering of InP with sample rotation [27, 185]. Compared with the low throughput of serial lithographic methods, this novel approach opened a promising route for the fabrication of uniform semicon-

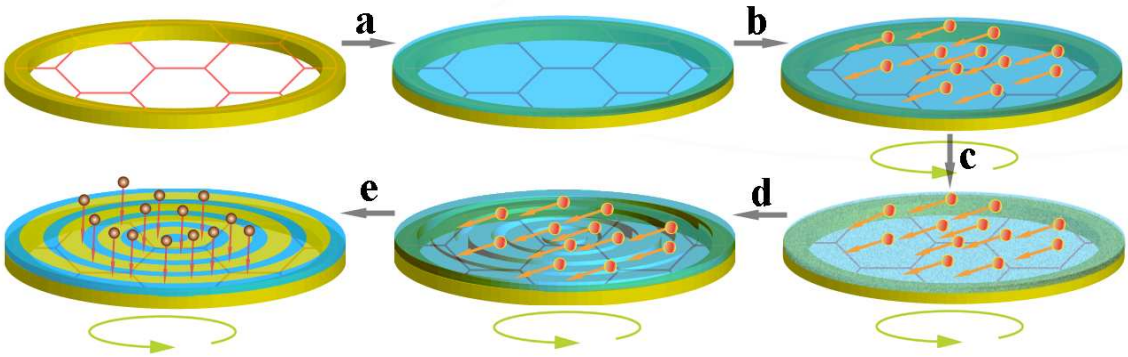


Figure 3.22: Schematic illustrations of the procedure. (a) A thin film was coated on the copper grid. (b) $Ar^+$ ions bombarded the rotating film. (c) Defects in the thin film were generated. (d) Defects self-assembled into periodical stripe-like patterns under the irradiation of $Ar^+$ ions. (e) The ordered patterns in the thin film was transferred to the deposited atoms. The whole apparatus was under vacuum, and the sample was rotating during ion bombardment and deposition.

ductor quantum dots ordered in a hexagonal array. In this section, it was found that ultrathin films can self assemble into the highly ordered stripe like patterns upon low energetic ion bombardment and these films can be used as templates to pattern metal and semiconductor structures.

### 3.3.1 Experimental

The polymer films containing 30 % bisphenol-F epoxy resin, 65% tatrahydrofuran and 5% methyl ethyl ketone were used in the experiments. We first coated the dilute polymer solution on the 200 mesh (lines/inch) copper grid, and then annealed at different temperatures for 1 hour for solidification. The ion bombardment experiments were carried out at room temperature in a commercial ion milling system with the pressure of $3 \times 10^{-3}$ Torr. 2 keV$\sim$5 keV $Ar^+$ ions with flux of $1 \times 10^{14}$ $cm^{-2}s^{-1}$ at an angle of 80° from normal were used. After well ordered patterns were induced by ion beam on the thin polymer film, we made deposition for copper and silicon. The sample was rotated during bombardment and deposition. The morphology and microstructure of coated films upon ion bombardment and disposition were mea-

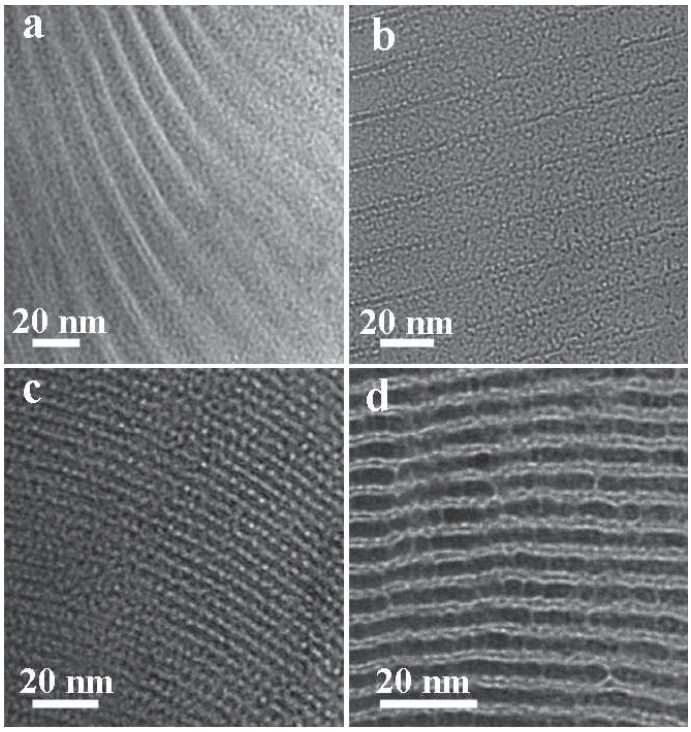


Figure 3.23: TEM images of patterns on the irradiated polymer films. The sample was irradiated by 4.2 keV $Ar^+$ ions at an angle of 80 from normal for different ion fluences. (a) The transition area from plain surface to striped surface is shown at the dose of $1 \times 10^{17}\text{cm}^{-2}$. (b) The well ordered patterns were formed when the dose is $4 \times 10^{17}\text{cm}^{-2}$. The wavelength shown in (a) and (b) is about 25 nm and the annealed temperature is 110°C. (c) With the same energy and dose as (b), when the annealed temperature is 130°C, the pattern with wavelength of 7 nm is observed. (d) HRTEM image of (c) showing the high density of networks. The sample is rotated at the speed of 4 rpm. The images were taken under defocus conditions.

sured by an analytical Transmission Electron Microscope (TEM). Fig. 3.22 shows the procedure used to prepare well-ordered nanopatterned structure of metal and semiconductor from an ultrathin film.

### 3.3.2 Results and Analysis

The bright-field TEM images of a polymer film after bombardment by 4.2 keV $Ar^+$ ions at an angle of $\sim 80°$ from normal at different ion fluences with a constant speed of rotation are shown in Fig. 3.23.

Before irradiation, no ordered features were observed, different from the well-ordered diblock polymers which were widely used as template for nanofabrications

[186, 187]. At an ion fluence of $1 \times 10^{17}\text{cm}^{-2}$, equivalent to an exposure time of 10 minutes, the sand like ripples with the wave length of 25 nm appear (Fig. 3.23a). It can be seen that polymers irradiated by low energy ions underwent the degradation by nuclear stopping in which chain scission, chain aggregation, and molecular emission occurred [188–190]. These effects are due to the large amount of energy storage in the molecular environment, which overcomes the binding energies of organic molecules. At higher fluence, the nucleation and growth of clusters of amorphous carbon and radiacals were generated, leading to the final structure that has little memory of original chain structure [191]. Two opposite effects occurred upon energetic ion irradiation of polymers [188]: one of which is related to crosslinking where two or more molecules were chemically joined by a covalent bond and second to a chain scission where the molecular bonds were broken and the overall chains were shortened, corresponding to the roughening and smoothing on the irradiated surface of bulk materials respectively [185]. These formation and recombination of varieties of production induced by energetic ions in polymer films far from the equilibrium can contribute to the pattern formation, similar to the ordered semicondutor dots on the single GaSb surface induced by the ion irradiation [185]. With the increase of exposure time, the polymer films evolve into striped patterns (Fig. 3.23b). The defocus TEM images show the oriented stripes seem to consist of bundles of small voids produced by the interaction between the gas, radicals and small molecules induced by irradiation.

The wider stripes can be attributed to the loss of mass of the polymers irradiated for a longer time [188]. Fig. 2a illustrates the special area that links the well ordered patterns and plain surface, from which we can find that the stripes result from the diffusion of shorter chain molecules through the interactions among the

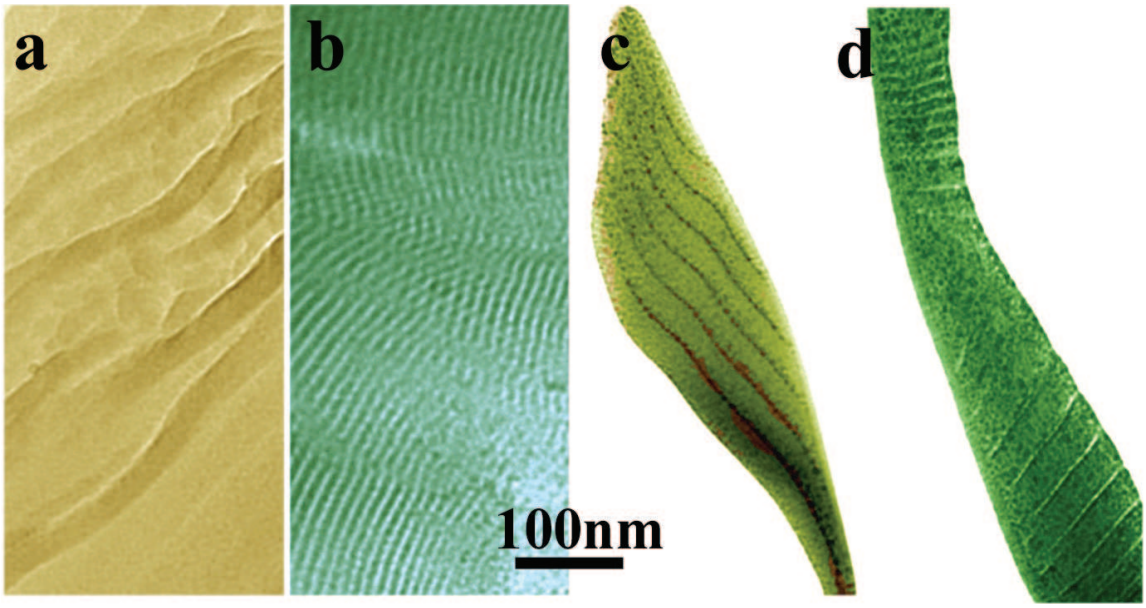


Figure 3.24: Complex patterns observed in thin film. These images are analogous to the patterns generated in nature but on nanometer scale. (a) Ripples in the sand with the fixed sample at the energy of 4.2 keV up to fluence of $5 \times 10^{16}$ cm$^{-2}$. (b) Fingerprints on the tips of fingers with the rotation of sample at the speed of 6 rpm. The energy is 4.2 keV and the fluence is $2 \times 10^{17}$ cm$^{-2}$. (c) Leaf-like structures on the films with the rotation speed of 6 rpm. The energy is 5 keV and the fluence is $6 \times 10^{17}$ cm$^{-2}$. (d) Worm-like structures with the same preparing conditions as those in (c) but with different boundary conditions.

ingredients induced by ion irradiation. Another pattern with wavelength of 7 nm was also found on the same component of polymer films but at different annealing temperatures as shown in Figs. 3.23c and 3.23d. The variation in pattern wavelengths can be attributed to the diffusion of different length of chains of molecules in the films: the longer chains in polymer film have less mobility and thus leading to the shorter wavelength. High resolution transmission electron microscope (HRTEM) image (Fig. 3.23d) of the nanostructure induced by $Ar^+$ ions with the exposure time of 30 minutes shows that the high density of networks of molecule chains formed, and thus the diffusion of molecules became slower, leading to the shorter wave length.

One interesting phenomenon observed on the irradiated polymer films is the nanostructures analogous to the patterns generated in the nature. Fig. 3.24 shows

some of these patterns (the colors are added by using Photoshop) induced under different conditions. This emphasizes one of important points in the theory of pattern formation outside of equilibrium, that similar patterns can occur in very different systems [61]. The variations of control parameters (exposure time, ion energy, rotation of sample, pressure, boundary conditions, etc.) result in the variations of the characteristics of patterns. For example, it shows that the higher speed of rotation, the shorter wavelength and better ordered patterns. The sand ripple shown in Fig. 3.24a is induced by the bombardment on the fixed samples with the energy of 4.2kev for 20 minutes, while Figs. 3.24b, 3.24c and 3.24d were taken at the rotation of 6 rpm of samples.

Commonly observed microdomain morphologies on the surface of irradiated polymers, termed ripples, striations or corrugations, appear to be similar with these on the inorganic material surface , depending on material structure and irradiation conditions [192–195]. Modern understanding of pattern formation is the concept of instability in which a phenomenon goes under the name of dissipative structure [61, 196]. The ion induced surface instability of solid is regarded as the superposition of interacting between the roughening instability and diffusion smoothing, which gives rise to waves propagating in different directions [64, 185]. The pattern selection was determined by the state that grows fastest near the instability [61]. A widely accepted theoretical approach describing the pattern formation on amorphous substrates was proposed by Bradley and Harper in which the surface instability is described by curvature dependent terms and surface diffusion terms. Nonlinear terms were taken into account in the development of this model by focusing on the roughening [63, 197] and redeposition [87]. In our case, the ultrathin polymer films were suspended on the grid, in which the interaction of defects induced by the irradiation is different from

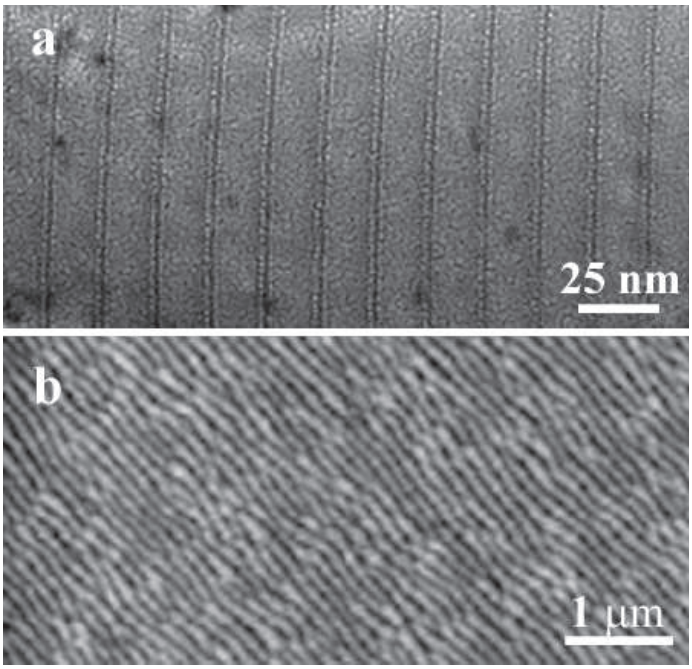


Figure 3.25: Different morphologies induced by the ion beam. (a) Patterns induced by ion beam on the polymer film with well ordered arrays in present work. (b) Patterns induced by ion beam on the bulk surface of Si from reference [24].

those on the surface of bulk materials previously studied (Fig. 3.25). By considering the nature of the effects of irradiation on the thin polymer film, it can be concluded that the main terms determining the formation of the well uniformly ordered patterns can be ascribed to the interaction of defects induced in the polymer films by the ion irradiation.

With respect to the potential application of this technique, we can use these thin patterned films as templates to fabricate the well-ordered metallic and semiconductor nanostructures. Because these ordered patterns come from the interaction of defects, they can provide the nucleation sites for the diffusion atoms, thus leading to the transfer of the patterns to the deposited materials. In order to move into their preferred nuclear sites before they aggregate into spherical shape on the normal surface, a high velocity of diffusion for the deposited atoms was needed. We deposited copper and silicon atoms, for example, on these ordered materials and found that

structures of nanocrystals formed on the film exactly follow the existing patterns (Fig. 3.26). For deposited silicon atoms, well ordered arrays of silicon with wavelength of 7 nm are observed (Fig. 3.26a). These nanolines consisting of deposited atoms are found to be polycrystalline (Fig. 3.26b), made of grains that generally extended across the full length of the striped patterns on the polymer film. The occupied stripes on the polymer films correspond to the defect domains, while the amorphous polymers 2 nm wide among these nanolines is related to the perfect domains of polymer film. Compared to the structure formed by deposited silicon atoms in Figs. 3.26a and b, Fig. 3.26c reveals that the nuclear domains for preferential nucleation sites are periodic structures with two different widths: 7 nm and 25 nm corresponding to the wavelength of Figs. 3.23b and 3.23c. When the spacing among these curves became uniform under the suitable irradiation conditions, we obtain the perfect lattice structure of silicon in Fig. 3.26a. Figs. 3.26d and e show the well-ordered copper dots on the polymer film with the diameter of 7 nm equal to the wavelength of silicon stripes. As it shows in Fig. 3.23c, at the beginning of ripples formation, the stripes induced by ion beam are composed of bundles of small voids. The deposited atoms can preferentially select these voids to nucleate and form well ordered dots. During deposition, the $Ar^+$ ions simultaneously bombard the film at energies of several thousand electronvolts. This ion beam assisted deposition enhances adhesion between deposited atoms and polymer films on the preferential nuclear sites [184].

We also did experiment on the carbon film as shown in Fig. 3.27 using the ion milling system. The exposure time is less than 2 minutes, compared with up to 30 minutes on the polymer film, due to the carbon film is sensitive to the ion beam. The stripe like patterns are observed with the wave length of about 150 nm taken under the defocus mode. Since the erosion rate depends on the local curvature with

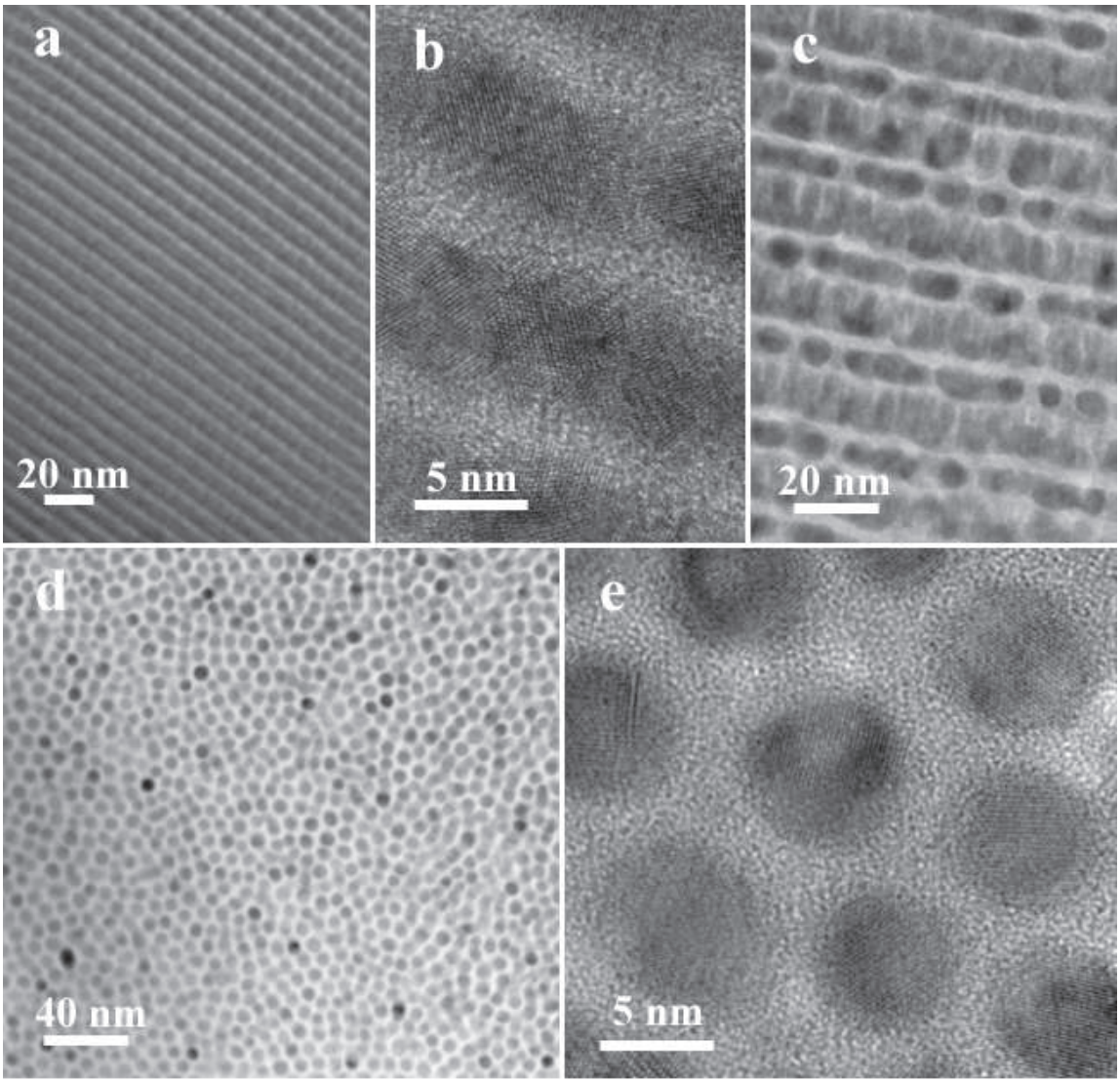


Figure 3.26: The structure of deposited silicon and copper patterns on the thin polymer film. Uniformly sized and shaped arrays of silicon and dots of copper on the scale of 7 nm are evident. (a) Randomly deposited silicon atoms guided by the patterns of film forms highly organized nanostrucutres. (b) HRTEM image of silicon arrays showing polycrystalline structures of copper patterns. (c) Two different widths of strips were observed for the periodic silicon structures, depending on the self-organized patterns of polymer films. (d) Well-ordered copper dots on the thin polymer film. (e) HRTEM image of copper dots.

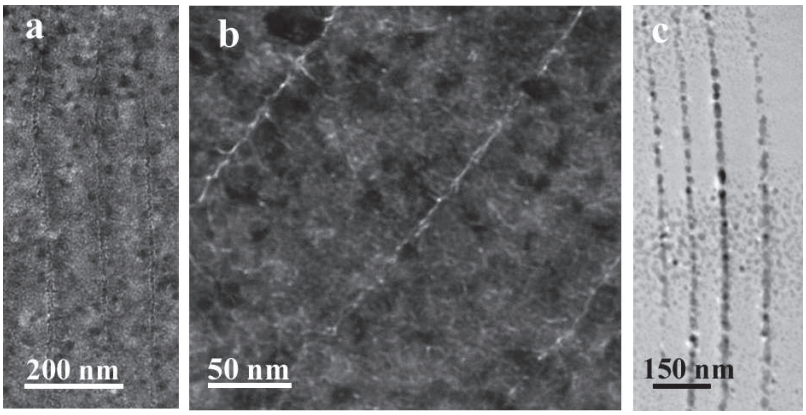


Figure 3.27: Pattern formation on the TEM carbon film. Ordered arrays of carbon on the scale of 150 nm can be observed. (a) Underfocus image of carbon film. (b) HRTEM overfocus image. (c) Image after deposition of copper showing the deposited copper atoms were guided by the patterns induced by the ion beam on the carbon film.

the surface diffusion, Bradley and Harper [64] derived a linear equation for surface morphology evolution by assuming Gaussian distribution of deposited energy. The wave length is given by

$$\lambda \sim 2K^{1/2} \tag{3.44}$$

where $K$ is surface diffusion coefficients. The larger wavelength on the surface of carbon film can be attributed to the easier movement of defects induced by ion beam. Fig. 3.27c shows the image after deposition of copper.

### 3.3.3 Conclusion

In summary, experiments describe a method for creating well-formed patterns through self-organization on the thin films by irradiation. Using these films as templates well-ordered metal and semiconductor nanowires can be fabricated by nucleation of deposited atoms on the preferential sites. This approach illustrated a convenient route for fabricating nanometer scale surface patterns for metals and semiconductors, which may have the potential applications for specific devices.

# CHAPTER IV

# Two Dimensional Pattern Formation under Ion Bombardment

## 4.1 Highly Ordered Ga Nanodroplets on GaAs Surface Induced by Focused Ion Beam Bombardment

With wide applications in sensors, optical devices and magnetic storage media, self-assembled nanostructures have attracted great interests in recent years [19, 66, 76, 154, 198, 199]. Self-assembly is typically induced at temperature below the melting point of particles, resulting in mechanically weak and often thermally and chemically unstable arrays [200, 201]. It is well-known that close to the melting point Ostwald ripening or coalescence often leads to non-uniform particle sizes during particle growth. Here it was shown that this normal physical behavior can be hindered under low energy ion bombardment and highly ordered and uniform hexagonal patterns can be induced. Formation of ordered quantum dots by low-energy ion sputtering on a surface has been reported in several semiconductor systems. Under normal incidence or off normal incidence with simultaneous rotation of the samples, Si [32], Ge [33], as well as a variety of III-V compounds (GaSb [26], InP [28], and InSb [29]) can form quantum dots on the surface. The mechanism involves the balance between roughening and smoothing actions, such as curvature dependent sputtering [63,64,77], thermal diffusion [90], redeposition and ion induced

diffusion [9, 65, 92], and viscous flow [10, 183]. In these processes the cone-like dots come from ion etching of the substrate, thus having the same composition as the matrix and containing high density of defects [26], and the degree of ordering is low. In this chapter, it was shown that, close to the melting point, the dynamic balance of mass loss and gain induced by low energetic ion bombardment can drive particles into highly ordered patterns.

GaAs (zinc blende structure, space group $F\bar{4}3m$) is an important semiconductor and is used to make devices such as microwave frequency integrated circuits, infrared light-emitting diodes, laser diodes and solar cells. The benefit of using GaAs in devices is that it generate less noise than most other types of semiconductor components and, as a result, is useful in weak-signal amplification applications. Furthermore. Unlike silicon cells, GaAs cells are relatively insensitive to heat and very resistant to radiation damage. This, along with its high efficiency, makes GaAs very desirable for space applications. Due to these benefits, GaAs is a suitable replacement for silicon in the manufacture of linear and digital integrated circuits.

### 4.1.1 Experimental

**Formation of GaAs microspikes by focus ion beam**

It has been reported that Ge, GaSb, and InP can form fibers or cones subjected to the ion bombardment [37, 202]. We found that microspikes of GaAs can be created by the focused ion beam (FIB) bombardment at oblique incident angle with ion energy of 30 keV. We suggest that combination of shadowing effect and redeposition contributes to the formation of microspikes.

Commercial available wafers of GaAs single crystal with (100) orientation were bombarded by a dual-beam (FIB+SEM) instrument (FEI Nova 200 Nanolab) at a variety of incident angles. The current of the beam was kept constant at about 5

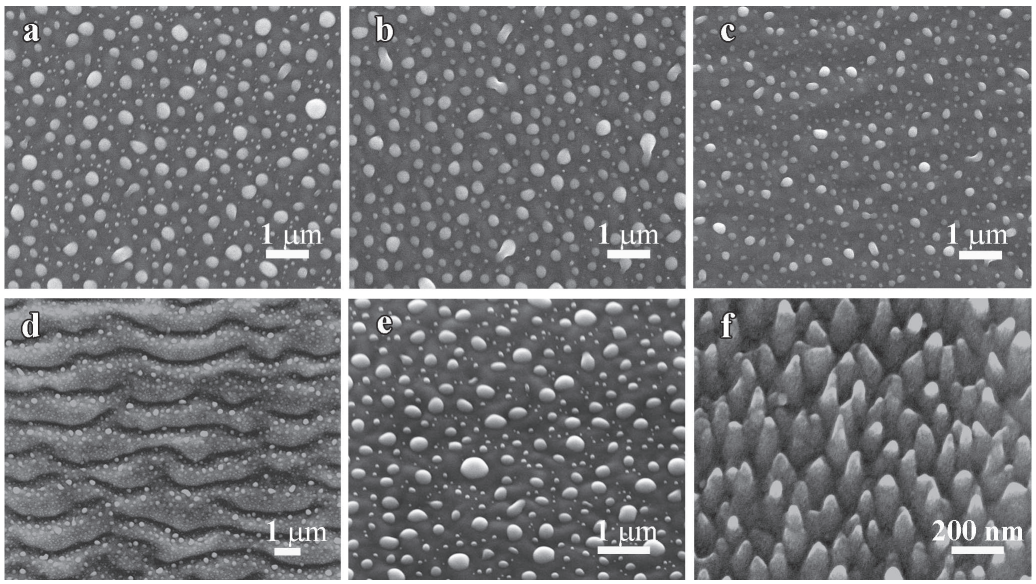


Figure 4.1: SEM images showing the morphological evolution of GaAs upon focused ion beam with a variety of incident angle. (a) Normal bombardment; (b) 20°; (c) 40°; (d) 60°; (e) viewed 52° from normal; (f) 70°. Ion energy 30 keV, flux $1.5 \times 10^{15}$ $cm^{-2}s^{-1}$, bombardment time 4 minutes.

nA with the energy of 30 keV $Ga^{+}$. Fig. 4.1 shows the morphological evolution of GaAs subjected to the FIB at the room temperature for different incident angles with constant exposure time of 4 minutes. For normal bombardment, droplets of liquid Ga were formed on the surface. The mechanism of droplet formation is due to aggregation of Ga on the surface of sample by preferential sputtering of As in GaAs, and additional implanted Ga from FIB. Using monte-carlo simulation (SRIM) shows that the sputtering yield of Ga and As is 3.25 and 6.87 respectively. Due to the balance of sputtering yield between droplet consisting of Ga and plan surface consisting of GaAs, it can be seen that there is a limitation of droplet growth. Furthermore, since the nucleation site is random on the surface, the total free moving Ga atoms on the surface should be shared by these nuclear sites. For incident angle of 30°, we found that droplet is still randomly distributed but the size becomes smaller. Due to shadowing effects, when the sample is tilted, the sputtering area of

plan surface decreases and new balance is obtained, giving rise to the small radius. At incident angle 60°, we observed ripples on which the droplets distributed. At incident angle of 70°, the conical spikes capped by a 40 nm ball were observed from the surface normal. The spikes are roughly aligned in rows with direction parallel to the incident ion. From sputtering theory, we know that the sputtering yield is smaller for positive curvature (sphere) than planar surface [64]. Therefore, at high incident angle, when the sputtering yield is larger for planar surface but is smaller than that for droplets, the shadowing effects occur for the fixed droplets, creating the conical microstructures with the beads at their tips. Fig. 4.2 shows the cross section view of cones on GaAs measured by TEM. The size of sphere is larger than the tip of cones, suggesting the redeposition of sputtered Ga on the original droplets. HRTEM image shows that spike is polycrystal (Fig. 4.2b) and droplet is amorphous. However, from low magnification images, the diffraction contrast image reveals that the droplet with radius of 40 nm is also polycrystal. Such small particle with melting temperature of 29°, becomes amorphous in HRTEM image induced by 300 keV electron beam.

**Formation of highly ordered Ga droplet by focus ion beam**

Commercially available wafers of GaAs single crystal with (100) orientation were used in our work. The ion bombardment experiments were carried out using a scanning electron microscope (SEM) equipped with a focused ion beam (FIB) instrument (FEI Nova 200 Nanolab, $Ga^+$ ion) in a vacuum of $2 \times 10^{-7}$ mbar at room temperature (close to the Ga melting point). The surface morphology was characterized by *in situ* SEM and *ex situ* transmission electron microscopy (TEM).

Fig. 4.3 shows the evolution of droplets on the GaAs surface subjected to 5 keV $Ga^+$ at fluence of $4.5 \times 10^{17}$ $cm^{-2}$ (5 minutes) and various incident angles. At normal bombardment (Figs. 4.3a and 4.3b), droplets with diameter up to 350 nm are

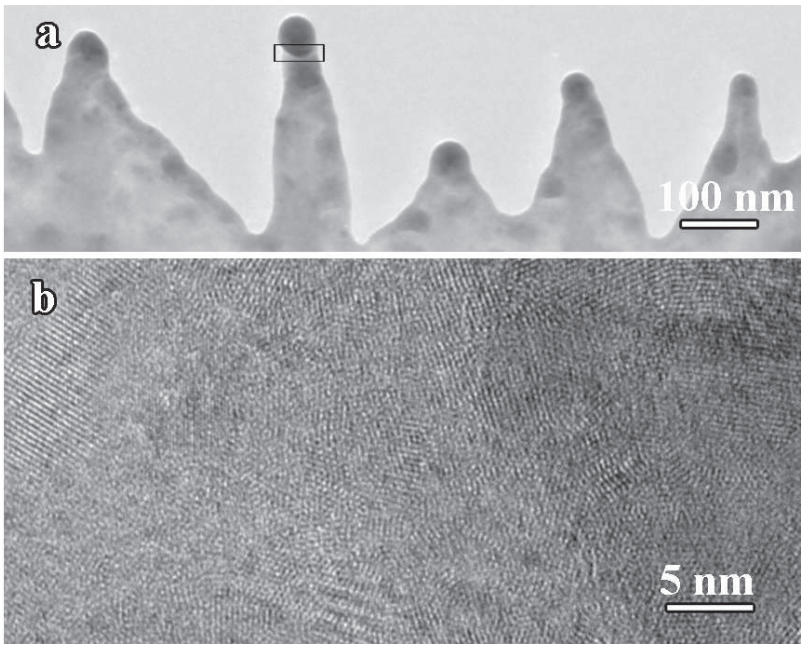


Figure 4.2: TEM images showing the cross-sectional view of cone structure. (a) Bright field image, the area indicted by rectangle showing the HRTEM image in (b). Ion energy 30 keV, flux $1.5 \times 10^{15}$ $cm^{-2}s^{-1}$, bombardment time 4 minutes.

observed, with the droplet size following a Gaussian distribution. The mechanism of droplet formation can be attributed to the preferential sputtering of As and clustering of the remaining Ga on the surface from both substrate and ion implantation. The composition of droplets can be identified as pure Ga by Energy Dispersive x-Ray spectrometry (EDS) analysis of the cross section sample using TEM (Fig. 4.4). *In situ* movies images show these clusters at normal bombardment undergo random walk and encounter collisions accompanied by liquid-like coalescence. The movement of droplets is a result of the dynamic bias from the sputtering of droplets, absorption of atoms along periphery or combination of droplets.

At off-normal bombardment (Figs. 4.3c-h), however, the droplets become uniform and nearly immobile, exhibiting a tendency to form regular sixfold patterns with increasing incident angle. Starting from the appearance of small domain of ordered droplets at low incident angle, the chain of droplets with fairly constant separation is

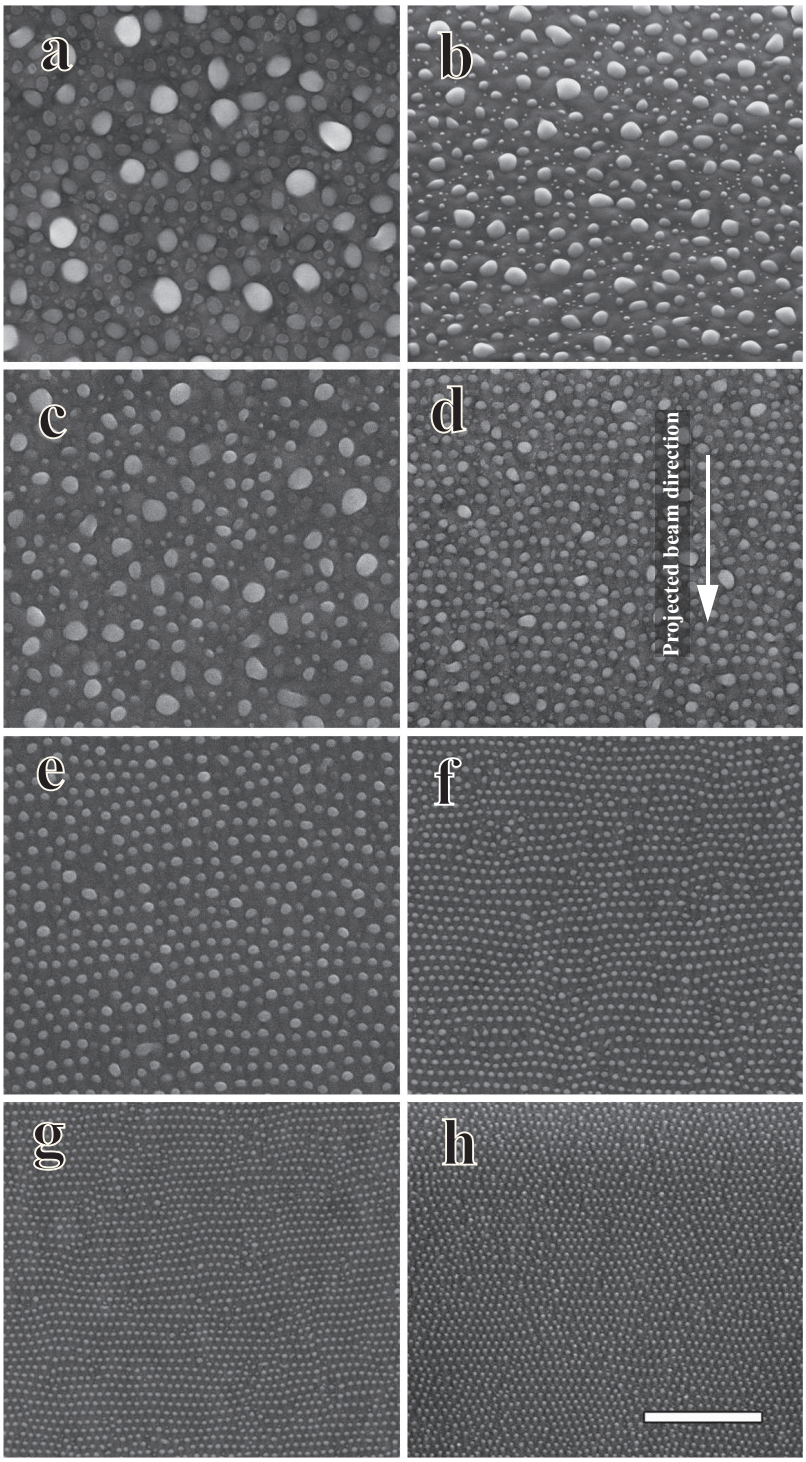


Figure 4.3: SEM images of morphological evolution of GaAs at various incident angles : (a) 0°, (b) 0°, viewed from 52° to sample normal, (c) 20°, (d) 25°, (e) 30°, (f) 40°, (g) 50°, (h) 60°. Ion energy 5 keV, flux $1.5 \times 10^{15}$ $cm^{-2}s^{-1}$, bombardment time 5 minutes, scale bar 1 $\mu$m.

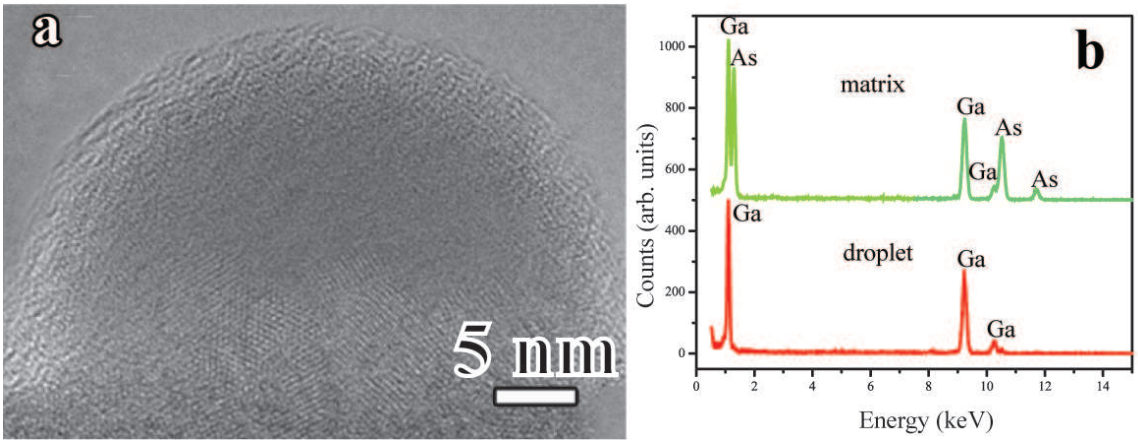


Figure 4.4: (a) Cross-sectional TEM image of one droplet. (b) EDS showing the composition of droplets. Ion energy 5 keV, flux $1.5 \times 10^{15}$ cm$^{-2}$s$^{-1}$, incident angle 35°.

obtained at incident angle larger than 30°. The chains of droplets which are always perpendicular to the projected ion beam direction shows that ordering is independent of the orientation of the substrate (Fig. 4.5). We observe through *in situ* movies that Brownian motion at normal bombardment is replaced by slightly directional walk at off-normal bombardment: a movement towards the projected ion beam direction in a zigzag manner.

The temporal evolution of highly ordered dot is investigated at fixed incident angle, energy and flux (Fig. 4.6). At an ion fluence of $3 \times 10^{16}$ cm$^{-2}$, equivalent to an exposure time 20 s, small dots with an average diameter of 50 nm appear, without preferred orientation and ordering. Further bombardment for 40 s, up to fluence of $9 \times 10^{16}$ cm$^{-2}$, leads to visible short range ordering (Fig. 4.6a). Continuous bombardment extends the ordered domain to the whole area. The edge dislocation is evident in the image (Figs. 4.6b and c).

Conditions for formation of ordered patterns can be summarized in Table 4.1

The evolution of wavelength and ordering of patterns can be well characterized by power spectral density (PSD) calculated from Fourier transform of the intensity of

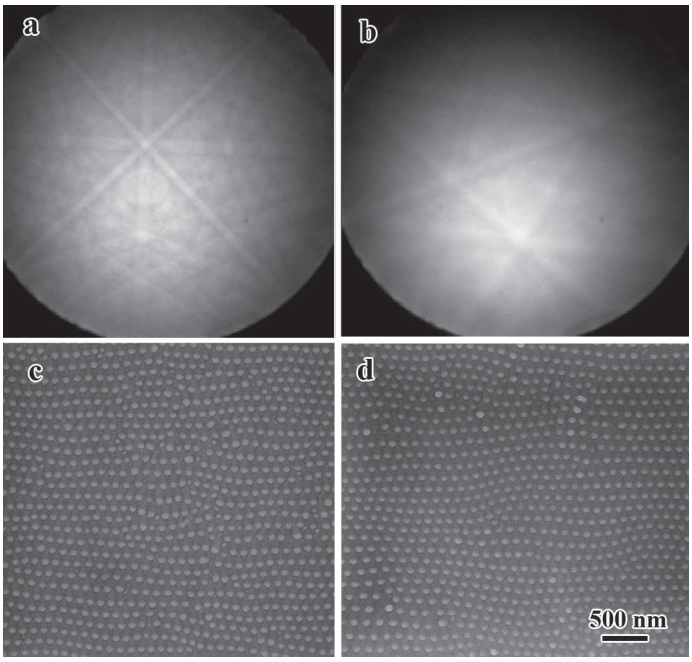


Figure 4.5: (a) and (b) Two different orientations of samples measured from EBSD (Electron Backscatter Diffraction). (c) and (d) Ordered pattern formation induced by ion bombardment from (a) and (b) respectively. Ion energy 5 keV, flux $1.5 \times 10^{15}$ $cm^{-2}s^{-1}$, bombardment time 5 minutes, incident angle 35°.

Table 4.1: Conditions for ordered pattern formation on $Ga^+$ irradiated GaAs

| Energy (keV) | Incident angle | Ordered pattern |
|---|---|---|
| 30 | $> 70°$ | ripples+randomly distributed Ga droplet |
| 20 | $> 70°$ | ripples+randomly distributed Ga droplet |
| 10 | $> 60°$ | ripples+randomly distributed Ga droplet, or hexagonally ordered Ga droplet |
| 5 | $> 30°$ | hexagonally ordered Ga droplet |

images. The angularly averaged PSD for various incident angles is shown in Fig. 4.7. The peaks are apparent for incident angle exceeding 23°, indicating that the surface features are highly ordered. The position of peaks in the PSD functions shows an average wavelength of patterns. The shift of peak position toward the larger wave number with the incident angle indicates the decrease of wavelength and particle size.

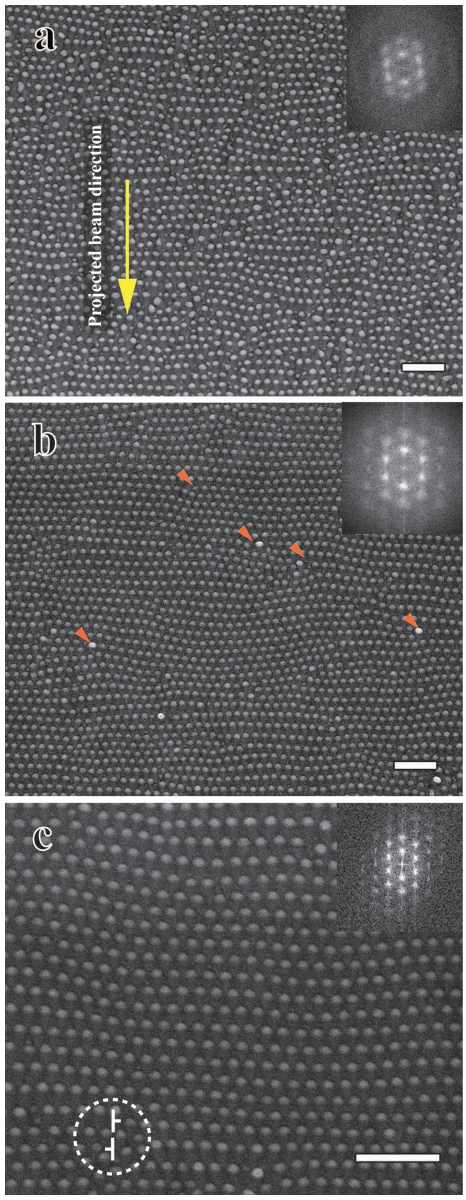


Figure 4.6: Droplet development at various bombardment time (SEM images): (a) 1 minute, (b) 20 minutes, (c) 30 minutes. High density of edge dislocations can be identified in (b), as indicted by small arrows. Insets are the Fast Fourier Transformation (FFT) spectrum. Dashed circle in (c) shows two opposite edge dislocations. Ion energy 5 keV, flux $1.5 \times 10^{15}$ cm$^{-2}$s$^{-1}$, incident angle 35°, scale bar 500 nm.

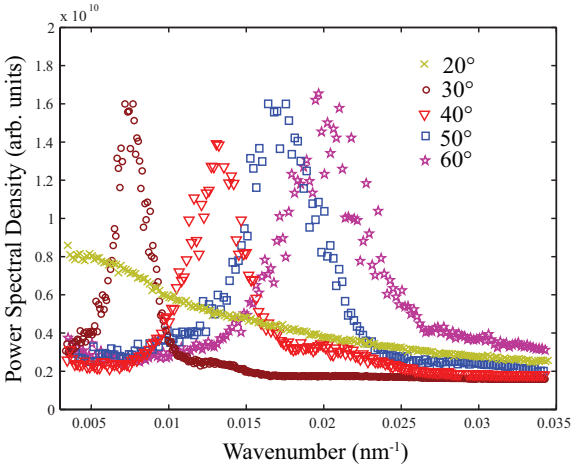


Figure 4.7: Evolution of radial power spectral density obtained from SEM images. The shift of peak position towards larger wavenumber with the incident angle reveals the decrease of wavelength.

### 4.1.2 Model

The mechanism underlying the pattern formation can be understood on the basis of sputtering and mass transportation. First, we should explain why the uniform droplets can be produced at off-normal bombardment. We know that the size of droplets is determined by the competition between the loss of atoms from the droplet induced by sputtering and gain of atoms supplied by the substrate. At off-normal bombardment, we can assume each droplet is surrounded by a local capture area or denuded zone in which all the Ga atoms generated in this zone is collected by surrounded droplet. For simplicity, the denuded zone is assumed to be a circle with radius of $\lambda$. If we further assume that accommodation coefficients are unity, at steady state, we have two balances: in the denuded zone, the loss of atoms to the droplets is compensated by the production within this area; for the droplet, all the atoms generated in the denuded zone is equal to the number of sputtered atoms from the droplet. The first condition gives a equation describing the evolution of radius with

respect to time. The quasi-stationary approximation is

$$\frac{dR}{dt} = A\left(1 - \frac{R^*}{R} + BR^2\right) \tag{4.1}$$

where $R$ is the droplet radius, $A$ is a positive parameter, $R^*$ is critical radius without sputtering, $B$ is a sputtering dependent parameter. This equation is determined by the solution of the diffusion equation in polar coordinations with a source term representing production of the Ga atoms within the capture volume. If $B = 0$, Eq. 4.13 reduces to a standard kinetic equation describing the process of Owstwald ripening driven by capillary induced diffusion with the mass conservation [203]. If we consider the sputtering on the droplet, we find $B < 0$. The growth rate starts to change from positive to negative when the radius reaches a certain value. This means that the radius can reach a steady state, leading to the uniform droplets. This mechanism is the key issue for the ordered pattern formation.

Another balance, where all the production of Ga atoms in the capture surface are absorbed by the droplet and these absorbed Ga atoms are equal to the sputtered Ga atoms on the surface of droplet, can demonstrate the relationship between droplet and its denuded zone. For off-normal bombardment with incident angle $\theta$, by considering shadow effects, we have equation

$$\frac{\lambda}{R} = \sqrt{4\alpha + \cos^{-1}\theta} \tag{4.2}$$

where $\alpha = (Y_{Ga} - 1/2)/(Y_{Ga} + 2\zeta)$, $Y_{Ga}$ is the sputtering yield of pure Ga bombarded by Ga ions, $\zeta$ is the implanted Ga ions fraction on the substrate surface. Taking $Y_{Ga} \approx 5$ [80], $\zeta = 0.1$ [204], we get $\lambda/R = 2.2 \sim 2.4$ for incident angle $30^\circ \sim 65^\circ$. This result is in excellent agreement with the experimental observations as shown in Fig. 4.8.

Inside exclusion area, the length $\lambda$ is characterized by the half mean diffusion

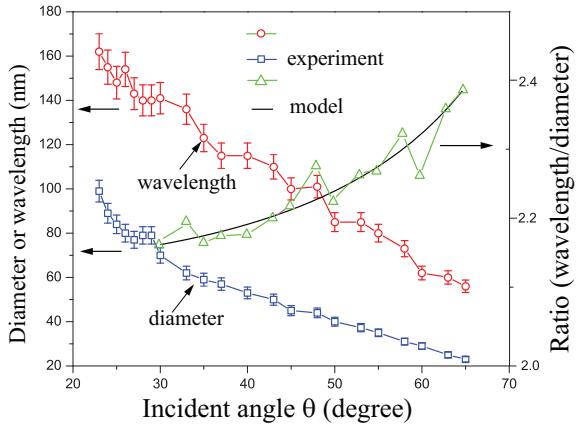


Figure 4.8: Evolution of droplet diameter and wavelength with incident angles and comparison of model with experimental data for the ratio of diameter to wavelength.

distance $\sqrt{D\tau}$, where $D$ is ion-enhanced diffusion coefficient, $\tau$ is the average life time of atoms. The normalized flux $(f/D)^{-\psi}$ is used to describe the scaling property of mean diffusion length, where $f$ is flux of deposition. The value of $\psi$ is $1\sim1/6$, depending on the ratio of $f/D$ [170]. If we consider the production of Ga atoms on the surface induced by the ion beam as deposition process, the decrease of droplet radius with the incident angle can be ascribed to the flux increasing with incidence.

Motivated by the convection induced self-assembly of colloidal particles [205] and one dimensional interstitial diffusion induced void lattice inside metals by high energy ion bombardment [93, 96], we propose a model for self-assembly based on directional mass loss and gain. It is known that for low energy etching the average energy distribution approximately satisfy the Gaussian distribution [77]. At normal bombardment, the energy deposited on the surface is isotropy for sputtering. Thus there is no preferential migration direction for Ga atoms on the surface of GaAs induced by the ion beam, giving rise to the random walking of droplets. At off-normal bombardment, however, the deposited energy on the surface is anisotropic: it has a symmetry axis perpendicular to the projected ion beam direction, but along the projected bean

direction there exists a net force acting on the Ga atoms in a manner analogous to the wind on the surface of water (Fig. 4.9a). This driving force tends to push the Ga atoms moving along the projected ion beam direction. On the other hand, the loss of atoms by sputtering on the surface of droplet is also directional: on the part of droplets which faces the ion beam direction. In addition, because of shadowing and exclusion zone effects, only migrating atoms generated between the droplets can have much higher flux to reach the droplets in an adjacent chain. Therefore, the supply of atoms can drive the droplets to adjust their position to the site which can obtain the largest source as shown in Fig. 4.9b. The center of mass driven by the competition of supply and loss of Ga atoms can move towards the projected ion beam direction in a zigzag manner as we observed in *in situ* electron microscopy. For a long time bombardment, when the droplets finish adjusting their position, the hexagonal pattern can be formed by the interaction of sputtering and anisotropy mass transport. High density of droplets, uniform size and mobility which are prerequisites for the formation of patterns are successfully fulfilled by the ion beam [206].

The ripple formation and ripple-nanodot transition can be explained by Bradley-Harper model or extended models [63, 64, 92]. These models are based on instability of surface and only apply to the patterns which are of the substrate material. In our case, the dots which are liquid and separated from substrate have the different composition with substrate. Under off-normal bombardment without rotation of sample, no Ga ripple was observed, which is contrary to the predictions of Bradley-Harper model. Our model is based on high density of dots on the surface. It can apply to patterns whose density is high enough that small adjustment can lead to the hexagonal pattern formation, similar to void lattice formation and highly ordered colloidal particle formation.

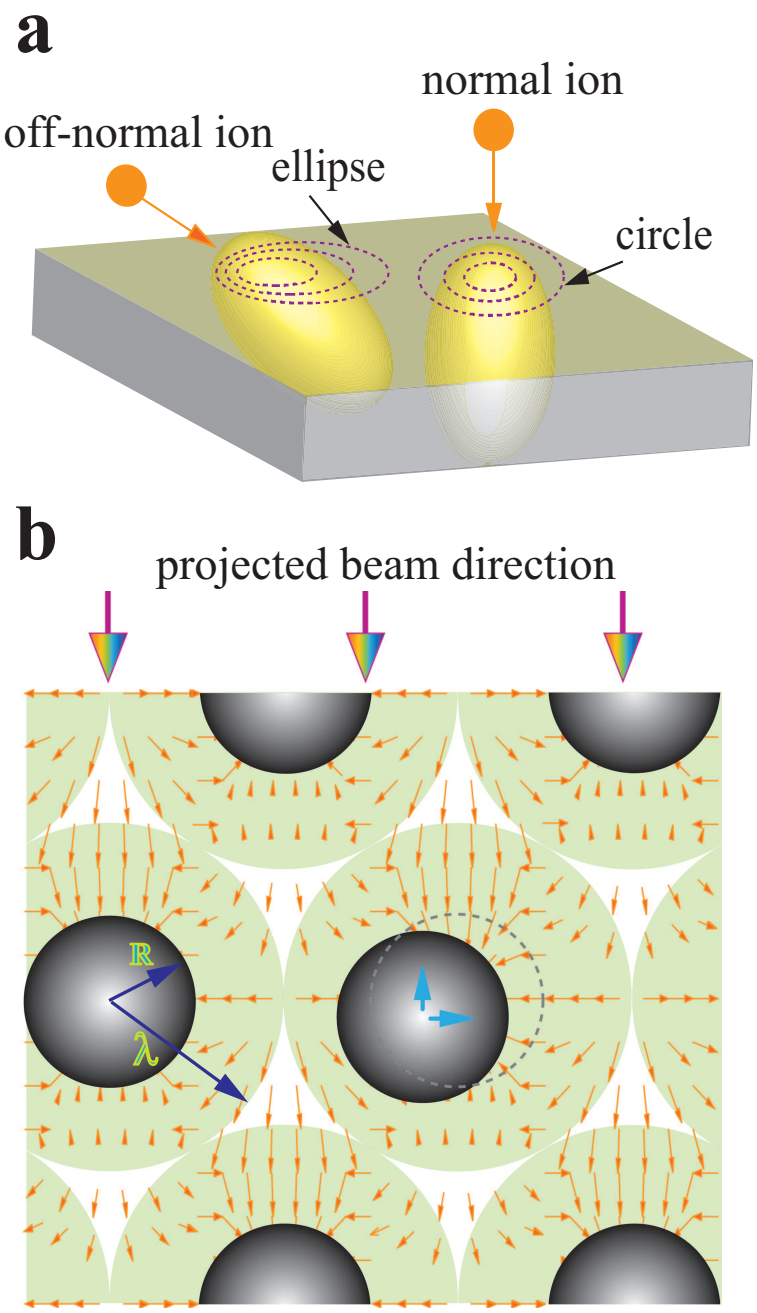


Figure 4.9: Schematic illustration of a model for the formation of ordered droplet patterns. (a) Average energy distribution for ion bombardment. For normal bombardment, the deposited energy on the surface is circular, while for off-normal bombardment it is elliptical where the energy contour along the projected beam direction is longer than other directions. The dashed red curves represent the equal energy contours. (b) Atom supply and movement directions that cause an off-center particle to move to the center of nanoparticle lattice. Small red arrows represent the direction and magnitude of local Ga atom migration induced by the ion beam on the substrate surface, radial dark shaded circle denotes the droplet with the exclusion zone given by light green, pure cyan arrows indicate the movement direction of droplets, dashed circle shows the final position of partially aligned droplets.

### 4.1.3 Discussion

**Preferential sputtering**

The mechanism of droplet formation can be attributed to the preferential sputtering of As [207] and clustering of the remaining Ga on the surface from both substrate and ion implantation. The theoretical work of preferential sputtering for two-compound system was conducted by Anderson and Sigmund [208]. For amorphous surface, the sputtering yield, defined as the number of surface atoms removed per incident ion, is proportional to the binding energy of pure elements and surface concentration [209, 210]. In our system, $Y_{Ga} = 2Y^*_{Ga} = Y^*_{As}$ [80, 204, 207], where $Y_{Ga}$ is the sputtering yield of pure Ga bombarded by Ga ions, $Y^*_{Ga}$ is the partial yield of Ga for compound GaAs, and $Y^*_{As}$ is the partial yield of As for compound GaAs. As shown in TEM images, there is an amorphous layer with 5∼7 nm thickness on the surface of GaAs under the bombardment of $1 \times 10^{15}$ cm$^{-2}$. Therefore, it is reasonable to assume that the surface of GaAs is disordered and satisfies the requirement of model proposed by Anderson and Sigmund [208]. Because the sputtering removes both target and implanted atoms, with the receding of the sample surface, the initial Gaussian shaped distribution of implanted atoms overlap, leading to an increase of concentration of implanted atoms at the surface. By considering both preferential sputtering and high dose implantation, the flux of Ga atoms on the surface induced by the Ga beam can be approximated as

$$Y = \frac{1}{2} Y_{Ga} I \cos^{-\gamma+1}\theta + \zeta I \tag{4.3}$$

where the first term on the right hand is due to preferential sputtering and second term is from implanted Ga atoms, $I$ is the ion flux, $\theta$ is the incident angle, the exponent $\gamma$ depends on the mass of ion and atom. Detailed calculations of $\gamma$ involve the average depth straggling of ions in the target and show that $\gamma \approx 1 \sim 2$ [117]. $\zeta$

is the implanted Ga ions fraction on the substrate surface, which can be derived as following: In the steady state under preferential sputtering conditions, the surface concentration can be found as [180]

$$f = (Y_I/Y_{As})[(\zeta/\zeta_{As})^{-1}] \tag{4.4}$$

where $f$ is the ratio of the sputtering yield of Ga atom to that of As atom, $Y_I$ and $Y_{As}$ are the partial yields for implanted Ga ion and As atom in matrix, $\zeta$ and $\zeta_{As}$ are the concentrations. At steady state $Y_I = 1$, $\zeta + \zeta_{As} = 0.5$, we have $\zeta = 0.5/(1 + fY_{As})$. Taking $f = 2$, $Y_{As} = 2$ [80], we have $\zeta = 0.1$.

**Droplet growth**

We suppose each nucleus to be three dimensional and of the shape of a spherical cap. The diffusion equation for the atoms is to be solved in the annular spherical shell $R \leq r \leq \lambda$, where $R$ is the radius of droplet, $\lambda$ is the radius of denuded zone. The concentration of point particles at radial position $r$ in the capture volume at time $t$ is $C(r, t)$ in unit of atoms per unit area. The choice of the capture volume implies there is no accumulation of Ga atoms between droplets. The concentration $C(r, t)$ is determined by the solution of the diffusion equation in polar coordinations with a source term representing production of the Ga atoms within the capture volume. For $r > R$, the diffusion equation is given by:

$$\frac{\partial C}{\partial t} = \frac{1}{r}\frac{\partial}{\partial r}\left[rD\frac{\partial C}{\partial r}\right] + Y \tag{4.5}$$

where $D$ is the diffusion coefficient of the Ga atoms and $Y$ is Ga flux given by Eq. 4.3. In order to make comparison with growth mechanism driven by Ostwald ripening, here we assume diffusion dominance for simplicity.

At the steady state, the migration of atoms to the droplets is compensated by the

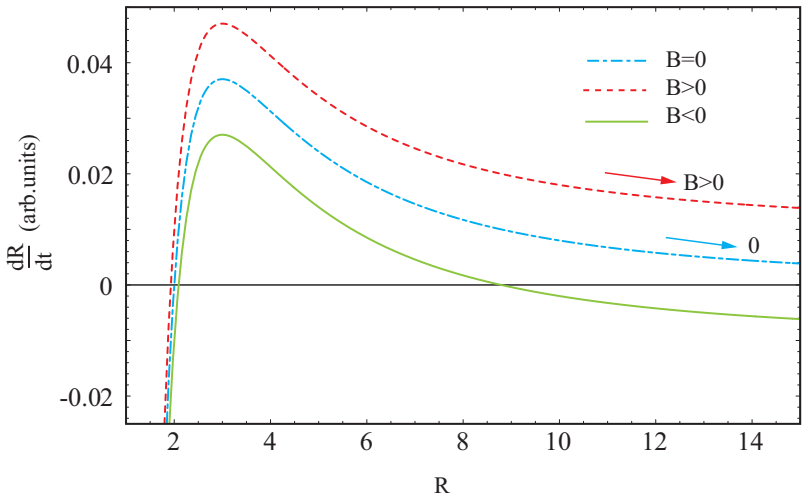


Figure 4.10: Growth rate as a function of radius for different conditions. $B = 0$ for mass conservation growth, $B = 0.01$ for growth with source, $B = -0.01$ for growth with sink larger than source. $R^* = 1$.

production within the capture volume. This quasi-stationary approximation gives

$$\frac{1}{r}\frac{\partial}{\partial r}\left[rD\frac{\partial C}{\partial r}\right] = -\frac{1}{2}(Y_{Ga} + 2\zeta)I \tag{4.6}$$

Here we substitute Eq. 4.3 and assume $\gamma = 1$ (taking the other $\gamma$ will not change the form). The solution of this equation gives

$$C(r) = K_1 \ln r + K_2 - \frac{(Y_{Ga} + 2\zeta)Ir^2}{8D} \tag{4.7}$$

The boundary conditions are

$$\begin{aligned} C(r) &= C_R \text{ at } r = R \\ C(r) &= C_\lambda \text{ at } r = \lambda \end{aligned} \tag{4.8}$$

Thus, the number of atoms attached per second by surface diffusion is

$$J = 2\pi R\left[D\frac{dC}{dr}\right]_{r=R} \tag{4.9}$$

Substituting Eqs. 4.7-4.8 into Eq. 4.9 yields

$$J = \frac{2\pi D(C_\lambda - C_R)}{\ln\left(\frac{\lambda}{R}\right)} + \frac{R^2(Y_{Ga} + 2\zeta)I\pi}{2}\left[\frac{\left(\frac{\lambda}{R}\right)^2 - 1}{\ln\left(\frac{\lambda}{R}\right)^2} - 1\right] \tag{4.10}$$

where two terms on the right hand of equation are positive for $\lambda/R > 1$. According to Gibbs-Thomson relationship, the equilibrium concentration $C_R$ is given by

$$C_R = C_0 + C_0 \left(\frac{2\Omega\gamma}{kT}\right)\frac{1}{R} \tag{4.11}$$

where $C_0$ is the concentration in equilibrium with a flat surface, $\Omega$ is atomic volume of Ga, $\gamma$ is nucleus-vapor interfacial tension, $k$ is Boltzmann constant, T is the absolute temperature. The rate equation is

$$\frac{d}{dt}\left[\frac{2\pi R^3}{3}\right] = (J - 2\pi R^2 Y_{Ga} I + \pi R^2 I)\Omega \tag{4.12}$$

where the term on the left hand is the variation of droplet volume with time, the second term in the parentheses on the right hand of equation is from sputtering of droplet due to ion bombardment, the third term is the rate of implanted ion in droplet. In our experiment, the contact angle for Ga droplet on the GaAs surface is close to 90°, which is smaller than that reported in the literature due to the amorphous surface of GaAs. Substituting Eqs. 4.10-4.11 into Eq. 4.12 gives

$$\frac{dR}{dt} = A\left(1 - \frac{R^*}{R} + BR^2\right) \tag{4.13}$$

where

$$\begin{aligned} A &= \frac{D(C_\lambda - C_0)\Omega}{R^2 \ln\left(\frac{\lambda}{R}\right)} \\ R^* &= \frac{2\Omega\gamma C_0}{kT(C_\lambda - C_0)} \\ B &= \frac{(Y_{Ga} + 2\zeta) I \ln\left(\frac{\lambda}{R}\right)}{4D(C_\lambda - C_0)} \left[\frac{\left(\frac{\lambda}{R}\right)^2 - 1}{\ln\left(\frac{\lambda}{R}\right)^2} - 1 - 4\left(\frac{Y_{Ga} - 0.5}{Y_{Ga} + 2\zeta}\right)\right] \end{aligned} \tag{4.14}$$

As growth proceeds, the area for creating diffusion atoms decreases while the sputtering area increases. Because the sputtering is proportional to the square of radius, the growth of radius leads to the sputtering dominant, giving rise to the

negative growth rate (Fig 4.10), and then the decrease of radius occurs. Thus the uniform size of droplets can be formed for long time bombardment. The balance between sputtering and supplies of atoms determine the limitation of radius. This is the key issue for the ordered pattern formation.

Another balance can be obtained by considering that all the production of Ga atoms in the capture surface are absorbed by the droplet and these absorbed Ga atoms are equal to the sputtered Ga atoms on the surface of droplet. If we consider shadowing effects on both droplets and matrix, we have

$$\frac{1}{2}\pi\left(\lambda^2 - \frac{R^2}{\cos\theta}\right)(Y_{Ga} + 2\zeta)I = 2\pi R^2(Y_{Ga} - \frac{1}{2})I \tag{4.15}$$

Here we assume that shadow area is $R^2/\cos\theta$ for droplet. Solving Eq. 4.15 gives

$$\frac{\lambda}{R} = \sqrt{4\alpha + \cos^{-1}\theta} \tag{4.16}$$

where $\alpha = (Y_{Ga} - 1/2)/(Y_{Ga} + 2\zeta)$. Taking $Y_{Ga} \approx 5$ [80], $\zeta = 0.1$, we get $\lambda/R = 2.2 \sim 2.4$ for incident angle $30^\circ \sim 65^\circ$.

**Morphology evolution at various fluences, energies, and incident angles**

Fig. 4.11 shows the SEM images of surface evolution of GaAs (100) subjected to 30 keV $Ga^+$ at normal incidence with varying exposure time. The distribution of droplets remains constant even after bombardment of 1.5 hour (corresponding fluence of $8.1 \times 10^{18}\text{cm}^{-2}$). A balance between supplies of Ga atoms from GaAS surface and loss of Ga atoms from Ga droplet surface is achieved after 2 minutes (Fig. 4.11 c). After a sputtering time ~20 s, corresponding to a fluence $\sim 3 \times 10^{16}$ $\text{cm}^{-2}$, the randomly distributed droplets with diameter from 30 nm to 150 nm are observed. As the sputtering proceeds, the coarsening process occurs, in which small particles shrink and disappear while larger particles grow with increasing time.

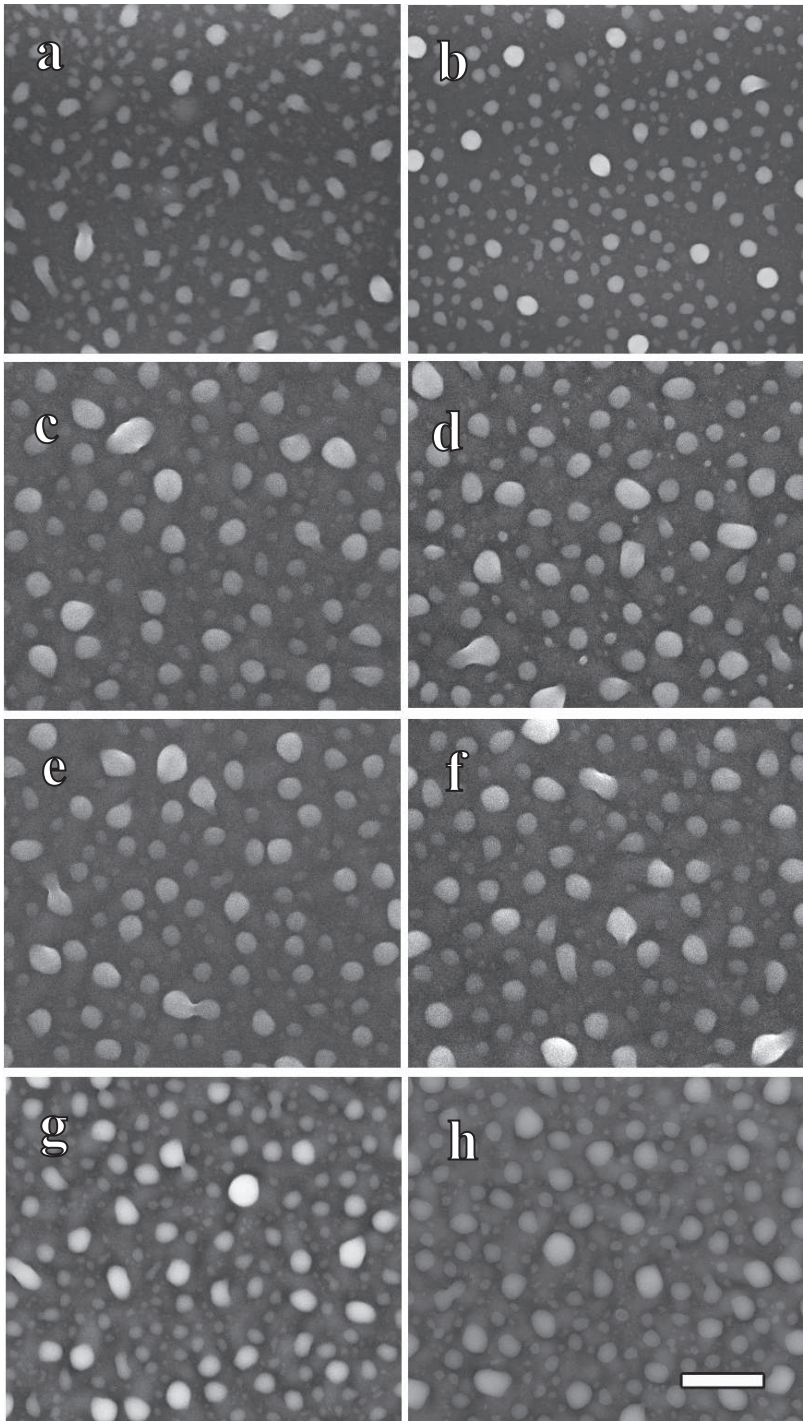


Figure 4.11: SEM images showing the droplet formation induced by 30 keV $Ga^+$ ion beam under normal incidence with the different exposure time. (a) 23 s, (b) 25 s, (c) 2 minute, (d) 3 minutes, (e) 10 minutes, (f)15 minutes, (g) 1 hour, (h) 1.5 hours. The flux is $1.5 \times 10^{15}$ $cm^{-2}s^{-1}$, the scale bar is 1 $\mu$m.

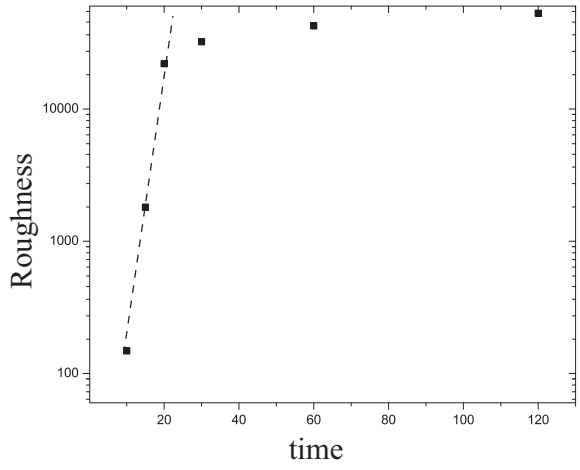


Figure 4.12: Surface roughness as a function of bombardment time induced by 30 keV $Ga^+$ ion beam under normal incidence. The flux is $1.5 \times 10^{15}$ $cm^{-2}s^{-1}$.

Droplet aggregate can be found in the images. However, after a sputtering time ∼60 s, corresponding to a fluence $\sim 9 \times 10^{16}$ $cm^{-2}$, opposite direction compared with the Ostwald ripening happens, in which the size of droplets slightly decreases and becomes uniform. The dot structure with a narrower distribution can be discerned with the increasing sputtering time. The sphere shape of droplets can be clearly observed in Fig. 4.11(h). For prolonged sputtering (sputtering time is 1.5 hours, corresponding fluence of $5.4 \times 10^{18} cm^{-2}$), the size and distribution of droplets remains constant, which means a saturation is achieved (Fig. 3.22(g)). The root-mean-square roughness (W) of surface, which gives the droplet amplitude, with ion fluence deduced from AFM data are plotted in Fig. 4.12. For low ion fluence, up to $3 \times 10^{17}$ $cm^{-2}$, the growth of surface satisfy exponential scaling properties. After ion fluence of $6 \times 10^{17}$ $cm^{-2}$, the surface morphology reaches a stationary state, i.e. the size, density, and roughness of droplets keep constant for further bombardment. These observations are consistent with the results shown by SEM images in Fig. 4.11.

As shown in fluence dependent droplet formation, before saturation, the size of droplet is larger for higher flux (Figs. 4.11(a) and (b)). If we fixed the exposure

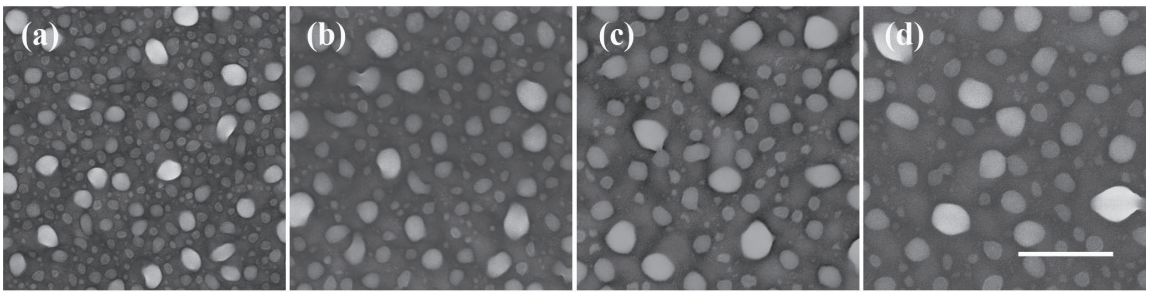


Figure 4.13: SEM images of surface morphology at normal incidence with ion energy (a) 5 keV, (b) 10 keV, (c) 20 keV, (d) 30 keV. The fluence is $4.5 \times 10^{17}$ cm$^{-2}$, the scale bar is 1 $\mu$m.

time, the surface morphology is the same for different flux. After saturation. the development of surface is flux independent as shown in Figs. 4.11(c) and (d).

Energy dependence of surface morphology was also examined at normal bombardment for the fixed flux and fluence. Fig. 4.13 shows the droplet patterns for ion sputtering at energies of 5, 20 , 20 and 30 keV, respectively. We set fluence to be high enough so that surface reaches its saturation state at each energy. As the ion energy increases from 5 keV to 30 keV, the size and roughness of droplets increase. The size distribution of droplet tends to have a narrow range at low energy.

Incidence angle dependent droplet evolution at 10 keV and 30 keV was also studied. We observed periodic patterns for energy of 10 keV when the incident angle is about 60° (Fig. 4.14). The degree of ordering is the same as that for 5 keV but with larger droplets. For energy larger than 10 keV, although the droplets become uniform and smaller with increasing incident angle, no ordered droplets can be observed (Fig. 4.15). Fig. 4.15 shows the droplet evolution with the incident angle at fixed energy 30 keV and fluence $4.5 \times 10^{17}$ cm$^{-2}$. The uniform droplets with radius of 35 nm are formed at incident angle of 70°.

*Ex situ* atomic force microscopy (AFM) measurements were carried out in tapping mode under ambient condition using phosphorus-doped Si cantilevers (Nanoscope

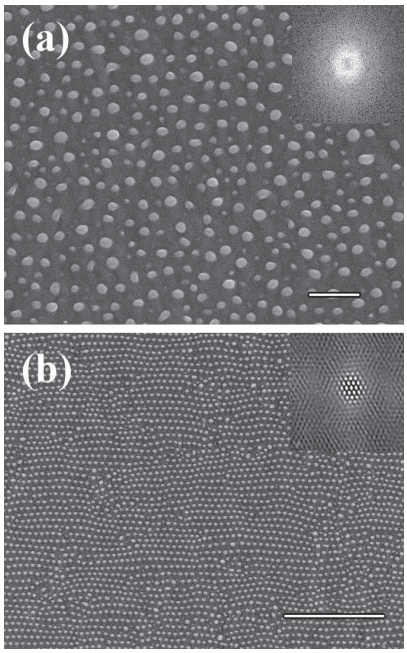


Figure 4.14: SEM images of droplet evolution for 10 keV ion energy at incident angle (a) 50° and (b) 60°. Insert in (a) is the FFT spectrums. Insert in (b) is the corresponding two-dimensional autocorrelation revealing the regularity and hexagonal ordering of dots. The fluence is kept constant at $4.5 \times 10^{17}$ cm$^{-2}$, scale bar is 2 $\mu$m.

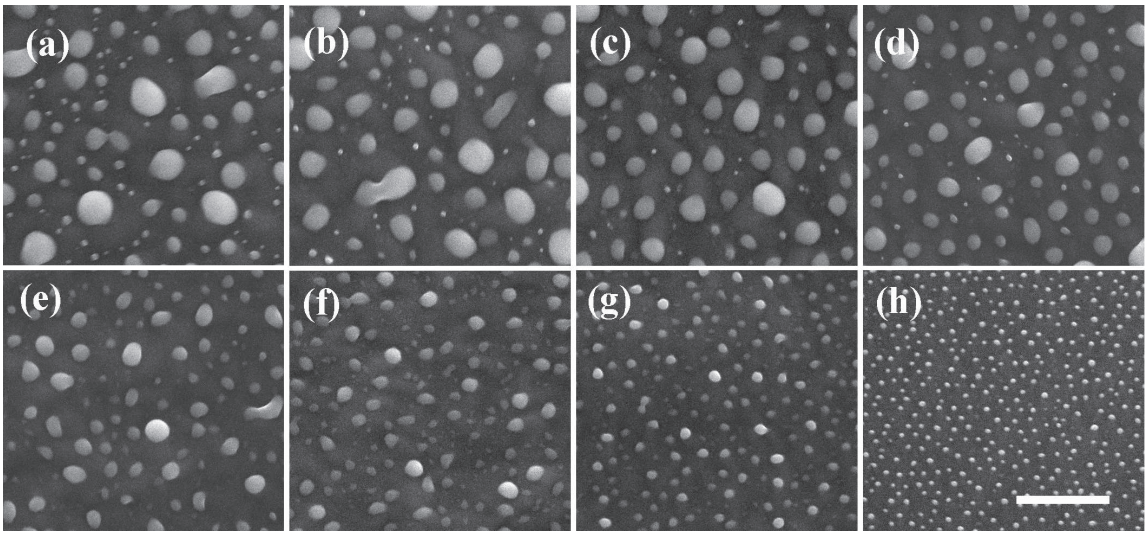


Figure 4.15: Morphological evolution of GaAs for 30 keV at various incident angles (SEM images): (a) 0°, (b) 10°, (c) 20°, (d) 30°, (e) 40°, (f) 50°, (g) 60°, (h) 70°. The energy is 30 keV, the fluence is $4.5 \times 10^{17}$ cm$^{-2}$, the scale bar is 1 $\mu$m.

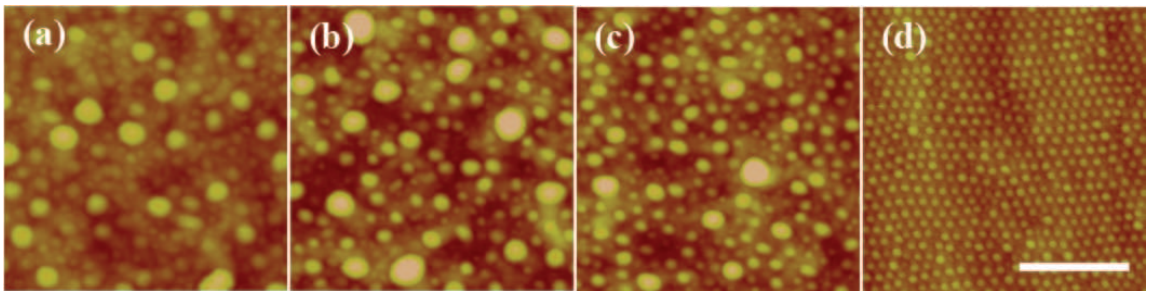


Figure 4.16: AFM images of ordered pattern formed with ion energy 5 keV and bombardment time 300 s at incident angle: (a) 0°, (b) 10°, (c) 20°, (d) 40°. The scale bar is 1 $\mu$m.

IV) (Fig. 4.16).

### 4.1.4 Conclusion

In conclusion, formation of a highly ordered, hexagonal pattern of Ga nanodroplets on the surface of single crystal GaAs induced by off-normal FIB without sample rotation has been characterized. it was proposed, at the melting point, the dynamic balance of directional mass loss and gain can drive droplets into highly ordered patterns. The sputtering induced droplet patterns presented here have potential applications in investigating fundamental physical phenomena, such as sputtering effect on the deposition, diffusion and aggregation model.

## 4.2 Self-assembly of Ordered Semiconductor Nanoholes via Ion Sputtering

Low energy ion bombardment on the materials surface can lead to the development of periodic patterns such as ripples, quantum dots, and nanodroplets [19,26,33,72,87]. This self-organized phenomenon displays a new rout for fabrication of ordered patterns over large-area in a short processing time in nanoscale beyond the limits of lithographic method. Generally, the formation and evolution of surface structure induced by energetic ions are determined by mechanisms which control the species

concentration on the surface [9,72,87,126]. To date four main mechanisms have been considered: sputtering, surface diffusion, redeposition, and viscous flow [23,63,64,92]. Because all these effects are surface profile dependent, for simplicity, small slope approximation was proposed and thus linear continuum equation was established for the explanation of morphology evolution at very beginning [64]. Therefore, it is believed that a dynamic balance between roughening due to curvature dependent sputtering and smoothing due to transport of mobile defects on the surface can attribute to the pattern evolution for a short time radiation. With bombardment proceeding, nonlinear effects start to dominate the surface dynamics and nonlinear equation was developed by considering surface profile changes [63, 87, 211]. For well ordered quantum dot formation under normal bombardment, it was found that, besides roughening and smoothing, redeposition plays a critical role in self-assembly. It was proposed that damped Kuramoto-Sivashinsky (DKS) growth model can successfully predict ordered dot formation [26, 27, 32, 212]. According to this model, the sign of nonlinear terms determines the dot or hole formation: positive nonlinear terms controls hexagonally ordered dot formation while negative nonlinear terms predicts hexagonally hole formation [88, 213]. However, to date experimental observation of highly ordered hole formation has been lacking. In this section, we report that hexagonally ordered holes on the Ge surface can be formed under low energy bombardment at normal incidence. Simulations of the evolution of surface morphology on the basis of damped Kuramoto-Sivashinsky (DKS) growth model have been performed to facilitate the interpretation of the experimental findings.

#### 4.2.1 Experiment and results

The commercial available Ge with (100) orientation was used in our experiment. The ion bombardment experiments were carried out using a focused ion beam (FIB)

instrument (FEI Nova 200 Nanolab, $Ga^+$ ion) equipped with a scanning electron microscope (SEM). The surface morphology was characterized by *in situ* scanning electron microscopy (SEM) and *ex situ* transmission electron microscopy (TEM) and atomic force microscopy (AFM). Fourian fast transformation (FFT) and power spectral density (PSD) were calculated to identify the ordering. Under normal bombardment with ion energy larger than 5 keV, worm-like structures were developed on Ge surface with large aspect ratio. When the energy is 5 keV, however, highly ordered hole arrays can be achieved. Fig.4.17 shows SEM images of a typical nanohole pattern induced on a (100) Ge surface by 5 keV ($Ga^+$) focused ion beam bombardment for 5 minutes. A perfect hexagonal arrangement of holes are observed within domains with size of 500 nm. Like polycrystalline structure, there are "grain boundaries" separating domains which oriented randomly to each other by lattice defects. The mean diameter and the spacing of the holes measured from SEM micrograph (Fig.4.17a) were 35 and 45 nm, respectively. The high magnification image in Fig. 4.17b shows main defect types in the hole lattice which interrupted periodic array of the holes. In order to identify substrate effects, we bombarded different orientation samples and found the ordering structure is orientation-independent. The amorphous layer induced by ion beam can lead to this orientation-dependent ordering structure. Fig. 4.18a shows AFM image obtained by taping model on a perfect ordered domain, from which we can find that besides ordered holes there are hexagonally ordered quantum dots with 20 nm diameter and 3 nm height around each hole . The combination of well ordered quantum dots and holes can be confirmed by cross-section profile from different orientation of hole structure (Fig. 4.18b) and three dimensional structure (Fig. 4.18c). Fig. 4.19 shows SEM images viewed from different directions. This honeycomb-like structure is reminiscent of hexagonal structures

in anodic alumina [214].

Dependence of holes on the bombardment time at fixed energy of 5 keV and flux of $2.2 \times 10^{15}$ $cm^{-2}s^{-1}$ is shown in Fig. 4.20. At very beginning time (t=3 s, Fig. 4.20a), corresponding to an ion fluence of $6.6 \times 10^{15}$ $cm^{-2}$, hole nucleation occurs. The network structure with broad hole size distribution can be observed, suggesting random nucleation sites. The hole formation can be attributed to the aggregation of vacancies of Ge atoms on the surface generated by energetic ion sputtering through surface diffusion. With bombardment proceeding (t=30 s, Fig. 4.20b), more surface Ge atoms are removed and visible short range ordering of holes can be observed within small domains where the hole becomes uniform by self-adjusting. These domains can grow during further bombardment (Figs. 4.20c and 4.20d). After exposure time of 240 s (4.20d), The hole size becomes uniform with average diameter of 35 nm and almost saturated domain size is developed. For longer bombardment times, the surface continues receding due to sputtering and the ordering domain slowly increases.

Structure and chemical characterization of naoholes induced by the ion beam is shown in Fig. 4.21. Cross-sectional TEM image shows that the hole has a dot shaped structure with a depth of 5 nm and sidewall angle of 60° to 70° (Fig. 4.21b). An amorphous layer with thickness of 5 nm is produced by energetic ions on the surface. This layer, consistent with penetration depth of ion calculated by Monte-Carlo simulation [80], remains constant during bombardment. High angle annular dark field (HAADF) image (Fig. 4.21c) shows the contrast variation of height in which the hole has darker contrast and distribution of elements inside sample. At bombardment temperature, the implanted Ga ions randomly distributed inside a morphinized Ge substrate, and no solid solution and compound with Ge can be found.

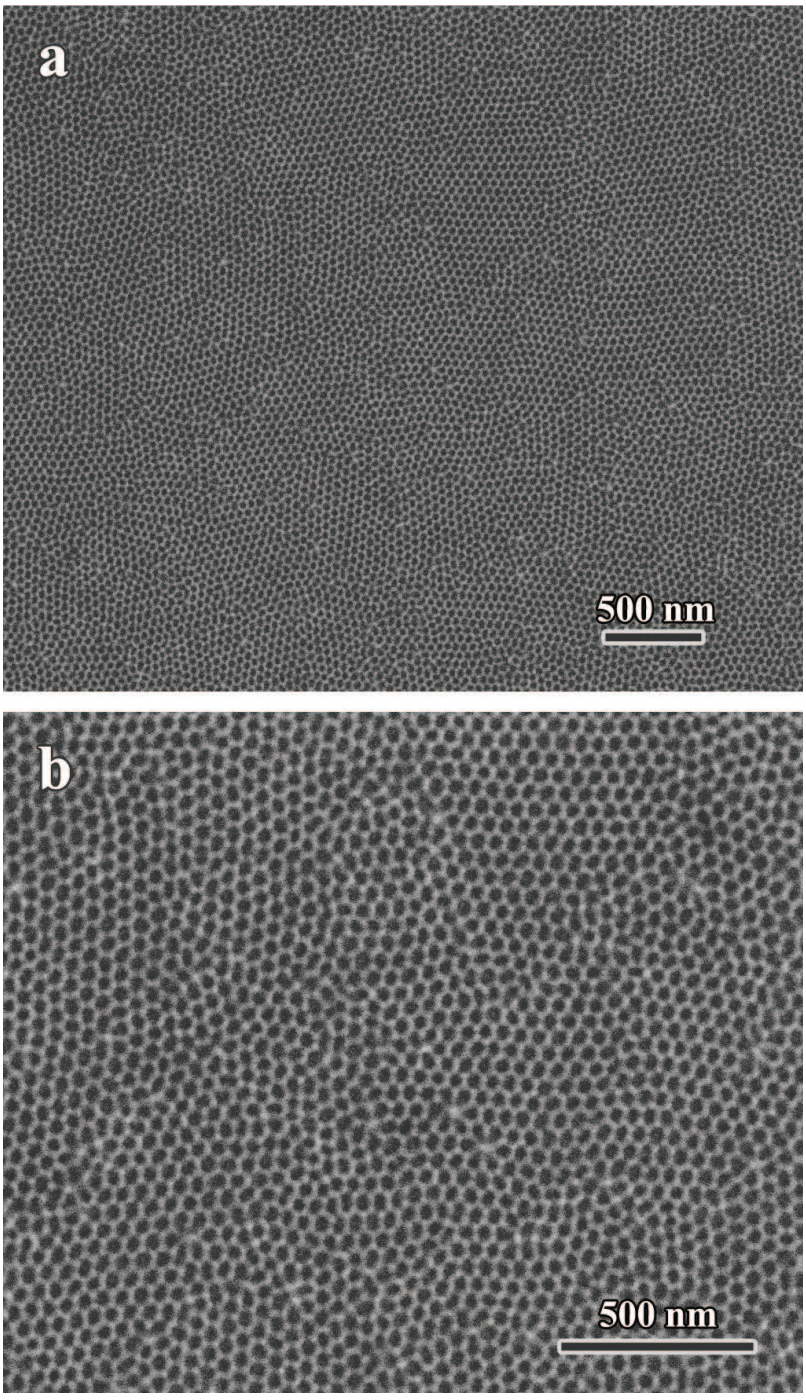


Figure 4.17: SEM images of hexagonally ordered nanoholes on Ge surface at low (a) and high (b) magnification. Ion energy 5 keV, flux $2.2 \times 10^{15}$ $cm^{-2}s^{-1}$, bombardment time 5 minutes.

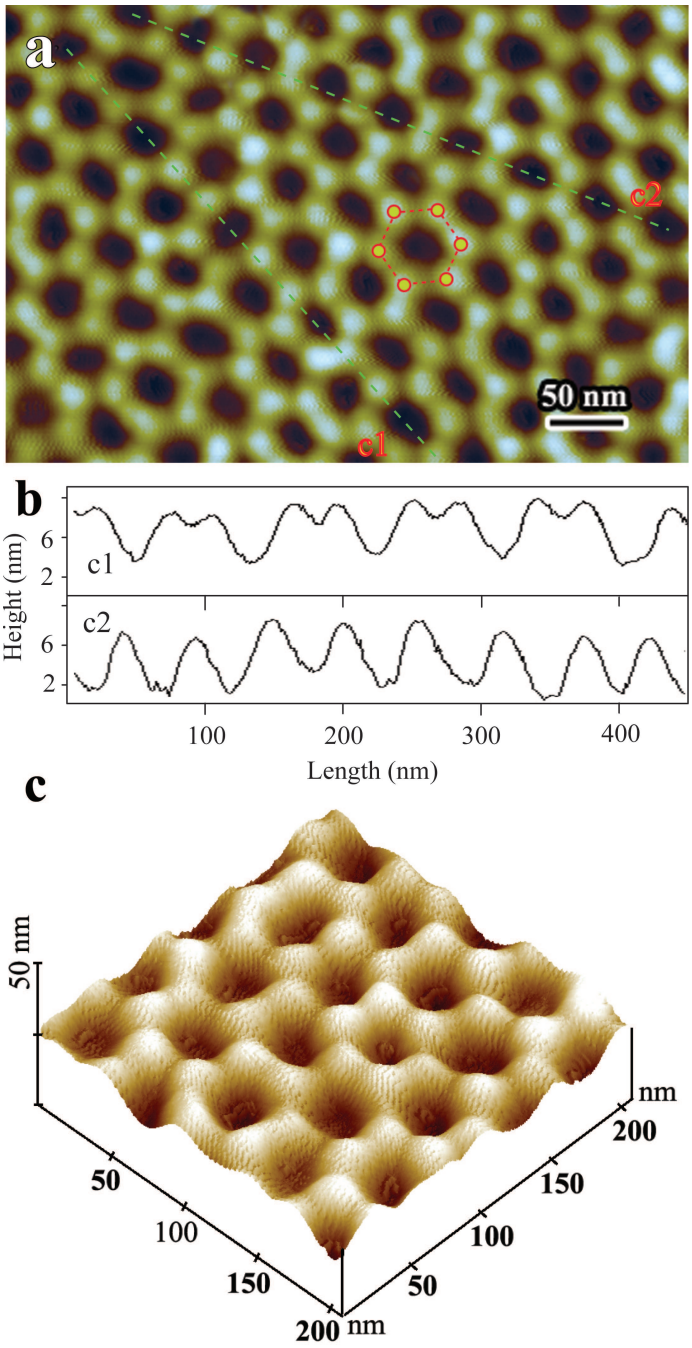


Figure 4.18: (a) AFM image of a hexagonally ordered hole domain showing a perfect hexagonal arrangement of bumps around each hole (indicated by circles and connected lines). (b) Corresponding cross section profile marked by dashed lines in (a), where top profile through the holes and bumps as shown by c1 in (a); bottom profile through the holes and middle of bumps as shown by c2 in (a). (c) 3D image of ordered pattern. Ion energy 5 keV, flux $2.2 \times 10^{15}$ $\mathrm{cm}^{-2}\mathrm{s}^{-1}$, bombardment time 5 minutes, scale bar 200 nm.

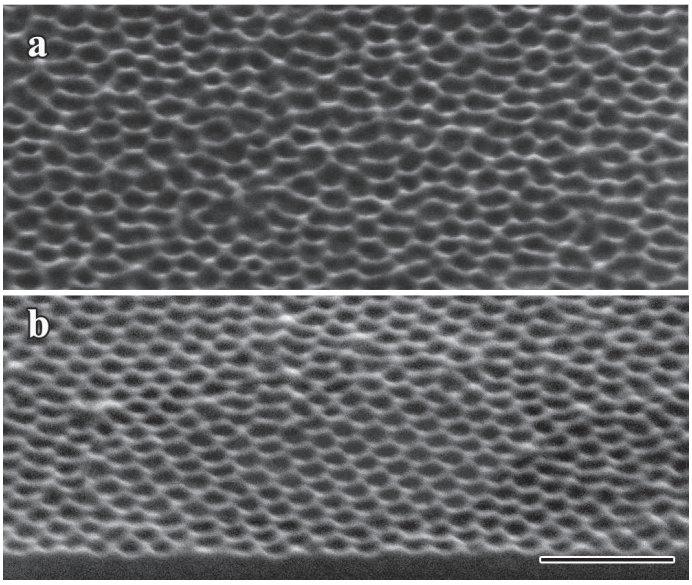


Figure 4.19: SEM images of ordered holes viewed from different directions: (a) normal to surface and (b) 52° from surface normal. Ion energy 5 keV, flux $2.2 \times 10^{15}$ $cm^{-2}s^{-1}$, bombardment time 5 minutes, scale bar 100 nm.

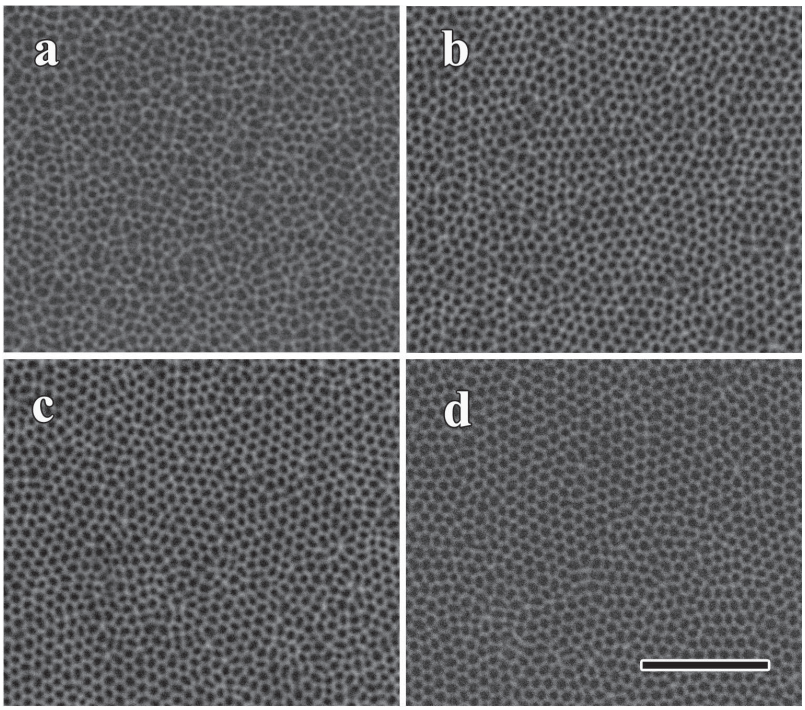


Figure 4.20: SEM images showing evolution of Ge surface at different times: (a) 3 s, (b) 30 s, (c) 90 s, and (d) 240 s. Ion energy 5 keV, flux $2.2 \times 10^{15}$ $cm^{-2}s^{-1}$, scale bar 200 nm.

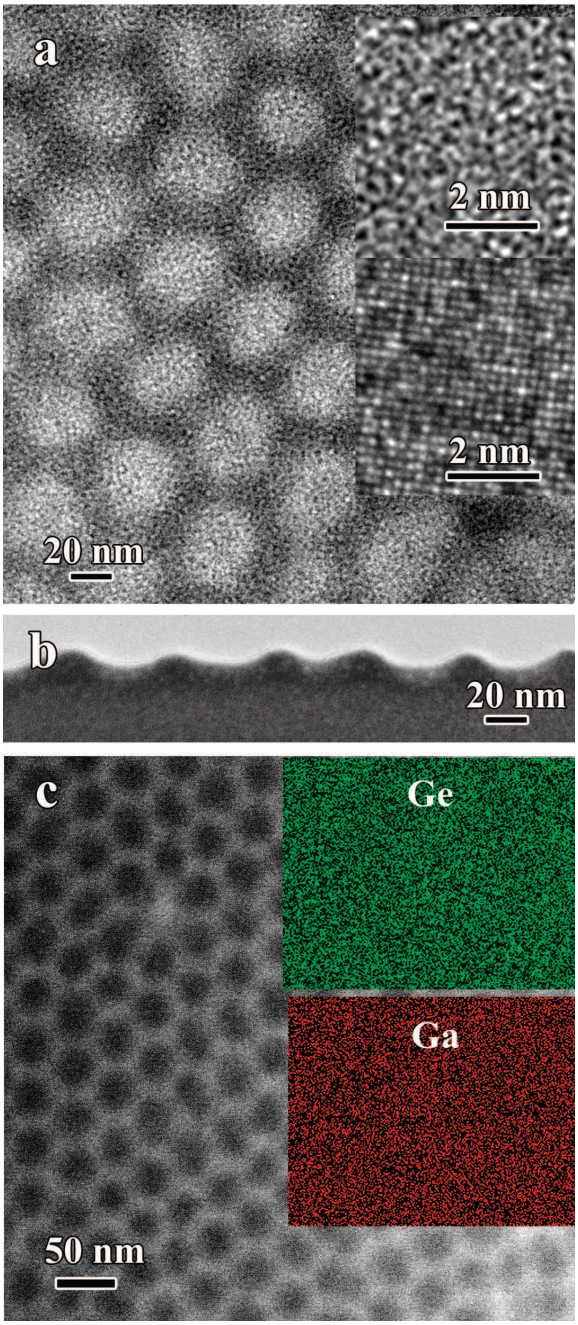


Figure 4.21: (a) TEM image of ordered holes on Ge surface. Inset shows HREM images before annealing (top) and after annealing at 600° (bottom). (b) Cross-sectional TEM image of the nanohole structures. (c) High angle annular dark field (HAADF) image. Insets show the energy dispersive x-ray spectrometry (EDS) mapping. Ion energy 5 keV, flux $2.2 \times 10^{15}$ cm$^{-2}$s$^{-1}$.

### 4.2.2 Discussion

For ordered pattern formation, it has been reported that DKS growth model can successfully predict ordered dot or hole formation during bombardment depending on the sign of nonlinear terms [88, 89, 213, 215]. According to this model, the positive nonlinear terms describe the dot formation and negative nonlinear terms predict hole formation. The DKS growth model is given by

$$\frac{\partial h}{\partial t} = -(\alpha + \nu\nabla^2 + D\nabla^4)h - \lambda(\nabla h)^2 + \eta \tag{4.17}$$

where $h(x, y, t)$ is the height of the bombarded surface described by coordination $x$ and $y$, $\nu$ is effective surface tension generated by the erosion process due to surface curvature or viscous flow due to surface stress, $D$ is effective diffusion coefficient from thermal diffusion, radiation induced diffusion, and viscous flow, $\lambda$ describes the tilt-dependent sputtering yield, $\eta$ is a Gaussian white noise resulting from the stochastic nature of erosion process, a damping term $-\alpha h$ accounts for the redeposition of sputtered species on the surface. Under normal bombardment, by rescaling coefficients, Eq. 4.17 yields an isotropic partial different equation with $\nu = D = \lambda = 1$ [89]. Therefore, for isotropic DSK model, the variation of $\alpha$ determines the morphology evolution.

Numerical simulation is performed on an equally spaced two-dimensional mesh of 512×512 by integration of Eq. 4.17 using standard discretization method with periodic boundary conditions. The integration starts from a random initial state with spatial step $dx = 0.5$, time step $dt = 0.005$, $\nu = D = \lambda = 1$, $\eta = 0$, and $\alpha = 0.23$. Fig. 4.22 shows the simulation results from Eq. 4.17. The random distribution of holes at the early time becomes highly ordered holes in the late time. The ordering is improved with increasing of time. Fig. 4.23 shows the 3-D simulation structures.

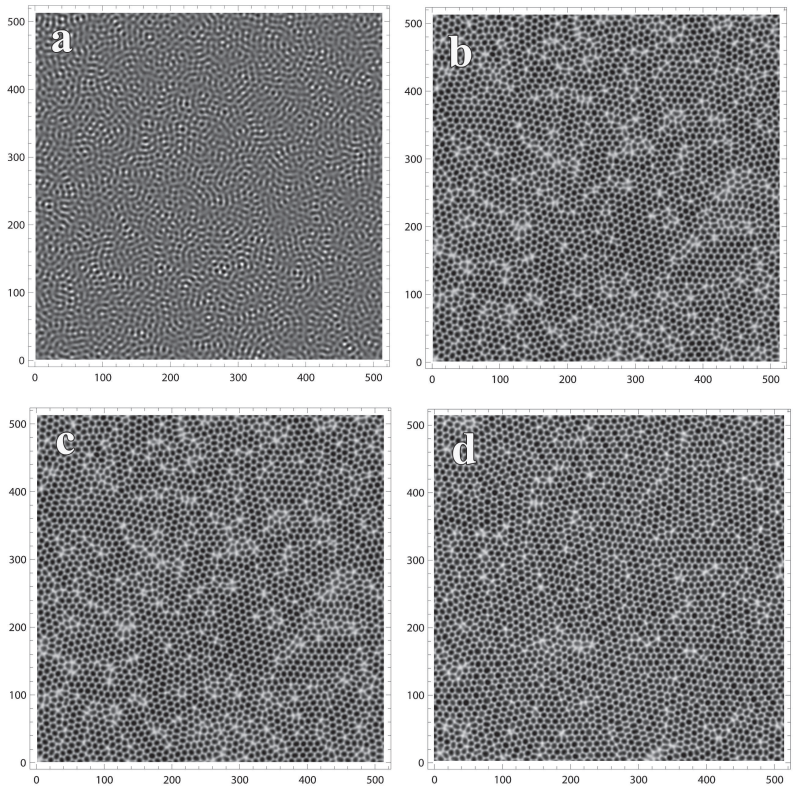


Figure 4.22: Numerical simulation from Eq. 7.1 showing the development of surface morphology with increasing time: (a) t=5 (iterations 1000), (b) t=100 (iterations 20000), (c) t=400 (iterations 80000), (d) t=750 (iterations 150000).

The defects are evident in the images.

Fig. 4.24 shows comparison of prediction of Eq. 4.17 with experimental observation produced from the same conditions in Figs. 4.17 and 4.18. Clearly, a striking similarity of surface morphology between theory and experiment from two dimensional images (Figs. 4.24a and d) and three dimensional images (Figs. 4.24b, c, and e) can be found. In particular, the perfect hexagonal arrangement of holes inside domains interrupted by grain-like boundaries and point defects predicted by Eq. 4.17 matches very well with experimental results. The ordering of patterns can be well characterized by PSD calculated from Fourier transform of the intensity of images. Fig. 4.24c shows angularly averaged PSD for patterns shown in Figs. 4.24a and d. The calculated PSD from simulation (Fig. 4.24a) is again in excellent agreement with

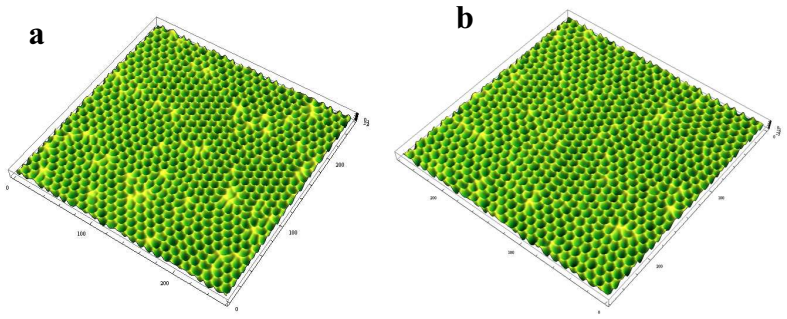


Figure 4.23: 3-D simulation results from Eq. 7.1 at different times: (a) t=100 (iterations 20000) and (b) t=400 (iterations 80000).

that from experimental data obtained by AFM measurement (Fig. 4.24d). Similar to experimental observations, hexagonally ordered dots around each hole can also be predicted by simulation in cross-section profile in Fig. 4.24a and three dimensional structure in Figs. 4.24b and c. These results confirm that DKS growth model can qualitatively explain hole formation in our experiment, where combination of sputtering, roughening, smoothing, and redeposition give rise to the ordered hole formation.

Visible light emission from semiconductor nanostructures has attracted significant attention due to potential optoelectronic applications. Fig. 4.25a shows Raman spectrum of optical phonon near wave number of 300 $cm^{-1}$ excited by a 530 nm laser after annealing. For unannealed sample, similar to amorphous structure, Raman spectra shows a broad bump around 275 $cm^{-1}$. With increasing annealing temperature, the sharp peak can be identified and shift to the position of bulk Ge, suggesting the well crystalline Ge. Photoluminescence (PL) spectra of ion-etched Ge after annealing at 600°C (Fig. 4.25b) shows broad but pronounced peak ranging from 500 nm to 700 nm with peak at about 630 nm. No weak peak can be observed for unannealed sample. The optical absorption spectrum of ion-etched Ge after annealing at 600°C shows blue shift in energy gap transition from 0.66 eV to 1.42 eV compared

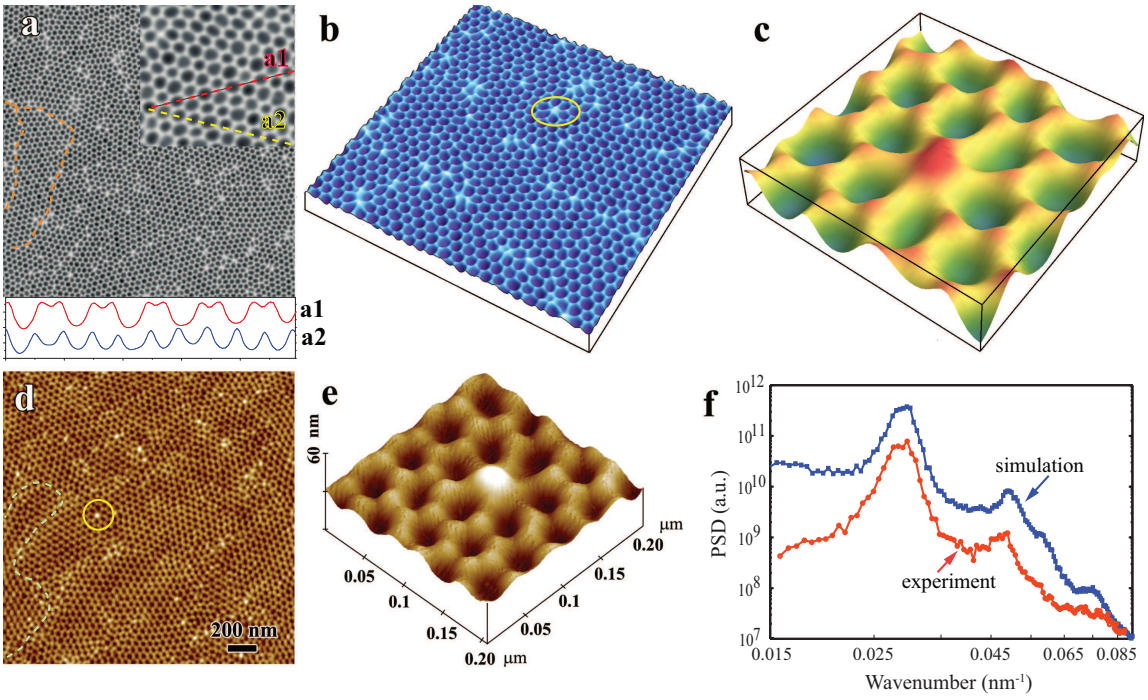


Figure 4.24: Comparison of surface morphology calculated by DKS equation with experimental observations. (a) Numerical simulation from Eq. 4.17 with $\alpha = 0.23$ at $t = 2000$ (iterations $4 \times 10^5$). Inset showing a high magnification image of an ordered hole domain and corresponding cross sections of surface topography. (b) 3D structure of numerical results. A point defect (a dot instead of a hole surrounded by six nearest holes) is shown by circle. (c) Enlarged segment of defect structure from the area marked by circle in (b). (d) AFM image of ordered patterns on Ge surface created by 5 keV ions for fluence of $6.6 \times 10^{17}$ cm$^{-2}$. Circle indicates a point defect. (e) Enlarged AFM image showing point defect indicated by circle in (d). (f) Log-log plot of the PSD curves obtained from (a) and (d). Dashed curves in (a) and (d) show line defects which separate the domains.

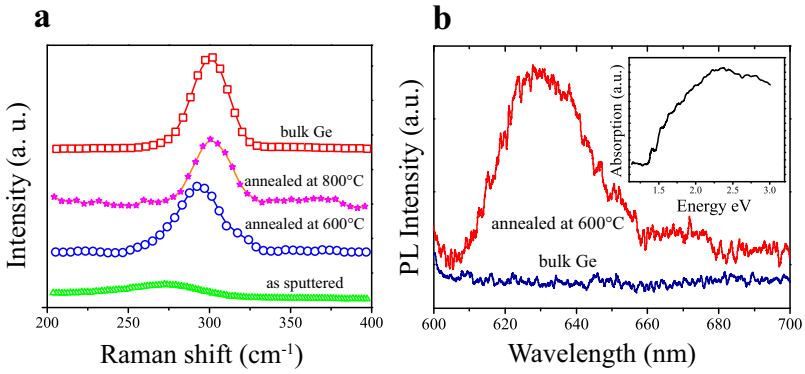


Figure 4.25: Optical properties of ion-etched Ge. (a) Raman spectra of samples annealed at different temperatures. (b) Room temperature photoluminescence (PL) spectra of Ge patterned with ordered nanoholes after annealing at 600°C. The spectra of bulk was given for comparison. Inset showing absorption spectrum of patterned Ge after annealing at 600°C. A 530 nm Ar ion laser was used for luminescence excitation.

with crystalline or amorphous bulk Ge. This band gap change can be attributed to the quantum confinement resulting from the dimensional reduction of hole wall thickness [88, 216].

### 4.2.3 Conclusion

In conclusion, it was shown that, in contrast to well ordered quantum dot formation in most ion sputtered semiconductors, highly ordered nanoholes were spontaneously generated on the surface of Ge. This observation signifies the importance of nonlinear effects in the pattern formation during ion bombardment in the long time limit. Our simulation, based on DKS model, provides 3-dimensional comparison. The excellent agreement between experimental observations and predictions of theory reveals that combination of ion sputtering, redeposition, viscous flow, and surface diffusion is responsible for the well ordered nanohole formation.

# CHAPTER V

# Three Dimensional Pattern Formation under Ion Bombardment

Since the discovery of three dimensional void lattice in irradiated materials [41], the spatial ordering of defects in diverse materials induced by the energetic particles has been extensively investigated during first two decades , including void lattice formation [41–43,48,94,95], bubble lattice formation [44,45], precipitate ordering [47], defect walls and vacancy loop ordering [49,50]. The detailed experimental conditions and characterization of lattice can be found in review papers [45, 58]. However, all these observations are performed on the planar view of samples after final structure formation. The 3-D void lattice was confirmed by different zone-axis TEM images from planar view samples. In contrast, we tried to get information of 3-D pattern formation along the ion penetration depth using cross-sectional TEM samples.

## 5.1 Void Lattice Formation

Table 5.1 shows a summary of the experimental conditions we have performed. The sample was irradiated in Environmental Molecular Science Laboratory (EMSL) of Pacific Northwest National Laboratory with the ion energy ranging from 3.2 to 5 MeV. Cross-sectional TEM sample was made by focused ion beam (FIB) as shown in Fig. 5.1.

Table 5.1: Irradiation conditions for void lattice formation

| Target | Ion | Energy (MeV) | Temperature (°C) | Fluence ($10^{16}$cm$^{-2}$) | Diameter (nm) |
|---|---|---|---|---|---|
| Mo-5%Ti-0.1%Zr | $Ni^+$ | 5 | 650 | 2 | 8 |
| Mo-5%Ti-0.1%Zr | $Ni^+$ | 3.2 | 650 | 4 | 8 |
| Mo-5%Ti-0.1%Zr | $Ni^+$ | 3.2 | 650 | 8 | 9 |
| Mo-5%Ti-0.1%Zr | $Ni^+$ | 5 | 650 | 10 | 10 |
| Mo-5%Ti-0.1%Zr | $Ni^+$ | 5 | 650 | 55 | 11 |

The void distribution with penetration depth was obtained as shown in Fig. 5.2. The average diameter rises from approximately 10 nm at 40 dpa to approximately 30 nm at 120 dpa. The density of small void at low dpa is higher than that in the peak position of implanted Ni ions. Unfortunately, we did not observe void lattice in cross-sectional samples under several radiation conditions (Table 5.1). Compared with previous studies [41, 48, 94], the temperatures used in our experiment are lower and other parameters (target, dose and fluence) are nearly the same. It is known that high temperature causes two competitive effects: enhance the lattice formation due to the increased mobility of species along special directions and destroy the lattice formation if temperature is high enough that random movement occurs. Thus there is a suitable temperature range where species can immigrate directed by the crystalline structure. This temperature is found to be around 0.3 $T_M$ to 0.5 $T_M$ [41,48,51,58,94].

## 5.2 Bubble Lattice Formation

Table 5.2: Irradiation conditions for bubble formation

| Target | Ion | Energy (keV) | Temperature (°C) | Fluence ($10^{16}$cm$^{-2}$) | Diameter (nm) |
|---|---|---|---|---|---|
| Mo-5%Ti-0.1%Zr | Ne | 100 | 550 | 0.8 | 3 |
| Mo-5%Ti-0.1%Zr | Ne | 160 | 550 | 1.2 | 3 |
| Mo | Ne+Kr | Ne 100, Ke 500 | 550 | 8 | 4 |
| Cu | He | 160 | 25 | 5.5 | 4∼ 150 |
| Au | He | 160 | 25 | 5.5 | 2∼ 150 |
| Cu | He | 30 | 25 | 5.5 | 3∼ 120 |
| Au | He | 30 | 25 | 5.5 | 4∼ 100 |
| Si | He | 160 | 25 | 5.5 | 4∼ 150 |

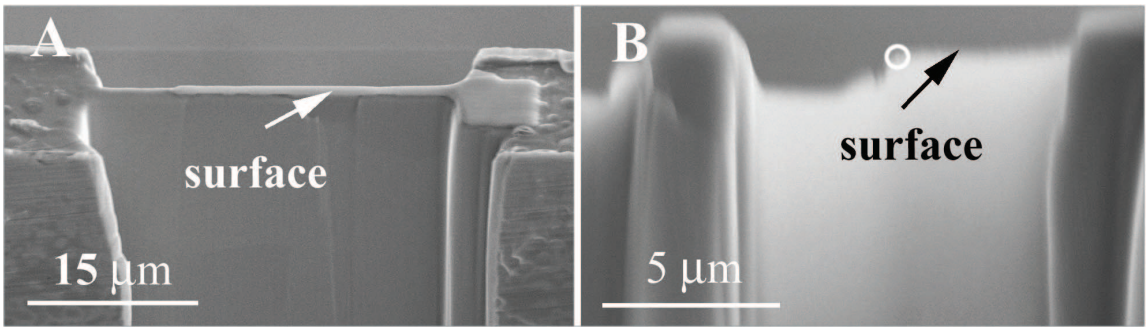


Figure 5.1: Using FIB to prepare cross section samples. The sample was first mechanically polished up to 20 $\mu$m in cross section direction and then cut by FIB in planar direction. (A) course cut using 20 nA ion beam current; (B) final SEM image using several pA ion beam current. Circle shows the area where HRTEM image was taken.

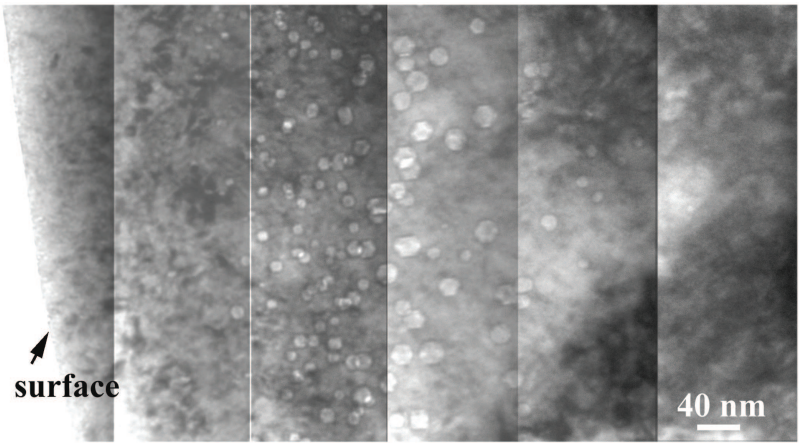


Figure 5.2: Electron micrographs showing the variation of void distribution with depth in the Mo-5%Ti-0.1%Zr (TZM) materials subjected to 5 MeV Ni ions up to dose of $5.5 \times 10^{17} \mathrm{cm}^{-2}$ at temperature of 650°C. The image illustrated the difference in the size of voids along depth.

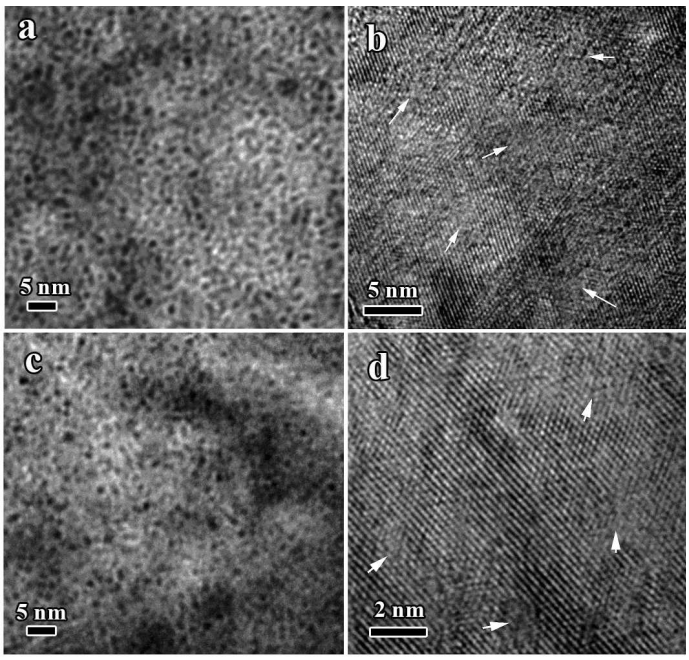


Figure 5.3: Snap shorts of *in situ* observation of void formation. The experiment was conducted with 500 keV He at temperature of 550°C up to dose of $7 \times 10^{16}$ cm$^{-2}$ (a, b) and $1.2 \times 10^{16}$ cm$^{-2}$ (c, d). Arrows show the bubble sites in HRTEM images.

### 5.2.1 *In situ* observation of bubble formation

Several efforts for *in situ* observation of bubble lattice formation on pure Mo and TZM (Mo-5%Ti-0.1%Zr) irradiated by Ne and Kr were made in Argonne National Lab (Table 5.2). Although bubble lattice did not appear (Fig. 5.3), we still obtained valuable information about evolution of bubble lattice, some of which were not observed before:

1) Bubbles appears at dose of $5 \times 10^{14}$ cm$^{-2}$ for 100 keV He irradiated Mo.

2) Bubbles do not change much in size from $5 \times 10^{14}$ cm$^{-2}$ to $10^{17}$cm$^{-2}$.

3) No observation of diffusion or any motion of bubbles.

4) Images are specimen area dependent.

5) Size of bubbles is about $2.5 \sim 4$ nm, spacing $2 \sim 7$ nm.

6) It shows that dose is not large enough to form ordered bubbles, but lattice was

formed with the same dose in irradiated bulk samples [46].

### 5.2.2 Bubble formation in He implanted Si

Fig. 5.4 shows cross-sectional TEM image of 160 keV He irradiated Si at room temperature with dose of $1 \times 10^{17} \mathrm{cm}^{-2}$. Extra large bubble can be found in the regime where He has a maximum concentration. Recently, the great interests of investigation of growth and thermal evolution of voids in Si by implantation of He have developed because the voids in Si exhibit strong gettering of transition metals. To date, the void is created in two steps inside bulk materials by most of experiments: as-implanted state to form small bubble and subsequently thermal annealing to form large void. A grand challenge is creating and assembling the voids on the semiconductor surface to construct functional structures. In this study, we show that void structure can be formed on the surface of Si by removing amorphous layer using focused ion beam in He implanted Si. High flux and high fluence were used to form large bubbles without annealing. At peak position where concentration of He is the largest, the non-spherical shaped bubble formed with size around 50 nm, while at deeper position spherical bubble with 2 nm in diameter can be found and uniformly distributed. The high dose and high dose rate can be responsible for this phenomenon. Using focused ion beam we can remove the surface amorphous layer and obtain network and void structure on the Si surface (Fig. 5.4c and d). This method opens up a promising new approach to the application of these voids in Si technology including, for example, nanoscale photonic and electronic devices.

### 5.2.3 Bubble formation in He implanted Cu and Au

It has been reported that bubble lattice can form in He implanted Cu and Au under certain irradiation conditions [45,59]. However, this information was obtained

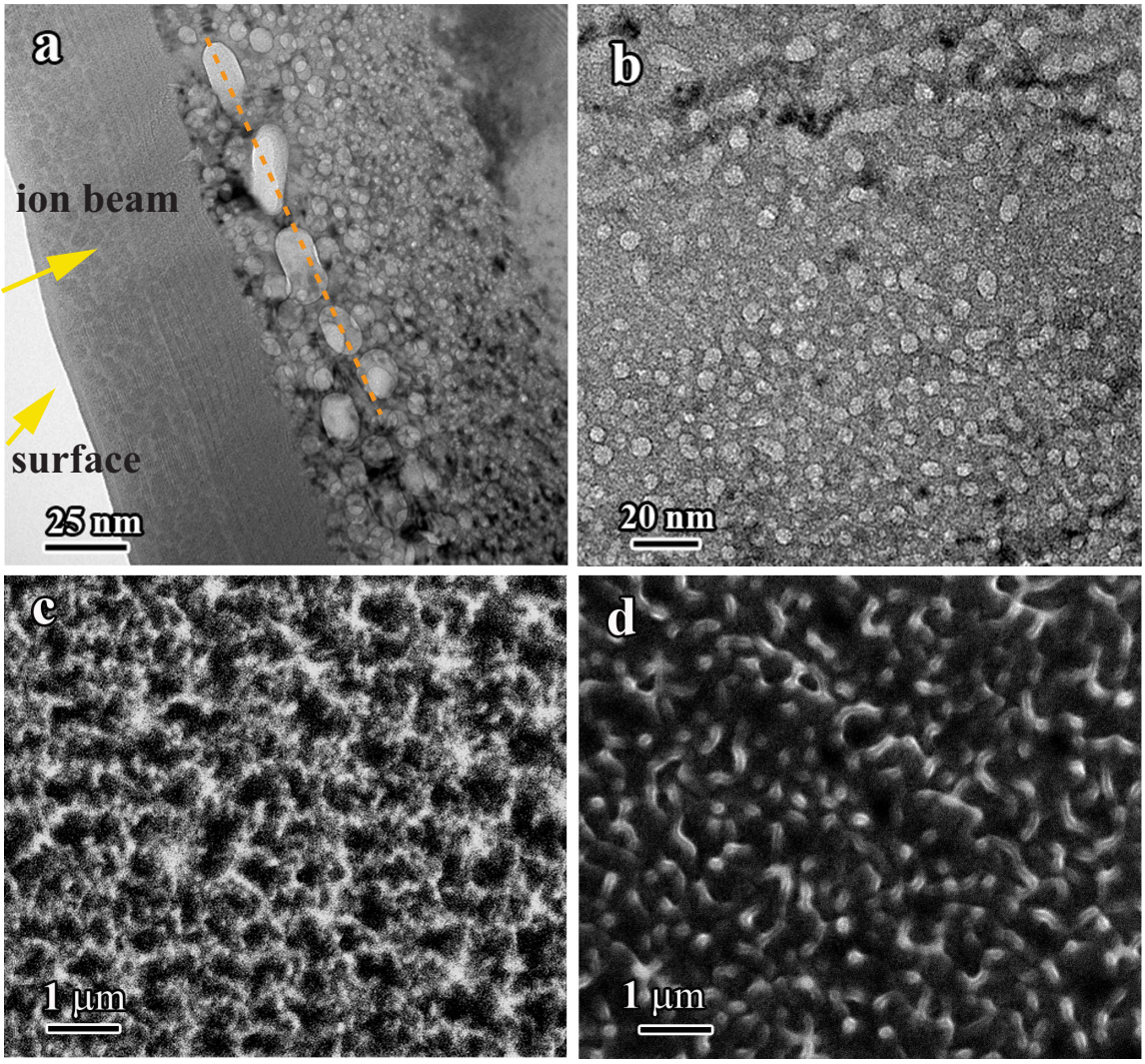


Figure 5.4: TEM images of ion irradiated Si. (a) Cross-section viewed image and (b) plan viewed image. (c) Network structure of Si after removing surface layer to the low penetration depth. (d) Void structure on the Si surface after removing amorphous layer to the peak position of implanted He. Dashed line shows the peak position of implanted He. The experiment was conducted with 30 keV He at room temperature up to dose of $1 \times 10^{17} \mathrm{cm}^{-2}$.

from plan view TEM images and as a consequence bubble distribution along penetration depth was lacking. In this study, with cross-sectional TEM samples made by ultramicrotome, we show that bubble lattice can only form before or after the peak position of implanted He. In addition, *in situ* TEM annealing reveals the development of faced bubbles that can be attributed to the preferential receding of crystals in which the facets of crystals with a low surface energy occupy more of the surface area of the resulting bubbles.

Fig. 5.5 shows cross-sectional bright field HAADF image of 30 keV He irradiated Cu with a flux of $1.5 \times 10^{13}$ $cm^{-2}s^{-1}$. The sample was prepared by Ultra-microstomy. The irradiation was conducted with 30 keV He at room temperature up to fluence of $5.5 \times 10^{16} cm^{-2}$ in the Michigan Ion Beam Laboratory (MIBL). Broad size distribution of bubbles can be observed in the peak depth of implanted He while uniformly distributed bubbles are formed before and after the peak position. It is well known that uniform size is a prerequisite for the ordered pattern formation. Thus ordered bubble lattice can only form before or after peak depth of implanted He. The number density and size of bubbles are mainly controlled by temperature, displacement rate and accumulated He concentration. For high flux and fluence, resolution of He from existing bubbles occurs by displacement cascades and secondary bubble nucleation can take place. At the beginning of implantation, multi-component nucleation process including diffusion and clustering of He ions contributed to bubble nucleation. At room temperature, the mobility of He atoms is relatively low or even negligible. For bubble growth, as indicated by cross-sectional image (Fig. 5.5), because the peak position has more implanted He ions as interstitials, the direct collision of implanted He instead of He diffusion is mainly responsible for bubble growth. The nucleation density results from a balance between the rates of formation and destruction of

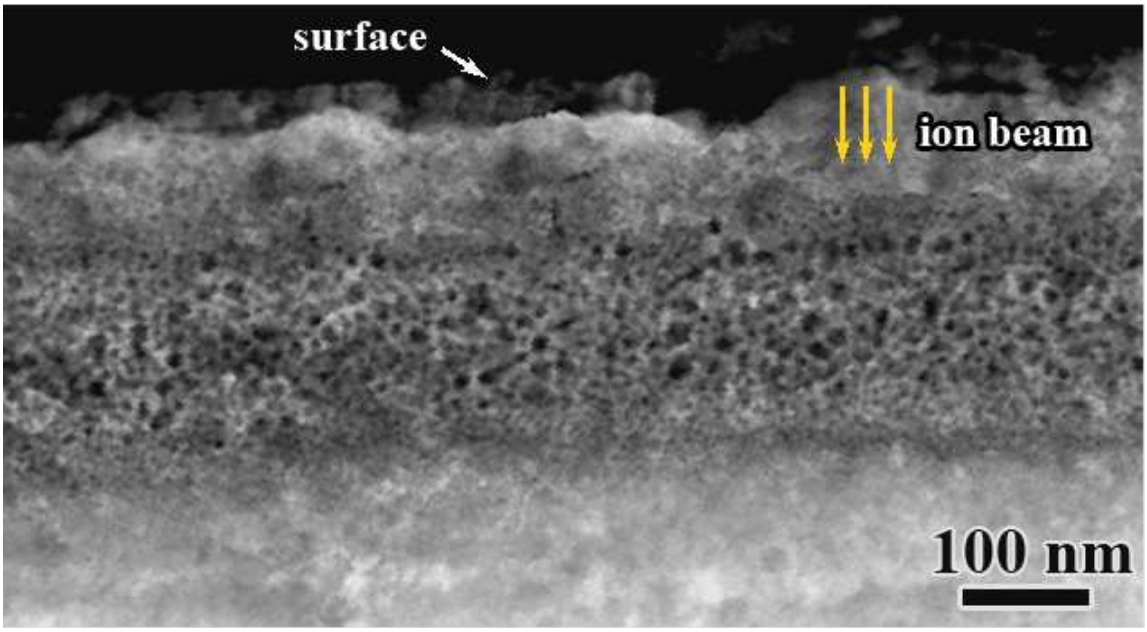


Figure 5.5: HAADF cross-sectional image showing bubble distribution on 30 keV He irradiated Cu where contrast is due to different thickness. The experiment was conducted with 30 keV He at room temperature up to dose of $5.5 \times 10^{17}\text{cm}^{-2}$.

bubble nuclei by implanted He ions.

This bubble distribution can be further confirmed by HAADF images. In Fig. 5.6, partially ordered bubbles appear before and after implanted He peak depth. A domain with perfect hexagonally ordered bubbles with lattice constant of 10 nm was observed before the peak depth (Fig. 5.7). The ordered bubble extended cross over 10 layers in ion beam direction.

Fig. 5.8 shows the dependence of bubble evolution on annealing temperature. With increasing temperature, only small fraction of bubbles grow following Ostwald ripening and coalescence while most of bubbles remain constant up to 500°C. In addition, density of bubbles in most areas does not change. Most bubbles remain stable until sample evaporates at temperature of 550°C. Due to the increase of pressure inside bubbles with temperature raising, the bubbles which are located closely enough to the surface will explode and disappear. It was found that substrate immediately

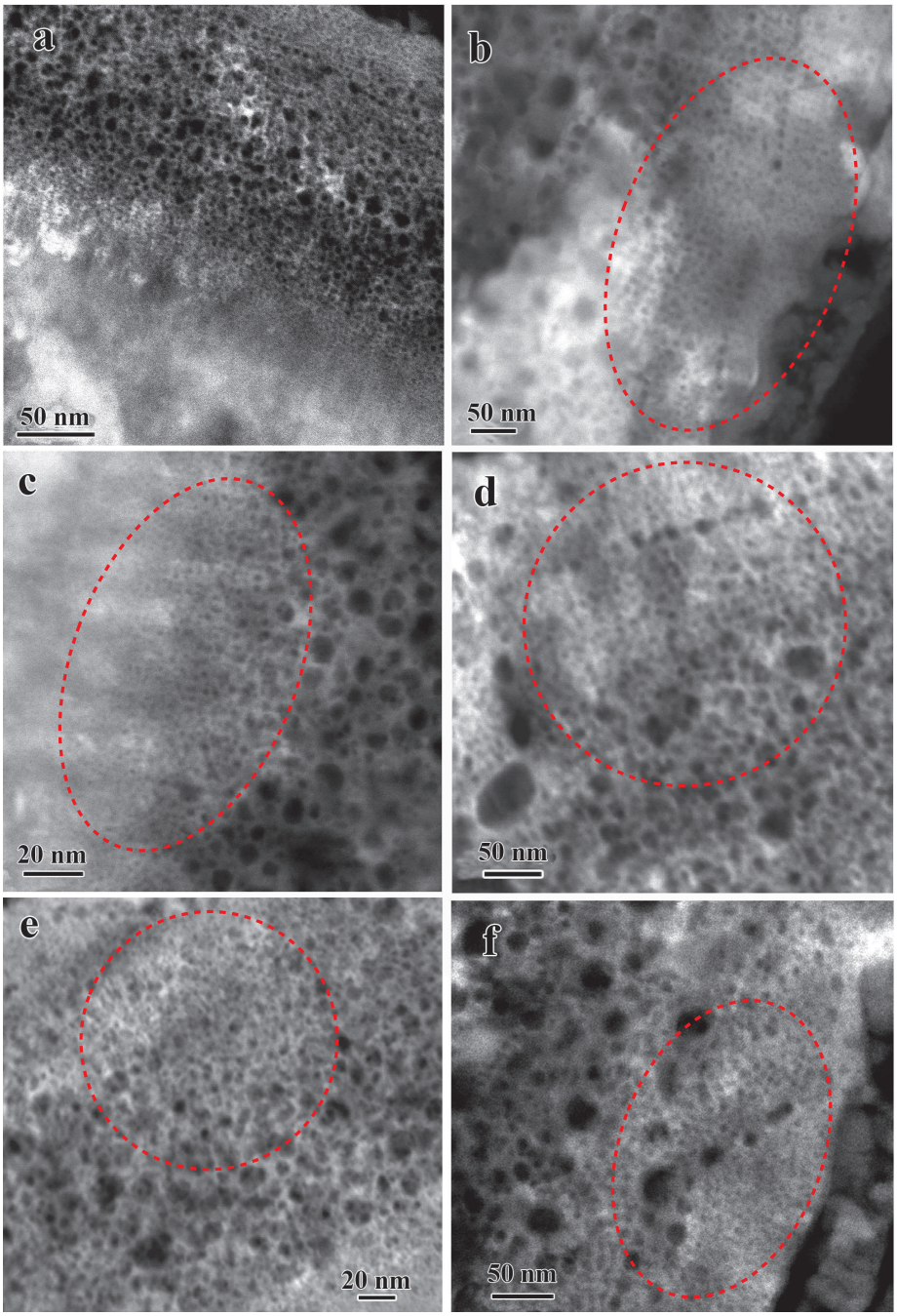


Figure 5.6: HAADF cross-sectional images showing partially ordered bubbles on 30 keV He irradiated Cu. (a) Cross-sectional image. (b) Enlarged image showing the partially ordered bubbles close to surface. (c) Ordered bubbles after peak depth. (e) and (f) The partially ordered bubbles formed before peak depth. Dashed curves denote the area where partially ordered bubbles can be observed.

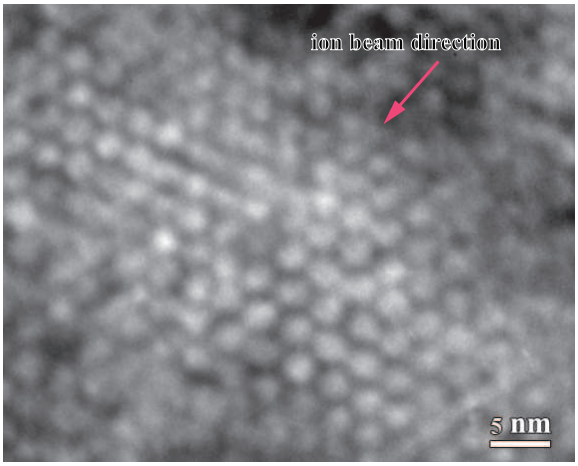


Figure 5.7: Cross-sectional TEM image showing the bubble lattice on the He irradiated Cu. The experiment was conducted with 30 keV He at room temperature with dose of $5.5 \times 10^{17}\text{cm}^{-2}$. Up to ten layers of ordered bubble can be observed.

restores to its original structure when bubble explodes.

Fig. 5.9 is plan view TEM image showing temperature dependence of bubble growth in He irradiated Au. Before annealing, uniformly distributed bubbles with diameter about 2 nm were formed by He implantation at room temperature. *In situ* TEM annealing shows that initially spherical bubbles deform into faceted shapes as they grow at temperature of about 400°C. Due-size of bubbles (2 nm and 20 nm) with uniform distribution was found in annealed sample, suggesting some bubbles does not change on annealing. Although the faceted bubbles are not ordered, there are preferential orientations for facets as indicated in Fig. 5.9b (viewed along zone axis of [100]). By tilting the sample to different zone axes, it was found that only one special shape of bubbles can be observed for each zone axis, and more importantly, all facets aligns with substrate {111} planes. Based on these conditions, we can expect that polyhedron composed of {111} planes with the same symmetry of substrate surrounds the bubble.

Following the Gibbs-Wulff model of crystal growth, the shape of crystal is deter-

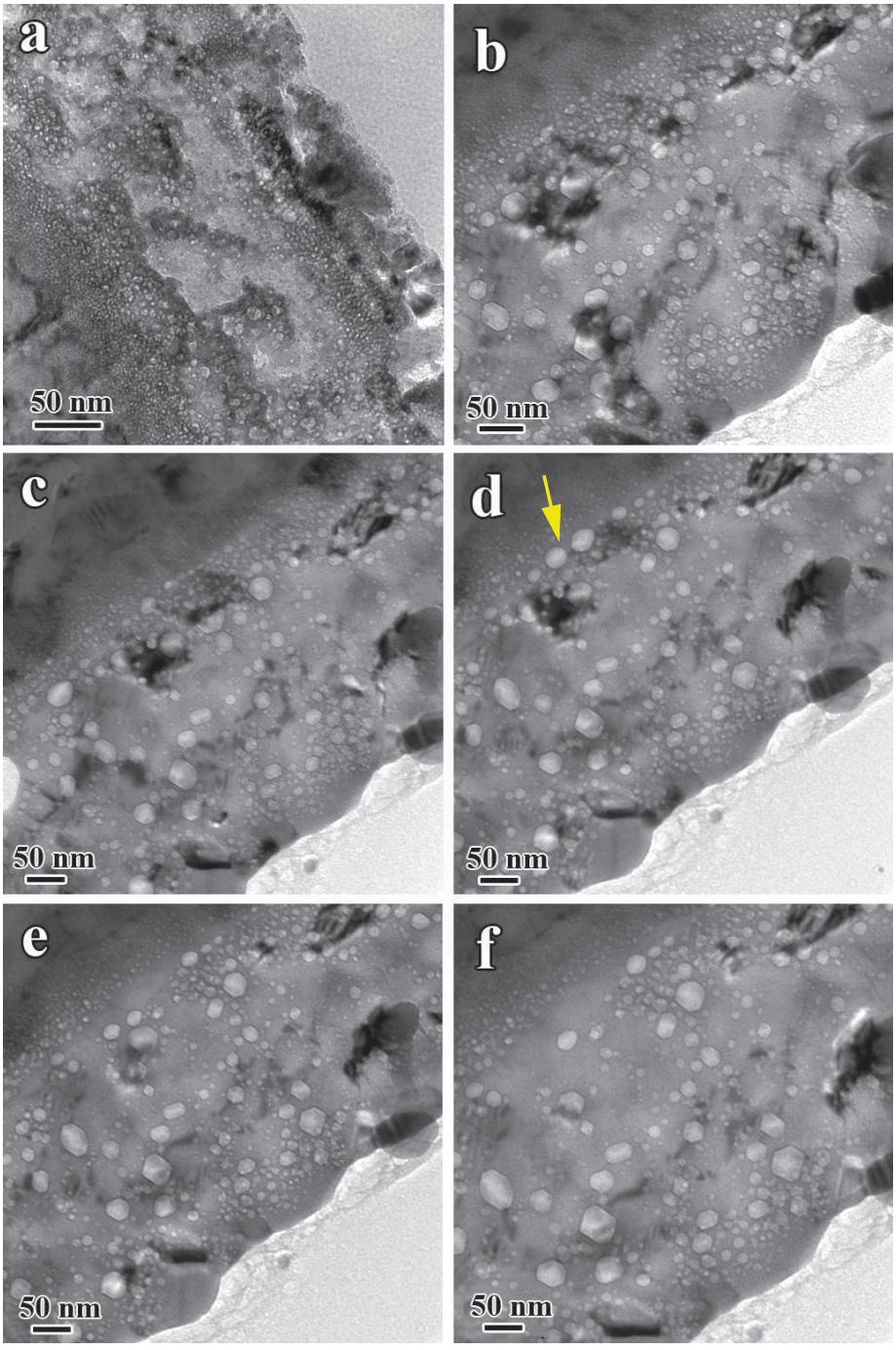


Figure 5.8: Dependence of bubble growth on the temperature (cross-sectional TEM under-focused images) in He irradiated Cu: (a) before annealing, (b) 400°C for half hour. (c) 450°C for half hour. (d) 500° C for 10 minutes. (e) 500°C for 15 minutes. (f) 500°C for 20 minutes. Arrow in (d) shows bubbles which disappear in (e).

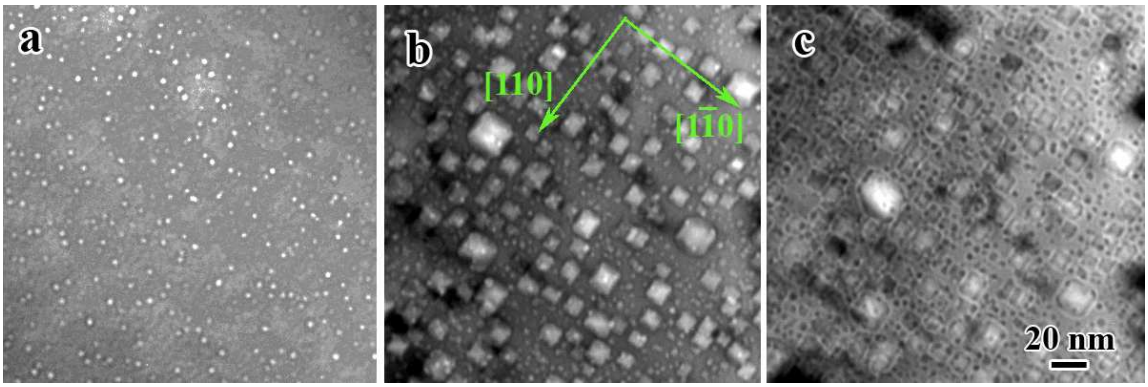


Figure 5.9: Dependence of bubble growth on the temperature (plan-view TEM images) in He irradiated Au: (a) before annealing, (b) 400°C for half hour (under focus image). (c) Over focus image of (b). Note the preferential orientation of facets.

mined by the minimum of surface energy. In our case, although crystal recedes due to bubble growth, the increased surface of crystal should also satisfy the minimum energy requirement. Because the lowest surface energy is {111} planes in FCC structure, in order to minimize the surface energy, the substrate needs to preferentially rearrange its surface by surface diffusion when bubble grows. Under this condition, the facets with lowest surface energy {111} planes will survive and occupy most of surface. Therefore, The growth of faceted bubbles can be attributed to the receding of crystals that satisfies the conditions of minimum surface energy requirement.

Geometric construction of polyhedron consisting of (111) planes shows octahedron shape (Fig. 5.10a). In most cases, truncated octahedron or a rounded edges and corns is energy favorable (Fig. 5.10b). Since it is embedded in substrate and consists of {111} substrate planes, the octahedron has the same symmetry as substrate. When viewed from zone axis of substrate, only one shape of octahedron can be observed. This prediction is consistent with experimental observations.

Comparison of experimental observations with the projected shape of octahedron for different zone axes is shown in Fig. 5.11. Square, parallelogram, and hexagon from

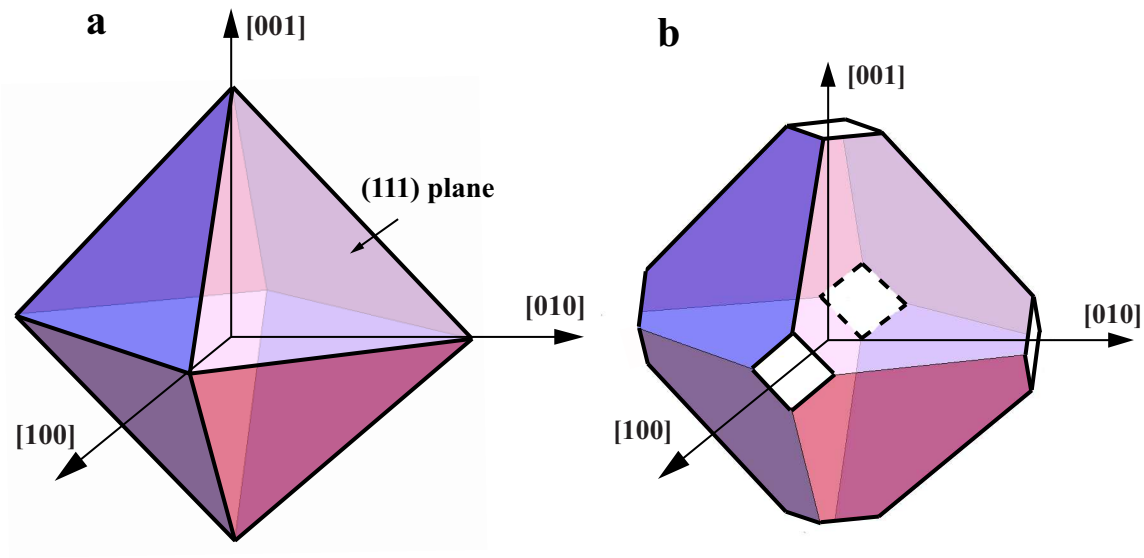


Figure 5.10: Schematic illustration of bubble shape consisting of {111} planes. (a) Octahedron (eight planes) and (b) truncated octahedron.

zone axes [100], [110], and [111] respectively are in good agreement with predictions of octahedron.

Rounded square shape are mostly found in enlarged images (Fig. 5.12). In HRTEM image (Fig. 5.13), octagon structure with orientation of [110] and [010] is clearly evident. It was found that bubbles with size of about 2 nm also have faceted shapes with the same symmetries as the matrix (Fig. 5.14). For polycrystal structure, no preferential accumulation of bubble in grain boundary was observed (Fig. 5.15a). But orientation of bubbles changes with the particles due to the different orientations of particles (Fig. 5.15b).

After faceted shape formation, bubbles show to be thermochemically stable. Stability of small bubbles at high temperature of 550° can be attributed to the faceted structures. Two main mechanisms, Ostwald ripening and migration of bubbles are responsible for bubble coarsening. Ostwald ripening is driven by differences in the pressure which are inversely proportional to the radius under thermodynamic equi-

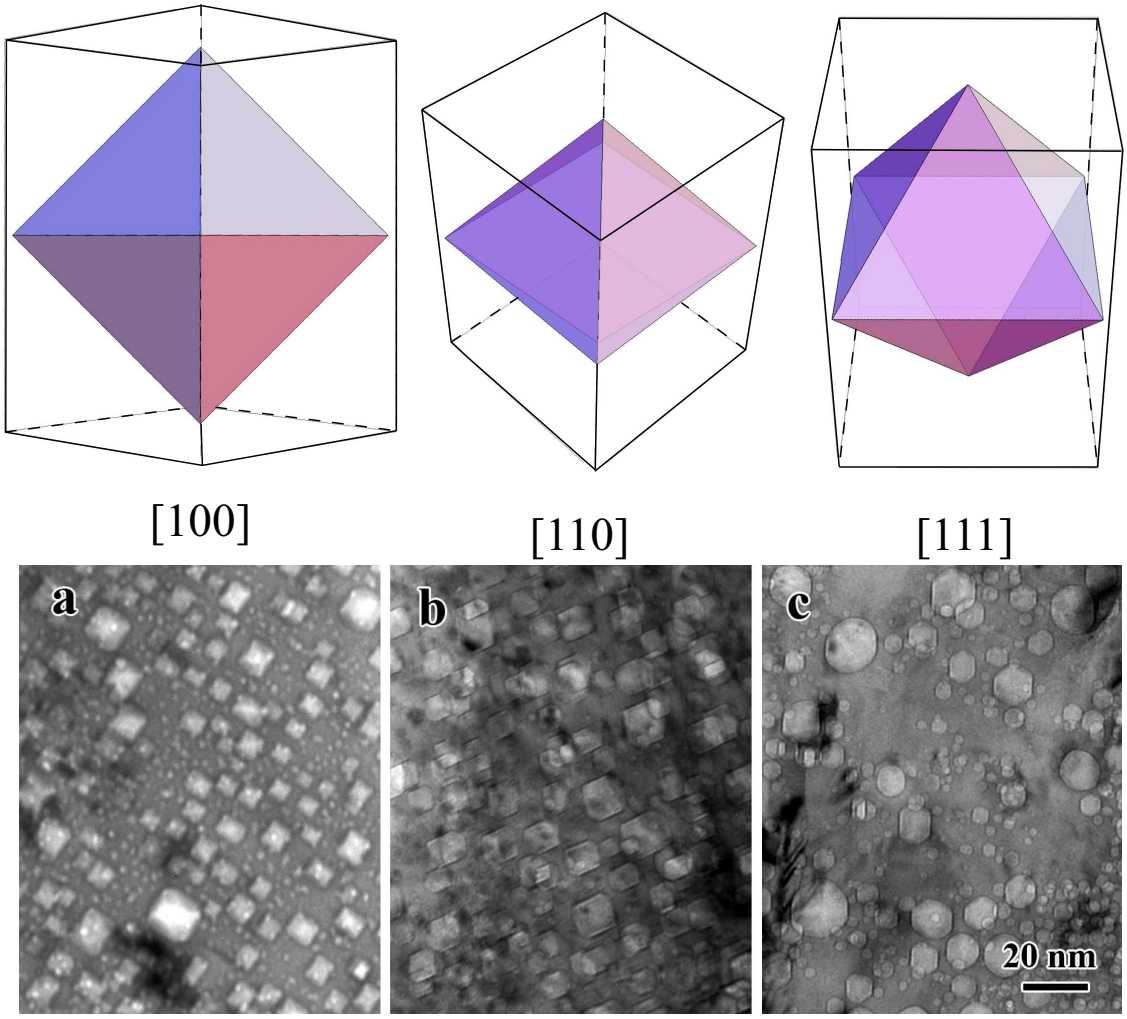


Figure 5.11: Comparison of experimental observations (bottom image) with projected shape of octahedron (top illustration) for different zone axes: (a) [100], square, (b) [110], parallelogram, and (c) [111], hexagon.

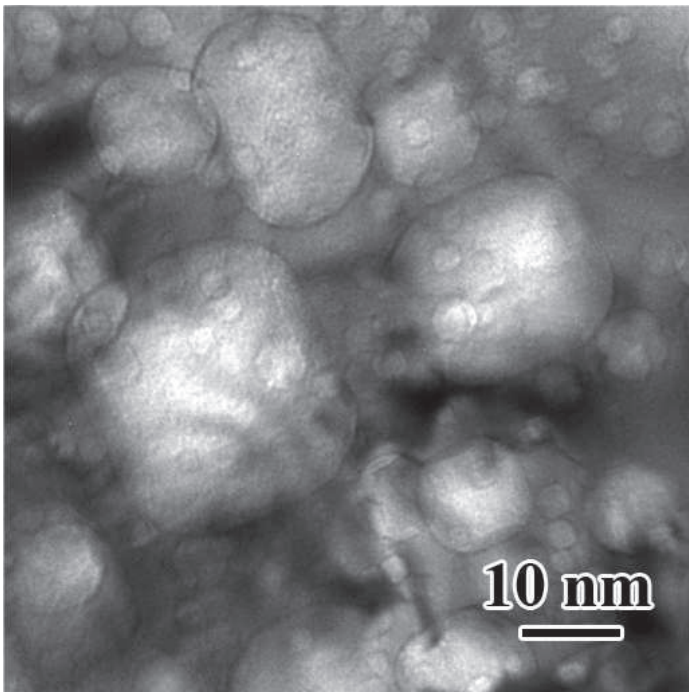


Figure 5.12: Enlarged image showing rounded square shape of bubbles viewed in [100] direction.

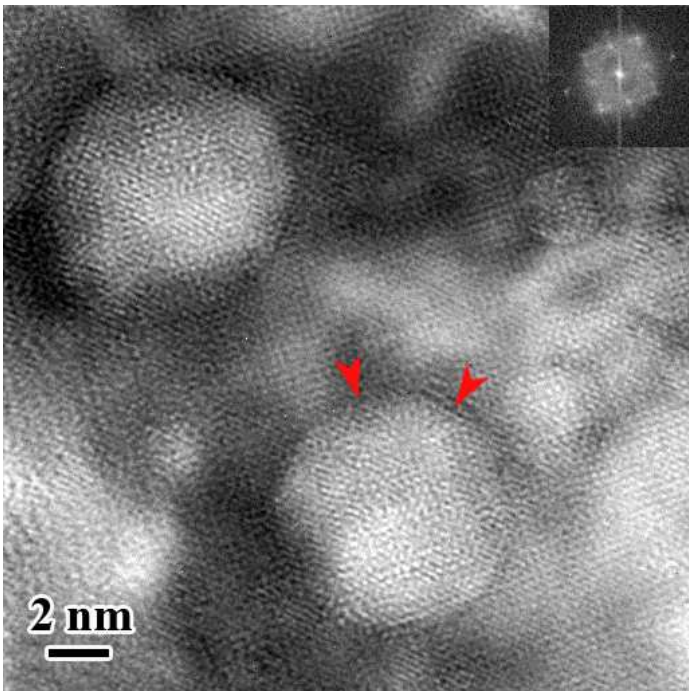


Figure 5.13: HRTEM image showing octagon structure of bubble viewed in [100] direction in 30 keV irradiated Au. Arrows indicate the orientation of bubble. Inset shows FFT (Fourier Fast Transformation) spectrum.

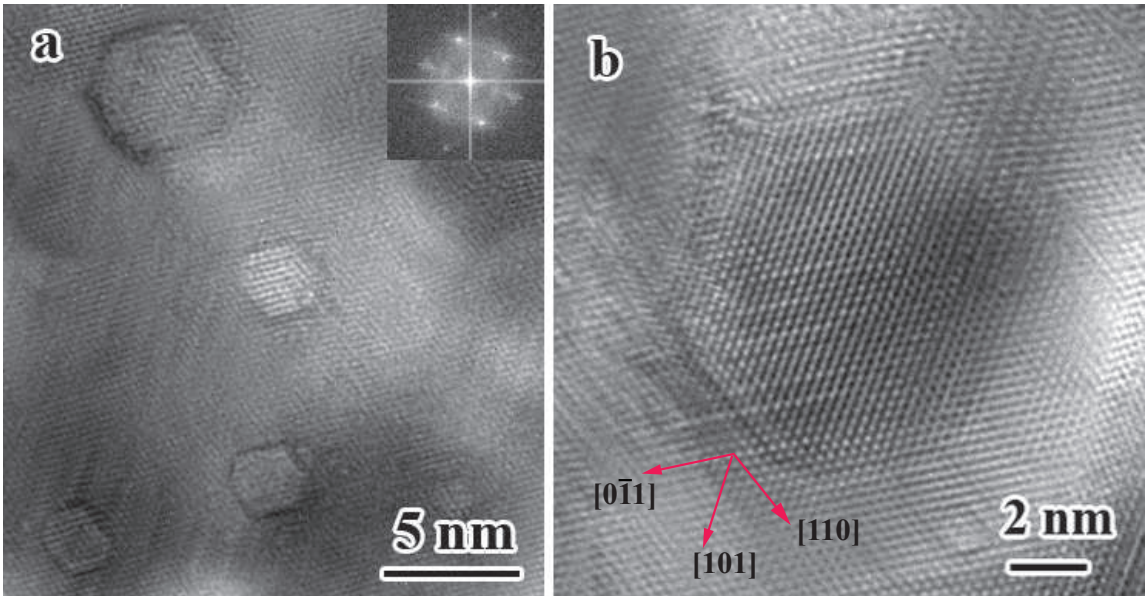


Figure 5.14: HRTEM image showing orientations of faceted bubbles related to substrate viewed in [$\bar{1}$11] direction in 30 keV irradiated Au. (a) Faceted bubbles with size of 2$\sim$ 5 nm. Inset shows FFT spectrum. (b) Orientation of a faceted bubble with size of 10 nm.

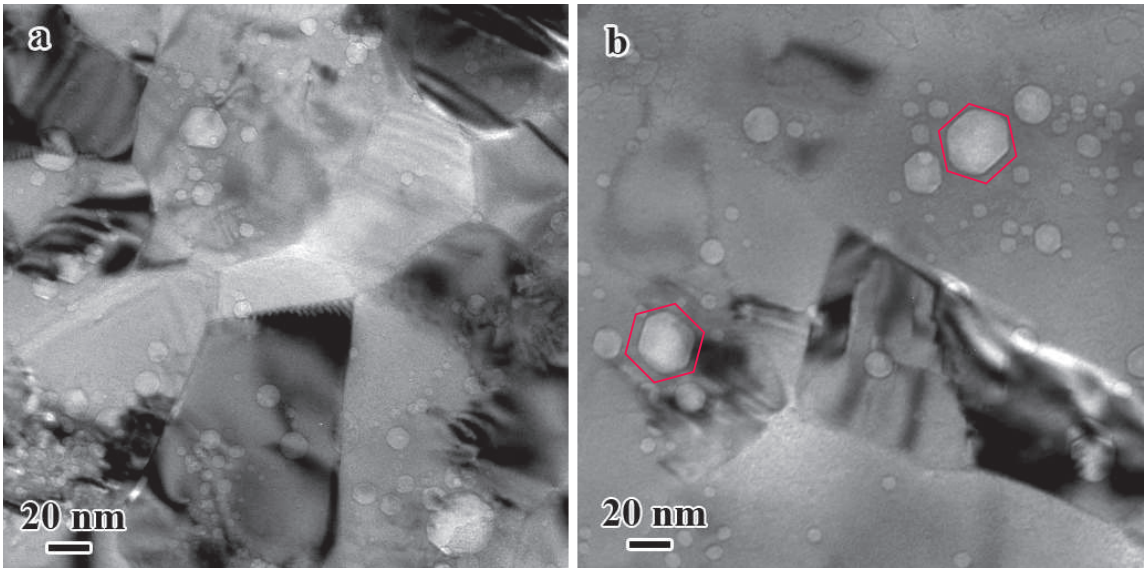


Figure 5.15: (a) Bubble distribution in polycrystalline Cu after half hour annealing at 450°. (b) Two different orientations of bubbles in two particles.

librium. Thus, small particles will disappear and large particle will grow. In our case, because the facets consist of {111} planes, the pressure is the same for different particles. Thus Ostwald ripening does not occurs except the change of bubble shape due to defects. Another mechanism for coarsening is bubble migration, depending on the surface diffusion of matrix atoms. At a given temperature, because all the bubbles have the same shape and arrange themselves in face to face contact, balance among different bubbles is reached. Migration of bubbles is hindered. Therefore, at high temperature, there is a limitation of growth of the bubbles once they form faceted shapes.

## 5.3 Discussion

### 5.3.1 Temperature, flux, dose, energy, and impurity effects on void/bubble lattice formation

#### Temperature

There are two stages for void formation: supersaturation of vacancies before voids can be nucleated and grown; and the supersaturated vacancies can move to the nucleation sites. In order to create a driving force for vacancies to move, minimum temperature is required, which is experimentally proved to be approximately 30 % of the melting point. However, above a certain temperature, thermal production of vacancies reduces the supersaturation of vacancies. This upper temperature limit is approximately 50% of the melting point in most metals. Because vacancies and interstials are produced in equal numbers during irradiation, the sinks which preferentially absorbs interstitials should exist. These sinks are assumed to be dislocations that are either present before irradiation or formed by the precipitation of interstitial atoms into dislocation loops.

Temperature dependence of void lattice formation has been reported on 3.1 MeV

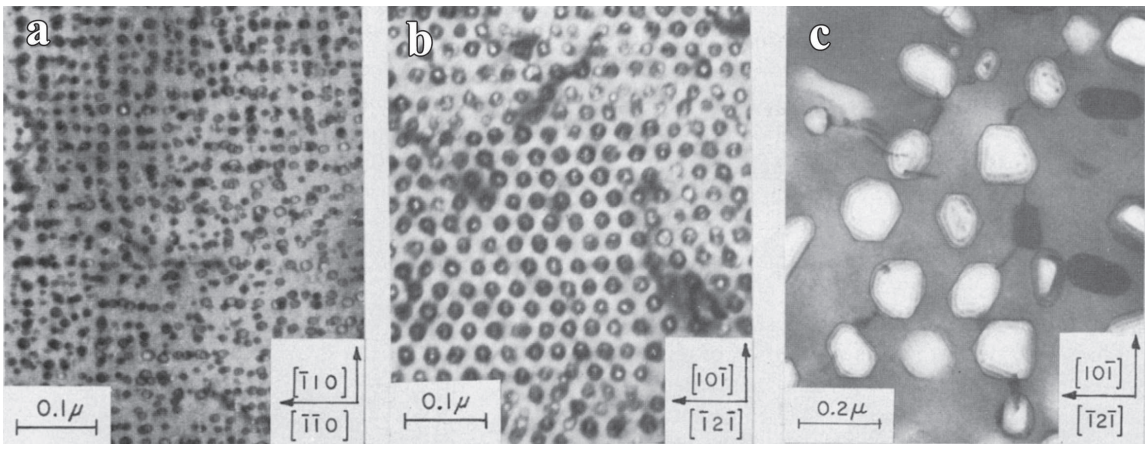


Figure 5.16: Temperature dependent evolution of bubble lattice: (a) 853°C, Nb+5500 PPM O, 50 DPA, 3.1 MeV $V^+$; (b) 880°C, Nb+1%Zr+3300 PPM O, 50 DPA, 3.1 MeV $V^+$; (c) 1015°C, Nb+1%Zr+4200 PPM O, 76 DPA, 3.1 MeV $Ni^+$ [53].

$V^+$ ion irradiated Nb [53]. The ordered void lattice formed at 880°C changes into randomly distributed voids at 1015°C (Fig. 5.16). The temperature for ordered void lattice formation ranges from 780 $\sim$ 880°C. And the spacing of void lattice is strongly dependent on the temperature of irradiation.

If density of randomly distributed void is high enough, it has been reported that, by considering elasticity and the dynamic diffusion process, annealing can give rise to the ordered void formation [109]. A phase field approach was employed and voids are treated as high vacancy concentration clusters. Elastic effects due to the existence of vacancies are calculated by the microelasticity theory. The free energy of mixing, interfacial energy and elastic strain energy were considered as the driving force for vacancy diffusion. The simulations suggest that the elastic anisotropy can induce orientational preference in vacancy diffusion, leading to the self-assembled voids to replicate the host crystal symmetry. As shown in Figs. 5.11- 5.14, faceted bubble with preferential orientation related to substrate is evident. However, because the source of interstitials whose continuous anisotropic diffusion is responsible for ordered

lattice formation is lacking during annealing, bubble can aggregate and grow, and as a consequence the same ordering as that shown in Fig. 1.9 can not be formed. As shown in Fig. 5.16c, even under irradiation, higher temperature annealing can also cause bubble to aggregate and destroy the ordered patterns. Thus the role of temperature can be summarized as following: at the beginning of irradiation, due to the preferential absorption of dislocations, the extra vacancies accumulate and form voids. At this stage, the temperature should be high enough that immigration of vacancy and interstitial is possible. As irradiation proceeds, the voids grow because of supply of vacancies. At this stage, if temperature is so high that coalescence of void occurs, the void can not form lattice (Fig. 5.16). Therefore, the temperature should be low enough that mobility of voids is suppressed. With continuous implantation, the saturation of interstitial absorption reaches and recombination between vacancy and interstitial keeps void size constant. But the anisotropic diffusion of interstitial along the close-packed directions should be driven by temperature. Therefore, the range of temperature which can make interstitial and vacancy move but not high enough to make void move is required for void lattice formation.

**Flux**

The ion flux and defect diffusion determine the defect mobility. The high ion flux can interrupt the diffusion of defects before defects reach their balance sites which are determined by temperature. Therefore, flux is always studied with diffusion coefficient. It can be expected that high (low) ion flux and high (low) temperature are favorable for ordered pattern formation. A suitable flux range related to temperature has been established in experiments. Fig. 5.17 shows the temperature and flux dependent ordered pattern formation for different ions irradiated Ni [58]. One important feature is that the ordered pattern (wall structure consisting of vacancies

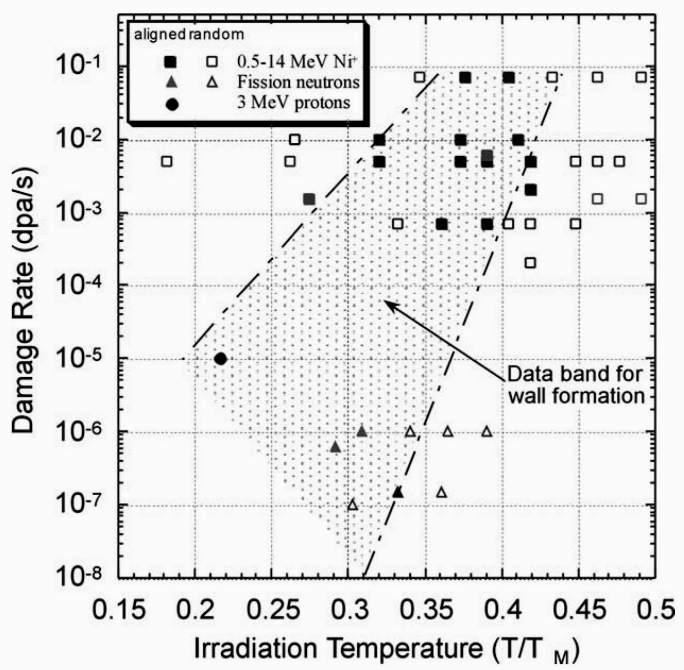


Figure 5.17: Temperature and dose dependent evolution of ordered patterns in irradiated nickel [58].

in this case as shown in Fig. 1.11) formation is achieved under the conditions of high (low) ion flux and high (low) temperature.

In a surface growth model for deposition, diffusion and aggregation system, the cluster size is determined by the competition between deposition and diffusion. The larger the flux, the less time is needed for deposited atoms to diffuse before meeting another atoms on the surface and consequently less spacing of clusters can be formed. The normalized flux $(f/D)^{-\psi}$ is used to describe the scaling property of mean diffusion length, where $f$ is flux of deposition, $D$ is diffusion coefficient. $D$ and $f$ are in unit of ML $s^{-1}$. The value of $\psi$ is 1$\sim$1/6, depending on the ratio of $f/D$ [170]. If we consider the production of vacancy induced by the ion beam bombardment as deposition process, the variation of radius with the flux and temperature can be ascribed to the ratio of these two terms.

**Dose**

It is well known that ordering starts from random distribution of defects and can be improved with continuous bombardment. The size of defect clusters also increases with increasing of dose. However, after ordered patterns forms, the size and ordering remain stable up to high damage levels. This reveals that at very beginning, dose provides the enough excess vacancies to form voids in random nuclear sites. The void will grow until the saturation of preferential absorption of interstials is reached. Beyond this critical dose, the recombination of vacancy and interstitial dominate and void stops growing. However, continuous bombardment provides a source of interstials whose anisotropic movement can improve the ordering before recombination with vacancies. Therefore, high dose is generally required for ordered pattern formation (Table. 1.2). The threshold dose for initial development of visible void ordering is a few DPA for BCC metals [41, 42, 53, 58]. Fully development void lattice can be achieved after dose levels of 30 DPA. 300 DAP for ordered void lattice has been reported on 7.5 MeV $Ta^+$ irradiated Nb at 800° [42]. The periodic arrays of dislocation loops and stacking-fault tetrahedral are generally observed at relatively low doses [42].

Because DPA is a function of penetration depth, as shown in cross-sectional TEM images of void distribution (Fig. 5.2), the largest DPA locates at the peak position of implanted ions and significant change of DPA also occurs close to peak position. Using dose (unite of ions/$cm^2$) to describe the damage level can not give the information of damage along the penetration depth.

**Energy**

When energetic ion passes through a material, there are two different energy loss mechanisms: electronic and nuclear collisions with the atoms. If energy transferred to the lattice atoms exceeds a threshold energy (normally 30 eV), displaced atoms are induced and Frenkel defects are created. Low energies (<1 keV) lead to the formation of isolated Frenkel defects while large energies (>1 keV) lead to displacement cascades characterized by a vacancy-rich core surrounded by self-interstitial atoms at their periphery. The ion energy determines the range of ion, displaced atoms density, and the size of cascade. From published experimental data (Table 1.2), generally, the energy for void lattice formation in metal is around several MeV. The two exceptions are 400 keV $Al^+$ irradiated Al and 400 keV $N^+$ irradiated Ni, but only partially ordered void arrangements are observed in these experiments [46,55]. Fig. 5.18 shows distribution of vacancy production along penetration depth calculated from Monte carlo simulation [80]. Due to dramatic change of vacancy density close to the peak position of implanted ions, the size of void is not uniform and as consequence the void lattice can not be formed in this region. Therefore, as shown in cross sectional TEM image for void distribution in Fig. 5.2 and bubble distribution in Fig. 5.6, a certain distance along which vacancy is uniformly generated is necessary for ordered pattern formation. This means that the penetration depth should be long enough for uniform void/bubble formation. In addition, several layers of ordered void and sputtering yield should be considered. If we assume that 5 void lattice unit cells are created along penetration depth for $Ni^+$ irradiated Nb, the length of these 5 cells is 175 nm from surface (from Table 1.2, the constant for void lattice is 35 nm). For 1 MeV $Ni^+$ ion irradiation, the average penetration depth is 300 nm (Fig. 5.18), and sputtering yield is 1.5 [80]. If the ion dose is $\sim 5 \times 10^{16}$ $cm^{-2}$ (from Table 1.2,

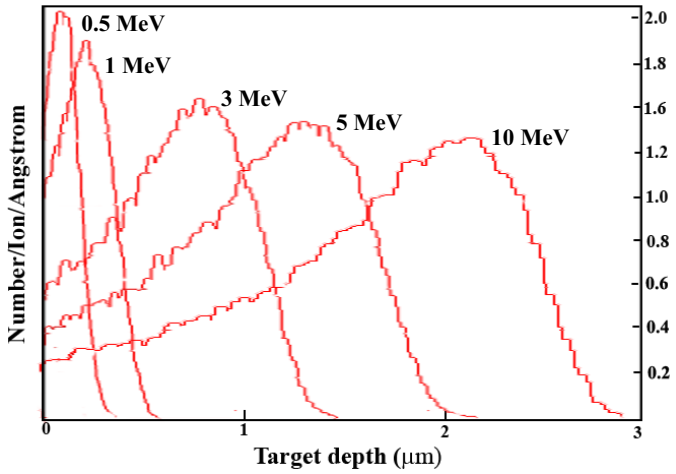


Figure 5.18: Variation of vacancies with penetration depth for different ion energies.

DPA= 30 $\sim$ 100), the thickness that is removed by ion can be $\sim$ 100 nm. By considering sputtering yield on the surface and thickness for randomly distributed voids, the penetration depth should be larger than 300 nm and corresponding ion energy should be higher than 1 MeV.

**Impurity effects**

The effect of alloying additions on void ordering is unclear. Several studies have observed similar void ordering behavior in Mo-0.5Ti [41, 43] and Nb-1Zr [53] alloys compared to the pure metals. Wiffen reported that void ordering was suppressed in Nb-1Zr compared to pure Nb [43]. However, it is possible that this difference may have been due to oxygen impurity effects rather than substitutional solute effects. Loomis observed that void ordering did not occur in Nb and Nb-1Zr specimens containing less than 60 ppm and 400 ppm oxygen, respectively [53].

## 5.4 Conclusion

In order to study the void/bubble distribution along penetration depth, cross-sectional TEM samples were made for ion irradiated materials. It was found that

uniform void/bubble is only formed before and after maximum concentration of implanted ions. The ordered He bubbles close to surface was found in cross sectional sample. The dependence of bubble evolution on the annealing temperature was studied. It was found that faceted bubbles are surrounded by {111} planes which are energy favorable. The parameters which affects void/bubble lattice formation were discussed.

# CHAPTER VI

# Summary and Future Work

## 6.1 Summary

Starting from sputtering yield, the ordered pattern formation in a broad range of materials was studied, including one-dimension periodic line arrays of Cu nanoparticles, two-dimensional patterns including highly ordered Ga droplets on the surface of GaAs, ordered nanocrystals on argon ion sputtered polymer film and hexagonally ordered nanoholes on the surface of Ge, and three-dimensional void/bubble formation in metals and semiconductors. In addition, the fundamental physical mechanisms underlying ordered pattern formation which involves ion sputtering, redeposition, viscous flow, and surface diffusion are determined through a combination of modeling and *in situ* and *ex-situ* observations.

Because all surface morphology changes are mainly determined by sputtering yield during ion irradiation, the sputtering yield was first discussed . An analytical formula is developed for the evolution of angular dependence of sputtering yields by extending Sigmund's theory. It was shown that the peak of sputtering yield at oblique incidence can be attributed to a balance between increased energy deposited on the surface by incident ion which enhances the sputtering yield and decreased depth traveled by recoil atom which reduces the sputtering yield. The predicted dependence

of sputtering yield on the incident angle is in good agreement with experimental observations.

The morphological evolution of ripples on $Cd_2Nb_2O_7$ pyrochlore induced by focused ion beam (FIB) bombardment has been followed by *in situ* electron microscopy. For a long time limit, the faceted ripples with terrace-like structure were observed at off-normal bombardment. The propagation direction oriented along the projected ion beam direction at the incident angles ranging from 35° to 65°. It was found that one side of terrace is perpendicular to the ion beam while the other side is parallel to the ion beam. The propagation velocity and direction were measured and discussed on the basis of this structure. A new model, based on the propagation of shock waves that self-selects a stable slope, has been developed for the explanation of this faceted ripple formation.

The development of copper nanolines induced by focused ion beam at normal bombardment has been investigated by *in situ* scanning electron microscopy. A periodic array of particles was observed when the width of lines reached a certain value. The stability of a nanowire is studied in terms of a model based on the Nichols and Mullins instability and curvature-dependent sputtering yield. A critical line width was found. When the line width is below this value, unstable mode whose wave vector is parallel to the line axis developed and a chain of periodic particle formed. When the width is above this critical value, the sputtering etching only leads to the decrease of width. The flux and temperature dependence of wavelength of nanoparticles was measured and explained based on this model.

Under off-normal bombardment without sample rotation, Ga droplets with size from 70 nm to 25 nm in diameter on the GaAs surface can self-assemble into a highly ordered hexagonal pattern instead of Ostwald ripening or coalescence. The

mechanism relies on a balance between anisotropic loss of atoms on the surface of droplets due to sputtering and anisotropic supply of atoms on the substrate surface due to preferential sputtering of As. The ratio of wavelength to the droplet radius predicted by this model is in excellent agreement with experimental observations.

Under certain sputtering conditions, highly ordered nanoholes were spontaneously generated on the Ge surface. Computer simulation demonstrates that this self-organized structure formation can be well explained by damped Kuramoto-Sivashinsky growth model involving interplay among ion sputtering, redeposition, viscous flow, and surface diffusion.

These nanosturctured materials exhibit considerably improvement of optical properties. For example, by irradiating the surface of a Ge wafer with low energetic ions, the originally shiny, flat surface is transformed into a hexagonally ordered, honeycomb-like structure of nano-scale holes. This patterned Ge possesses a high surface area and a considerable blue shift energy gap.

## 6.2 Suggestions for Future Work

This thesis addressed the pattern formation in a variety of materials under ion bombardment and provided a fundamental understanding of the dynamic mechanism involving sputtering, diffusion, viscous flow and redeposition. However, there are still many aspects of research that merit further consideration and investigation.

1. The well ordered nanocrystalline materials on the ion-sputtered thin polymer films have been fabricated. However, the effects of temperature, flux, incident angle were not studied due to the limitation of equipment. More efforts are need to invest the fabrication conditions in which we can further understand the mechanism and control our output.

2. Propagation of ripples was measured on the $Cd_2Nb_2O_7$ pyrochlore and a universal mechanism was proposed. General conclusions are more easily to draw from typical materials such as Si and $SiO_2$ than from more complicated materials. The further experiments using general materials are needed. In addition, the model in the thesis did not take any other effects into account that can cause redistribution of material (diffusion, viscous flow, redeposition) and therefore can change the slopes of the terraces. These effects can be studied by measuring temperature dependent propagation of ripples. Once obtained these experimental data, the dominant mechanism (slope-dependent sputtering, curvature-dependent sputtering, diffusion, viscous flow, redeposition) will be determined.

3. Although three dimensional numerical simulation from DKS model is consistent with the experimental observations, the physical meaning of each parameter related to sputtering yield was not clear. Based on Sigmund theory, the linear and nonlinear partial differential equation for pattern formation has been derived. Because the parameters describing the sputtering yield are very complex and some of them are not available, the values of parameters are assumed instead of calculation from sputtering yield when performing simulation. Thus efforts in the future can be focused on the determination of parameters from sputtering yield. Furthermore, due to the nonlinear effects, the simulation should be carried out for a longer time than that used in this thesis. And the comparison between nonlinear and linear simulations is beneficial to deep understanding the propagation mechanism.

4. The perfect hexagonal arrangement of droplet has been fabricated via ion sputtering. It was shown that the longer the exposure time the better the ordering can be obtained. In the experiment, the longest exposure time is one and half hours. It is well known that nonlinear effects will dominate for a lone time limit and

change the initial patterns. For example, the discontinuity of ripple was observed in ion erosion of $Cd_2Nb_2O_7$ pyrochlore for only about several minutes due to the nonlinear effects. The critical time when the nonlinear effects start to dominate is not known for Ga-Ge system. And consequently, What happened to well ordered nano-droplets under the non-linear effects is not known either. Therefore, long enough time exposure is valuable for improvement of understanding of this novel pattern formation.

5. It was found the hexagonally ordered nano-Ga droplet patterns remains intact after annealing at the temperature of 300°C . Since the melting point of bulk Ga is around 30°C, what is the mechanism for thermal stability? and what is the special interface structure between droplet and substrate? From spectrum of element mapping measured from STEM, the droplet consists of pure Ga and rich Ga was found on the surface of substrate due to preferential sputtering of As. What is the composition effects on the thermal stability? In addition, under certain irradiation conditions, the cone structure with the Ga droplet on the tip of cone was formed and ripples can also be induced. Hence, the systematical investigation of this system to establish the relationship between irradiation condition and structure is a major topic in the future.

6. The application of highly ordered Ga patterns can be studied in the future. One idea is to oxidize Ga droplet to form semiconductor. It has been shown that, from theory and experiment, this special arrangement semiconductor has unique optical properties and can be used in light emitting devices and solar cell devices. Many questions still surround the material properties, the source of the unique optoelectronic behavior, and other potential applications.

7. It was suggested that the balance of gain and loss of mass can limit the

growth of patterns under ion bombardment because sputtering occurs on both the substrate and ion-induced clusters (particles, droplets, holes). As a consequence, at steady state, the fixed size distribution of clusters form. Under this condition, inverse Ostwald ripening, i.e. the small clusters grow up at the expense of the larger clusters, can appear. However, although *in-situ* movie shows this interesting phenomenon, no kinetic formula was derived. Similar to the approach used to analyze the stability of Cu line in the thesis, by considering sputtering, diffusion and other mechanisms, this formula can easily be obtained in the future.

8. The fabrication of porous Si is an active research topic due to the significant improvement of physical properties and potential application in optical and electrical devices. One of this approach is to use ion sputtering to produce porous structure. Although this porous structures has been successfully created on the Ge, GASb and other semiconductors, no such features can be induced on the Si surface by ion sputtering so far. It was shown that damped Kuramoto-Sivashinsky (DKS) growth model can well predict the ion-induced pattern formation on the surface. If DKS growth model is universal, it can be also applied to the nanofibers on the Si surface. From DKS model, the redeposition and slope dependent sputtering play a critical role in pattern formation. Under this guidance, porous Si may be created in the future by changing irradiation parameters.

9. More efforts are needed to study the three dimensional void/bubble lattice formation. It has been reported that void/bubble can be created inside BCC and FCC metals under certain conditions. For void lattice formation, high temperature ($0.3 \sim 0.5T_M$), high energy (several MeV), and high dose (several tens dpa) are the prerequisites. Due to the limitation of existing equipment, all these conditions can not be satisfied simultaneously. And consequently, although numerical experiments

on void lattice formation has been tried, the void lattice was not experimentally observed so far. For bubble formation, cross-sectional information about bubble lattice was observed in our experiments. In order to fabricate and resolve the fundamental understanding of void/bubble lattice formation, the following suggestions can be made: (a) Single crystalline instead of polycrystal metals can be used in irradiation experiment. These samples should be electronically polished and annealed at temperature close to melting point. (b) It was found that bubble lattice formed in a narrow strip before and after peak position of implanted gas, which means the ordered bubble lattice prefers to form at low dose area. If this is true, lower fluence can be use to reach the same pattern. More experiments on the change of flux, temperature, energy, and fluence are needed to investigate void lattice formation. (c) If high fluence can be available, the high temperature and high dose which can not be reached simultaneously can be replaced by low temperature and low flux. The experiment may be carried out by existing equipment.

Part of the results contained in this thesis work has been published in or submitted to the following journals:

- **Q. M. Wei**, K. D. Li, J. Lian, L. M. Wang, "Angular dependence of sputtering yield of amorphous and polycrystalline materials", *Journal of Physics D-Applied Physics* 41 (2008) 172002
- **Q. M. Wei**, W. X. Li, K. Sun, J. Lian, L. M. Wang, "Morphological instability of Cu nanolines induced by $Ga^+$-ion bombardment: in-situ scanning electron microscopy and theoretical model", *Journal of Applied Physics* 103 (2008) 074306
- **Q. M. Wei**, J. Lian, S. Zhu, W. X. Li,, K. Sun, L. M. Wang, "Ordered inorganic nanocrystals on ion sputtered polymer film", *Chemical Physics Letters* 452 (2008) 124
- **Q. M. Wei**, J. Lian, W. Lu, L. M. Wang, "Highly ordered Ga nanodroplets on a GaAs surface formed by a focused ion beam", *Physical Review Letters* 100 (2008) 076103
- **Q. M. Wei**, K. D. Li, L. M. Wang, "Influence of the surface morphology on sputtering yields", *Journal of Physics D-Applied Physics,* revision
- **Q. M. Wei**, X. L. Zhou, B. Joshi, Y. B. Chen, K. D. Li, Q. H. Wei, K. Sun, L. M. Wang, "Self-assembly of ordered semiconductor nanoholes via ion sputtering", *Advanced Materials*, submitted

- **Q. M. Wei**, J. Lian, S. Zhu, L. A. Boatner, L. M. Wang, R. C. Ewing, "Shocks in ripples on pyrochlore induced by ion beam", *Physical Review B*, revision
- **Q. M. Wei**, K. Sun, L. M. Wang, "Guided Ge self-organization by focused ion beam", to be submitted
- **Q. M. Wei**, J. Lian, K. Sun, L. M. Wang, "Evolution of spherical particles under ion beam bombardment", to be submitted.
- X. L. Zhou, **Q. M. Wei**, L. M. Wang, and K. Sun, "Optical characteristics of highly ordered gallium oxide nano particles on GaAs", *Journal of Physics B*, (accepted)
- G. Ran , J. M. Zhang , **Q. M. Wei**, S. Q. Xi , X. T. Zu, L. M. Wang, "The effects of carbon coating on nanoripples induced by focused ion beam", *Applied Physics Letters*, (accepted)
- J. Lian, W. Zhou, **Q. M. Wei**, L. M. Wang, L. A. Boatner, R. C. Ewing, "Simultaneous formation of surface ripples and metallic nanodots induced by phase decomposition and focused ion beam patterning", *Applied Physics Letters* 88 (2006) 093112
- J. M. Zhang, **Q. M. Wei**, J. Lian, W. L. Jiang, W. J. Weber, R. C. Ewing, "Self-assembly of well-aligned 3C-SiC ripples by focused ion beam", *Applied Physics Letters*, 92 (2008) 193107
- X. Xiang, X. T. Zu, S. Zhu, **Q. M. Wei**, C. F. Zhang, K. Sun, L. M. Wang, "ZnO nanoparticles embedded in sapphire fabricated by ion implantation and annealing", *Nanotechnology*, 17 (2006) 2636

# APPENDICES

## APPENDIX A

# Wavelength from BH model

From Eq. 1.7, if we introduce a periodic perturbation function

$$h(x, y, t) = A \exp[i(k_1 x + k_2 y - \omega t) + rt] \tag{A.1}$$

the largest value of $r$ gives rise to the wavelength and orientation. Substituting Eq. A.1 to Eq. 1.7 gives

$$r = -(\nu_x k_1^2 + \nu_2 k_2^2) - K(k_1^2 + k_2^2)^2 \tag{A.2}$$

If $\nu_x < \nu_y$, the wave vector selected is $\mathbf{k} = k_1 \mathbf{x}$, where

$$k_1^2 = \nu_x / K \tag{A.3}$$

If, on the other hand, $\nu_y < \nu_x$, the observed wave vector is $\mathbf{k} = k_2 \mathbf{y}$, where

$$k_1^2 = \nu_y / K \tag{A.4}$$

Wavelength is given by $\lambda = 2\pi/k$. Substituting Eqs. 3.10, 3.11, and 3.13 into Eqs, A.3 or A.4, we obtain Eq. 1.8. Because the value of $\nu_x$ is smaller than that of $\nu_y$ for low incident angle while it is larger at high incident angle, the ripple wave vector is parallel to the projected ion beam direction when the incident angle is less than critical value, while the wave vector is perpendicular to the projected ion beam when the angle of attack is close to grazing incidence.

# APPENDIX B

# Numerical solution of PDE

## B.1 shock wave

In the following we sketch the numerical procedure used in solving shock wave equation (Eq. 3.21) governing the surface dynamics. The initial sinusoidal surface curve was assumed and we use Mathematica software to draw trajectories from 100 equally spaced points according to the slope and local incident angle (Eqs. 3.22 and 3.23). Fig. 3.13 is obtained from the following program.

```
% Clear constant %
Clear[n, w, Y, θ, A, B, x, g, f, k, l, h, Q]
% Variables: n is equally spaced point, w is incident angle, Y is sputtering yield
(here we assume a^2/2α^2 = 8 in Eq. 3.23), θ is incident angle, A is derivative of Y
with respect of θ, B is slope of trajectories (Eq. 3.22) %
n = 100
w = 40/180*π
Y = cos[θ] exp[−4 cos^2[θ]]
A = D[Y, θ]
B = (sin[θ] cos[θ]*A - Y)/(cos^2[θ]*A)
θ= Abs[π - w + Arctan[cos[x]]]
% x is step size. one period (2π) is calculated %
x = 2 π/n*i
% f[i] is slope for each point, g[i1] is sine curve %
Do[f[i] = B, {i, 0, n}]
Do[g[i1] = sin[2π/n*i1], {i1, 0, n}]
% Establishes coordinates (k[i2] and l[i3]) and trajectories (h[i4]), and plot %
Do[k[i2] = (2π/n*i2)*cos[w] + g[i2]*sin[w], {i2, 0, n}]
Do[l[i3] = -(2π/n*i3)*sin[w] + g[i3]*cos[w], {i3, 0, n}]
Do[h[i4] = l[i4] + (z - k[i4])*f[i4], {i4, 0, n}]
Q = Plot[Evaluate[Table[h[i6], {i6, 0, n}]], {z, -2, 2*π}, PlotRange → {{-2, 2π},
{2, -6}}, AspectRatio → 1]
```

## B.2 DKS growth model

Using standard discretization method with periodic boundary conditions, Eq. 4.17 can be numerically solved as following. Due to perpendicular bombardment, we have $\nu = D = \lambda = 1$. Only parameter $\alpha$ can be adjusted to give different morphologies.

```
% Clear constant %
Clear[t, x, m, n, f1, f2, i,j, v, k]
% Parameter definitions : t is the time step, x is step size , m is the size of the
box, n is the iteration, α is a damping parameter in Eq. 4.17 %
t = 0.005
x = 0.5
m = 512
n = 1000000
α = 0.23
% Initialize morphology to randomize %
SeedRandom[]
Do[f2[i, k] = 0.01 Random[], {i, -2, m + 2}, {k, -2, m + 2}]
% Begin time iteration %
For[j = 0, j ¡ n, j = j + 1,
% Calculate integration, here ∇h=(f2[i + 1, k] - f2[i - 1, k])^2/4/x^2,∇^2h=(f2[i +
1, k] - 2 f2[i, k] + f2[i - 1, k])/x^2,∇^4h=(f2[i + 2, k] - 4 f2[i + 1, k] + 6 f2[i, k]
- 4 f2[i - 1, k] + f2[i - 2, k])+2(-f2[i + 1, k + 1] + 2 f2[i + 1, k] - f2[i + 1, k - 1]
+2 (f2[i, k + 1] - 2 f2[i, k] + f2[i, k - 1]) - f2[i - 1, k + 1] + 2 f2[i - 1, k] - f2
[i - 1, k - 1])/x^4%
Do[f2[i, k] = f2[i, k] - t*f2[i + 1, k]/x^2 + 2 ∗ t/x^2 ∗ f2[i, k] − t ∗ f2[i − 1, k]/x^2−
t/x^4 ∗ (f2[i + 2, k] − 4f2[i + 1, k] + 6f2[i, k] − 4f2[i − 1, k] + f2[i − 2, k]) − t/x^2
*(f2[i + 1, k] - f2[i - 1, k])^2/4−α *t*f2[i, k] - t*f2[i, k + 1]/x^2 + 2 ∗ t/x^2 ∗ f2[i, k] − t∗
f2[i, k - 1]/x^2 − t/x^4 ∗ (f2[i, k + 2] − 4f2[i, k + 1] + 6f2[i, k] − 4f2[i, k − 1] + f2[i,
k - 2]) -t/x^2 ∗ (f2[i, k + 1] − f2[i, k − 1])^2/4 + 2 ∗ t/x^4 ∗ (−f2[i + 1, k + 1] + 2f2
[i + 1, k] - f2[i + 1, k - 1] + 2 (f2[i, k + 1] - 2 f2[i, k] + f2[i, k - 1]) - f2[i - 1, k +
1] + 2 f2 [i - 1, k] - f2[i - 1, k - 1]), {i, 0, m}, {k, 0, m}];
% Test for periodic boundary conditions %
Do[f2[-2, k] = f2[m - 2, k]; f2[-1, k] = f2[m - 1, k]; f2[m + 2, k] = f2[2, k]; f2[m +
1, k] = f2[1, k], {k, -2, m + 2}];
Do[f2[i, -2] = f2[i, m - 2]; f2[i, -1] = f2[i, m - 1]; f2[i, m + 2] = f2[i, 2]; f2[i,
m + 1] = f2[i, 1], {i, -2, m + 2}]]
% Plot %
ge = Table[f2[i, k], i, 0, m, {k, 0, m}];
ListDensityPlot[ge, Mesh → False, PlotLabel → {j, Date[]}]
```

# APPENDIX C

## Energy dependence of Ge surface morphology

Fig. C.1 shows evolution of Ge surface morphology under normal bombardment with ion energy larger than 5 keV. Worm-like structures were developed on Ge surface with large aspect ratio .

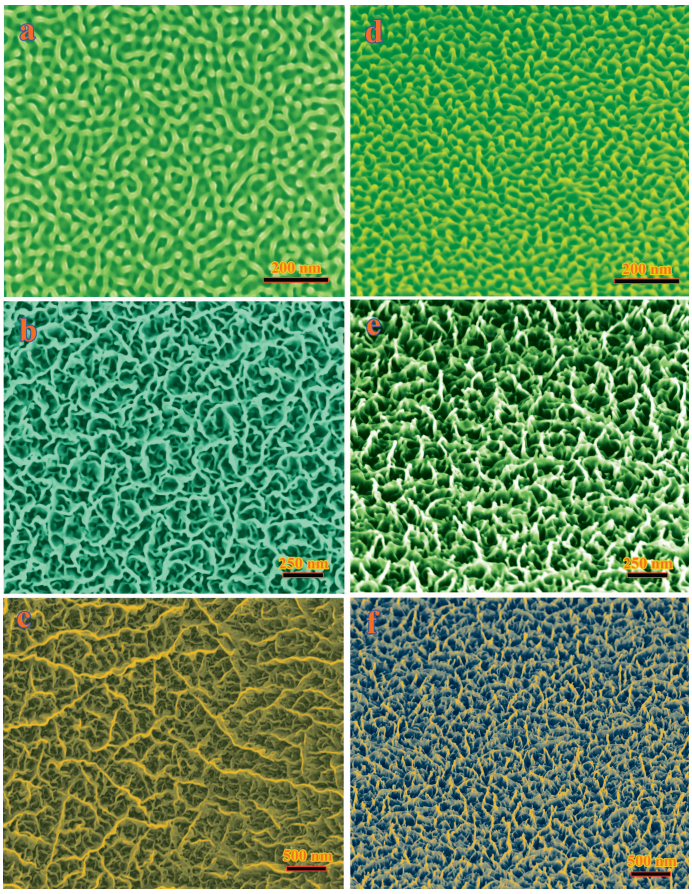


Figure C.1: SEM images of surface morphology at different energies. Left collum (images viewed from normal of surface): (a) 10 keV, (b) 20 keV, (c) 30 keV; right collum: the corresponding images viewed from 52° to the normal. Flux $2.2 \times 10^{15}$ $\mathrm{cm}^{-2}\mathrm{s}^{-1}$, bombardment time 5 minutes.

## APPENDIX D

# Bubble formation in electron-induced $CaF_2$

In contrast to ion-induced void/bubble formation, electron beam can also induce ordered patterns in some materials. Actually, The first observation of irradiation-induced nano-scale ordered patterns was array of defects in fluorite ($CaF_2$) before the voids were observed in irradiated metals. It was suggested that these ordered arrays are composed of calcium and anisotropic diffusion of F elements leads to the formation of ordered arrangement of calcium. However, From our experimental data (Fig. D.1), including STEM mapping (thickness and element) and subsequent annealing treatment, we found that these arrays consist of F instead of Ca.

In order to confirm our observation, we also performed experiments on the electron-irradiated $BaF_2$. It is well known that ordered clusters can not be formed in $BaF_2$, but the composition of clusters, according to the mechanism of formation of ordered patterns in $CaF_2$, should be Ba. Because the structure of Ba is body centered cubic (BCC) while the $BaF_2$ is face centered cubic (FCC), if cluster is composed of Ba, the lattice should be different between cluster and substrate. As shown in HRTEM image Fig. D.2, however, no difference can be found. Thus it can be drawn a conclusion that the clusters is bubble or void instead of Ba. Because the formation of void involves the movement of cations and ionization can not force the cations to move, the clusters are bubbles consisting of anions. According to the model based

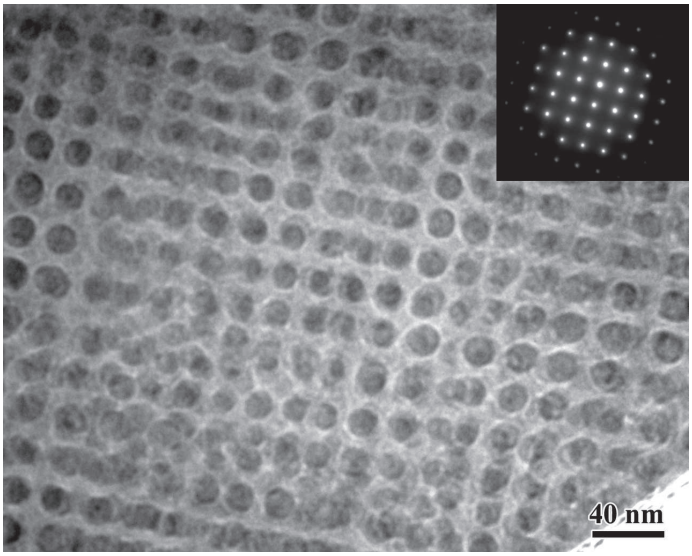


Figure D.1: Over focused TEM bright field image showing electron induced bubble lattice formation in $CaF_2$. Inset showing the diffraction patterns of substrate. Fluence $2 \times 10^{21}$e/cm$^2$, energy 300 keV.

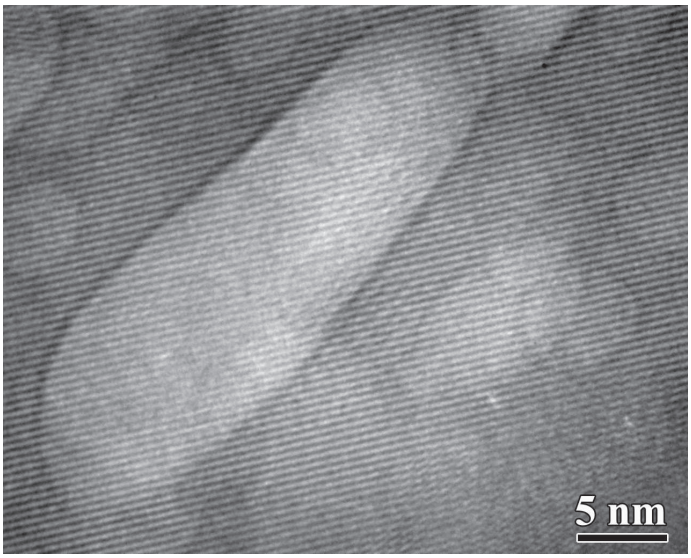


Figure D.2: HRTEM showing the electron induced bubble formation in $BaF_2$. Energy 300 keV, room temperature, fluence $2 \times 10^{22}$ e/cm$^2$.

on crystallographic anisotropic diffusion of self-interstitial atoms (SIAs) in host materials [41, 47, 48, 93–98], the anisotropic diffusion of F inside crystalline $CaF_2$ gives rise to the ordered bubble formation.

# BIBLIOGRAPHY

# BIBLIOGRAPHY


[1] M. Navez, C. Sella, and D. Chaperot. *Comptes Rendus.* **254**, 240 (1962).

[2] S. Rusponi, C. Boragno, and U. Valbusa. *Phys. Rev. Lett.* **78**, 2795 (1997).

[3] S. Rusponi, G. Costantini, C. Boragno, and U. Valbusa. *Phys. Rev. Lett.* **81**, 2735 (1998).

[4] S. Rusponi, G. Costantini, C. Boragno, and U. Valbusa. *Phys. Rev. Lett.* **81**, 4184 (1998).

[5] G. Carter, M. J. Nobes, F. Paton, and J. S. Williams. *Radiat. Eff.* **33**, 65 (1977).

[6] K. Elst, W. Vandervorst, J. Alay, J. Snauwaert, and L. Hellemans. *J. Vac. Sci. Tech. B* **11**, 1968 (1993).

[7] G. Carter and V. Vishnyakov. *Surf. Interface Anal.* **23**, 514 (1995).

[8] J. J. Vajo, R. E. Doty, and E.-H. Cirlin. *J. Vac. Sci. Tech. A* **14**, 2709 (1996).

[9] J. Erlebacher, M. J. Aziz, E. Chason, M. B. Sinclair, and J. A. Floro. *Phys. Rev. Lett.* **82**, 2330 (1999).

[10] E. Chason, T. M. Mayer, B. K. Kellerman, D. T. McIlroy, and A. J. Howard. *Phys. Rev. Lett.* **72**, 3040 (1994).

[11] C. M. Demanet *et al. Surf. Interface Anal.* **23**, 433 (1995).

[12] T. M. Mayer, E. Chason, and A. J. Howard. *J. Appl. Phys.* **76**, 1633 (1994).

[13] S. Habenicht, K. P. Lieb, J. Koch, and A. D. Wieck. *Phys. Rev. B* **65**, 115327 (2005).

[14] F. A. Stevie, P. M. SKahora, D. S. Simons, and P. Chi. *J. Vac. Sci. Tech. A* **6**, 76 (1988).

[15] K. Wittmaack. *J. Vac. Sci. Tech. A* **8**, 2246 (1990).

[16] S. W. Maclaren, J. E. Baker, N. L. Finnegan, and C. M. Loxton. *J. Vac. Sci. Tech. A* **10**, 468 (1992).

[17] C. C. Umbach, R. L. Headrick, B. H. Cooper, J. M. Balkely, and E. Chason. *Bull. Am. Phys. Soc.* **44**, 706 (1999).

[18] G. Garter and V. Vishnyakov. *Phys. Rev. B* **54**, 17647 (1996).

[19] A.-D. Brown, J. Erlebacher, W. L. Chan, and E. Chason. *Phys. Rev. Lett.* **95**, 056101 (2005).

[20] A.-D. Brown, and J. Erlebacher. *Phys. Rev. B* **72**, 075350 (2005).

[21] S. Park, B. Kahng, H. Jeong, and A.-L. Barabási. *Phys. Rev. Lett.* **83**, 3486 (1999).

[22] D. P. Datta and T. K. Chini. *Phys. Rev. B.* **69**, 235313 (2004).

[23] P. F. A. Alkemade. *Phy. Rev. lett.* **96**, 107602 (2006).

[24] B. Ziberi, F. Frost, Th. Höche, and B. Rauschenbach. *Phys. Rev. B* **72**, 235310 (2005).

[25] A. Karen, K. Okuno, F. Soeda, and A. Ishitani. *J. Vac. Sci. Tech. A* **4**, 2247 (1991).

[26] S. Facsko *et al. Science* **285**, 1551 (1999).

[27] F. Frost, A. Schindler, and F. Bigl. *Phys. Rev. Lett.* **85**, 4116 (2000).

[28] F. Frost, and B. Rauschenbach. *Appl. Phys. A* **77**, 1 (2003).

[29] F. Frost, B. Ziberi, T. Höche, B. Rauschenbach. *Nucl. Instrum. Methods Phys. Res. B* **216**, 9 (2004).

[30] B. Ziberi, F. Frost, and B. Rauschenbach. *Appl. Phys. Lett.* **88**, 173115 (2006).

[31] B. Ziberi, F. Frost, and B. Rauschenbach. *Surf. Sci.* **600**, 3757 (2006).

[32] R. Gago *et al. Phys. Rev. B* **73**, 155414 (2006).

[33] B. Ziberi, F. Frost, M. Tartz, H. Neumann, and B. Rauschenbach. *Appl. Phys. Lett.* **92**, 063102. (2008).

[34] T. Bobek, S. Facsko, H. Kurz, T. Dekorsy, M. Xu, and C. Teichert. *Phys. Rev. B* **68**, 085324 (2003).

[35] R. Gago, L. Vzquez, R. Cuerno, M. Varela, C. Ballesteros, and J. M. Albella. *Appl. Phys. Lett.* **73**, 3316 (2001).

[36] R. Gago, L. Vzquez, O. Plantevin, J. A. Sánchez-García, M. Varela, and M. C. Ballesteros. *Phys. Rev. B* **73**, 155414 (2006).

[37] Y. Yuba, S. Hazama, K. Gamo. *Nucl. Instrum. Methods Phys. Res. B* **206**, 648 (2003).

[38] T. Allmers, M. Donath, and G. Rangelov. *J. Vac. Sci. Tech. B* **24**, 582 (2006).

[39] F. Ludwig, C. R. Eddy, O. Malis, R. L. Headrick. *Appl. Phys. Lett.* **81**, 2770 (2002).

[40] G. Ozaydin, A. S. özcan, Y. Wang, K. F. Ludwig, H. Zhou, R. L. Headrick, and D. P. Siddons. *Appl. Phys. Lett.* **87**, 163104 (2005).

[41] J. H. Evans. *Nature* **229**, 403 (1971).

[42] G. L. Kulcinski, J. L. Brimhall, H. E. Kissinger. In *National Technical Information Service,* Corbett, J. W. and Iannello, L. C., editors, p. 465 (Springfield, VA, 1972, Albany, NY).

[43] W. F. Wiffen. In *National technical Information Service,* Corbett, J. W. and Iannello, L. C., editors, p. 386 (Springfield, VA, 1972, Albany, NY).

[44] S. Sass and B. L. Eyre. *Philos. Mag.* **27**, 1447 (1973).

[45] P. B. Johnson, D. J. Mazey, and J. H. Evens. *Radiat. Eff.* **78**, 147 (1983).

[46] D. J. Mazey and J. H. Evans. *J. Nucl. Mater.* **138**, 16 (1986).

[47] J. H. Evans and D. J. Mazey. *J. Phys. F* **15**, L1 (1985).

[48] J. H. Evans. *J. Nucl. Mat.* **132**, 147 (1985).

[49] A. Jostons and K. Farrel. *Radiat. Eff.* **15**, 217 (1972).

[50] J. O. Stiegler and K. Farrel. *Scr. Metall.* **8**, 651 (1974).

[51] G. Martin. *J. Nucl. Matt.* **205**, 394 (1993).

[52] C. Cawthorn and E. J. Fulton. *Nature* **216**, 575 (1967).

[53] B. A. Loomis, S. B. Gerber, and A. Taylor. *J. Nucl. Mat.* **68**, 19 (1977).

[54] A. Hoesewell and B. N. Singh. *Radiat. Eff.* **102**, 1 (1987).

[55] L. J. Chen and A. J. Ardel. *J. Nucl. Mat.* **75**, 177 (1978).

[56] K. Farrell and N. H. Packan. *J. Nucl. Mat.* **85-86**, 683 (1979).

[57] S. J. Zinle, B. N. Singh. *J. Nucl. Mat.* **283-287**, 306 (2000).

[58] N. M. Ghoniem, D. Walgraeef. and S. J. Zinkle. *J. Comput. Aided Mater. Des.* **8**, 1 (2002).

[59] P. B. Johnson, R. W. Thomson, and D. J. Mazey. *Nature* **347**, 265 (1990).

[60] W. Jäger, P. Ehrhart, and W. Schilling. *Soild State Phenomena* **3-4**, 297 (1988).

[61] M. C. Cross and P. C. Hohenberg. *Rev. Mod. Phys.* **65**, 851 (1993).

[62] D. Walgraef, J. Lauzeral, and N.M. Ghoniem. *Phy. Rev. B* **53**, 14782 (1996).

[63] R. Cuerno and A.-L. Barabási. *Phys. Rev. Lett.* **74**, 4746 (1995).

[64] R. Bradly and J. Harper. *J. Vac. Sci. Tech. A* **6**, 2390 (1988).

[65] M. A. Makeev, R. Cuerno, and A.-L. Barabási. *Nucl. Instrum. Methods Phys. Res., Sect. B* **197**, 185 (2002).

[66] J. Muñoz-García, M. Castro, and R. Cuerno. *Phys. Rev. Lett.* **96**, 086101 (2006).

[67] U. Valbusa, C. Boragno, and F. B. de Mongeot. *J. Phys. Condens. Matter* **14**, 8153 (2002).

[68] D. Walgraef, and N. M. Ghoniem. *Phys. Rev. B.* **39**, 8867 (1989).

[69] D. Walgraef and N.M. Ghoniem. *Phy. Rev. B* **52**, 3951 (1995).

[70] M. Nastasi, J. W. Mayer, J. K. Hirvonen. *Ion-solid Interactions: Fundamentals and Applications*. Cambridge University press, Cambridge, UK, (1996).

[71] J. Lindhard, V. Nielsen, and M. Scharff. *Mat. Fys. Medd. Dan. Vid. Selsk.* **36**, 10 (1968).

[72] Q. M. Wei, J. Lian, W. Lu, and L. M. Wang. *Phys. Rev. Lett.* **100**, 076103 (2008).

[73] Q. M. Wei, J. Lian, S. Zhu, K. Sun, W. X. Li, and L. M. Wang. *Chem. Phys. Lett.* **452**, 124 (2008).

[74] J. Lian *et al. Nano. Lett.* **6**, 1047 (2006).

[75] K. Zhao, R. S. Averback, and D. G. Cahill. *Appl. Phys. Lett.* **89**, 053103 (2006).

[76] A. Cuenat, H. B. George, K, C. Chang, J. M. Blakely, and M. J. Aziz. *Adv. Mater.* **17**, 2845 (2005).

[77] P. Sigmund. *Phys. Rev.* **184**, 383 (1969).

[78] P. Sigmund. *J. Mater. Sci.* **8**, 1545 (1973).

[79] J. Lindhard, V. Nielsen, and M. Scharff. *Mat. Fys. Medd. Dan. Vid. Selsk.* **36**, 10 (1968).

[80] J. F. Ziegler, J. P. Biersack, and U. Litttmark. *The stopping and range of ions in solid*, volume **1**, 53. Pergamon Press (1985).

[81] V. S. Sementkowski. *Prog. Surf. Sci.* **64**, 1 (2000).

[82] J. Bohdansky, J. Roth, and H. L. Bay. *J. Appl. Phys.* **51**, 2861 (1980).

[83] Y. Yamamura, N. Matsunami, and N. Itoh. *Rad. Eff.* **71**, 65 (1983).

[84] N. Matsunami *et al.* . *At. Data Nucl. Data Tables* **31**, 1 (1984).

[85] Y. Yamamura and N. Itoh. *Ion Beam Assisted Film Growth*, chapter 4. Elsevier (1989).

[86] J. Bohdansky. *Nucl. Instrum. Methods Phys. Res. B* **2**, 587 (1984).

[87] M. Castro, R. Cuerno, L. Vázquez, and R. Gago. *Phys. Rev. Lett.* **94**, 016102 (2005).

[88] S. Facsko, T. Bobek, A. Stahl, H. Kurz, and T. Dekorsy. *Phys. Rev. B* **69**, 153412 (2004).

[89] S. Vogel and S. J. Linz. *Europhys. Lett.* **75**, 884 (2006).

[90] W. W. Mullins. *J. Appl. Phys.* **28**, 333 (1957).

[91] M. Rost and J. Krug. *Phys. Rev. Lett.* **75**, 3849 (1995).

[92] R. Cuerno *et al. Phys. Rev. Lett.* **71**, 195405 (2005).

[93] A. J. E. Foreman. *AERE-R-7135, Atomic Energy Research Establishment* (1972).

[94] J. H. Evans. *Phy. Rev. E* **119**, 180 (1983).

[95] J. H. Evans. *Phil. Mag.* **85**, 1177 (2005).

[96] C. H. Woo, and W. Frank. *J. Nucl. Matt.* **137**, 7 (1985).

[97] C. H. Woo, and W. Frank. *J. Nucl. Matt.* **140**, 214 (1986).

[98] C. H. Woo, B. N. Singh, and A. A. Semenov. *J. Nucl. Matt.* **239**, 7 (1996).

[99] K. Malen, R. Bullough. In *Voids Formed by Irradiation of Reactor Materials,* S. F. Pugh, M. H. L. and Morris, D. I. R., editors, P. 109. Harwell AERE, (1971).

[100] A. M. Stoneham. *J. Phys. F.* **1**, 778 (1971).

[101] V. K. Tewary, and R. Bullough. *J. Phys. F* **2**, L69 (1972).

[102] V. N. Kuzovkov, E.A. Kotomin, and W. vonniessen. *Phys. Rev. E* **54**, 6128 (19996).

[103] G. Martin. *Phil. Mag.* **32**, 615 (1975).

[104] G. Martin. *Phy. Rev. B* **30**, 1424 (1984).

[105] R. Bullough, B.L. Eyre, and K. Krishan. *Proc. Roy. Soc. London Series A* **346**, 81 (1975).

[106] K. Krishan. *Nature* **287**, 420 (1980).

[107] S. M. Murphy. *Europhys. Lett.* **3**, 1267 (1987).

[108] R. A. Enrique, and P. Bellon. *Phys. Rev. B.* **6313**, 134111 (2001).

[109] H. C. Yu and W. Lu. *Acta Mater.* **53**, 1799 (2005).

[110] V.I. Dubinko, P.N. Ostapchuk, and V.V. Slezov. *J. Nucl. Matt.* **161**, 239 (1989).

[111] G.W. Greenwood, A.J.E. Foreman, and D.E. Rimmer. *Phy. Rev. E* **1**, 305 (1959).

[112] J. M. Bao, M. Tabbal, T. K, S. Charnvanichborikarn, J. S. Williams, M. J. Aziz1, and F. Capasso. *Opt. Expr.* **15**, 6727 (2007).

[113] M. Tabbal, T. Kim, J. M. Warrender, M. J. Aziz, B. L. Cardozo and R. S. Goldman. *J. Vac. Sci. Tech. B* **25**, 1847 (2007).

[114] T.-H. Her, R. J. Finlay, C. Wu, S. Deliwala, and E. Mazur. *Appl. Phys. Lett.* **73**, 1673 (1998).

[115] C. H. Crouch, J. E. Carey, J. M. Warrender, M. J. Aziz, E. Mazurb, F. Y. Génin. *Appl. Phys. Lett.* **84**, 1850 (2004).

[116] P. Sigmund. *Appl. Phys. Lett.* **14**, 114 (1969).

[117] Y. Yamamura. *Rad. Eff.* **80**, 57 (1984).

[118] H. Hansen, C. Polop, T. Michely, A. Friedrich, H. M. Urbassek. *Phys. Rev. Lett.* **92**, 246106 (2004).

[119] G. Carter. *J. Appl. Phys.* **85**, 455 (1999).

[120] M. A. Makeev and A.-L. Barabási. *Appl. Phys. Lett.* **73**, 1445 (1998).

[121] G. Falcone and P. Sigmund. *Appl. Phys.* **25**, 307 (1981).

[122] T. J. Whetten, A. A. Armstead, T. A. Grzybowski, and A. L. Ruoff. *J. Vac. Sci. Tech. A* **2**, 477 (1984).

[123] H. Oechsner. *Z. Physik* **261**, 37 (1973).

[124] P. Wetz, W. Kruger, A. Scharmann, and K. H. Schartner. *Rad. Meas.* **27**, 569 (1997).

[125] K. B. Winterbon, P. Sigmund, and J. B. Sanders. *Mat. Fys. Medd. Dan Vid. Selsk.* **37**, 5 (1970).

[126] Q. M. Wei, W. X. Li, K. Sun, J. Lian, L. M. Wang,. *J. Appl. Phys.* **103**, 074306 (2008).

[127] J. P. Biersack and W. Eckstein. *Appl. Phys. A* **34**, 73 (1984).

[128] M. Küstner, W. Eckstein, and E. Hechtl, J. Roth. *J. Nucl. Mater.* **265**, 22 (1999).

[129] D. N. Ruzic. *Nucl. Instrum. Methods Phys. Res. B* **47**, 118 (1990).

[130] M. A. Makeev and A.-L. Barabási. *Nucl. Instrum. Methods Phys. Res. B* **222**, 335 (2004).

[131] M. A. Makeev and A.-L. Barabási. *Nucl. Instrum. Methods Phys. Res. B* **222**, 316 (2004).

[132] D. P. Adam, M. J. Vasile, T. M. Mayer, and V. C. Hodges. *J. Vac. Sci. Technol. B* **21**, 2334 (2003).

[133] T. K. Chili, F. Okuyama, M. Tanemura, and K. Nordlund. *Phys. Rev. B* **67**, 205403 (2003).

[134] Q. M. Wei, K. D. Li, and L. M. Wang. *J. Phys. D: Appl. Phys.* **41**, 172002 (2008).

[135] M. Stepanova, S. K. Dew, and I. P. Soshnikov. *Phys. Rev. B* **66**, 125407 (2002).

[136] M. Küstner, W. Eckstein, and E. Hechtl, J. Roth. *Nucl. Instrum. Methods Phys. Res. B* **145**, 320 (1998).

[137] T. J. Whetten, A. A. Armstead, T. A. Grzybowski, and A. L. Ruoff. *J. Vac. Sci. Tech. A* **8**, 2246 (1990).

[138] P. Sigmund. *Sputtering by Ion Bombardment Physics and Applications*, volume 1. Springer, Berlin, (1981).

[139] P. Wetz *et al. Rad. Meas.* **27**, 569 (1997).

[140] W. Eckstein. *Nucl. Instrum. Methods Phys. Res. B* **232**, 108 (2005).

[141] S. Rusponi *et al. Phys. Rev. Lett.* **81**, 4184 (1998).

[142] G. Carter. *Phys. Rev. B* **59**, 1669 (1999).

[143] M. J. Nobes, J. S. Colligon, and G. Carter. *J. Mater. Sci.* **4**, 730 (1969).

[144] G. Carter, J. S. Colligon, and M. J. Nobes. *J. Mat. Sci.* **6**, 115 (1971).

[145] G. Carter, J. S. Colligon, and M. J. Nobes. *J. Mat. Sci.* **8**, 1473 (1973).

[146] D. J. Barber, F. C. Frank, M. Moss, J. W. Steeds, I. S. T. Tsong. *J. Mater. Sci.* **8**, 1030 (1973).

[147] J. Lian, X. T. Zu, K. V. G. Kutty, J. Chen, L. M. Wang, and R. C. Ewing. *Phys. Rev. B* **66**, 054108 (2002).

[148] J. Lian, L. M. Wang, S. X. Wang, J. Chen, L. A. Boatner, and R. C. Ewing. *Phys. Rev. Lett.* **87**, 145901 (2001).

[149] T. C. Kim *et al. Phys. Rev. Lett.* **92**, 246104 (2004).

[150] R. Cuerno *et al. Phys. Rev. Lett.* **75**, 4464 (1995).

[151] S. Park *et al. Phys. Rev. Lett.* **83**, 3486 (1999).

[152] A. S. Rudy, and V. K. Smirnov. *Nucl. Instrum. Methods Phys. Res., Sect. B* **159**, 52 (1999).

[153] T. Aste and U. Valbusa. *Physica A* **332**, 548 (2004).

[154] P. F. A. Alkemade. *Phys. Rev. Lett.* **96**, 107602 (2006).

[155] R. Smith, G. Carter, and M. J. Nobes. *Proc. R. Soc. Lond. A* **407**, 405 (1986).

[156] G. B. Whitham. *Linear and Non-linear Waves.* Wiley-Interscience, New York, (1974).

[157] E. Chason and W. L. Chan. *Nucl. Instrum. Methods Phys. Res., Sect. B* **242**, 232 (2006).

[158] S. Facsko *et al. Appl. Phys. Lett.* **80**, 130 (2002).

[159] L. Rayleigh. *Pro. London Math. Soc.* **10**, 4 (1878).

[160] F. A. Nichols and W. W. Mullins. *Trans. Metall. Soc. AIME* **233**, 1840 (1965).

[161] C. Redon, F. Brochard-Wyart, and F. Rondelez. *Phys. Rev. Lett.* **66**, 715 (1991).

[162] E. Chason, W. L. Chan, and M. S. Bharathi. *Phys. Rev. B* **74**, 224103 (2006).

[163] W. L. Chan and E. Chason. *Phys. Rev. B* **72**, 165418 (2005).

[164] W. L. Chan, N. Pavenayotin, and E. Chason. *Phys. Rev. B* **69**, 245413 (2004).

[165] W. L. Chan and E. Chason. *J. Appl. Phys.* **101**, 121301 (2007).

[166] R. L. Schoebel. *J. Appl. Phys..* **40**, 614 (1969).

[167] G. Ehrlich and H. Hudda. *J. Chem. Phys.* **44**, 1039 (1966).

[168] R. M. V. Murty, T. Curcic, A. Judy, and B. H. CooperRusponi, G. Costantini, C. Boragno, and U. Valbusa. *Phys. Rev. Lett.* **80**, 4713 (1998).

[169] J. Villain. *J. Phys. I* **1**, 19 (1991).

[170] P. Jesen *et al. Phys. Rev. E* **50**, 618 (1994).

[171] T. Michely and G. Comsa. *Nucl. Instr. and Meth. B* **82**, 207 (1993).

[172] M. Ritter, M. Stindtmann, M. Farle, K. Baberschke. *Surf. Sci.* **348**, 246 (1997).

[173] H. J. Ernst. *Surf. Sci.* **383**, L755 (1997).

[174] C. Herring. *J. Appl. Phys.* **74**, 301 (1950).

[175] M. A. Makeev, R. Cuerno, and A.-L. Barabási. *Appl. Phys. Lett.* **71**, 2800 (1997).

[176] W. R. Tyson and W. A. Miller. *Surf. Sci.* **62**, 267 (1977).

[177] U. Kürpick, A. Kara, and T. S. Rahman. *Phys. Rev. Lett.* **78**, 1086 (1997).

[178] M. E. T. Molares, A. G. Balogh, T. W. Cornelius, R. Neumann, and C. Trautmann. *App. Phys. Lett.* **85**, 5337 (2004).

[179] R. Bullough, B. L. Eyre, and K. Krishan. *J. Nucl. Mat.* **346**, 81 (1975).

[180] C. A. Volkert and A. M. Minor. *MRS Bull.* **32**, 389 (2007).

[181] H. S. Carlslaw and J. C. Jaeger. *Conduction of Heat in Solids.* Oxford University press, Oxford, UK, (1959).

[182] C. C. Umbach, R. L. Headrick, and K. C. Chang. *Phys. Rev. Lett.* **87**, 246104 (2001).

[183] S. G. Mayr, and R. S. Averback. *Phys. Rev. Lett.* **87**, 196106 (2001).

[184] R. L. Clough. *Nucl. Instrum. Methods Phys. Res. B* **185**, 8 (2001).

[185] S. Fracsko *et al. Science* **285**, 1551 (1999).

[186] S. O. Kim *et al. Nature* **424**, 411 (2001).

[187] W. A. Lpoes and H. M. Jaeger. *Nature* **414**, 735 (2001).

[188] L. Calcagno, G. Compagnini, and G. Foti. *Nucl. Instrum. Methods Phys. Res. B* **65**, 413 (1992).

[189] L. Calcagno and G. Foti. *Nucl. Instrum. Methods Phys. Res. B* **59**, 1153 (1991).

[190] C. D. Sofield *et al. Nucl. Instrum. Methods Phys. Res. B* **67**, 432 (1992).

[191] J. P. Salvetat *et al. Phys. Rev. B* **55**, 6238 (1997).

[192] P. J. Goodhew. *Nature* **235**, 437 (1972).

[193] M. Kojima, and H. Satake. *J. Polym. Sci. B* **20**, 2153 (1982).

[194] B. J. Spit. *polymer* **4**, 109 (1962).

[195] L. C. Sawyer. *J. Polym. Sci. C* **22**, 347 (1984).

[196] J. P. Follub and J. S. Langer. *Rev. Mod. Phys.* **71**, S396 (1999).

[197] P. Meakin. *Phys. Rep. Rev. Sec. Phys. Lett.* **235**, 189 (1993).

[198] M. L. Anderson, N. C. Bartelt, P. J. Feibelman, B. S. Swartzentruber, and G. L. Kellogg. *Phys. Rev. Lett.* **98**, 096106 (2007).

[199] E. V. Shevchenko *et al. Nature* **439**, 55 (2006).

[200] H. Fan *et al. Science* **304**, 567 (2004).

[201] F. X. Redl, K. S. Cho, C. B. Murray, and S. O'Brian. *Nature* **423**, 968 (2003).

[202] L. M. Wang and R. C. Birtcher. *Phil. Mag.* **64**, 1209 (1991).

[203] B. K. Chakraverty. *J. Phys. Chem. Solids* **28**, 2413 (1967).

[204] H. H. Anderson. In *Ion Implantation and Beam Processing,* Williams, J. S. and Poate, J. M., editors. Academic Press, New York, (1984).

[205] Z. Mitov and E. Kumacheva. *Phys. Rev. Lett.* **81**, 3427 (1998).

[206] G. M. Whitesides and B. Grybowski. *Science* **295**, 2418 (2002).

[207] I. L. Singer, J. S. Murday, and J. Comes. *J. Vac. Sci. Tech.* **18**, 161 (1981).

[208] N. Anderson and P. Sigmund. *Mat. Fys. Medd. Dan. Vid. Selsk.* **39**, 3 (1974).

[209] J. B. Malherbe, W. O. Barnard, I. Le R. Strydom, and C. W. Louw. *Surf. Interf. Anal.* **18**, 491 (1992).

[210] F. L. Williams and D. Nason. *Surf. Sci.* **45**, 377 (1975).

[211] J. Muñoz-García, M. Castro, and R. Cuerno. *Phys. Rev. Lett.* **96**, 086101 (2006).

[212] A. Pascale, I. Berbezier, A. Ronda, and P. C. Kelires. *Phys. Rev. B* **77**, 075311 (2008).

[213] B. Kahng, H. Jeong, and A.-L. Barabási. *Appl. Phys. Lett.* **78**, 805 (2001).

[214] F. Y. Li, L. Zhang, and R. M. Metzger. *Chem. Mater.* **10**, 2470 (1998).

[215] M. Paniconi and K. R. Elder. *Phys. Rev. E* **56**, 2713 (1997).

[216] G. S. Armatas and M. G. Kanatzidis. *Science* **313**, 817 (2006).